國立臺灣大學工學院土木工程學系

博士論文

Department of Civil Engineering

College of Engineering

National Taiwan University

Doctoral Dissertation

透明的紊流底床載傳輸：以折射率近似的材料

研究內部流場及其結構

Turbulent bed-load made transparent: internal flow structure from

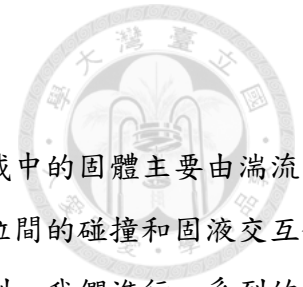refractive-index-matched experiments

倪瑋傑

Wei-Jay Ni

指導教授：卡艾瑋 博士

Thesis Advisor: Dr. Hervé Capart

中華民國 107 年 7 月

July, 2018

摘要

紊流底床載傳輸是改變地貌的主要地球物理現象之一，它不像懸浮載中的固體主要由湍流支持，也不像土石流藉由固體顆粒間的碰撞主導固體顆粒。紊流、顆粒間的碰撞和固液交互作用力在紊流底床載傳輸中相互影響且不可忽略。為理解這些耦合機制，我們進行一系列的物理實驗，研究在理想條件下之紊流底床載傳輸：牛頓液體於穩定和近均勻的紊流流場條件下在矩形通道中流經可沖蝕底床之底床載傳輸，我們於水槽實驗中應用了三個實驗邊界條件：光滑牆壁光滑槽底、光滑壁面粗糙槽底和粗糙壁面粗糙槽底預期看到不同之流場變化。實驗材料選擇折射率近似的物質—固體顆粒採用相同粒徑之球形聚甲基丙烯酸甲酯(PMMA)顆粒，液體則採用染色之對位傘花烴（para-cymene），藉此特性可對水槽全斷面進行內部成像分析測量。在成像測量中，我們使用橫向鐳射掃描來獲得固體和液體於水槽全斷面的運動資料，另外開發縱向掃描法以獲得掃描體積內之固體體積比分布。在此基礎上，我們採用體積相平均法計算高解析度的固相和液相的平均速度分布和固體濃度分佈。影像測量結果與水槽的出口通量比對確認滿足守衡條件。我們通過將斷面上之流場強度分佈劃分為傳輸域、總流通域和清液域，計算與輸砂率相關的因素，得出輸砂率組成因素與運動學無因次參數:流度數，與動力無因次參數：希爾斯數的關係符合對數方程。最後以光滑壁面邊界的兩組實驗資料，假設二相均為連續體且斷面方向速度、濃度均勻分布，計算並建立固液兩相動量平衡方程中每一項的實驗垂直剖面資料，發現需考慮對流加速項才可得到滿足力平衡並進而計算出固液兩相之剪切應力分布與阻力分布。由這些應力剖面資料我們測試分子運動學理論和阻力關係經驗式，本研究證實在穩態紊流底床載傳輸、雷諾數介於約 5000-12000 之條件下，除濃度過低與過高之固體傳輸層外，其固體正向與剪切應力滿足分子動力學理之本構關係，我們還發現源自孔隙介值流和顆粒流體化試驗的阻力關係經驗式，經考慮顆粒擾動速度之貢獻後可描述於紊流底床載傳輸二相於相對流場中之阻力關係。

Abstract

The bed-load transport is one of the major geophysical phenomena that change the landscape, it doesn't like suspended-load transport for which the solid is primarily supported by turbulence, and it doesn't like the debris flow which is dominated by the collisions between solid grains. The mechanism of turbulence, granular collisions, and inter-phase forces all play a role and mutually influence each other in the turbulence bed-load transport, and none of these can be neglected. To understand these coupled mechanism, we conducted series of physical experiments to explore the turbulent bed-load transport under idealized conditions: steady and nearly uniform turbulent flow of Newtonian liquid over erodible and identical deposits in a rectangular channel, we applied 3 boundary conditions to the experiments: smooth wall smooth floor, smooth wall rough floor and rough wall rough floor. The refractive-index-matched materials, the identical and spherical PMMA beads as solid grains and para-cymene as the liquid, were adopted and were applied the internal imaging measurements to the liquid-granular flow. For imaging measurements, we used transverse laser scans to acquire the motion of solid and liquid over the channel cross-section, and we developed longitudinal scans method to obtain the solid fraction distribution over the channel cross section. With the measurements, we calculated the averaged velocity distribution of solid and liquid phases, the solid fraction distributions by the volumetric phase-averaging approach with high resolution. The results were validated by measured discharges from the channel outlet and in good agreement. The internal flow structures were characterized by dividing the flow into transport domain, flow domain, and clear liquid domain to calculate the factors related to transport rate, we found the relationship between the factors composing transport rate and kinematic parameter, Mobility number, and dynamic parameter, Shields number. Further, for the experiments of the smooth wall cases, we established each term of the momentum balance equations for solid and liquid phases, we found that the convective acceleration term might be large and need to be considered, the shear stress profiles of solid and liquid were also obtained. From those profiles we tested the stress relation described by kinetic theory and the drag relation by empirical law, we confirmed that for steady state turbulent bed-load transport, and with Reynolds number range 5000-12000, the solid stresses could be described by the constitutive relations of the kinetic theory. We also found that the drag force relation derived from fixed pack and fluidization cell could be applied to turbulent bed-load if the contribution from solid velocity fluctuation was considered.
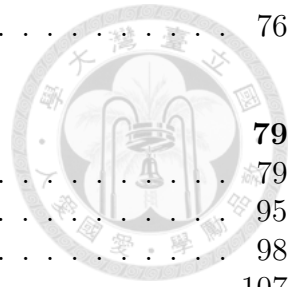
Contents

---

[1]Most of the materials in this Chapter was earlier presented in the publication: Ni, W.-J., and Capart, H. (2015). Cross-sectional imaging of refractive-index-matched liquid-granular flows. *Experiments in Fluids* 56, 163.

[2]Most of the materials in this Chapter was earlier presented in the publication: Ni, W.-J., and Capart, H. (2015). Cross-sectional imaging of refractive-index-matched liquid-granular flows. *Experiments in Fluids* 56, 163.

---

[3]Most of the materials presented in this Chapter was earlier presented in the publication: Ni, W.-J. and Capart, H. (2018) Stresses and drag in turbulent bed-load from refractive-index-matched experiments. *Geophysical Research Letters*, in press, GRL57678.
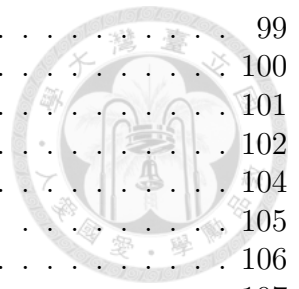
List of Figures

List of Tables

Introduction

Bed-load transport is one of the primary processes affecting river change (*Bagnold*, 1956; *Frey and Church*, 2009), although laminar bed-load is possible in laboratory experiments (*Aussillous et al.*, 2013; *Houssais et al.*, 2015; *Allen and Kudrolli*, 2017), in natural rivers bed-load is driven by turbulent water flow water. Under severe flooding condition,like those due to typhoons in Taiwan, bed-load transport ratio can become very high, causing serious damage to the infrastructures, landscape and threatening people's homes and lives.
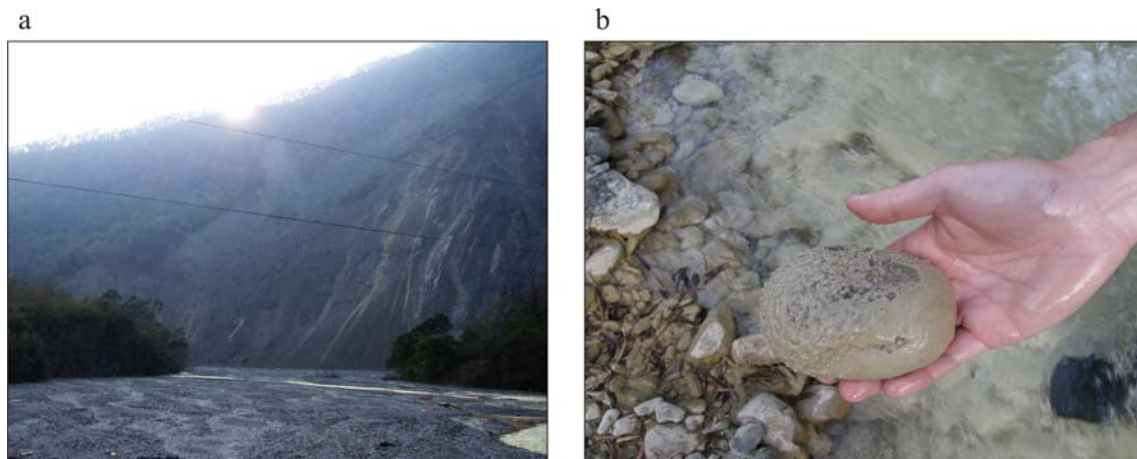
Figure 1 The natural channel in the mountain: **a** Laonong river at low level and **b** its coarse deposits. (photos by H. Capart)

Figure 1 shows a valley in Laonong river watershed, which locates in a mountainous region of Kaohsung, Taiwan. the photo was taken when the water level were relatively low, large portions of river bank and abandoned channels were exposed, and many coarse grains, like pebbles and gravels, can be observed spreading around the bank, the typical size of the grain is shown in Figure 1**b**. While during the one of the serious extreme weather event: Typhoon Morakot hitted Taiwan in 2009, the heavy rain brought tons of water into the valley and created a flood reaching bankfull discharge at the same site, as shown in Figure 2**a** , the very large and muddy discharge carrying with wood, fine sand and coarse grains flow rapidly down to the valley, destroyed the foundation of the road and bridge piers, houses near river were destroyed, too. Another example is Lu-shan in Nantou county, the town is located near Wushe stream, the place suffered huge losses and damages during the Typhoon Sinlaku in 2008, the landslides in upstream reach brought large amount of debris into the stream, these debris mixed with fine and coarse grains were taken by the flood and transported directly to the downstream reservoir, Figure 2**b** illustrates the aftermath of flooding in Lu-shan, the original valley was buried by the deposits, although we can't measured the depth of bed-load transport layer while it was

flooding, but we can estimate the amount of deposits the flood brought. To measured the bed-load transport under the conditions like Figure 2a is nearly impossible till now, the muddy water and strong flow make it inaccessible, we don't know exactly how the coarse grain be transported, how thick the transport layer was? and how the bed-load transport rate distributed in the cross section and how it varied with different type of river bank? these questions need be answered by the scientists and engineers.
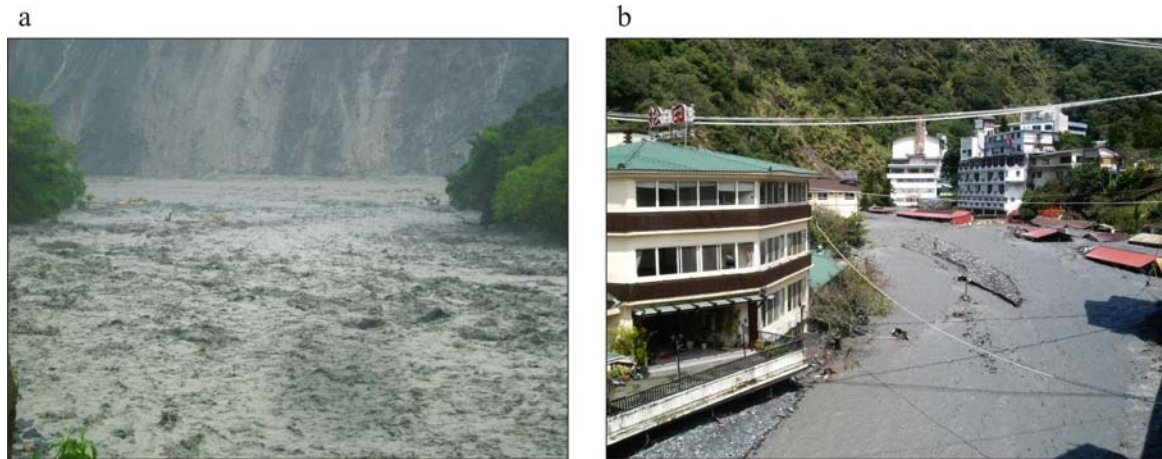
Figure 2 The Laonong river during Typhoon Morakot and Lushan after Typhoon Sinlaku; **a** Laonong river at bankfull discharge, the same site as Figure 1; **b** over one floor deposition brought by the stream in Lu-shan after the flood caused by Typhoon Sinlaku. (photos by local people, provided by H. Capart)

The turbulent bed-load transport is a special case of the sediment transport phenomena, it doesn't like suspended-load transport for which the solid is primarily supported by turbulence, and it doesn't like the debris flow which is dominated by the collisions between solid grains. these mechanisms, turbulence, granular collision, and the inter-phase forces all play a role in the turbulent bed-load transport, none of them is negligible, and they mutually influence the motion and the distribution of the solid and liquid phase in the mixture. To understanding these coupled mechanism, we have to measure the motion, distribution and proportions with good spatial coverage for solid and liquid phases. We adopt the physical experiment as th method to explore the turbulent bed-load transport under the idealized conditions, which is contrary to the complexity encountered in nature, the flow condition of the experiments would be steady state, nearly uniform turbulent flow of Newtonian liquid in a straight channel over erodible deposit which were composed of identical and spherical grains. Although we bring the phenomena to the laboratory scale, the challenges for measurements are still unsolved, to measure the flow behavior without making interruptions and to acquire as much information for both phases as possible are what we concerned.

Many experimenters use opaque grains with water or other transparent liquid then observe the solid and liquid behavior from the transparent channel side wall, leaving the internal flow unobserved (*Sumer et al.*, 1996; *Capart et al.*, 2002; *Spinewine et al.*, 2011; *Armanini et al.*, 2005; *Capart and Fraccarollo*, 2011; *Spinewine and Capart*, 2011). Figure 3 shows the example of experiment using opaque grains and water, the experiments were conducted by Prof. L. Fraccarollo at University of Trento, they used white cylindrical PVC
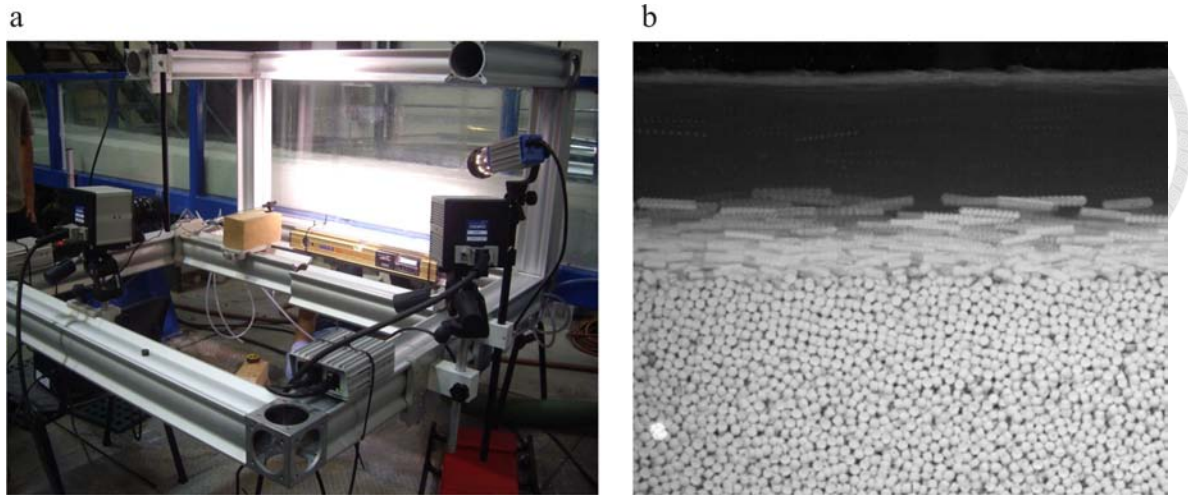
Figure 3 The bed-load transport experiments using PVC grains and water in wide channel, University of Trento; **a** the experimental set-up; **b** the footage recorded through side wall.(photo taken by H. Capart at University of Trento lab of Prof. L. Fraccarollo)

grains and water for the experiments, a thick layer of grains were put into the channel as the erodible deposits, and made the flow uniform by adjusting the channel inclination, near-wall the measurements of particle velocity and solid fraction profiles were acquired using PTV and laser stripes. Another approach is developed by using a narrow channel that only allowed one layer of grains moving inside the channel (*Chi*, 2007; *Böhm et al.*, 2006; *Frey*, 2014), the images of experiments from Prof. P. Frey are illustrated in Figure 4 ,they used glass grains and water flowing in a narrow channel, an artificial roughness layer was installed on the channel floor, the configuration reduced the flow to 2 dimensional, and obtained the measured profiles of solid velocity and solid fraction.
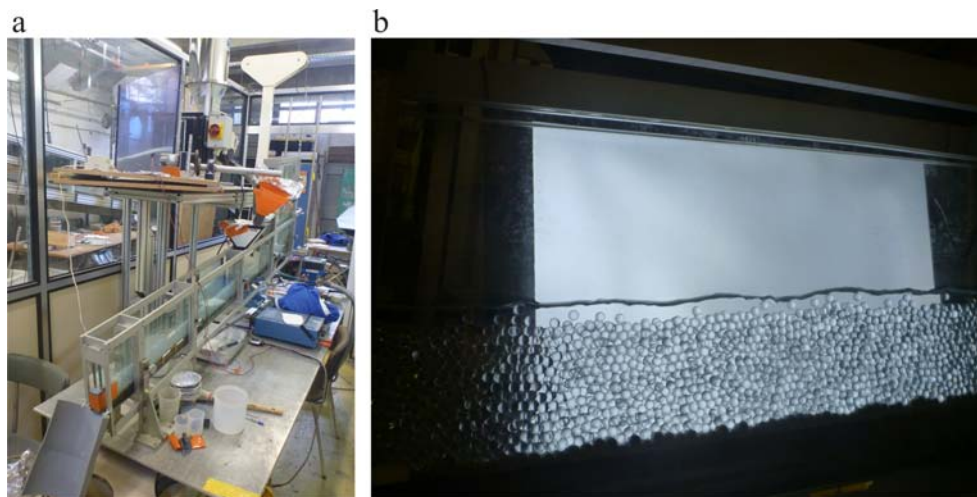
Figure 4 The bed-load transport experiments using glass grains and water in narrow channel; **a** the experimental set-up; **b** the footage recorded through side wall.(photos taken by H. Capart at Université de Grenoble lab of Prof. P. Frey)

For the internal imaging measurements, it have been applied to the liquid-granular flow but restricted to single profiles (*Revil-Baudard et al.*, 2015) or planar cross sections

3

through the flow in the transverse (*Chi*, 2007) or in the longitudinal direction (*Mouilleron et al.*, 2009; *Aussillous et al.*, 2013; *Houssais et al.*, 2015). For the static or quasi-static granular assembly, various researcher have reported tomographic measurements acquired from volumetric scan (*Konagai et al.*, 1992; *Huang et al.*, 2008; *Dijksman et al.*, 2012; *Brodu et al.*, 2015). Simultaneous velocity and concentration measurements have also been acquired by MRI and acoustic methods (*Ovarlez et al.*, 2006; *Revil-Baudard et al.*, 2015). Whether acquired by optical or other techniques, the resolution of the velocity and concentration measurements has so far been limited to scales greater than the grain diameter, except for special circumstances like mono-layers (*Frey*, 2014) or systems composed of only a few large spheres (*Hsu and Capart*, 2007).

To overcome these limitations, we use the refractive index-matched liquid and solid materials to make the mixture transparent, and we adopted the volumetric laser scanning to highlight the solid and liquid over a three dimensional volume, and measure the velocities and concentration using the imaging agorithms describe in *Ni and Capart* (2015), the concept is illustrated in Figure 5. Similar techniques have been reported earlier which were applied to the laminar bed-load (*Aussillous et al.*, 2013; *Houssais et al.*, 2015; *Allen and Kudrolli*, 2017). Here we applied the method to conduct turbulent bed-load experiments and determine the principle contributions to the solid discharge and to the momentum balance of each phase.
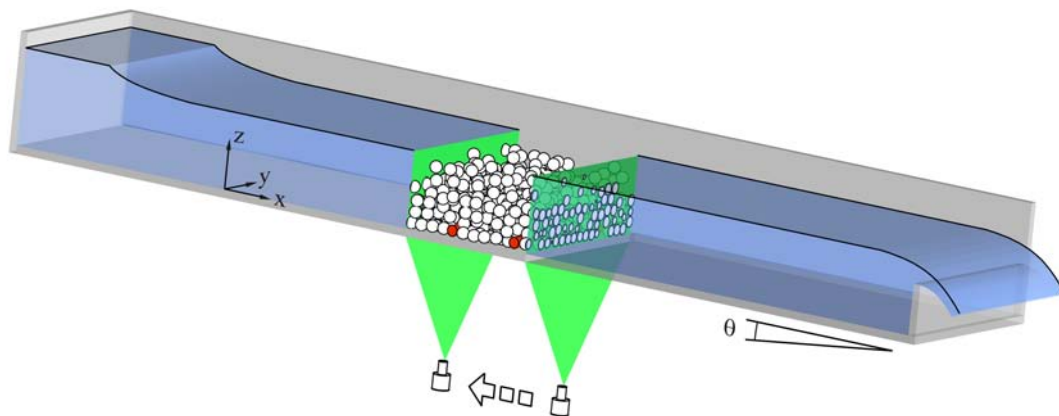
Figure 5 The conceptual sketch of the bed-load transport experiment using refractive-index-matched materials, the grains (white) immersed in the liquid were invisible (blue), except for being illuminated by the laser sheet (green), channel boundary could be changed by installing cylinders (red) on the channel floor or along the side walls.

In chapter 1 We introduce the design and operation of the experiments to create a steady and uniform turbulent bed-load flow using refractive index-matched materials, the jet entrainment mechanism were used to transport the solid grain and liquid. Some specific treatments needed for the RIM materials. The procedure of experiments and the flow conditions of each experiment were also explained in detail, as well as the three channel boundaries we adopted. Several characteristic tests were done to obtain the material properties and they are introduced in the last section.

In chapter 2, we introduce the methods we adopted to measure the solid and liquid veloc-

ity by using transverse laser scanning, we explain the measurement set-up and imaging method we used, explain the improvements we had done to reduce the error. We introduce the method called longitudinal scanning to obtain the grain positions and velocities one by one over the entire scanning voxel.

In Chapter 3, we calculated the averaged distribution of physical quantities with respect to specific plane in the scanned voxel. First, we introduce the phase-averaging approach described by *Drew* (1983), this volume-averaging based approach help us to calculate averaging velocity and volume fraction distribution from the PTV data. Second, we took averaged to the data over the longitudinal and cross-sectional direction , showing the flow patterns and grain organizations for different channel boundaries. As the results, We obtained the averaged solid velocity, liquid velocity and solid fraction maps over $[y, z]$ and $[x, z]$ plane with grid size 10 times finer than grain diameter. Finally we calculated the volumetric solid and liquid discharge for all runs, and compared them with the discharges we measured at channel outlet during experiments to check the validity of measurements by mass balance relation.

In Chapter 4, we develop a method to describe and characterize the internal flow structure by using the averaged maps of solid fraction, solid velocity and liquid velocity, and calculate the factors related to th e bed-load transport in order to quantify and show what are the major factors that dominate the change of the flow for various channel boundaries, and to compare the factors with the classical bed-load transport relations. In Sec. 4.1, we developed a method to divide the cross-sectional flow maps into different domains using the averaged solid and total discharge maps, and we defined the domain of total flow, the bed-load transport domain, and clear liquid domain. The comparisons were made with 3 channel boundaries to show the influences of the boundaries on the solid and total discharge distribution. In Section 4.2, we used the defined domains to calculate a series of bed-load transport factors from the discharge maps, reduced the maps to the factors related to solid fraction, transport area, and transport velocity, then tested the dependency of the factors and the total solid discharge. Finally, in Section 4.3, we made the factors dimensionless then compared them with the kinematic parameter, the Mobility number, and dynamic parameter, the Shields number, to clarify how the kinematic and dynamic parameters respond to the variation of flow factors caused by channel boundary change, and we also tested some choices of variables that be used to normalize the Mobility number and Shields number.

In Chapter 5, we selected the experiments closed to two dimensional sheet flow for further analysis. The objective is to establish the momentum balance equations for solid and liquid phase by the data measured from experiments, and characterize the growth and decays of the shear stresses and the inter-phases force within the flow and transport layers, and compared with the theories and empirical laws. First we would use the phase-averaging maps obtained in Chapter 3 to calculate the vertical profiles for both phases by depth integration method, then recovered each terms in the two dimensional momentum balance equation for steady state turbulent bed-load flow, these would be introduced in Section 5.1. In Section 5.2 we would test the stresses relations and drag force relation which were adopted to model the particle flow and sediment transport, the profiles of granular pressure P_S and liquid shear stress τ_L were calculated directly from measurements, and the solid shear stress and the drag force f_D profiles which were deduced from the mo-

mentum balance equations.For shear stresses and granular pressure, we normalized these data and compared with the predictions of kinetic theory (*Jenkins and Hanes*, 1998). For drag force, we adopt the empirical relation proposed by *Di Felice* (1994), after verifying the relation applied to seepage tests and the experiments, we found that to applied the relation to turbulent bed-load condition, the contribution from granular collisions must be considered.

6
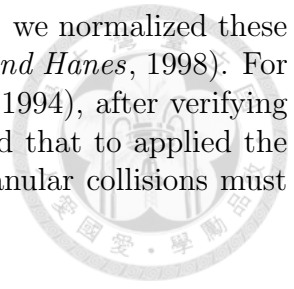
Chapter 1

Turbulent bed-load experiments

In this chapter we introduce the design and operation of the experiments, explained the configurations to create a steady and uniform turbulent bed-load flow using refractive index-matched materials, the jet entrainment mechanism were chose to transport the solid grain and liquid steady, and we also introduced the specific treatments needed for the RIM materials. The procedures of experiments and the flow conditions of each experiment were also explained in detail, as well as the three channel boundaries we applied to the experiments. Several characteristic tests that we have done for obtaining the material properties were introduced in the last section.

1.1 Refractive-index-matched materials

The materials we chose for the experiments are refractive index-matched, this property makes the solid-liquid mixture optical accessible, the liquid is para-cymene which is the organic liquid oil with composition of 1-methyl-4-(1- methylethyl)-59 benzene, imported from Millenium Specialty Chemicals Inc.. The solid grains are 7 mm in diameter spherical grains made by transparent PMMA. The index of the liquid is about 1.489 and of the PMMA is about 1.49, because there is still a little difference in refractive index, the temperature control is crucial for the index matching performance, after a series of tests we found that the best temperature for index matching is about 17°C, the effect of refractive index matching is illustrated as Figure 1.1. The basic properties of the PMMA grains and Para-cymene were obtained by series of tests, they are listed in Tabel 1.4, the detailed description of the tests were documented in Section 1.4.
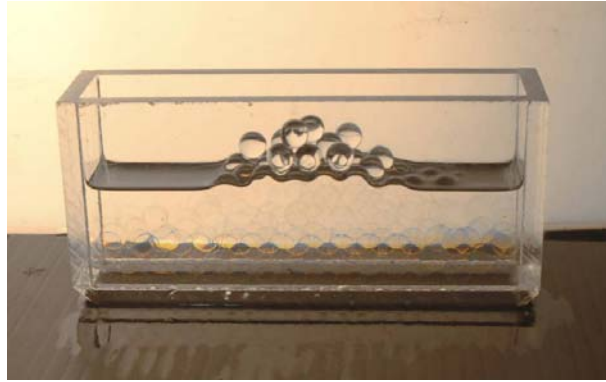
Figure 1.1 The refractive-index matched materials: PMMA solid spheres and para-cymene.

1.2 Experimental-setup and procedures

1.2.1 Experimental set-up
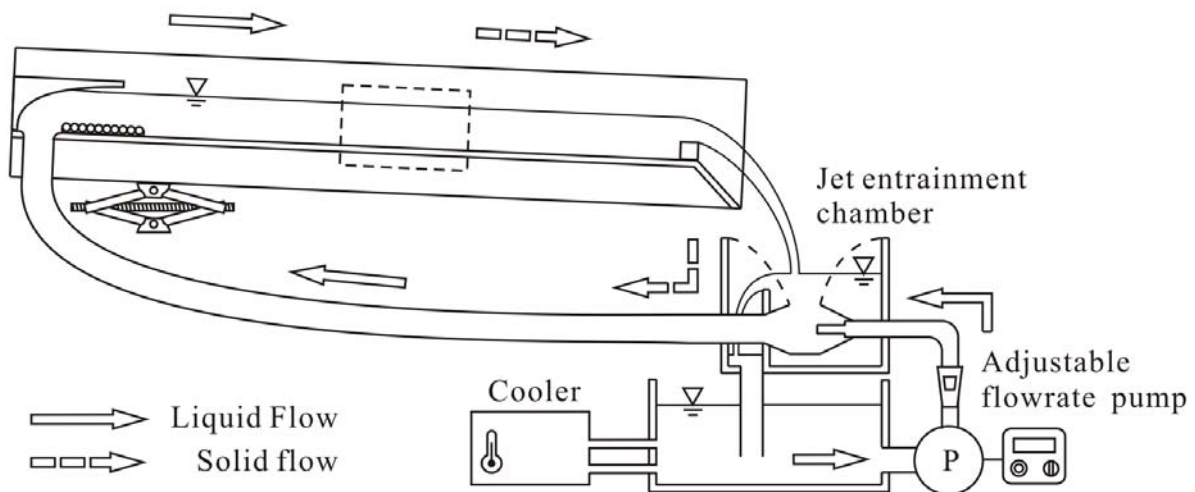
Figure 1.2 Conceptual sketch of the channel and the circulation system.

The set-up were composed by the channel and circulation system (Figure 1.2), they were customized to meet two objectives, to make the flow uniform condition over longitudinal direction and establishing the steady. To satisfying first objective, we built a channel which can quickly change the slope an adjust the transverse level. The channel is 1.3 meters in length and 0.12 m in width, the side walls and the bottom were made by transparent PMMA plates for optical accessibility. To prevent the light reflection, the adhesive used for the channel were mixed with coal powder to make it black, and the joint area covered by the adhesive were limited to under 2 mm in width to preserve the area for observation and measurements. The channel is supported by the adjustable devices (Figure 1.3), the upstream support was made by two scissor-jack, which allowed us to change channel slope quickly and is permitted to make fine-adjustment of the level in transverse direction. we also install the level-adjusting function to the hinge attached to the downstream channel. The channel outlet is blocked by a sill to keep 4 layers of grains as deposit, the sill was glued with 5 rows of grains to add roughness here (Figure 1.4**a**),

over the sill a copper-made spillway (Figure 1.4**b**) was installed to guide the solid-liquid mixture dropping into the jet-pump tank.
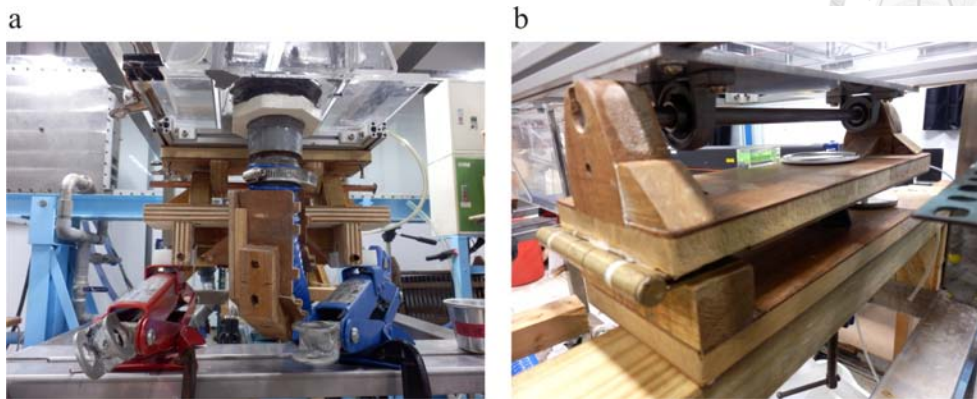
Figure 1.3 The supports of the channel: **a** Two scissor-jacks which were mounted on the bottom of the flume can could the slope of channel and the level could be tuned transversely; **b** the hinge located on the downstream channel was also level-adjustable.
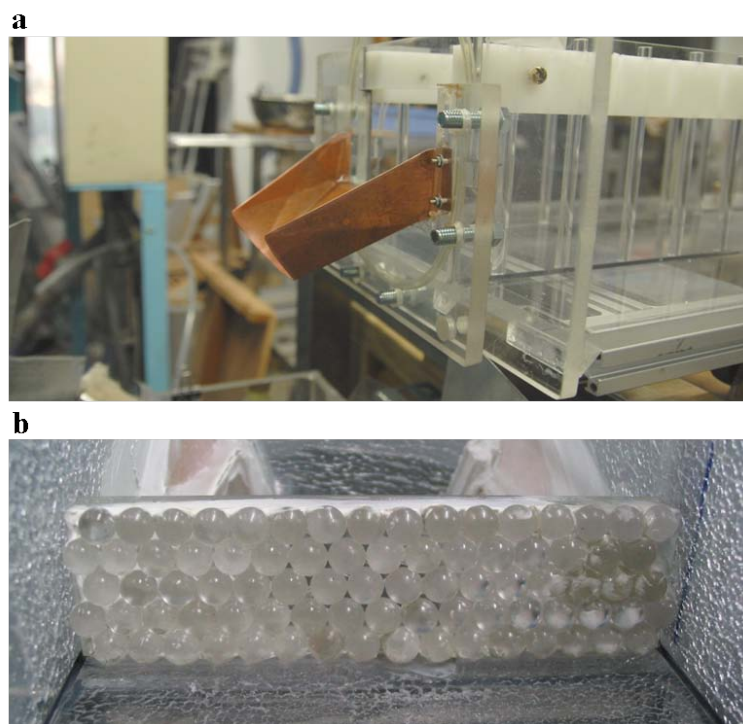
Figure 1.4 the outlet of the channel, **a** channel sill, 5 rows of grains were glued inside to provide roughness and leave 3 to 4 layers of deposit in the channel; **b** the spillway which guide the solid-liquid mixture to the jet pump.

To satisfy the steady flow condition, we built a jet entrainment chamber system (jet pump for short) to transport both liquid and solid grains into the channel. The jet pump is powered by a three-phase centrifugal pump, from the operation panel we can tuned the liquid discharge into the jet chamber, the detail illustration of the tank is shown in Figure 1.5. it was separated into 2 parts: the constant-head jet pump chamber and the drainage zone. In the constant-head jet pump chamber, the high pressure inflow would be ejected

9

through the nozzle, which creates a high-velocity/ low pressure zone near the nozzle inside the mixing tube, an orifice opened on the mixing tube connected with a mesh funnel, the funnel catches solid-liquid mixture flowing out of the channel, part of the liquid would drop through the mesh into the drainage zone and go back to the reservoir, while the other part of liquid would flow into the jet chamber with solid grains, for the solid grains they would fall into the funnel and be pulled into the mixing chamber by the high velocity jet, then the mixture in the mixing chamber would be transported through pipe to the channel, the excessive liquid in the constant-head jet chamber would be drained to the drainage zone via an overflow bore. When the circulation within the system became stable, the liquid level here would be constant, which establish the constant head environment that keeps the steady supply of liquid and solid through jet.
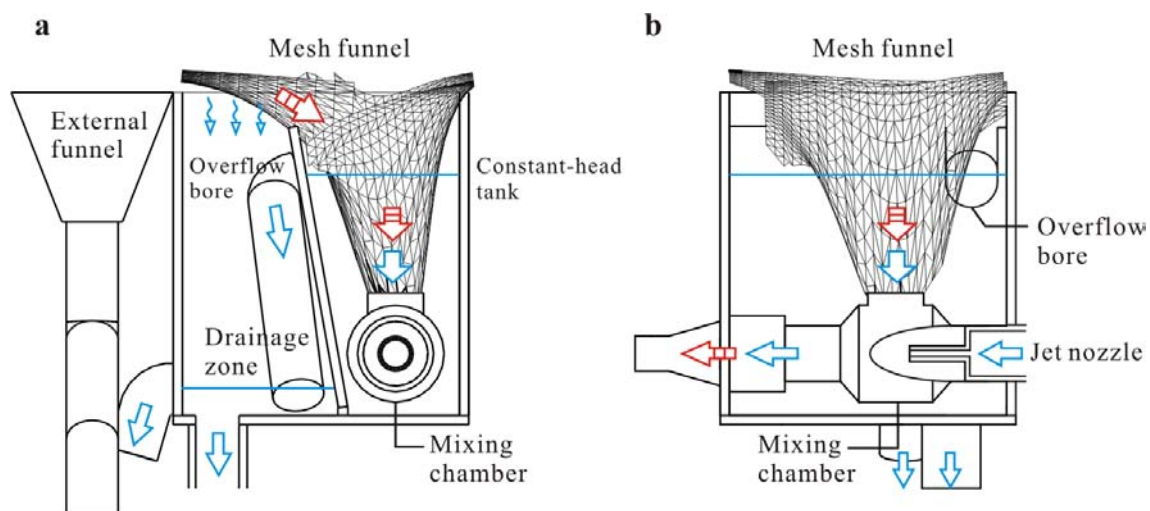
Figure 1.5 The jet-pump tank is responsible for the transportation of solid-liquid mixture to the channel; **a** the front view of the tank, the tank have a constant-head zone in which the jet nozzle and the mixing chamber were installed, and a drainage zone which let the excessive flow back to the reservoir, the mesh funnel would confined the solid grains circulating through the jet-pump to channel; **b** the organization of the jet nozzle, mixing chamber and the tube connected to the channel.

1.2.2   Experiment procedure

Three factors in the experiments need to be considered with care in order to provide consistent initial conditions for each experiments. First, the slope and the level of the channel needs to be adjusted carefully, otherwise the flow condition would be far from the uniform flow. Secondly, the temperature of the liquid have to be controlled around 17°C to sustain refractive index matched condition during the experiment, temperature control device and procedure were needed. Thirdly, the saturation of solid grains should be the same for each runs of experiment, the traditional way to fulfill the demand is by immersing solid into liquid for a long period of time, let solid be fully saturated, but in our case the method cannot be applied because Para-cymene would gradually etch the PMMA, causing deflections on the PMMA surface, generating noises to image processing, thus we used vacuum bottle method to accelerate the process and keep saturation of solid grains the same for each runs.

The level of the flume were exam carefully before conducting experiment, bubble level sensors helped to to this job, and level could be adjusted by two screws supports fixed on the bottom of the flume, as shown in Figure 11, this procedure had to be done before each runs to guarantee the uniform flow condition.

To maintain the temperature would be not easy, the temperature had to be low enough to keep refractive index, however if the temperature was lower than dew point of the surrounding air, dew would be condensed on the surface of channel and grains exposed in the air, the quality of images filmed during the experiment would be poor. The problem could be solved partially by following steps: air conditioner would be operated before the experiment to keep room temperature as low as possible, reducing the chance of dew forming on channel. The 80 liters of liquid would be restored in the refrigerator, and poured into the reservoir just before we start the experiment. A water cooling system consisted of portable cooler and cooler fins were in operation during the experiment to maintain the low temperature of liquid. Some preparation works needs to be done before experiments.

1. All liquid would be put into the refrigerator for a day.

2. Pick the bad grain out, the PMMA grain would be damaged after series of experiments for repeat shearing and colliding, some serious damage, like cracked from inside, could hurt other grains and broken into pieces, and strong glare would be happened if the laser hit the bad grain.

3. Use the constant number of grains to keep the number of grains in the system the same over different runs of experiment.

For the channel boundaries, we chose three boundary types: smooth wall smooth floor (SWSF), smooth wall rough floor (SWRF) and rough wall rough floor (RWRF), and conducted a series of experiments by variation of total discharge for each type of boundary, the configurations are shown in Figure 1.6. For SWSF, the boundary is the smooth surface of channel walls and channel floor. For SWSF, we put cylinders of 7mm in diameters on the floor with center to center distance equaling to $6D$ (42mm), the arrangement provided a condition that the organized layering of the solid grains would be interrupted every 42mm, and on the other hand the walls remained smooth. For RWRF, both walls and floor were installled with PMMA cylinders, except 1 run (check which one), the distance between cylinder center is also set to 42mm, the arrangement added more roughness to the boundary and we hope to see how the flow structure responds to the boundary variations.

The final work is cleaning, a intensive wash work needed to be done just right after the experiment because para cymene is corrosive to the PMMA, if we leaved the liquid on the PMMA surface and let it dried out, the surface would become rough, this seriously influence the optical property of grains, so the grains would be washed for three times using Ultrasonic Cleaner and soap solution, the channel needs to be cleaned by dry and soft fabrics, for the SWRF and RWRF cases, the cylinders also needed to be cleaned, and more over, needed to be polished, the whole cleanup process would takes about 2 3 hours.

11
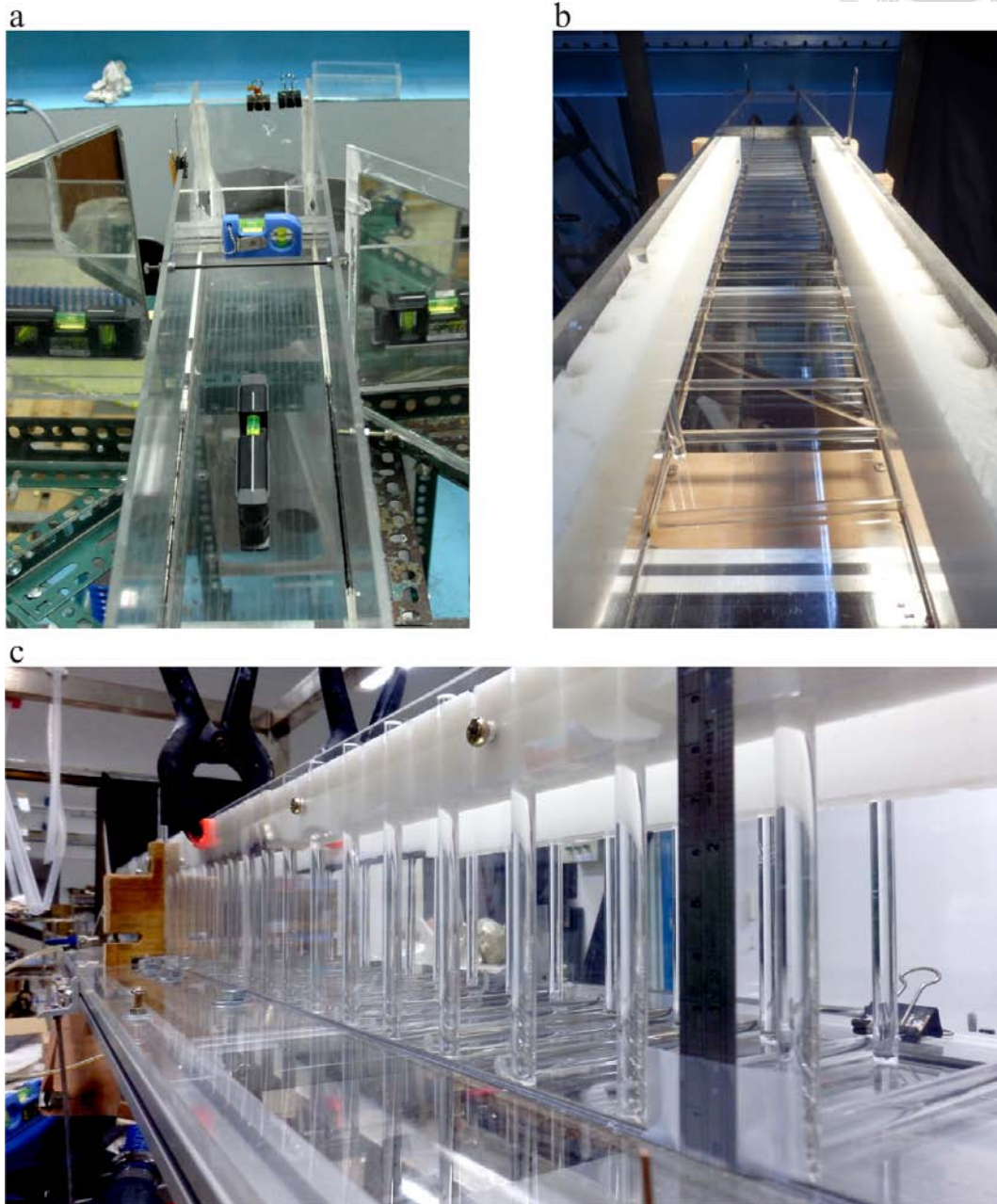
Figure 1.6 Three boundary conditions of the channel adopted in the experiments: **a** smooth wall smooth floor (SWSF for abbreviation); **a** smooth wall rough floor (SWRF) and **c** rough wall rough floor (RWRF).

After introducing the preparation and the finishing works, the experimental procedures would be explained below:

1. Set and adjust the channel transverse level. Meanwhile put all grains into the vacuum bottles, fill the bottle with para cymene, then vacuum the bottle for 3 minutes, then turn of the valve on the bottle to keep negative pressure and put it into the refrigerator to cool them down.

2. Set up the laser sheet and high speed camera for the transverse scan.

3. Take the liquid out of the refrigerator and pour the liquid into the reservoir gently, be careful, avoid eye contacted to the liquid, it hurts. some water might be on the bottom the container so we leave the last cup of para cymene inside the container.

4. Take the grains inside the vacuumed bottle out of the refrigerator, pour those grains into the channel directly.

5. Turn on the pump tho draw liquid into the channel just after the previous step, the reason is to prevent dew forming on the surface of grains.

6. Adjust the liquid discharge to the desired quantity, then make adjustment to the channel slope until the flow depth is constant over the longitudinal direction.

7. Wait for 5 minutes to make sure there is no variation on the level of free surface, then we performed the transverse scan.

8. Measure the flow depth.

9. Adjust the setting of laser sheet and camera to perform hr longitudinal scan.

10. Measure the discharge at outlet, to be careful not to touch the camera because the camera calibration have not done yet.

11. Take the grains out of the channel and circulation system, block the sill by a plate to raise the liquid level, put the calibration target into the channel and immersed fully in the liquid, then record the calibration image for longitudinal scan.

12. Turn off the pump, wait until the liquid is in still, then take some photos to capture the channel inclination.

13. Draw the liquid out of the reservoir and put them back to the refrigerator.

14. wash and clean everything.

1.3 Measurements during experiments

Three measurements were performed during experiments: the flow depth, solid and liquid discharge and the channel slope. The flow depth was measured from the side walls after the flow is steady and uniform, the measurement was performed to both side of channel to check if there is any level problems.

For the outlet measurement, it is an intrusive method to obtain the solid and liquid discharge by intercepting the flow and collecting the mixture for a period, then calculate the discharges by weights and duration we measured. Because its intrusive and this would intercept the flow system, it would change the flow condition and alter the performance of jet entrainment, therefore the measurement would be performed after the laser scanning procedure had finished and the whole duration should be within 3 second to reduce the variation of jet entrainment performance. We used a customized funnel to intercept the flow and guided the flow into a bucket, then we measured the weights of solid and liquid right way, a correction parameter was applied to the grain weight measurement to recover the grain dry weight. the duration was measured by by a stopwatch at first, but the results showed large uncertainty so for the later experiments (SWRF and RWRF) we measured the duration by recording the process, then calculate the duration frame by frame, this method showed better results.

For the measurement of the channel slope, at first (SWSF) we measured this value by a U shaped soft pvc tube filled with water, and calculate the slope by the water level difference in the upstream and downstream tube, but this method cannot fully represents the slope when the slope range is around $1° - 2°$, thus for later experiments (SWRF and RWRF) we simply retain some liquid inside the channel, then measured the channel slope by the angle between free surface and channel floor, this method also show a better relation between direct measurement and imaging measurements. The detailed data of experimental conditions for three channle boundaries are listed in Table 1.1, 1.2 and 1.3.

14

Table 1.1 The conditions for the SWSF experiments

exp. ID	θ	Z_{max}	Q_L		Q_S		C_S
	[°]	[mm]	[g/s]	[cm^3/s]	[g/s]	[cm^3/s]	[cm^3 cm^{-3}]
20131119	1.59	52.0	921.34	1077.59	111.06	132.16	0.109
20131122	1.79	52.0	1141.74	1335.37	138.52	164.84	0.110
20131202	1.22	46.0	494.82	578.74	31.55	37.54	0.061
20131206	1.50	50.0	945.75	1106.15	97.77	116.34	0.095
20131225	1.74	52.0	1109.08	1297.17	151.86	180.71	0.122
20131227	1.56	51.0	1141.77	1335.40	142.26	169.29	0.113
20140107	1.50	48.0	728.33	851.85	91.30	108.64	0.113
20140121	1.39	48.0	532.42	622.71	46.36	55.17	0.081
20140124	1.68	53.0	1105.60	1293.10	148.06	176.19	0.120
20140127	1.74	51.0	892.17	1043.48	129.11	153.64	0.128
20140207	1.62	50.0	884.48	1034.48	112.12	133.43	0.114
20140211	1.45	48.0	668.76	782.18	75.30	89.61	0.103
20140214	1.39	43.0	335.29	392.16	23.07	27.45	0.065
20140223	1.56	48.0	849.34	993.38	99.96	118.95	0.107
20140228	1.79	53.0	1084.12	1267.97	152.92	181.98	0.126

Table 1.2 The conditions for the SWRF experiments

exp. ID	θ	Z_{max}	Q_L		Q_S		C_S
	[°]	[mm]	[g/s]	[cm^3/s]	[g/s]	[cm^3/s]	[cm^3 cm^{-3}]
20160323	1.51	50.0	855.00	1000.00	73.29	61.59	0.058
20160330	1.54	54.5	1120.54	1310.57	121.67	102.24	0.072
20160331	1.30	48.0	611.56	715.28	39.25	32.98	0.044
20160408	1.68	55.0	1279.67	1496.69	156.20	131.26	0.081
20160413	1.40	50.0	794.16	928.84	58.51	49.17	0.050
20160419	1.52	54.0	1136.86	1329.66	113.30	95.21	0.067
20160428	1.69	54.0	1256.56	1469.66	137.92	115.90	0.073
20160517	1.53	52.0	1001.91	1171.82	94.83	79.69	0.064

15
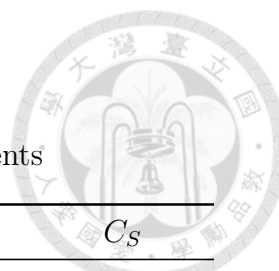
Table 1.3 The conditions for the RWRF experiments

exp. ID	θ	Z_{max}	Q_L		Q_S		C_S
	[°]	[mm]	[g/s]	[cm^3/s]	[g/s]	[cm^3/s]	[cm^3 cm^{-3}]
20160105	2.200	56.00	1002.83	1172.9	134.60	160.2	0.120
20160108	1.609	51.00	676.36	791.1	61.82	73.6	0.085
20160112	1.330	50.00	744.91	871.2	45.76	54.5	0.059
20160113	1.816	53.00	1034.91	1210.4	84.87	101.0	0.077
20160115	2.045	55.00	1029.34	1203.9	113.10	134.6	0.101
20160119	1.793	50.00	712.54	833.4	52.00	61.9	0.069
20160120	1.839	54.00	1088.36	1272.9	91.96	109.4	0.079
20160121	1.333	48.00	564.90	660.7	27.28	32.5	0.047
20160126	1.701	52.50	750.66	877.96	68.21	81.17	0.085
20160202	1.839	54.00	1083.95	1267.78	99.69	118.63	0.086
20160215	1.471	50.00	641.88	750.74	41.07	48.87	0.061
20160217	1.999	54.50	1190.54	1392.45	114.47	136.22	0.089
20160225	1.609	51.00	833.43	974.77	81.53	97.02	0.091
20160322	1.414	48.00	581.77	680.43	28.66	34.11	0.048

Figure 1.7 The method that measured the flow discharge directly using a customized funnel, which intercepted the flow and guided the mixture of flow to a bucket to measurements for 1–3 seconds.
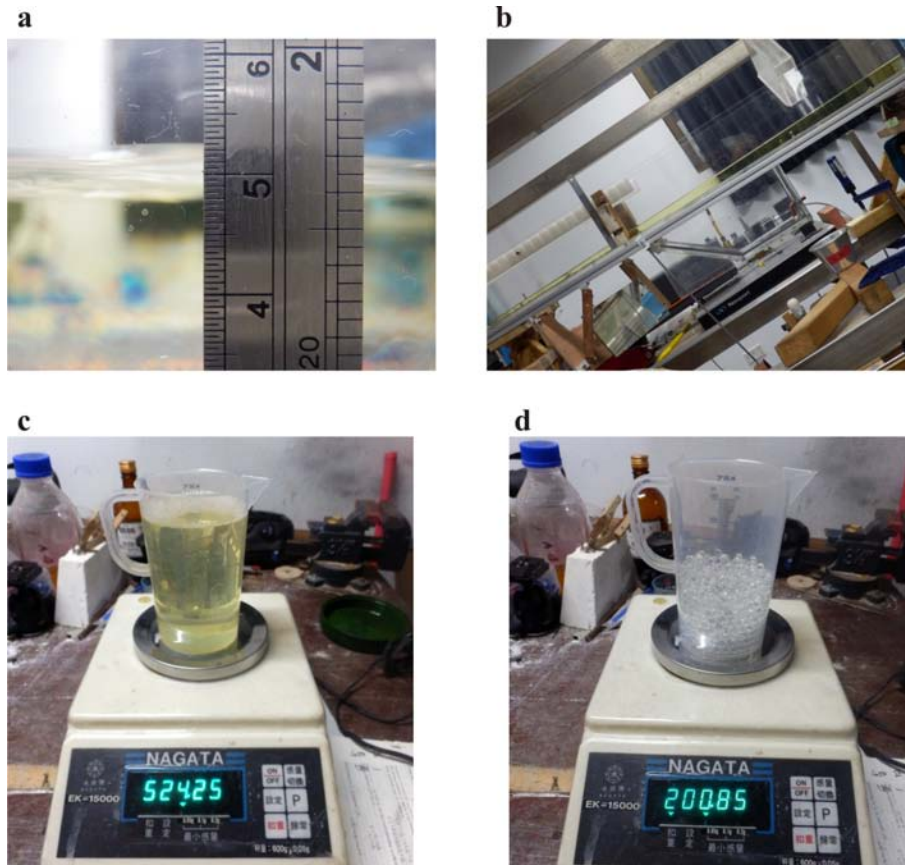
Figure 1.8 The measurements of depth, slope and discharges: **a** the total depth of the flow was measured by a ruler through the side walls at upstream and downstream locations; **b** The slope of the channel was determined by the angle between still liquid free surface and the aluminum beam mounted to the channel bottom; **c**, **d** both solid and liquid which were collected at outlet were measured using High Precision Digital Scale with ± 0.05g accuracy.

1.4 Characterization tests

Several tests were performed to obtain the basic material properties for liquid and solid. We measured the specific weight of solid by pycnometer tests, conducted a head-on collision tests in the air to obtain the coefficient of restitution, conducted the tilting board tests to evaluate the static and kinetic friction coefficient for solid grains to the PMMA plate. For the liquid we tested the specific gravity, and measured the viscosity by the Ostwald viscosimeter. These properties which were measured and took average value from series of tests were listed in Table 1.4, the detailed steps and procedures of each tests were introduced by the following section.
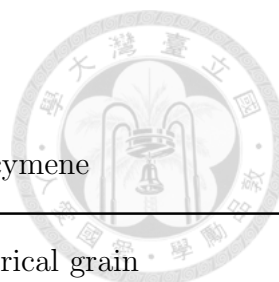
Table 1.4 Properties of the PMMA grains and para-cymene

Solid:			PMMA spherical grain
Parameter	Value	Test method	Comments
Density ρ_S [g cm^{-3}]	1.19	Pycnometer	Average of 2 tests, see sec. 1.4.1.
Diameter D [mm]	7		
Solid fraction of the random packing c_0[m^3 m^{-3}]	0.597	Packed in a tank, see sec. 5.3.	Measuring the weight of grain while the seepage tests, averaged of 2 tests
Static friction angle α [°]	30	Tilting board	Measuring the maximun tilting angle for the specimen in p-cymene, averaged over 21 tests, see sec.1.4.3.
Kinetic friction angle [°]	19	Tilting board	Measuring sliding acceleration of the specimen after attained static friction angle, then obtained by force balance, averaged over 21 tests, see sec.1.4.3.
Coefficient of restitution e [-]	0.94	Air-canon head-on collision	Using the DIY air canons to eject 2 particles flying oppositely to collide, obtained the coefficient by 3D velocities before and after collision by imaging analysis, see sec.1.4.2.
Terminal velocity w_T [m s^{-1}]	0.26	Drop grain into p-cymene tank	Averaged from 21 tests, see sec.1.4.5.
Liqid:			Para-cymene
Density ρ_L [g cm^{-3}]	0.855	Hydrometer	
Viscosity μ [kg m^{-1}s^{-1}]	9.8×10^{-4}	Ostwald viscosimeter	Averaged from 10 tests and comparing with the tests of water, see sec.1.4.4.

1.4.1 Specific gravity of PMMA grains and Para-cymene

The specific gravity of PMMA particles were measured by using pycnometer, it helps us to obtain the sample volume and weight with high precision. Two tests were performed and we took the average value of the two to obtained the specific gravity. The experimental procedure is described below.
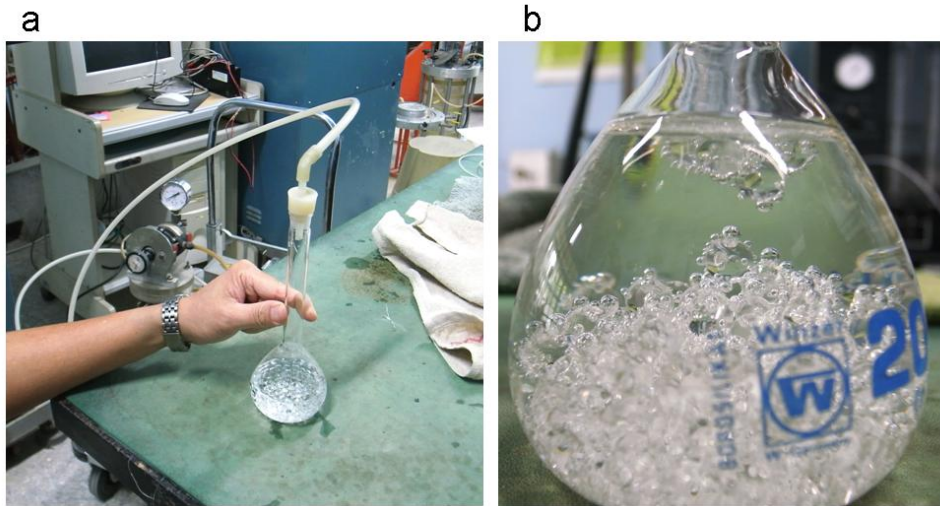
Figure 1.9 **a** The bottle of particle-water mixture was vacuumed to eliminate the air bubbles trapped in the pore of the granular pack; **b** A lots of bubbles are stick to the surface of the particles.

1. Record the temperature of room (air) and the distilled water to be used.Record the temperature of room (air) and the distilled water to be used.

2. Measure the dry weight of the pycnometer, W_b.

3. Put dried test sample into the pycnometer and measure the weight, $W_b + W_g$.

4. Measure the weight of the lid W_L.

5. Put the distilled water into the bottle which contained the samples to th bottom of the neck, connect the bottle to a vacuum pump to helps the trapped air bubbles flow to the surface (Figure 1.9).

6. After checking no air bubbles were trapped, fill the bottle with water gently until it reached the top of the neck, forming a convex surface, then wipe out the excessive water with the lid. This step can ensure the consistent volume we used in the bottle and avoid air-trapping. Dry the bottle outside then measure the weight, $W_b + W_g + WL + W_pw$, where W_{pw} is the pore water weight.

7. Clean and dry the bottle, fill with water into the same bottle, put lid on and measure the total weight, $W_b + W_w + WL$.

The volume of the sample can be obtained sample weight and results of step 6 and 7, the averaged specific gravity equals to 1.19, the measurement data was listed in 1.5.
The specific gravity of p-cymene is evaluated by hydrometer, it float on the liquid and we can directly read the specific gravity on it. the value is 0.856.

Table 1.5 The results of specific gravity tests

Air Temp. [°C]		24	
Water emp. [°C]		26	
item	weight detail	test 1 [g]	test 2[g]
1	Bottle id	p7	p3
2	Wb	81.74	80.76
3	Wb + Wg	129.60	127.72
4	WL	16.07	16.07
5	Wb+Wg+WL+Wpw	321.01	320.22
6	Wb+WL+Ww	313.24	312.55
7	Wg = 3-2	47.86	46.96
8	Vg= 7+6-5	40.09	39.29
9	SW =7/8	1.19	1.20
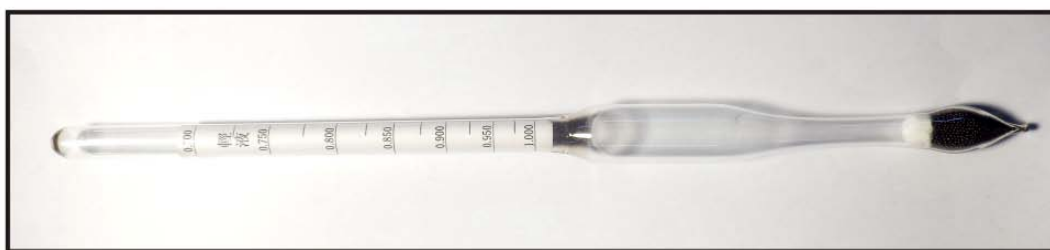
Figure 1.10 The hydrometer for measuring liquid specific gravity.

1.4.2 Coefficient of restitution

The coefficient of restitution for grain-to-grain collision is evaluated by this tests, The particle-to-particle collisions had been studid in a viscous liquid (*Yang and Hunt*, 2006) or in the air (*Foerster et al.*, 1994). To simplify the condition, we didn′t consider the rotation of the grain and did the test in the air. we designed and built a collision test device which allowed two PMMA grains to fly toward each other, collide, then rebound to the resultant directions. We also set a stereo imaging configuration to record the collision process from 2 distinct view angle, and obtained the 3D velocities by PTV analysis before and after collision for two test grains, then evaluated the coefficient of restitution by the PTV results.

The set-up is shown in Figure 1.11, two copper-made gun barrels with 4cm in length and 0.8cm in diameter were mounted on a aluminum beam which provides a firm and stable foundation for the set-up (Figure 1.11**a**). One barrel , labeled as X^-,was fixed on the beam, while the other barrel, labeled as x^+, was mounted about 6cm away from the X^-, and fixed on a adjustable angle mount kit which provides the precision adjustment for the trajectory (Figure 1.11**b**). The gun barrels were powered by high pressure air jet which was provided by a air compressor, the air was triggered by a handle valve, once the we switch on the valve air would put the canons, PMMA grain, flying through the barrels and colliding in the zone between two barrels, which we called the collision zone.
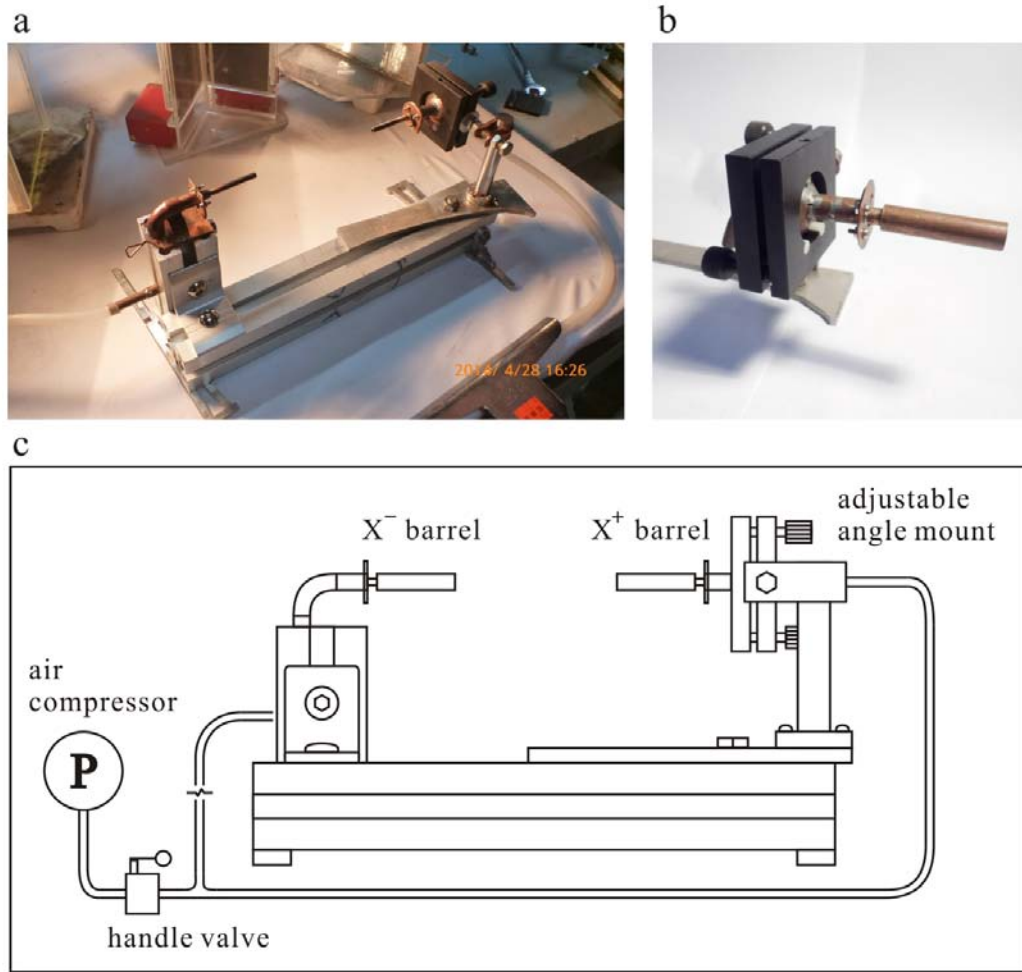
Figure 1.11 The set-up of the head-on collision tests: **a** the experimental set-up for the particle head-on collision, the barrel was for 3mm particles; **b** the 8mm barrels for PMMA particles mounted on a lens adjustment kit for aiming; **c** The sketch of the set-up, A air compressor was connected to the air guns of both sides, a handle valve was the trigger to shoot the particles simultaneously.

Since the trajectories of the grains were 3 dimensional, we arranged the stereo imaging set-up to capture and analysis the collision process. It was composed of 2 rear mirror and the center mirrors which were set 90 degree, it is shown in Figure 1.12**a**, we can see the calibration target placed in the collision zone from two distinct view angle by adjusting the angle of two rear mirrors, the image on the center mirrors after adjustment is shown in Figure 1.12**b**. We use high speed camera to record the process, the fps was set to 1500 frame per second because the whole process inside the collision zone was about 0.05s.

22
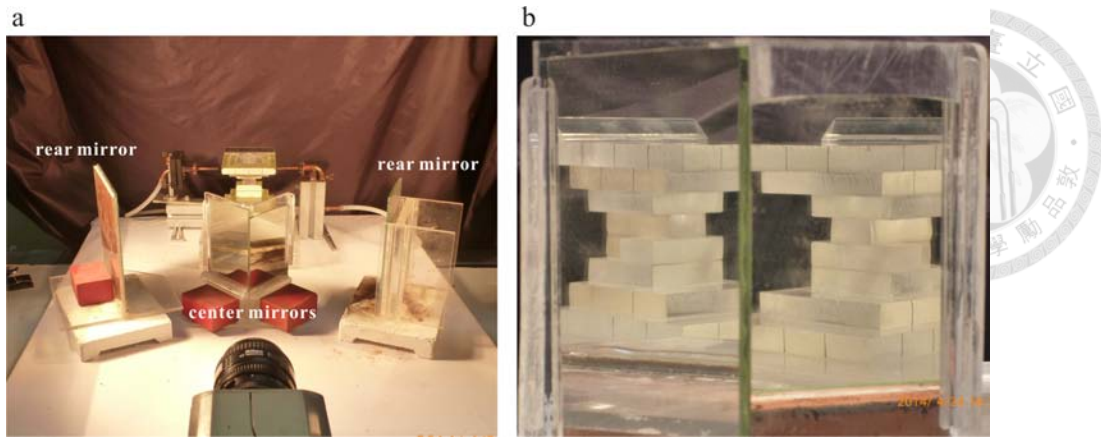
Figure 1.12 The set-up and calibration method for stereo imaging: **a** the configuration of mirrors and camera for stereo imaging, the calibration target was placed between barrels, two rear mirrors reflected image of the zone between two barrels to the center mirror, allow filming the process using one camera; **b** the image of the calibration target acquired via the center mirror.
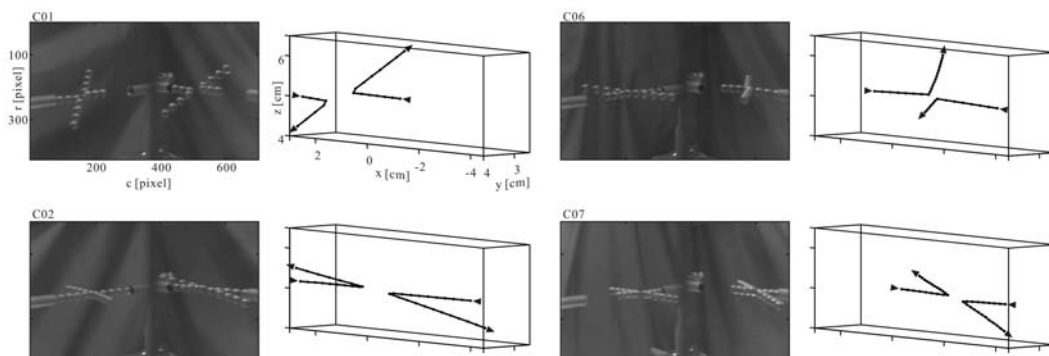
Figure 1.13 Time-elapse images and PTV results, selected examples.

23
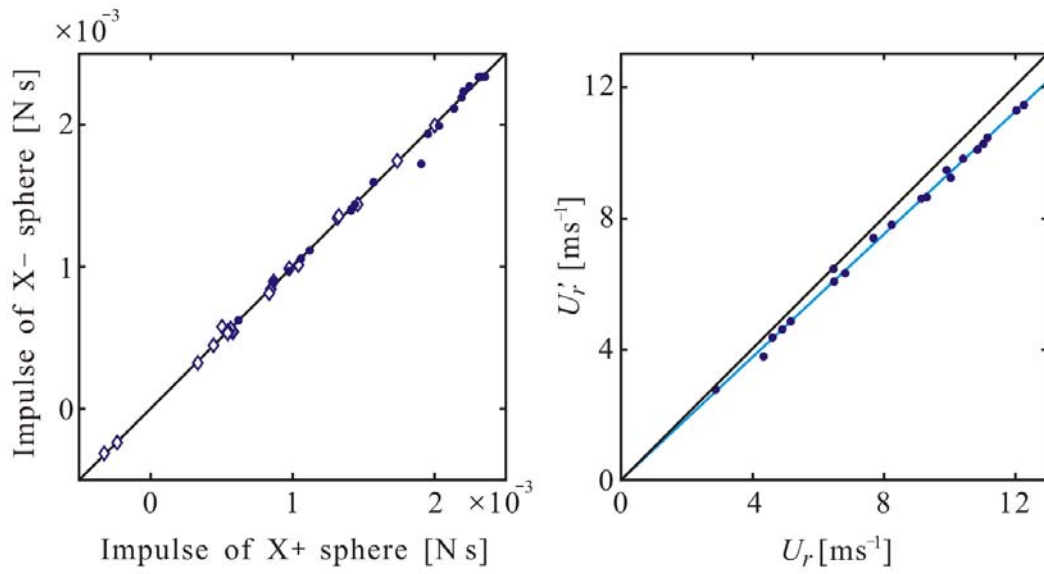
Figure 1.14 **a** The momentum impulse of the grains from X^- and X^+ direction; **b** the incident and resultant relative velocities in the center-to-center direction in the instance of collision.

1.4.3 Angle of friction for the particle-wall contact submerged in P-cymene
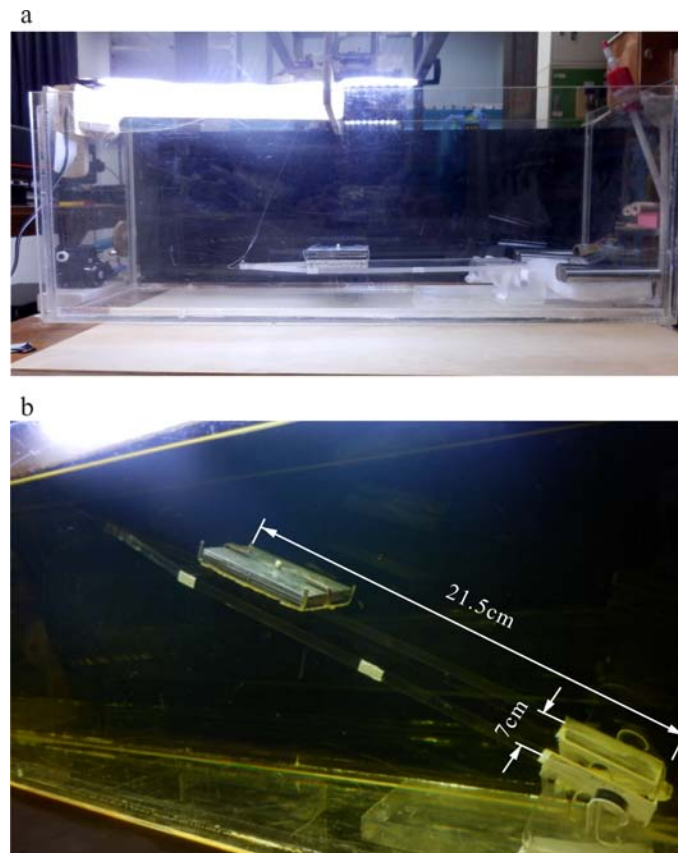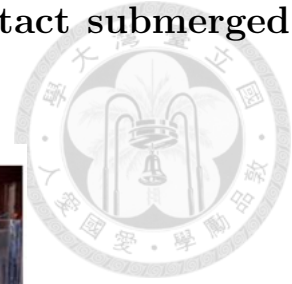
Figure 1.15 The tilting board test apparatus: **a** the snapshot before the test; **b** the snapshot during the test, note that the grains glued on the specimen and the PMMA board are transparent in the p-cymene, which make the specimen look as if it floats in the liquid.
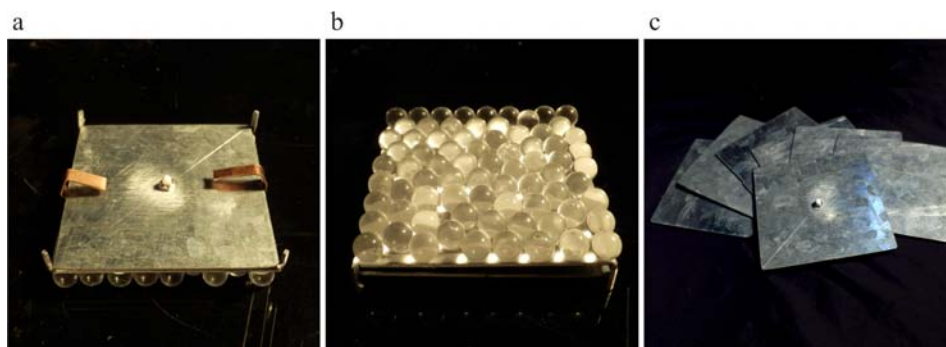
Figure 1.16 The composition of the specimen and weights: **a** The specimen base;**b** the bottom of the specimen were glued with PMMA particles; **c** Seven iron loading plates provides different loading condition.

The tilting board test was adopted to evaluated the angle of friction for grain-wall contact, they all made by PMMA. The advantage of this method is that not only static angle of

friction can be obtained by measuring the inclination of board, but the kinetic angle of friction can be evaluated by capturing the specimen acceleration and deriving the force balance relation. Since everything would be submerged in a tank filled with p-cymene, it means everything need to be built by ourself to make the apparatus survived in p-cymene environment.
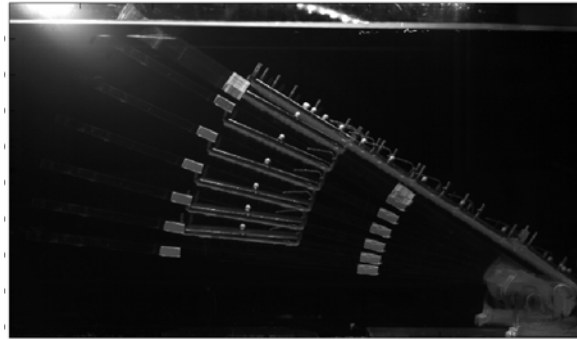
Figure 1.17 A time-lapse long-exposure photo shows the process of the tilting board test.

We designed and built the tilt board using water jet machine, the parts were made by PMMA, as shown in Figure 1.15 , the dimension of the board is 21cm long and 7cm in width, the board end was connected with a hinge covered with thin teflon plate for smooth rotation, and a motor-cable system outside the tank was used to control the table inclination.

For making the specimen and the loading board, we randomly pick PMMA grains and glued them onto a 6cm x 6cm iron made base by a thick layer of glue, then put the whole thing upside down on a rigid plane to drying out, making each grain could touch the surface (Figure 1.16**ab**) Seven loading plates were cut in the same dimensions, and a white, small, round particle was glued on one of the loading plate for PTV purpose(Figure 1.16**c**). The reason we chose the iron plate to make specimen base and loads because of its high specific gravity, which enable us to make the loading range wider and helps to reduce the exposed area when the specimen moving in th liquid, so as to reduce the drag force. The whole process were recorded by a high speed camera, from the footages we could measure the static friction slope on the one hand, and evaluated the displacement, velocity and acceleration by the small white dot on the sliding specimen on the other hand. The test steps are listed below

1. Before testing, clean the tilting table and the specimen by washing and drying, things like sands or small fiber threads attached on the surface could seriously influence the test result.

2. Place the board set inside the tank, then fill it with the p-cymnene.

3. Put calibration target on the table to calibrate the camera position.

4. Put specimen with one iron load on the middle of the table, turn on the motor to slowly tilt the table.

Table 1.6 The mass and volume of the test specimen with different loads

Test block	W [g]	V [cm^3]
base	49.45	-
base+1	76.90	22.90
base+1:2	103.50	26.60
base+1:3	130.80	29.95
base+1:4	157.70	33.40
base+1:5	184.35	36.90
base+1:6	211.45	40.25
base+1:7	238.45	43.95
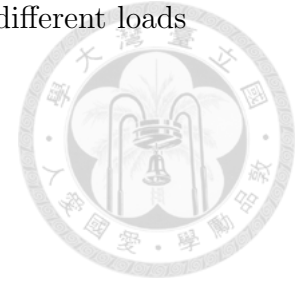
5. When the specimen began to slide, at this moment the inclination of the board would be measured, while the sliding process was also recorded for further imaging analysis, this is the single run of test.

6. We repeated the steps to obtain several data of specific loading condition, then changed the loading by adding one weight then started for another round.

If the specimen couldn't slide straightly to the bottom or even fall from the table in the middle section, we took it as a failure one and it would be excluded. 7 rounds of tests (21 tests in total) with different loading conditions were performed.

Table 1.7 The mass, volume, static frictional angle and averaged acceleration measured for each tests

ID	M	Vol.	α_0	$\bar{a}$	ID	M	Vol.	α_0	$\bar{a}$
	[g]	[cm^3]	[°]	[cm s^{-2}]		[g]	[cm^3]	[°]	[cm s^{-2}]
p1_1	76.90	22.90	27.02	114.88	p5_2	184.35	36.90	30.91	175.17
p2_1	103.50	26.60	31.64	136.24	p6_2	211.45	40.25	28.04	179.52
p3_1	130.80	29.95	32.12	160.62	p7_2	238.45	43.95	30.56	186.82
p4_1	157.70	33.40	26.55	112.42	p1_3	76.90	22.90	29.26	155.41
p5_1	184.35	36.90	28.19	161.30	p3_3	130.80	29.95	29.39	132.84
p6_1	211.45	40.25	29.09	174.40	p5_3	184.35	36.90	29.31	154.04
p7_1	238.45	43.95	30.93	208.72	p7_5	238.45	43.95	30.69	163.60
p1_2	76.90	22.90	27.84	131.75	p1_4	76.90	22.90	32.86	114.03
p2_2	103.50	26.60	29.59	144.73	p3_4	130.80	29.95	31.57	138.97
p3_2	130.80	29.95	33.38	180.56	p5_4	184.35	36.90	30.46	181.85
p4_2	157.70	33.40	28.90	131.51					
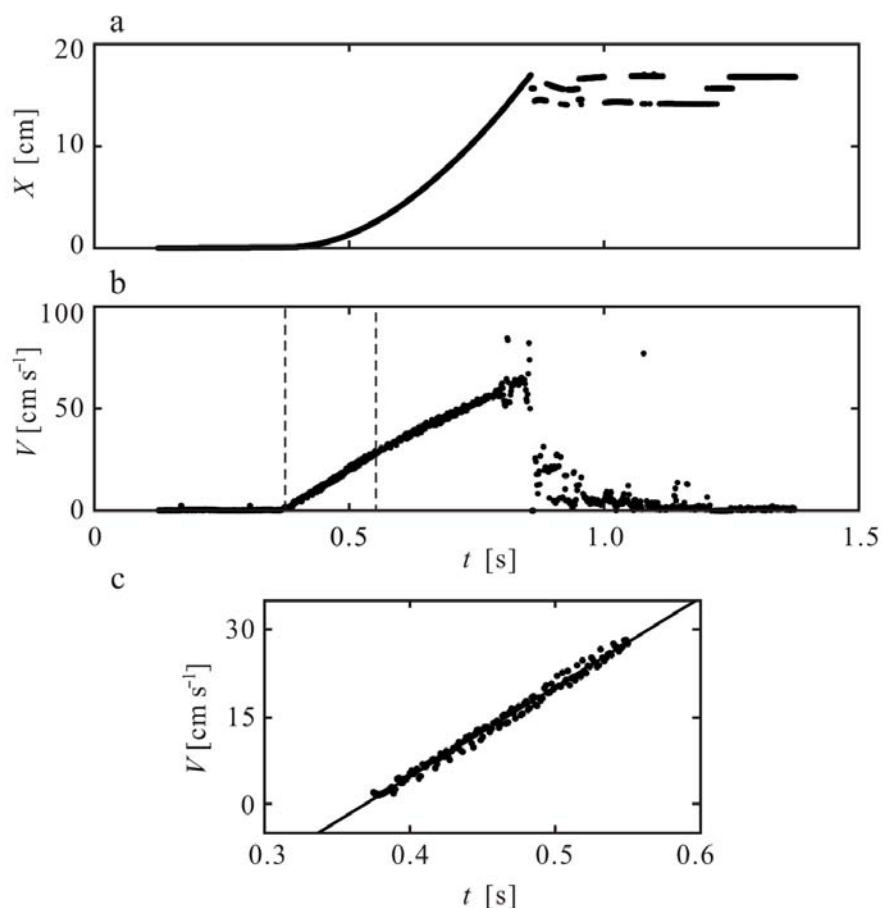
Figure 1.18 The analysis of the tilting board test: **a** the displacement the specimen versus time; **b** the instant velocities versus time, the section bounded dash lines represent where the velocity varied linearly with time; **c** enlarged view of linear section in **a**, we could obtained the acceleration by linear regression applied to these points. Results are from the test: p5-3.
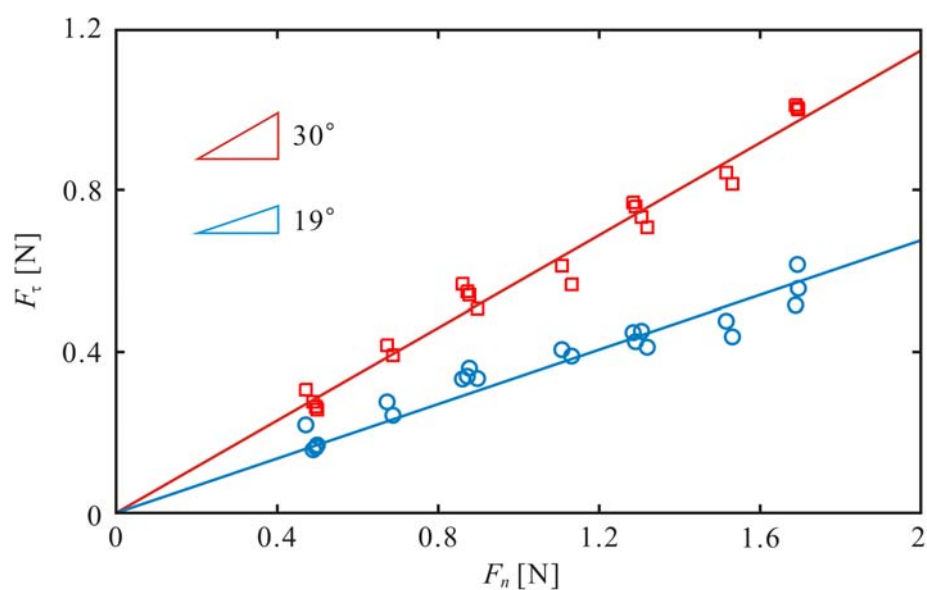
Figure 1.19 The fitting results of static and kinematic friction angle.

1.4.4 Viscosity test
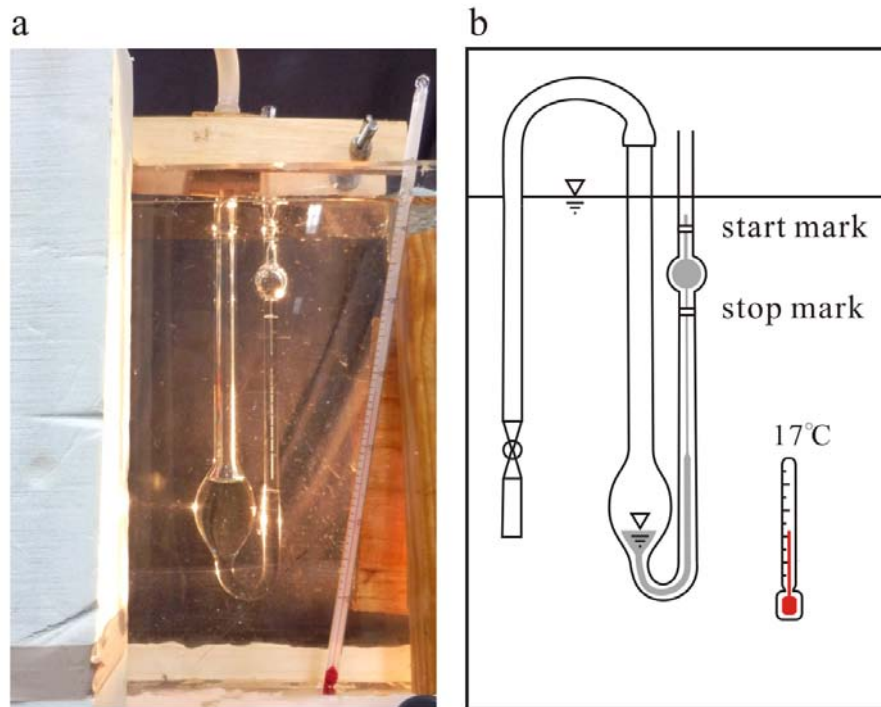
Figure 1.20 The set-up of viscosity test. The viscometer were bathed in the 17 degree cold water to make temperature of test liquid to be constant.

Viscosity is an important parameter of liquid relating to shear and forces between phases, we adopt the Ostwald viscosimeter method (Figure 1.20) to measure viscosity for its simplicity for the Newtonian fluid. The viscosimeter is a U-shaped glass tube, two reservoirs locate at the high and low position of the U tube, connected through a long, thin circular passage, there are two marks above an below the upper reservoir, which helps for the measurements, the idea is based on Poiseuille's law, it states that for incompressible Newtonian fluid passing through a capillary tube, the discharge for the liquid flowing through the tube is related to the pressure gradient, liquid viscosity, tube length and diameter,

$$\Delta P = \frac{128 \mu L Q}{\pi d^4} \tag{1.1}$$

where P is the hydrostatic pressure, μ is the dynamic viscosity, L and d represent the length and diameter of the capillary tube, Q is the discharge. We replace $Q = V/t$ and $P = \rho g H$, and put value relating to the viscometer to the RHS, we have

$$\frac{\mu}{\rho t} = \frac{\pi d^4 g \Delta H}{128 L V} = const. \tag{1.2}$$

for a given volume of two liquid, like water and p-cymene, the relation between viscosities, times it took to flow, and the densities is like this.

$$\frac{\mu_w}{\rho_w t_w} = \frac{\mu_{pc}}{\rho_{pc} t_{pc}} \tag{1.3}$$
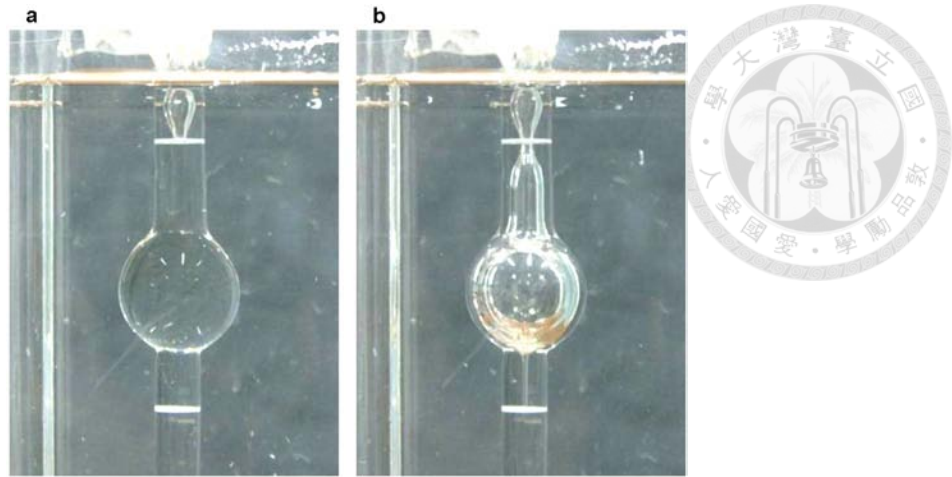
Figure 1.21 The images illustrated the surface-dropping process in viscometer: **a** the free surface at the start mark; **b** the free surface dropped to the end mark.

Once we knew the properties of the reference liquid and the densities of both liquid, the viscosity of the unknown liquid can be calculated by comparing the flowing time of two liquid, which could be measured using the viscometer. The tests were performed under a cold water bath at 17 $°C$, which is consist with the bed-load experimental condition, first we added about $20cm^3$ test liquid into the left reservoir (Figure 1.20), then push the liquid moving to the upper reservoir by blowing the air into the tube, when the free surface exceeded the start mark about 5mm, we stopped blowing and recorded the surface dropping from start mark to stop mark by camera (Figure 1.21), and we calculated the duration taken by each frames of the footage, ten tests were performed for each liquid and we took the mean value of the time to calculate the viscosity of p-cymene, the tests records and results are listed in Tabel 1.8.

Table 1.8 The viscometer test data

Date	20170831					
Liquid	Temp.[°C]	ρ_L[g cm^{-3}]	W_T[g]	W_{tube}[g]	W_L[g]	V_L[cm^3]
p-cymene	17	0.855	69.5	52.4	17.1	20
footage id	fps	frame1	frameEnd	frame total	T [s]	T$_{ave}$ [s]
pic_0307	59.94	9	3376	3367	56.17	56.19
pic_0308	59.94	21	3391	3370	56.22	
pic_0309	59.94	339	3684	3345	55.81	
pic_0310	59.94	29	3422	3393	56.61	
pic_0311	59.94	25	3401	3376	56.32	
pic_0312	59.94	40	3414	3374	56.29	
pic_0313	59.94	-	-	-	56.27	
pic_0314	59.94	-	-	-	56.17	
pic_0316	59.94	-	-	-	56.03	
pic_0317	59.94	-	-	-	56.03	
Date	20170901					
Liquid	Temp.[°C]	ρ_L[g cm^{-3}]	W_T[g]	W_{tube}[g]	W_L[g]	V_L[cm^3]
water	17	1	72.3	52.5	19.8	19.8
footage id	fps	frame1	frameEnd	frame total	T [s]	T$_{ave}$ [s]
pic_0322	59.94	15	3203	3188	53.19	52.98
pic_0323	59.94	137	3322	3185	53.14	
pic_0324	59.94	87	3267	3180	53.05	
pic_0325	59.94	-	-	-	52.83	
pic_0326	59.94	15	1604	1589	53.02	
pic_0327	29.97	-	-	-	52.93	
pic_0328	29.97	-	-	-	52.83	
pic_0329	29.97	56	1661	1605	53.55	
pic_0332	29.97	41	1618	1577	52.62	
pic_0333	59.94	98	3253	3155	52.64	

Kin. Vis. of water at 17°C[m^{2}s^{-1}]
1.081E-06
Kin. Vis. of p-cymene at 17°C [m^{2}s^{-1}]
1.147E-06
Dyn. Vis. of p-cymene at 17°C [kg m^{-1}s^{-1}]
9.804E-04

1.4.5 Terminal velocity test
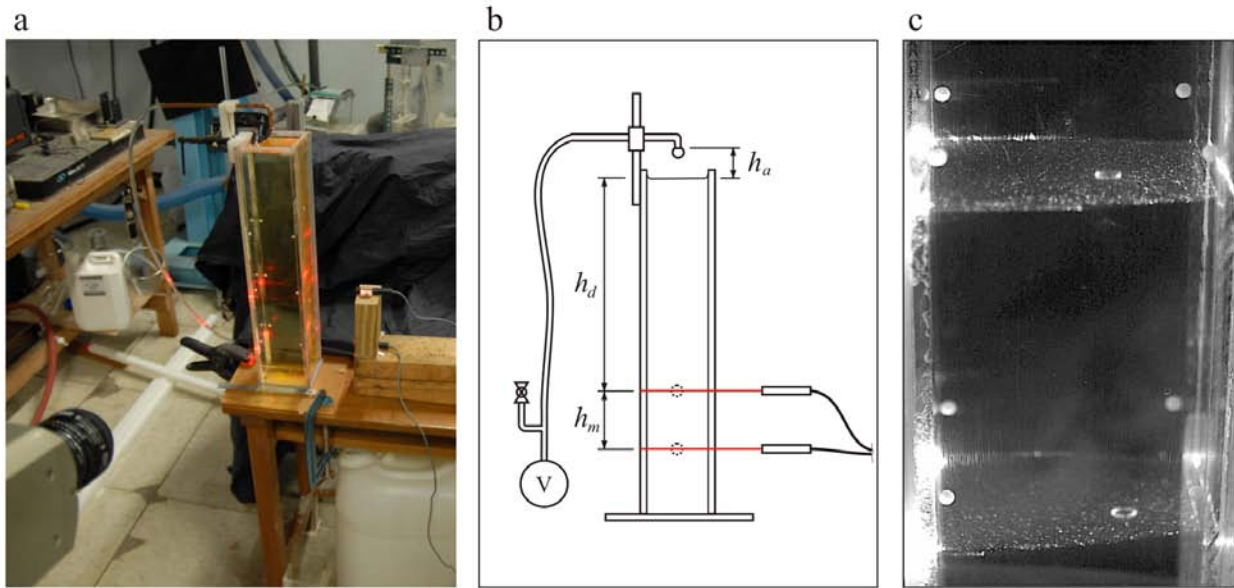
Figure 1.22 The experimental set-up for terminal velocity measurement: **a** the snapshot of experimental set-up; **b** the conceptual sketch the set-up, a particle release system and two laser sheets are mounted to help measuring falling velocity; **c** the time-lapse image shows the PMMA grain were highlighted as ellipse ring while it passed through one laser sheet to another.

The terminal velocity of PMMA particle in the p-cymene were tested by dropping a particle into a tank filled with p-cymene, and measure its velocity. One of the problems is to control the particle falling in a consistent way. Because of the nature of refractive-index-matched materials, particle positions needs to be highlighted for estimating falling velocity. We develop a vacuum system to fix releasing problem, for the second problem we used fixed laser sheets to locate the particle in the tank.

To improve the falling condition, a particle-release system was built to minimize the initial rotation of the particle and guarantee the consistency for all tests (see Figure 1.22**b**), we use a vacuum pump to create a negative air pressure and connected it to a bended copper tube, then we blocked the opening by the test particle which would be hold by atmosphere pressure, a bypass tube was used as the trigger, If the valve of bypass was open, the negative pressure of the copper tube would vanish and the particle would drop into the liquid, The set-up is illustrated in Figure 1.22.

The tank's dimension is 8cm x 8cm in cross section and 50cm in height, we assume that the particle would attain the terminal velocity as it traveled over a distance $h_d = 25.4cm$, after that the particle reaches the falling speed. Then it would pass through two horizontal laser sheet planes, the particle would be highlighted twice as shown in Figure 1.22**c**, its locations and times could be determined precisely. The inter-distance of two laser sheet plane, h_m, is about 10cm, the falling processes between laser sheets were recorded

32

by high speed camera. 3 initial elevations h_a above the liquid surface were set to check if the traveling distance was long enough for particle to attain terminal velocity, the results show positive answer, 21 tests were performed, the average terminal velocity equals to $26.86\pm0.8cm/s$, the data of measurements were listed in Table 1.9.
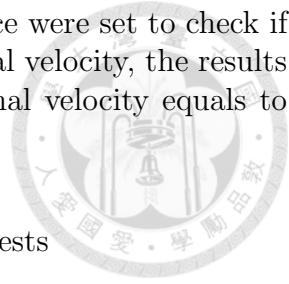
Table 1.9 experimental data of terminal velocity tests

h_a	no.	fps	sp	ep	h_m	h_m/T
mm		1/t	frame	frame	mm	cm/s
10	d1	350	17	152	103.31	26.59
10	d2	400	32	186	102.61	26.48
10	t1	200	11	86	103.54	27.25
10	t2	180	16	83	103.44	27.38
10	t3	200	12	85	103.34	27.93
10	t4	200	25	99	103.15	27.51
10	t5	220	12	94	103.54	27.44
15	d01	200	2	80	103.74	26.26
15	d02	250	39	137	103.37	26.10
15	t01	210	29	109	103.69	26.88
15	t02	230	16	100	103.69	28.06
15	t03	200	15	93	103.67	26.25
15	t04	250	23	117	103.70	27.29
15	t05	240	20	109	103.69	27.65
25	d01	250	16	113	103.98	26.53
25	D2	300	17	132	103.94	26.88
25	d3	300	65	180	103.93	26.88
25	T01	200	12	86	103.40	27.57
25	t02	200	11	88	103.61	26.57
25	T04	240	41	136	103.41	25.85
25	t05	240	33	133	103.66	24.63
					mean:	26.86

33

1.5   Conclusion

In this Chapter, we introduce the experimental set-up for steady turbulent bed-load flow, the steps and cautions of experiments are explained. The steady re-circulation of solid grains was achieved by jet entrainment mechanism. it was verified again that the temperature of the mixture is crucial to the index matching condition, in our case is about 17°C. The uniform flow condition was achieved by changing channel slope, since the variation of the slope is little (1° to 2°), checking the uniform condition by ruler may not as accurate as we expected. We measured the channel slope, flow depth and the outlet discharge for solid and liquid during the experiments, these data were used to verify or check the data obtained from imaging analysis. A series of tests werer also performed to obtained the basic properties of both grains and liquid, the data were not only used for the turbulent bed-load experiment itself, but also be used for the numerical modelling or theory verification.

Chapter 2

Laser scan image acquisition and processing [1]

The purpose of using RIM materials is to measure the behaviors of solid and liquid inside the flow, therefore in this chapter we introduce the methods we adopted to measure the solid and liquid velocity using transverse laser scanning and particle tracking algorithm, we would explain the improvements we had done to reduce the error. Then we introduce the method called longitudinal scanning to obtain the grain positions and velocities for each scanned grains over the image voxel.

2.1 Experimental set-up for laser scan acquisition

The methods of imaging measurements are using laser sheet to highlight the specific 2D plane inside the flow, which makes the motion of solid particles and liquid visible, we scanned the laser sheet over the channel and the process would be recorded by high-speed camera for further quantitative analysis. The laser is Coherent Innova 70c, 5W Argon laser system which generates a concentrated green light beam with 514.5nm in wave length and 1.5mm in beam diameter. The laser was connected with a fiber cable to safely transmit the high power laser beam to the sheet generator which split the beam into a sector-shaped laser sheet. To resolve separately solid and liquid motions, the liquid was mixed with a laser-induced fluorescent dye (pyrromethene 567, Exciton Inc.), and seeded with 50 μm tracer particles. The sheet generator was mounted on a linear trolley system to provide the steady scanning. The high speed camera we use is Phantom V4.3, Vision research Inc, for choices of the lens, 35 mm lens was for the transverse scan and 50 mm lens was for the longitudinal scan, the f number was set to 5.6 to keep sufficient brightness and the depth of field.

For transverse laser scan, the laser sheet is aligned parallel to the channel walls, and scans across the channel, the camera recorded the scan process through the channel sidewall (for the case SWRF and RWRF), as illustrated in Figure 2.2 or through a mirror to achieve the same perspective (for the case SWSF), as shown in Figure 2.1**a** and **b**. The range of laser sheet is about 12 cm long, the laser scan speed is about 7 mm/s, the camera filmed

---

[1]Most of the materials in this Chapter was earlier presented in the publication: Ni, W.-J., and Capart, H. (2015). Cross-sectional imaging of refractive-index-matched liquid-granular flows. *Experiments in Fluids* 56, 163.

with the resolution set to about 400 pixels x 250 pixlels, the frame rate was set to 600-700 fps, the footage length was up to 20 s.

Even with matched refractive indexes and temperature control, a gradual loss of focus is incurred as light propagates through the heterogeneous medium. For spheres, this blurring was shown by *Patil and Liburdy* (2012) to depend on the number of grains intercepting the light path, causing loss of focus beyond approximately 10 grains. Because the ratio of channel width to grain diameter $B/D = (120 \text{ mm})/(7 \text{ mm}) \approx 17$ exceeds this limit in our experiments, image quality degrades when the laser is over two third of channel width away from the sidewall. We therefore acquired two transverse scans for each run, imaging one from the left and one from the right to obtain the two image sequences $I_L(c, r, k)$ and $I_R(c, r, k)$.
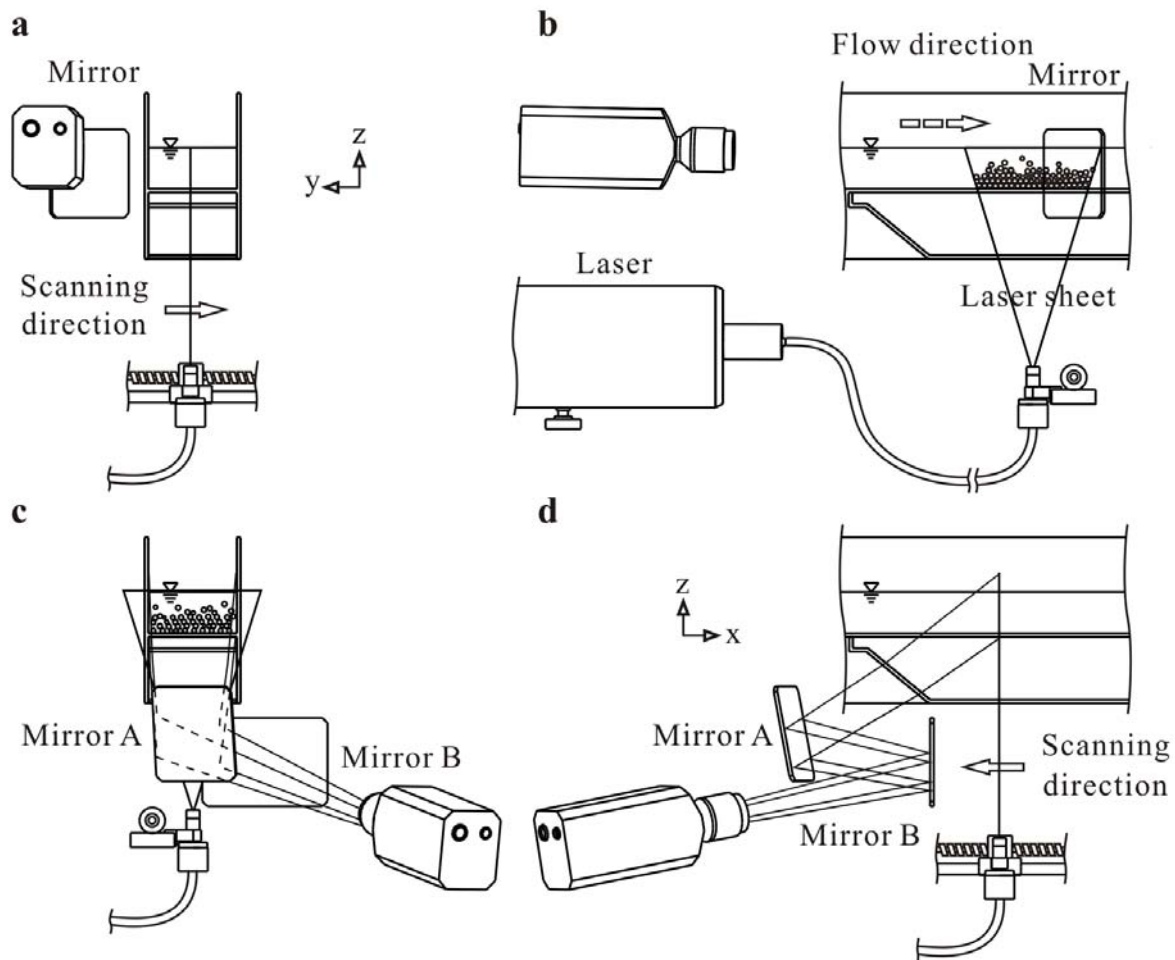
Figure 2.1 The arrangement of laser scan system and camera of transverse scanning **ab** and longitudinal scanning **cd** . The mirror was not necessary for the transverse scanning and was removed for SWRF and RWRF cases.
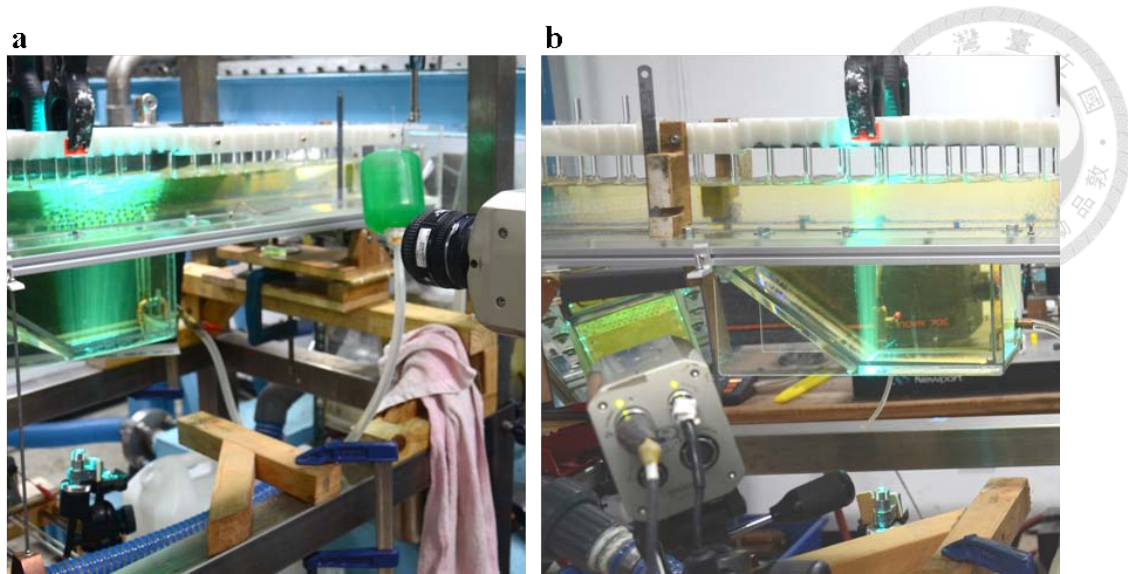
Figure 2.2 The configurations for laser sheet and camera of **a** the transverse scanning and **b** the longitudinal scanning during experiments, the configurations were set for the experiments SWRF and RWRF.

For longitudinal laser scan, the laser sheet was aligned normal to the channel walls and bottom, and scanned to upstream, the configuration as shown in Figure 2.1**cd**, and Figure 2.2**b**. This alignment and scan direction captured every solid grains within the scanned volume in the channel, no matter the grain was moving or stationary. Under the channel, a trapezoidal prism filled with para-cymene mounted to the channel floor, one side of the prism is parallel to the floor, which is allowed the laser sheet to pass without refraction, the slant side of the prism is the window for the camera to record, as image distortion due to refraction across the air-wall-liquid boundary increases nonlinearly with departures of the camera axis away from the wall normal *Spinewine et al.* (2003). The camera recording via mirror(s) is necessary for the longitudinal scan because of the tight space under the channel.
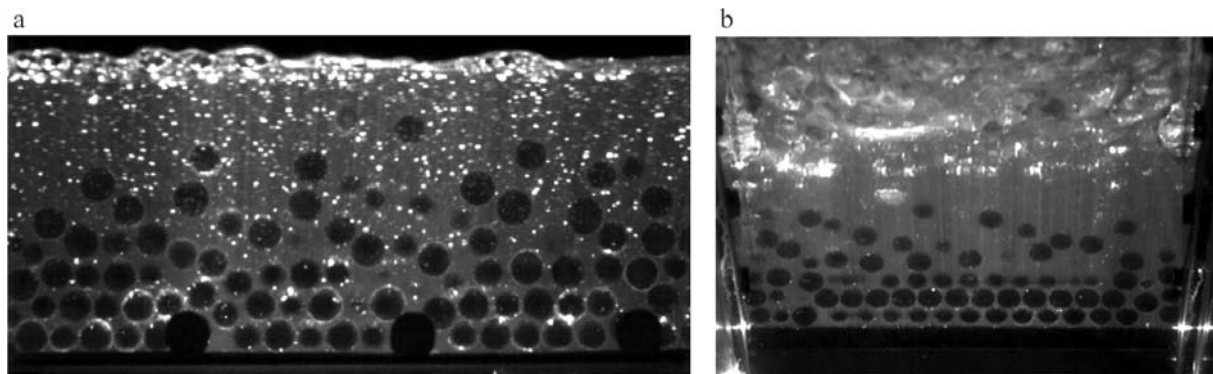
Figure 2.3 The images of footage acquired from **a** the transverse scanning and **b** longitudinal scanning.

The range of longitudinal scan is from 7 to 12 cm, the scan speed is about 10 mm/s, the camera resolution was set to 400 pixels x 300 pixels approximately, for the frame rate it is in a range of 900-1100 fps, with the higher resolution and frame rate, the footage length

37

would be reduced to 10 s. The scan acquired in this configuration yields the bottom camera footage $I_B(c, r, k)$. The raw images of the transverse scan and longitudinal scan are shown in Figure 2.3.

2.2 Calibration and image ortho-rectification

For each camera viewpoint, left, right and bottom, the following equation is used to transform between the physical coordinates (x, y, z) and image coordinates (c, r)

$$
\begin{pmatrix} \lambda c \\ \lambda r \\ b\lambda \end{pmatrix} = \mathbf{A}_V \begin{pmatrix} x \\ y \\ z \end{pmatrix} + \mathbf{b}_V \tag{2.1}
$$

Here λ is the depth coordinate of each point, $\mathbf{A}_V$ a 3 by 3 invertible matrix, and $\mathbf{b}_V$ a 3 by 1 column vector. Calibration of the 12 unknown coefficients of matrix $\mathbf{A}_V$ and vector $\mathbf{b}_V$ is performed using the least squares procedure described in *Spinewine et al.* (2003). This relies on 14 calibration points of known coordinates (x, y, z) placed along the channel sidewalls, with image coordinates (c, r) clearly identifiable on the scans. During scans, the time-evolving position of the laser plane must also be known. For the transverse scans, this is deduced from the times at which the laser plane intercepts the sidewalls, yielding the transverse laser position history.

$$
Y_\Pi(t) = Y_\Pi(0) + V_\Pi t \tag{2.2}
$$

For the longitudinal scans, the progress of the laser scan is monitored in a different way, by tracking the intersection of the laser plane with the channel bottom *Ni and Capart* (2006). This yields the longitudinal laser position history

$$
X_\Pi(t) = X_\Pi(0) + U_\Pi t \tag{2.3}
$$

where $U_\Pi < 0$ as the laser travels from downstream to upstream. The calibration points for transverse scan and longitudinal scan are illustrated in Figure 2.4, for transverse scan, the calibration points were tiny cross marks etched on the channel walls, these marks would be shined when laser sheet passed through the walls while they would be nearly invisible when laser sheet was inside the channel. For longitudinal scan, the calibration step was conducted after the experiment, it is necessary to clear all particles inside channel and fill it with p-cymene again, then we put the calibration target into the channel, made it sticked to the wall of channel right wall (for the consistency of coordinates between two scan), and beneath the p-cymene surface(for the under-liquid calibration).

The raw footage is not convenient to work with for two reasons. First, due to foreshortening, the scale of objects seen on the raw camera images depends on their distance away from the camera. Likewise, because the camera axis is not always orthogonal to the laser plane, the shapes of the grain cross sections incur some degree of distortion, transforming circles into ellipses. Since we seek to harvest from these images objects of known physical size and shape (spherical grains of identical diameter D, producing circular cross sections when cut by the laser plane), it is convenient to ortho-rectify the footage prior to further processing. Based on the calibrated camera viewpoints and known laser position histories,
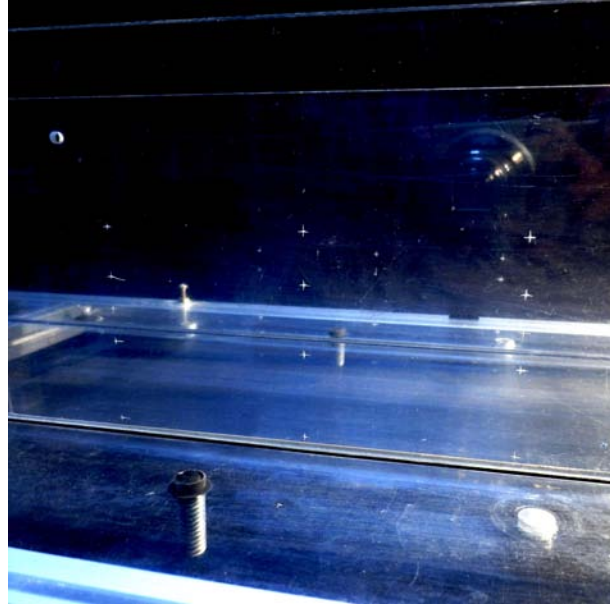
Figure 2.4 The calibration points scratched as white crosses on the channel side walls .

this is done using source to target mapping (Burger and Burge 2008; Huang et al. 2008). For the transverse scans, we first introduce the discrete Cartesian grid:

$$(x_j, z_i) = (x_0 + j\Delta x, z_0 + i\Delta z) \tag{2.4}$$

for which we set $\Delta x = \Delta z = 0.25$ mm. Next, this grid is projected onto the image plane using transformation Eq. (2.1) specialized to

$$\begin{pmatrix} (\lambda c)_{i,j}^{(k)} \\ (\lambda r)_{i,j}^{(k)} \\ (\lambda)_{i,j}^{(k)} \end{pmatrix} = \mathbf{A}_V \begin{pmatrix} x_j \\ Y_\Pi(t^{(k)}) \\ z_i \end{pmatrix} + \mathbf{b}_V \tag{2.5}$$

followed by the division,

$$c_{i,j}^{(k)} = \frac{(\lambda c)_{i,j}^{(k)}}{(\lambda)_{i,j}^{(k)}} \tag{2.6}$$

$$r_{i,j}^{(k)} = \frac{(\lambda r)_{i,j}^{(k)}}{(\lambda)_{i,j}^{(k)}} \tag{2.7}$$

Finally, brightness values $I_{i,j}^{(k)}$ are sampled at positions $(c_{i,j}^{(k)}, r_{i,j}^{(k)})$ by bilinear interpolation from the original image $I(c, r, k)$. The set x_j, z_i, $t^{(k)}$, $I_{i,j}^{(k)}$ obtained by this procedure defines the ortho-rectified footage $I_V(x, z, t)$. Unlike the original footage, the ortho-rectified footage records all objects at a known, uniform scale and with undistorted shapes in the plane (x, z). Although (x, z, t) take discrete values, we later drop the indices i,j,k for simplicity, and to allow these indices to be used for other purposes. We apply the same procedure to the longitudinal scan footage $I_B(c, r, k)$ to obtain the corresponding ortho-rectified footage $I_B(y, z, t)$. In an abstract sense, these voxel images can be interpreted as three-dimensional cross sections through four-dimensional physical space time (x, y, z, t),

39

along the paths $(x, Y_\Pi(t), z, t)$ (for the transverse scans) and $(X_\Pi(t), y, z, t)$ (for the longitudinal scans) traveled by the moving laser plane. The calibrations of both scans are shown in Figure 2.5.
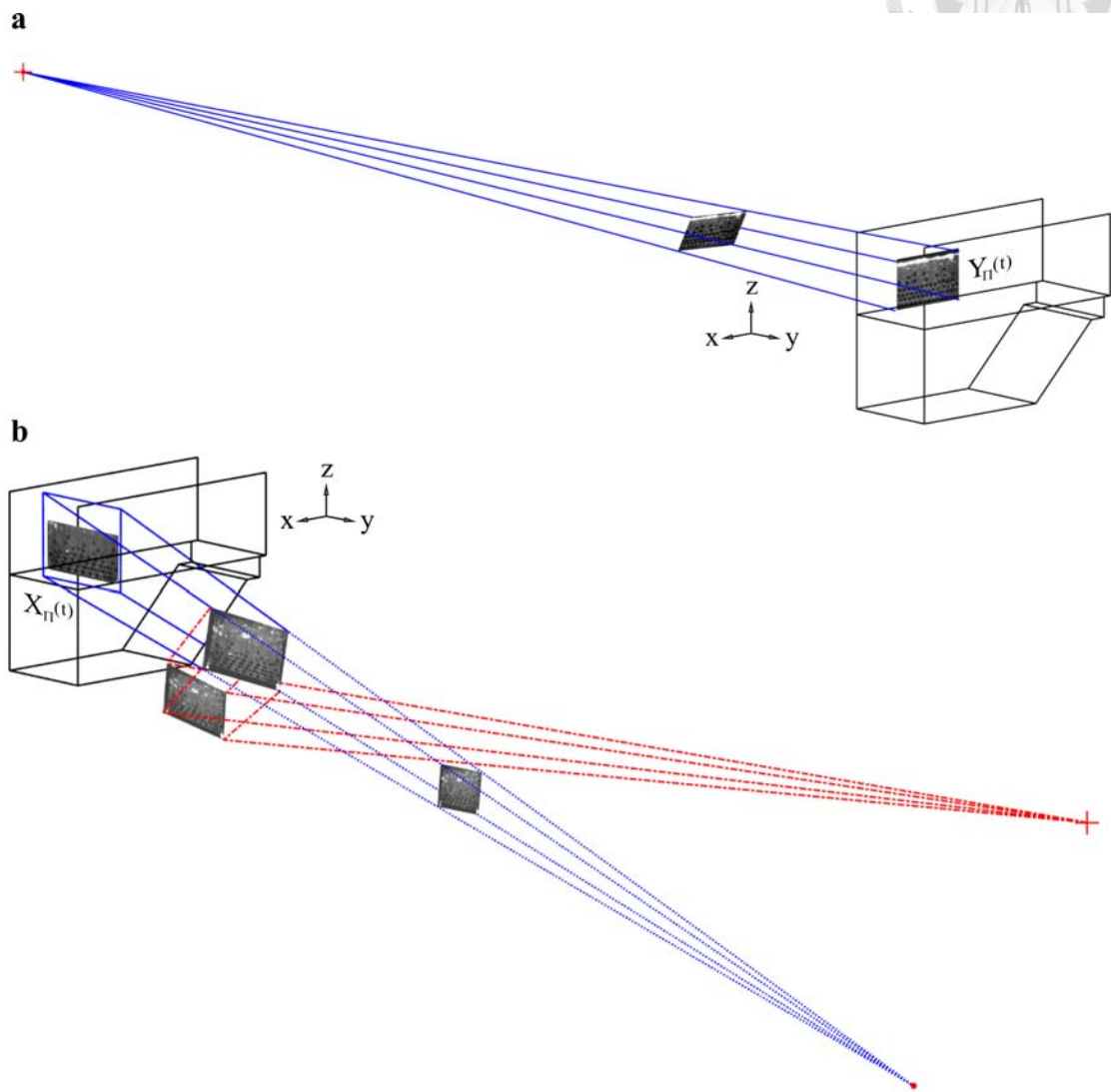
Figure 2.5 The calibration results show the position and orientation of high-speed camera and the laser sheet for **a** the transverse scan and **b** the longitudinal scan.

2.3   Transverse scan processing

Two different fields are extracted from the transverse scans: grain velocities and liquid velocities, both in the plane of the slowly moving laser. As explained earlier, the ortho-rectified footage is used to capture grain velocities, as this facilitates the identification of objects of know scale and shape. To capture liquid velocities, however, ortho-rectification is not needed since the point-like tracer particles have neither size nor shape. We therefore go back to the original footage to avoid the small loss of resolution incurred by image resampling. The corresponding processing steps are presented separately in the following two sub-sections.

40

2.3.1   Solid grain identification and tracking

A typical ortho-rectified image extracted from a transverse scan is illustrated in Figure 2.6. As can be seen, the image features objects characterized by very different brightness levels. At the top, a very bright horizontal stripe is produced at the intersection of the flow free surface with the laser plane. Below this surface, the tracer particles used to seed the liquid shine brightly under laser illumination. Relatively bright circular halos are also produced at the intersection of the laser plane with the spherical grains. At the next brightness level, the dyed liquid shows up as a relatively uniform gray, save for bright caustics caused by glancing laser-sphere intersections. Finally, the interiors of the spherical grains are recorded as dark cores. Unless some pre-processing is applied, it is likely that the brightest features will overwhelm the less contrasted grain images. Another deficiency of the image is that the brightness levels vary longitudinally, due to the uneven brightness of the laser sheet over its angular spread. This is made clearer in Figure 2.6 **b**, which profiles the brightness quartiles $I_{25}(x)$ and $I_{75}(x)$, where $I_p(x)$ is the brightness exceeded by p percent of the pixels in each column x. To equalize levels and highlight the brightness range of the solid grains, a corrected brightness is calculated using

$$J(x,z) = \frac{I(x,z) - I_{25}(x)}{I_{75}(x) + 1} \qquad (2.8)$$

, then restricted to range $0 \leq J \leq J_{max}$ using the statement,

$$J(x,z) = max(0, min(J, J_{max})) \qquad (2.9)$$

where J_{max} is a maximum brightness set to curtail the influence of bright glares. The resulting image $J(x,z)$ is illustrated in Figure 2.6 c.

The next step is to automatically identify granular positions. For the transverse scans, our objective is not to capture all visible grains, but only those that can be most reliably identified and precisely positioned. Accordingly, we focus on grains that are cut by the laser near their centre, producing nearly equatorial halos of diameter equal to the sphere diameter D = 7 mm. Spheres cut too away from the centre, producing smaller cross sections or unclear end caps are excluded from the analysis. Although off-centre spheres could also be captured, an ambiguity would remain as to whether the true center of the sphere lies to the le ft or to the right of the laser plane. For spheres cut by the laser plane near the equator, by contrast, the transverse position of the sphere coincides with the known location Y_{Π} of the laser plane.
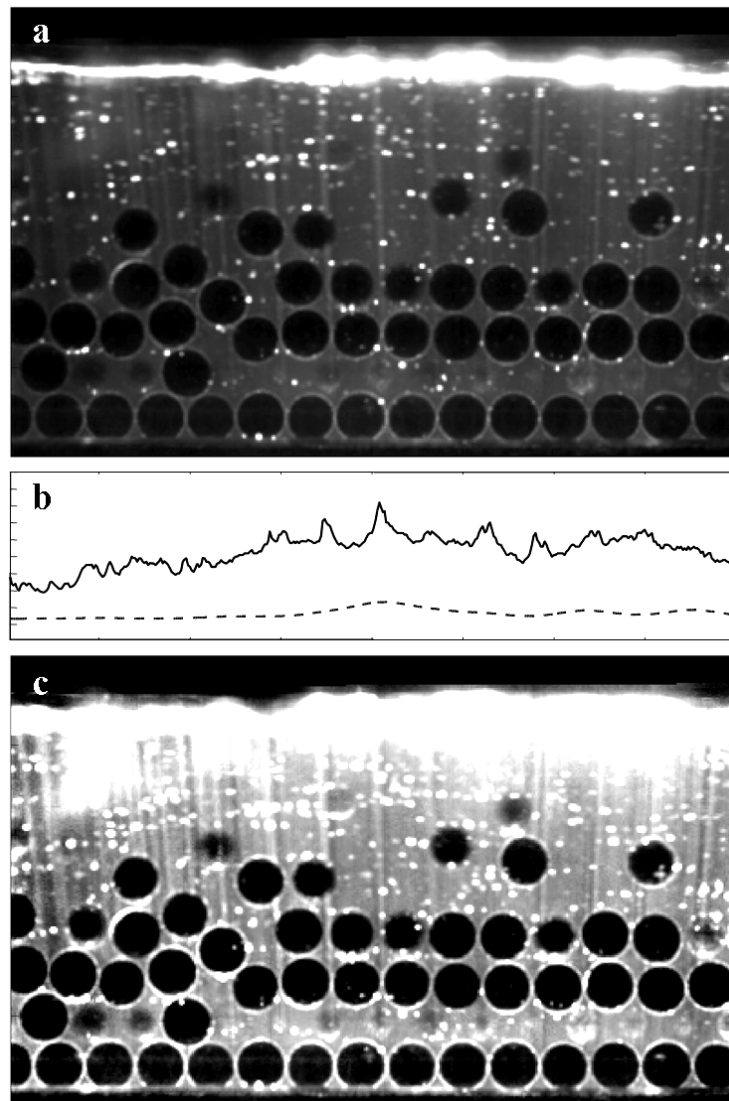
Figure 2.6 Image pre-processing for the transverse scanning: **a** ortho-rectified image; **b** longitudinal brightness distribution; **c** image after brightness equalization.
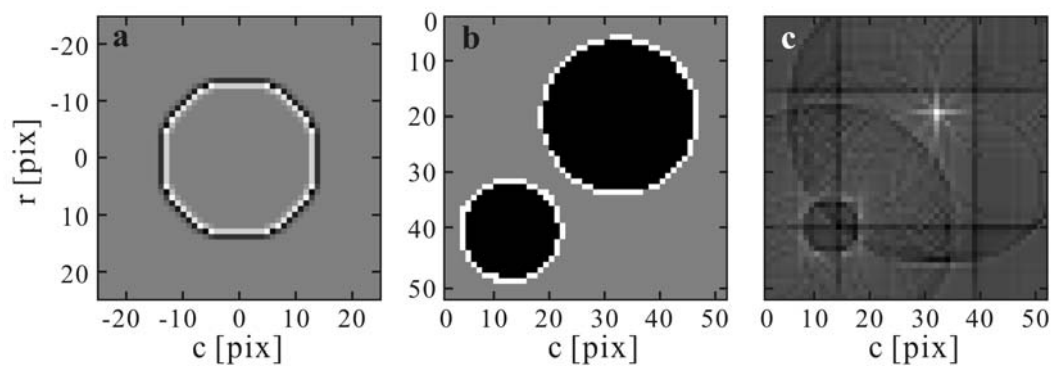

Figure 2.7 Halo identification principle: **a** convolution filter; **b** synthetic image with two halos with different diameters; **c** synthetic image after convolution, yielding a brightness peak at the center of the halo provided that th e halo diameter matches the filter diameter.

To capture these equatorial halos, we convolute image J with a discrete filter F that mimics the brightness distribution of the target object. Using index notation, the resulting filtered image K is obtained from the discrete convolution

$$K_{i,j} = \sum_m \sum_n J_{i-m,j-n} F_{m,n} \qquad (2.10)$$

To construct filter F, we define first the hat function

$$H_{i,j} = \begin{cases} 1, x_j^2 + z_i^2 < R^2 \\ 0, otherwise \end{cases} \qquad (2.11)$$

where $(x_j, z_i) = (j\Delta x, i\Delta z)$ and R is the radius of the solid spheres. We then convolute H with the discrete Laplace operator proposed by *Jähne* (1995).

$$L_{m,n} = \frac{1}{4} \begin{pmatrix} 1 & 2 & 1 \\ 2 & -12 & 2 \\ 1 & 2 & 1 \end{pmatrix} \qquad (2.12)$$

to obtain

$$F_{i,j} = \sum_m \sum_n H_{i-m,j-n} L_{m,n} \qquad (2.13)$$

The filter F constructed in this fashion features two concentric rings of non-zero values, respectively negative and positive, immediately inside and outside of a circle of radius R (Figure 2.7**a**). A particularly strong convolution response is therefore generated when the filter F covers a circular ring with dark pixels on the inside and bright pixels on the outside, matching the targeted grains with their dark inside cores and bright outside halos. As demonstrated on a synthetic image example in Figure 2.7**b c.**, the filter highlights only grain cross sections of the desired target size R, which produce strong brightness maxima on the transformed image K. These steps are further illustrated for an actual image in Figure 2.8**a b**. For the experimental images, improved results are obtained by suppressing over-bright pixels of the equalized image J (above a set brightness threshold) prior to convolution with the filter F. This is done by replacing the over-bright values by the average brightness of the whole image (Figure 2.8**a**).

As in *Capart et al.* (2002) we harvest in-plane grain positions $(X_i^{(k)}, Z_i^{(k)})$ at successive times $t^{(k)}$ by identifying local brightness maxima on successive filtered images $K^{(k)}$, and refining their position to sub-pixel accuracy using quadratic fits. To avoid erroneous identification, we calculate for each possible grain position a quality indicator β, defined as the mean brightness averaged around the perimeter divided by the mean brightness inside the circle. Only those positions with β values above a set threshold are then retained for further analysis (Figure 2.8**c**). For the transverse scan, not all spheres must be captured, but erroneously identified spheres must be avoided. To avoid false positives, the threshold for the quality indicator β was therefore set to the relatively high value of 3.

To obtain velocity vectors, nearest-neighbor matching (see *Capart et al.* (2002)) is used to establish the pairing $j(i)$ between successive grain positions $(X_i^{(k)}, Z_i^{(k)},)$ and $(X_j^{(k+1)}, Z_j^{(k+1)})$ most likely to be associated with one and the same physical particle. The corresponding velocity components are calculated from
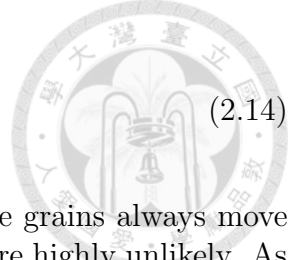
$$U_i^{(k)} = \frac{X_{j(i)}^{(k+1)} - X_i^{(k)}}{t^{(k+1)} - t^{(k)}}, W_i^{(k)} = \frac{Z_{j(i)}^{(k+1)} - Z_i^{(k)}}{t^{(k+1)} - t^{(k)}}. \tag{2.14}$$

The resulting velocity vectors are illustrated in Figure 2.8**d**. As the grains always move less than one grain radius from one image to the next, mismatches are highly unlikely. As illustrated on Figure 2.8d., only the clearest, full-size grain cross-sections are captured on each image, with the others disregarded. Over the entire image sequence, however, the procedure harvests more than enough vectors to produce a well-resolved velocity field. Although only two velocity components (U, W) are recorded for each velocity vector, moreover, the corresponding sphere center positions $(X_i^{(k)}, Y_i^{(k)}, Z_i^{(k)})$ are known in 3D since $Y_i^{(k)} = Y_\Pi(t^{(k)})$ coincides with the known transverse position of the laser plane.
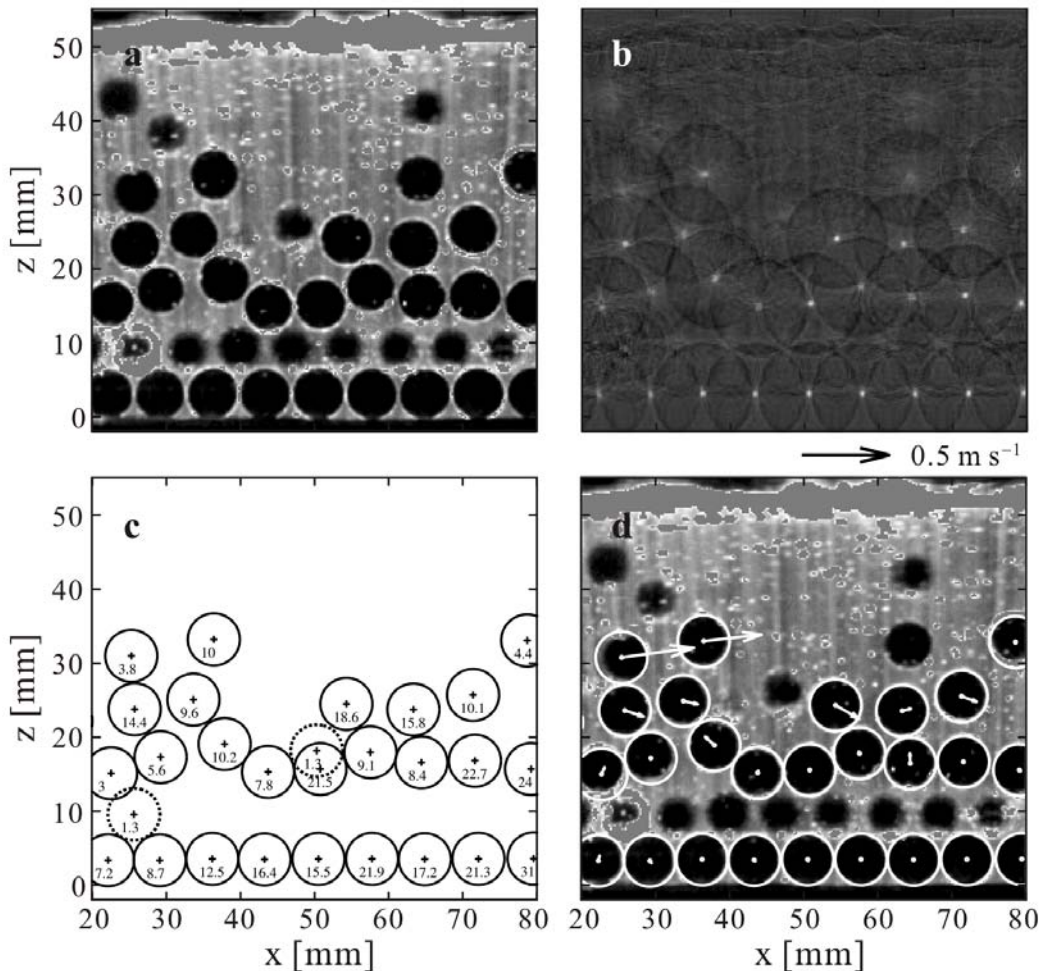
Figure 2.8 Solid grain tracking on transverse scan images (half image close-up): **a** equalized, ortho-rectified image J with over-bright pixel black-out; **b** filtered image K produced by the convolution with the filter F; **c** captured grains with the corresponding values of brightness ratio β; **d** screened grains and their velocity vectors.

2.3.2 Liquid tracer identification and tracking

To avoid loss of resolution, the liquid tracer particles are identified on the original images instead of the ortho-rectified footage. To disambiguate between the moving liquid tracers and other bright features also present in the image, three pre-processing steps are applied prior to particle capture. The first consists in equalizing the longitudinal brightness distribution, as explained previously when discussing the capture of solid grains (Figure 2.9**a**). The second step is to subtract from each image a moving average of 6-21 surrounding frames (Figure 2.9**b**). This suppresses the bright, but slowly evolving features of the images such as the flow free surface and laser caustics. The third step consists in masking out the locations of the solid grains. For this purpose, dark grain cores are first identified as regions with brightness below a set threshold. A morphological dilation is then performed to expand these cores and cover the surrounding bright halos of the solid grains (Figure 2.9**c**). For this operation, a diamond-shaped structuring element of radius equal to 2 pixels is used (Shapiro and Stockman 2001). For the thick bright line of the free surface reflection would be identified and excluded in the same way (Figure 2.9**d**). The resulting background-subtracted, masked image is illustrated in Figure 2.9**e**.
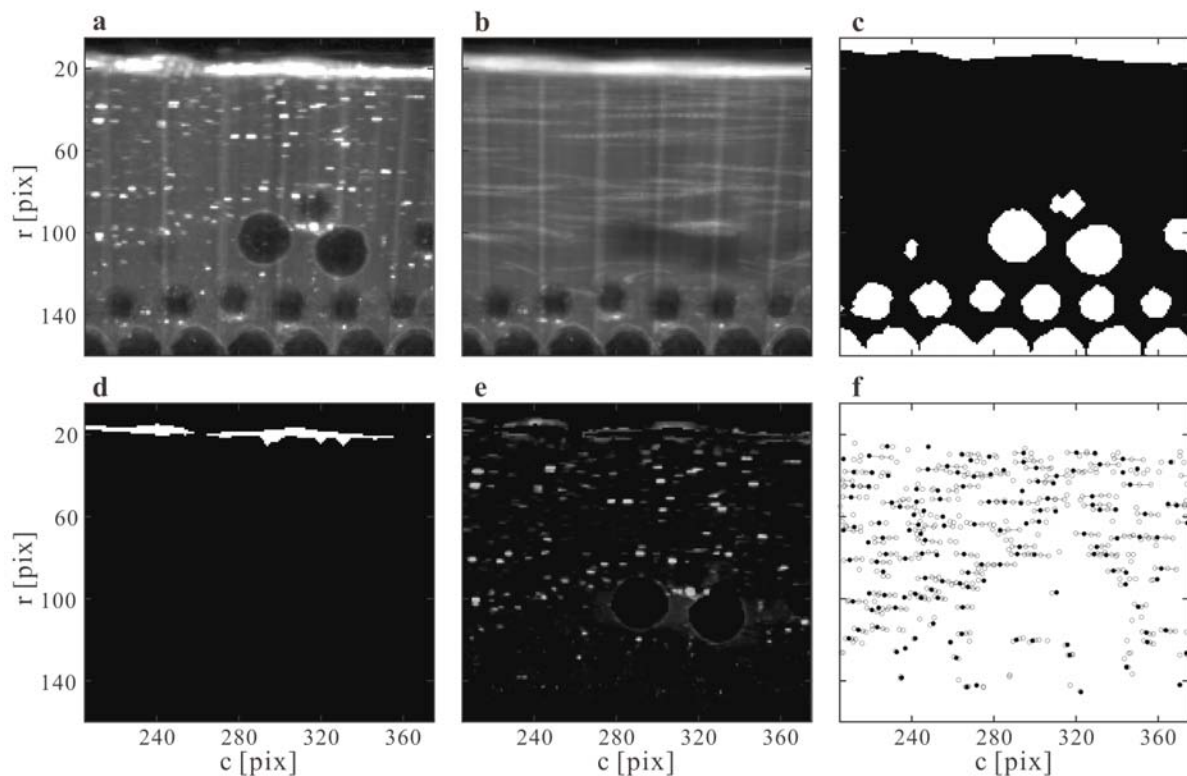
Figure 2.9 Liquid tracer tracking on transverse scan images:**a** the raw image; **b** slowly evolving background obtained by averaging 6-21 surrounding images; **c** the mask represents the area occupied by solid grains; **d** the mask represents the area occupied by thick lines of free surface reflection; **e** background-subtracted, masked image in which area of solid and free surface is removed from consideration; **f** tracer particle tracks extracted from four successive background-subtracted, masked images.

On the pre-processed images, the tracer particles are identified and positioned using the methods described in *Capart et al.* (2002). After convolution with a Laplacian-of-Gaussian

filter (*Jähne* (1995)), particle positions are identified as local brightness maxima of the convoluted image, then refined to sub-pixel accuracy using quadratic fits. For each image acquired at time $t^{(k)}$, this yields a set of particle image positions $(c_i^{(k)}, r_i^{(k)})$. To convert from image coordinates to physical coordinates, the transformation (1) is used subject to the constraint $y = Y_\Pi(t^{(k)})$ associated with the known position of the laser plane. This produces the sets $(x_i^{(k)}, z_i^{(k)})$ of identified liquid tracer particle positions at successive times $t^{(k)}$.

To track particles over successive frames, we use the following path-tracking procedure. The optimum pairing connecting particle positions $(x_i^{(k)}, z_i^{(k)}{}_1)$ and $(x_j^{(k+1)}, z_j^{(k+1)})$ most likely to correspond to one and the same physical particle is obtained by considering four successive times $t^{(k-1)}$, $t^{(k)}$, $t^{(k+1)}$, and $t^{(k+2)}$. For each candidate pair (i, j), particle positions at times $t^{(k)}$ and $t^{(k+1)}$ are tentatively extrapolated forward and back to times $t^{(k-1)}$ and $t^{(k+2)}$, using the formulas

$$x_{i,j}^{(k+2)} = x_i^{(k)} + 2(x_j^{(k+1)} - x_i^{(k)}), \tag{2.15}$$

$$x_{i,j}^{(k-1)} = x_i^{(k)} - (x_j^{(k+1)} - x_i^{(k)}). \tag{2.16}$$

Next, the distances $\delta_{i,j}^{(k+2)}$ and $\delta_{i,j}^{(k-1)}$ between the extrapolated positions $(x_{i,j}^{(k+2)}, (x_{i,j}^{(k-1)}$ and the nearest particles actually observed on frames $t^{(k+2)}$ and $t^{(k-1)}$ can be ascertained. An affinity function $a_{i,j}$ measuring the likelihood of pair (i, j) can then be calculated from

$$a_{i,j} = exp(-\delta_{i,j}^2) \tag{2.17}$$

where

$$\delta_{i,j} = max(\delta_{i,j}^{(k-1)}, \delta_{i,j}^{(k+2)}) \tag{2.18}$$

To score well, tracks must therefore be consistent with particle positions observed at all four successive instants. Finally, the optimum pairing $j(i)$ is obtained by maximizing the product of affinities

$$\prod_i^{max} a_{i,j(i)} \tag{2.19}$$

subject to the constraint that the pairing $j(i)$ must be one-to-one. In practice, we are content with the approximate optimum found by selecting maxima one by one using

$$(i_{max}, j_{max}) = \arg\max_{i,j} a_{i,j} \tag{2.20}$$

where the operator arg max returns the arguments (i, j) that maximize the affinity $a_{i,j}$, then removing already paired particles from further consideration. Pairs with insufficiently high affinities (smaller than a set threshold) are also removed from consideration. Because this method exploits information from four successive frames, it is more robust than methods based on nearest-neighbor or pattern matching *Capart et al.* (2002). The tracks acquired in this fashion are illustrated in Figure 2.9**f**. After the pairing $j(i)$ is established, the liquid tracer velocities are obtained from

$$u_i^{(k)} = \frac{x_{j(i)}^{(k+1)} - x_i^{(k)}}{t^{(k+1)} - t^{(k)}}, w_i^{(k)} = \frac{z_{j(i)}^{(k+1)} - z_i^{(k)}}{t^{(k+1)} - t^{(k)}}, \tag{2.21}$$

Once again, only the in-plane components (u, w) of the liquid tracer velocities are obtained, but the corresponding 3D tracer positions $(x_i^{(k)}, y_i^{(k)}, z_i^{(k)})$ are all known, since $y_i^{(k)} = Y_\Pi(t^{(k)})$ coincides with the known transverse position of the laser plane.

47

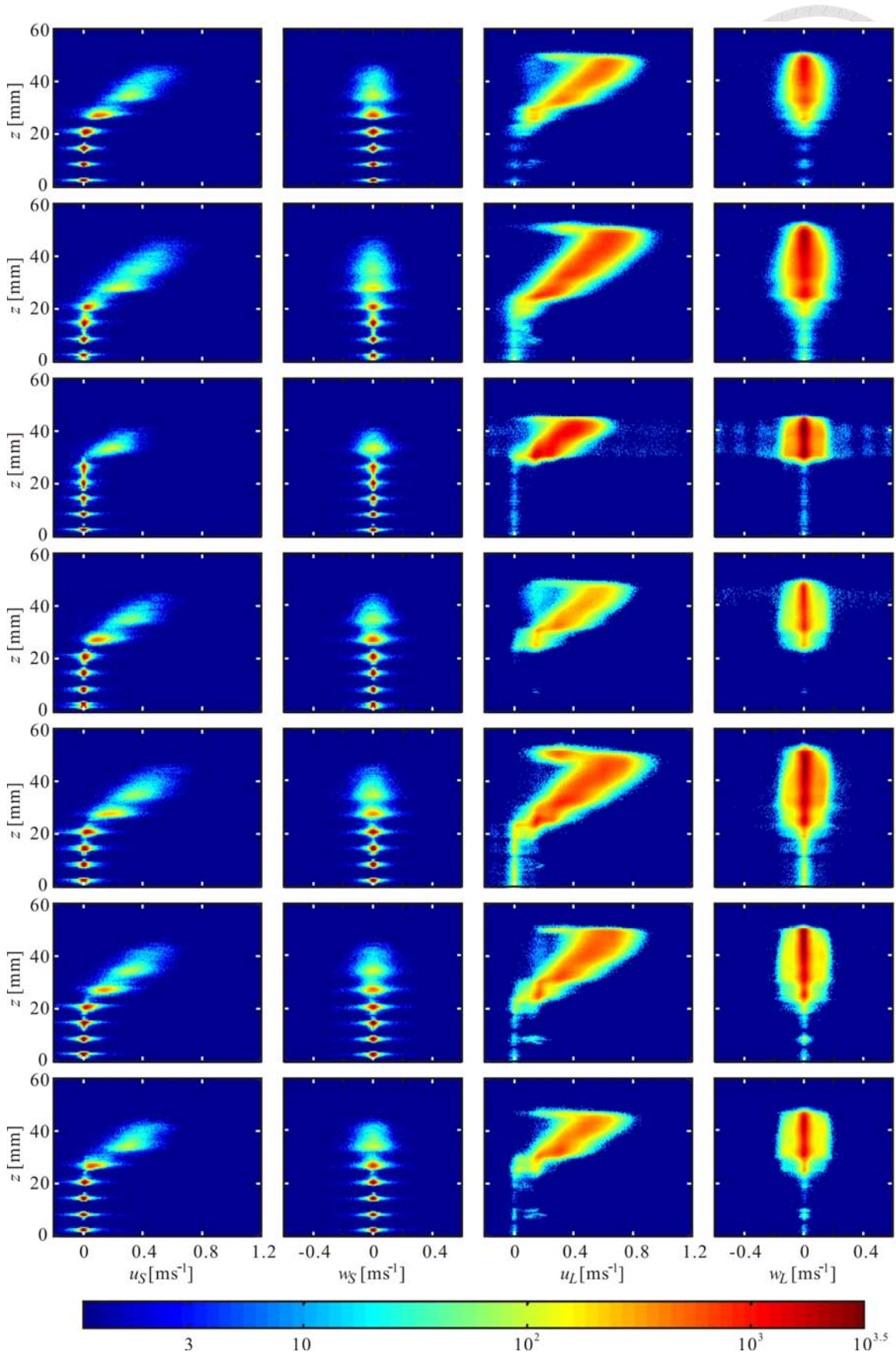### 2.3.3 Velocity binning maps along z axis

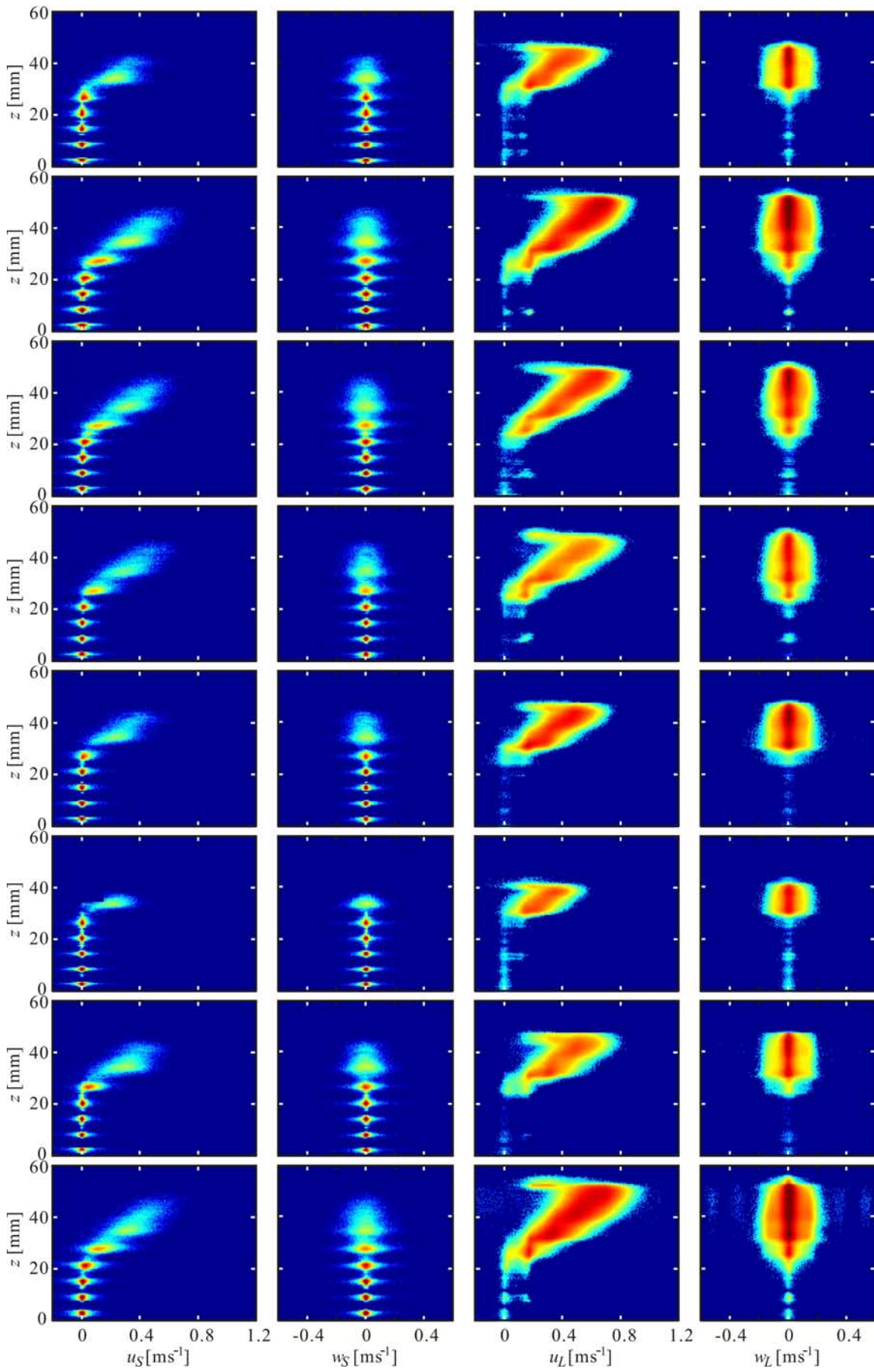Figure 2.10 Velocity binning maps along z for SWSF: 1-7.
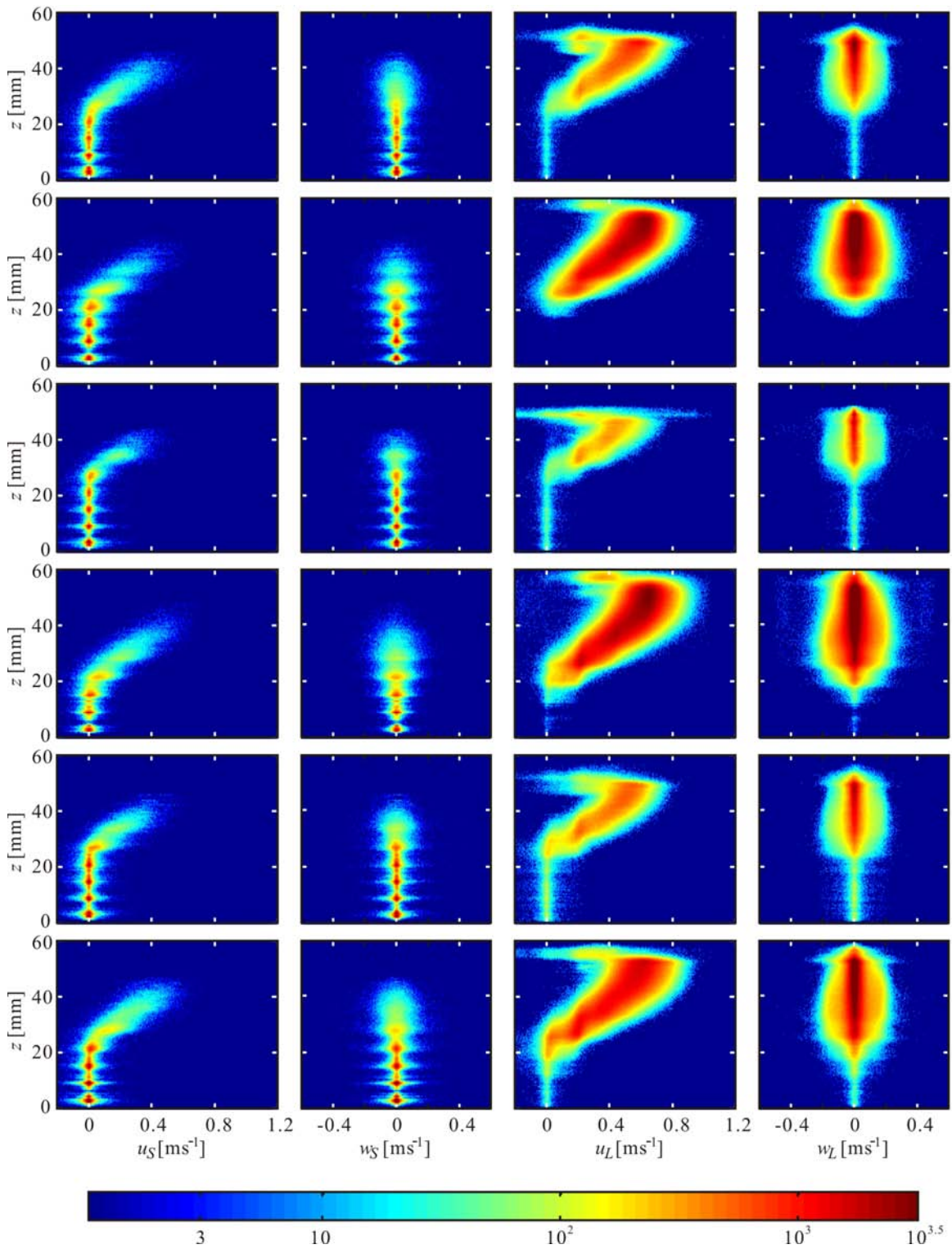
49

Figure 2.11 SWSF: 8-15.

50

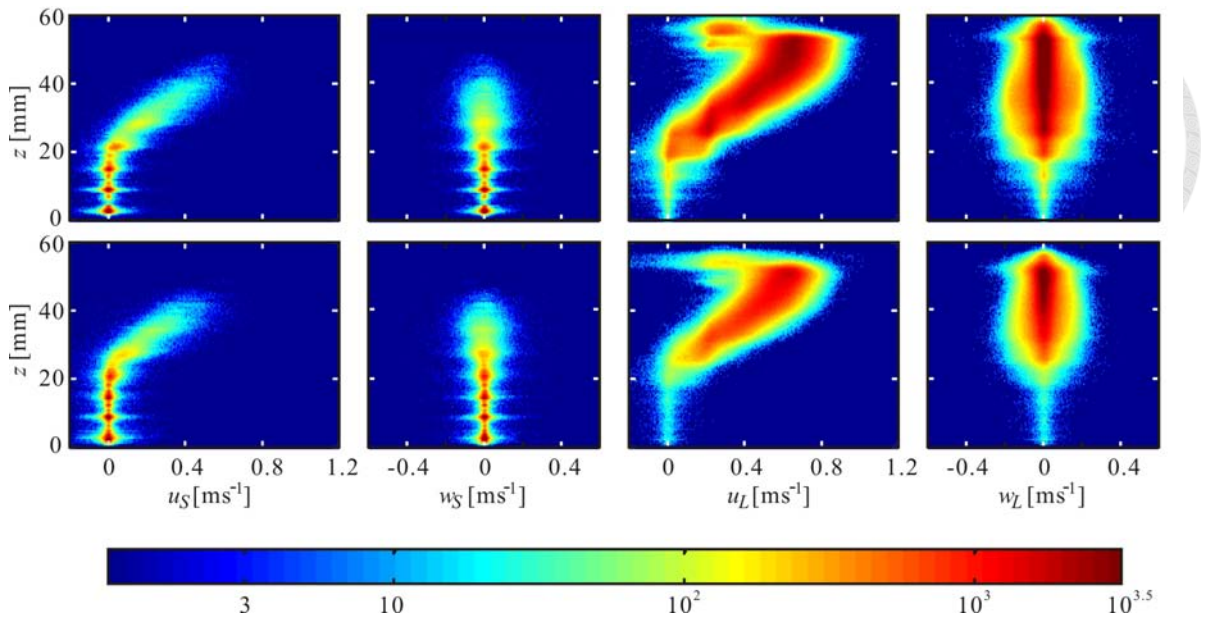Figure 2.12 Velocity binning maps along z for SWRF: 1-6.
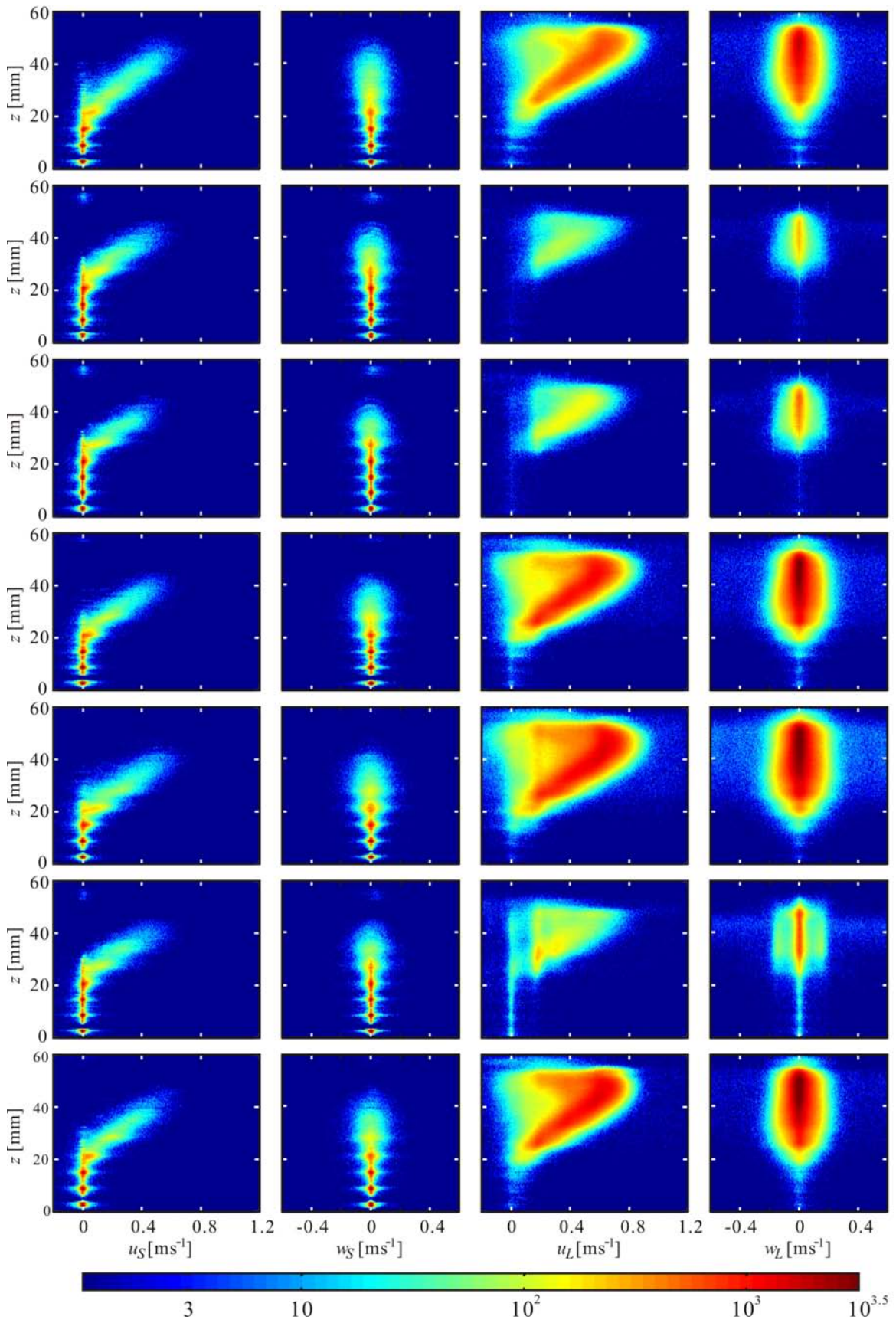
51

Figure 2.13 SWRF: 7-8.

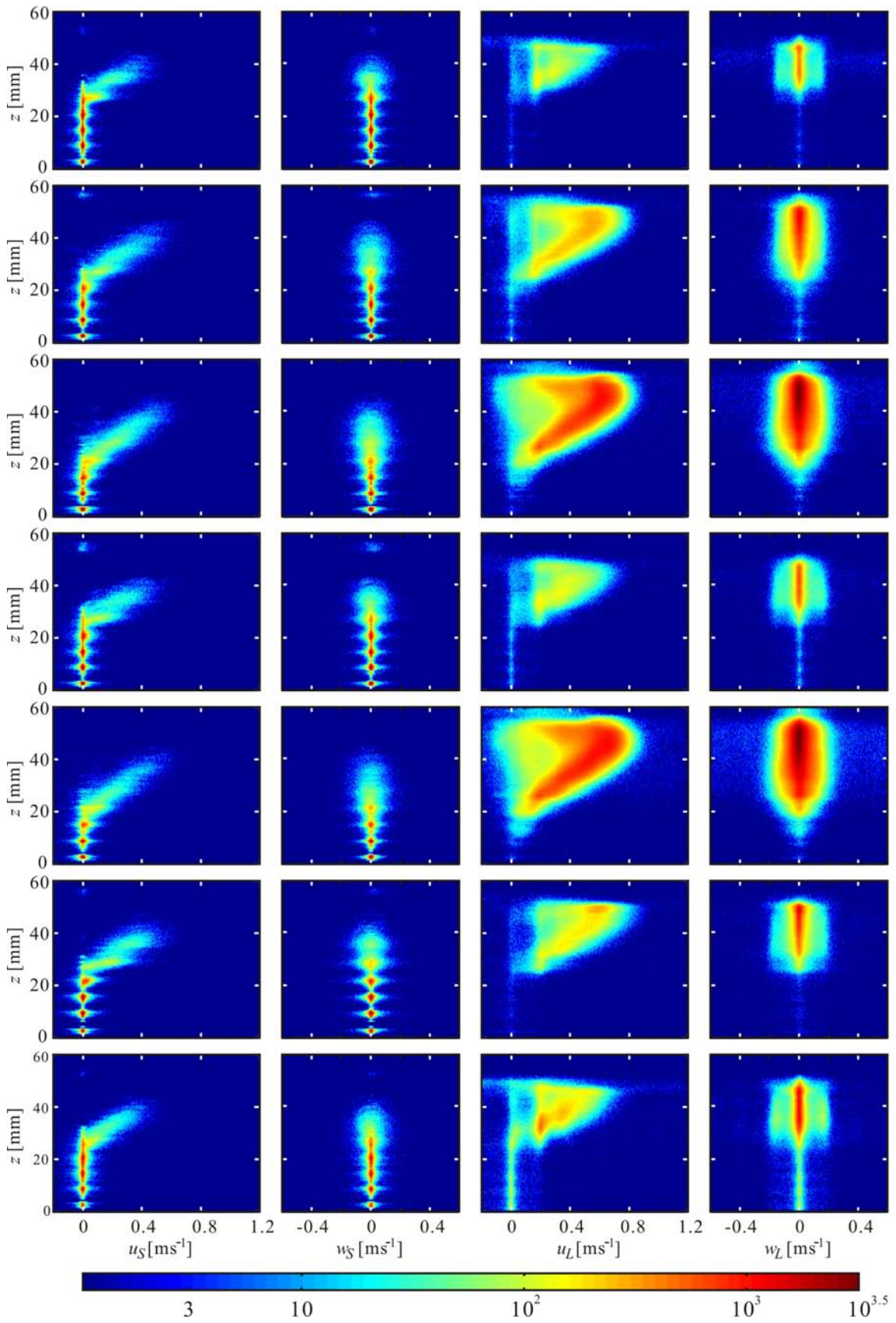Figure 2.14 Velocity binning maps along z for RWRF: 1-7.

Figure 2.15 RWRF: 8-14.

54

2.4 Longitudinal scan processing

Whereas the transverse laser scans yields grain and liquid motions parallel to the laser plane, the longitudinal scan captures the passage of grains through the plane. As a spherical grain traverses the plane, the intersection of its surface with the laser plane yields a circular cross section of increasing then decreasing radius. This occurs for stationary as well as moving grains, as the laser sweeps across them by traveling upstream. The three velocity components of the crossing grains can then be deduced from the duration of the crossing event, inversely proportional to the normal component of the grain speed relative to the plane, and from the lateral and vertical drift of the boundary cross section during the crossing event. Because the variation in time of the laser-cut cross section leaves a three-dimensional record of the passage of a grain, moreover, the identification of grains is greatly facilitated. As found earlier by *Huang et al.* (2008), pattern recognition is much more reliable in 3D than in 2D. As a result, whereas only a subset of visible grains can be reliably identified automatically from 2D images of their cross sections (see the transverse scan example of Figure 2.8), nearly all crossing spheres can be identified from the longitudinal scan. This reliable record of the presence or absence of grains can then be exploited to determine the volume fractions occupied by the grains and liquid, respectively.

Our proposed algorithm proceeds in three main steps. First, identify from the footage cross-section centers $Y_C^{(k)}(t)$, $Z_C^{(k)}(t)$ and start and end times $t_1^{(k)}$ and $t_2^{(k)}$ associated with a single grain crossing event k. Second, extract a corresponding set of grain boundary points $(y_i^{(k)}, z_i^{(k)}, t_i^{(k)})$. Third, find the grain crossing position and velocity vectors $(\mathbf{X}_k, \mathbf{U}_k)$ that best fit the boundary points $(y_i^{(k)}, z_i^{(k)}, t_i^{(k)})$. Although generalizations may be possible to grains of different sizes and shapes, in this work we consider only spherical grains of identical diameter D. The necessary processing steps are detailed in the following three sections.

2.4.1 Identification of grain crossing trajectories

To identify grain crossing trajectories, the ortho-rectified bottom camera footage $I_B(y, z, t)$ acquired during the longitudinal laser scan is processed as follows. First, sphere cross-sections are identified on individual frames using the approach outlined earlier, yielding sets of cross section centers of coordinates (Y_j, Z_j) at successive times t. For the longitudinal scan, false positives can be screened out at later steps of the analysis. The threshold for the quality indicator β was therefore set to 2, a lower value than for the transverse scan, to capture nearly all crossing particles. Nearest-neighbor matching (see *Jähne* (1995); *Capart et al.* (2002)) is then used to connect together the cross section centers corresponding to one and the same crossing sphere k, yielding the raw trajectories $(X_C^{(k)}(t), Y_C^{(k)}(t), Z_C^{(k)}(t))$. Here $X_C^{(k)}(t) = X_\Pi(t)$ is the location of the laser scanning plane at time t, and subscript C denotes the centers of the sphere cross sections (as cut by the laser scanning plane), not the centers of the spheres themselves. A deficiency of these raw trajectories is that they only capture part of the crossing events, when spheres are cut near the middle and the corresponding cross sections have sufficient areas. When spheres are cut near their end caps, by contrast, their cross sections are not reliably detected.

In Figure 2.16, we illustrate this problem using a time-space image, obtained by slicing through the ortho-rectified voxel image at a given transverse location. On such images,

scanned spherical grains are recorded as dark ellipses, compressed or elongated depending on the speed at which they cross the scanning plane. Here three crossing spheres can be identified at the center of the image (Figure 2.16**a**), and we focus on the capture of the middle sphere. As shown in Figure 2.16**b**, the halo capture step is only able to identify halo centers (white dots) over a limited portion of the sphere crossing event. To address this deficiency, we extend each raw trajectory as follows. Centered on mean path position $(\overline{Y}_C^{(k)}, \overline{Z}_C^{(k)})$, a voxel column of square cross section $\Delta Y \times \Delta Z$ and dimensions $\Delta Y == \Delta Z = 0.6D$ is first extended to a longer duration than the original raw trajectory. At each time t, the voxel column cross-sectional area A occupied by dark pixels (below a set illumination threshold) is calculated, yielding function $A(t)$. This function is smoothed by Gaussian filtering (see *Jähne* (1995)) into the filtered function $\tilde{A}(t)$, and normalized by $\Delta Y \times \Delta Z$ to obtain

$$\alpha(t) = \frac{\tilde{A}(t)}{\Delta Y \Delta Z} \tag{2.22}$$
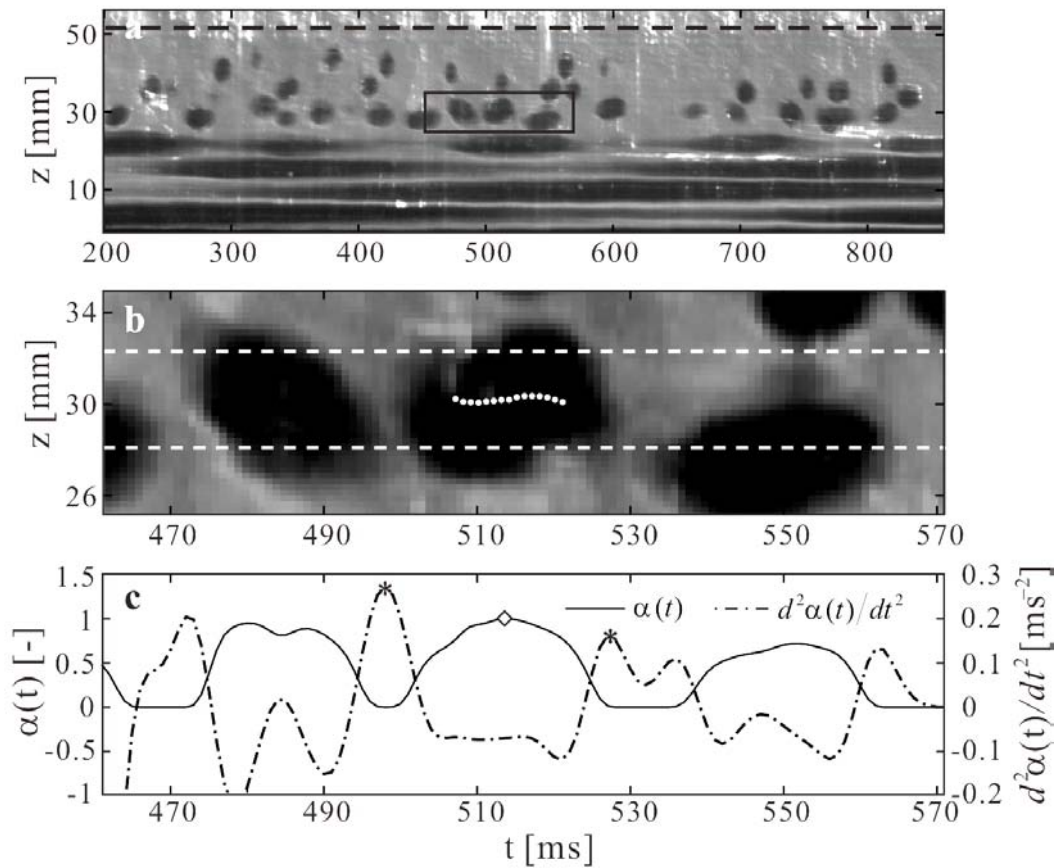
Figure 2.16 Identificatin of grain crossing trajectories from the longitudinal scan: **a** time-space image extracted from scan at transverse coordinate $y = 60mm$; **b** close-up showing a raw grain crossing trajectories (dots) and the limits of the voxel column (dashed lines) used to estimate the duration of the crossing event; **c** dark pixel ratio function $\alpha(t)$ and its second derivative $\partial^2 \alpha(t)/\partial t^2$ used to identify t_1 and t_2, the start and end times of the crossing event.

Upon differentiating twice, left and right maxima of the resulting curvature function $\mathbf{d}^2\alpha/\mathbf{d}t^2$ are located, providing estimates of the crossing event start and end times $t_1^{(k)}$ and $t_2^{(k)}$ (Figure 2.16**c**). Finally, a constant velocity trajectory of the form

$$\tilde{\mathbf{X}}_C^{(k)}(t) = \mathbf{X}_1^{(k)} + (t - t_1^{(k)}) \frac{\mathbf{X}_2^{(k)} - \mathbf{X}_1^{(k)}}{t_2^{(k)} - t_1^{(k)}} \tag{2.23}$$

is fitted by least squares to the raw trajectory data . The processed trajectory (2.23) both regularizes the raw trajectory and extends it to the longer interval $t_1^{(k)} \le t \le t_2^{(k)}$.
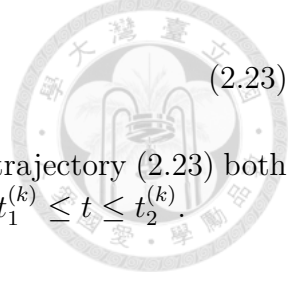
2.4.2 Extraction of grain boundary points and Least-squares fitting of granular position and velocity vectors

At each time t over interval $t_1^{(k)} \le t \le t_2^{(k)}$, Eq. (2.23) provides a first estimate of the location of the center $(\tilde{Y}_C^{(k)}, \tilde{Z}_C^{(k)})$ of the grain cross section, as cut by the scanning laser plane. To improve upon this estimate, we go back to the footage and use the following method to harvest grain boundary points around $(\tilde{Y}_C^{(k)}, \tilde{Z}_C^{(k)})$. Isolating a neighborhood of the laser scan image $I_B(y, z, t)$, a local radial derivative of the image illumination is calculated using

$$\frac{\partial I_B}{\partial r} = \frac{\partial I_B}{\partial y} \frac{y - \tilde{Y}_C^{(k)}}{r} + \frac{\partial I_B}{\partial z} \frac{z - \tilde{Z}_C^{(k)}}{r} \tag{2.24}$$

where

$$r = \sqrt{(y - \tilde{Y}_C^{(k)})^2 + (z - \tilde{Z}_C^{(k)})^2} \tag{2.25}$$

Points $(y_i^{(k)}, z_i^{(k)}, t_i^{(k)})$ lying on the granular boundary are then harvested as the set of pixels positions where $\partial I / \partial r$ is above a given threshold, and such that $r < 1.2 R_C^{(k)}(t)$, where

$$R_C^{(k)}(t) = R \sqrt{1 - \frac{(2t - t_1^{(k)} - t_2^{(k)})^2}{(t_2^{(k)} - t_1^{(k)})^2}} \tag{2.26}$$

is a preliminary estimate of the time-evolving radius of the sphere cross section as cut by the laser plane. This latter condition is introduced to avoid harvesting points from nearby sphere surfaces. In the next subsection, we explain how the set of boundary points $(y_i^{(k)}, z_i^{(k)}, t_i^{(k)})$ associated with a single sphere crossing event k can be further processed to better estimate the position and velocity of the crossing sphere.

The sphere boundary points obtained using the method of the previous subsection lie at the intersection of two loci in four-dimensional physical space-time (x, y, z, t). The first locus is the traveling laser plane, defined by the implicit equation

$$x - X_\Pi(t) = 0, \tag{2.27}$$

$$X_\Pi(t) = X_\Pi(0) + U_\Pi t. \tag{2.28}$$

The second locus is the set of points belonging to the moving boundary of the sphere

$$(x - X(t))^2 + (y - Y(t))^2 + (z - Z(t))^2 = R^2. \tag{2.29}$$

57

Assuming an approximately constant grain velocity over the duration of the crossing event, moreover,

$$\mathbf{X}(t) = \mathbf{X}_k + \mathbf{U}_k(t - t_k), \tag{2.30}$$

where the time t_k at which the sphere centre crosses the laser plane is given by

$$t_k = \frac{X_k - X_\Pi(0)}{U_\Pi}. \tag{2.31}$$

The intersection of the two loci is therefore defined by the implicit equation

$$F(y, z, t; \mathbf{X}_k, \mathbf{U}_k) = (X_\Pi - X(t))^2 + (Y_\Pi - Y(t))^2 + (Z_\Pi - Z(t))^2 R^2 = 0. \tag{2.32}$$

The desired sphere crossing position and velocity components can thus be obtained from

$$(\mathbf{X}_k, \mathbf{U}_k) = \underset{\mathbf{X}_k, \mathbf{U}_k}{\arg\min} \sum_i F^2(y_i^{(k)}, z_i^{(k)}, t_i^{(k)}; \mathbf{X}_k, \mathbf{U}_k), \tag{2.33}$$

where the arg min operator returns the arguments that minimize the given function. In practice, the six unknown arguments $(X_k, Y_k, Z_k, U_k, V_k$ and $W_k)$ are obtained by successive Gauss-Newton iterations (*Björk*, 1996). To succeed, a good initial guess for the crossing position and velocity vectors must be provided. For this we choose

$$\mathbf{X}_k = \frac{\mathbf{X}_1^{(k)} + \mathbf{X}_2^{(k)}}{2}, \tag{2.34}$$

$$\mathbf{U}_k = \frac{\mathbf{X}_2^{(k)} - \mathbf{X}_1^{(k)}}{t_2^{(k)} - t_1^{(k)}}. \tag{2.35}$$

where $t_1^{(k)}$ and $t_2^{(k)}$ are the crossing event start and end times estimated earlier, and $\mathbf{X}_1^{(k)}$, $\mathbf{X}_2^{(k)}$ are the corresponding end intercepts of the fitted trajectories Eq.(2.23). Boundary points $(y_i^{(k)}, z_i^{(k)}, t_i^{(k)})$, and the corresponding surfaces associated with best fit position and velocity vectors $(\mathbf{X}_k, \mathbf{U}_k,)$ are illustrated in Figure 2.17 for a set of three neighboring spheres extracted from the imaging footage. The surfaces are sheared ellipsoids of revolution, with lengths equal to the duration of their crossing events (inversely proportional to crossing velocity U_k). Fast moving grains thus register as squashed pancakes, and slower grains as dilated cigars (Figure 2.17**a**). The granular velocity components (V_k, W_k) in the plane of the scanning laser, on the other hand, govern the extent and direction of ellipsoid shearing, most visible when the ellipsoids are seen head on (Figure 2.17**b**). Conversely, it is these apparent deformations of the grain surfaces when they cross the laser plane that makes it possible to deduce the three granular velocity components (U_k, V_k, W_k). We propose the term "grain crossing velocimetry" to refer to the above approach and algorithms.

Results from the capture and fitting procedure are illustrated in Figure 2.18, for a partial segment of an experimental sequence. Figure 2.18**a** shows a vertical time slice (z, t) through the footage, obtained by concatenating pixel columns acquired at the same transverse position $y = 60$ mm (along the channel centerline). Figure 2.18**b**, likewise, shows a horizontal time slice (y, t) through the same footage, cut at elevation 30 mm. On such slices, the solid grains show up as dark, sheared ellipses. Depending on their relative velocity, fast or slow, through the laser scanning plane, the grain shapes are either shortened
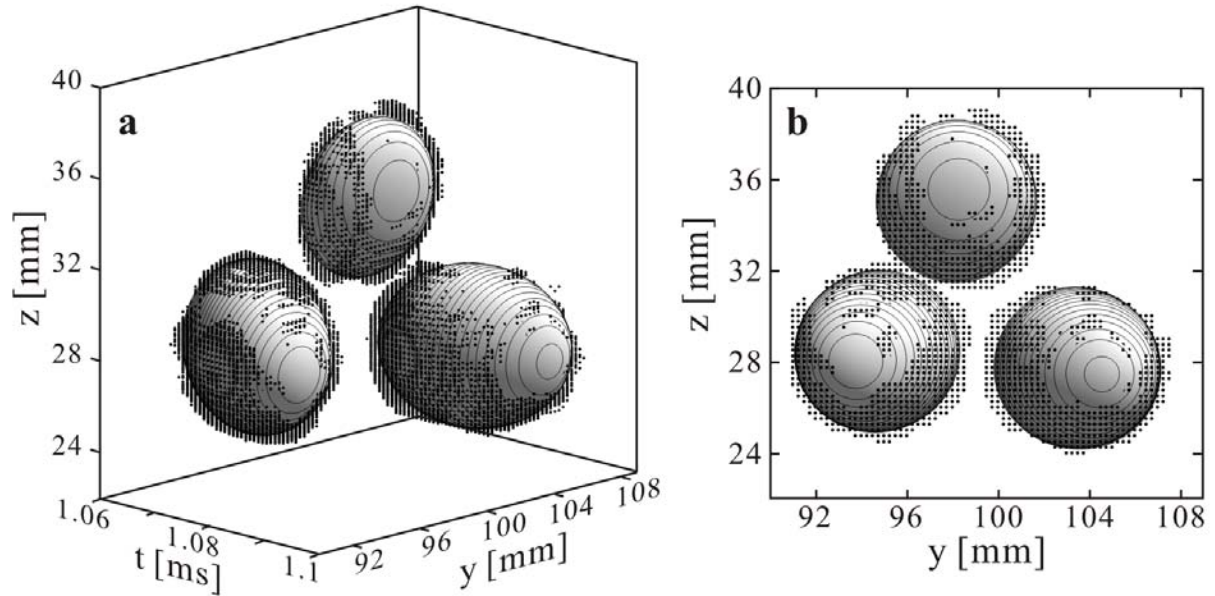
Figure 2.17 Boundary points and the best-fit sheared ellipsoids of revolution for three neighboring grains, capturing the deformation of the grain cross sectionsas they cross the laser scanning plane:**a** oblique view; **b** frontal view

or elongated. This is most visible on the vertical slice (Figure 2.18**a**), which features a clear contrast between the highly elongated grains at the bottom (corresponding to the stationary bed deposit), and the highly shortened grains at the top (corresponding to fast moving grains at the top of the transport layer). On the horizontal slice (Figure 2.18**b**), grain velocities are confined to a smaller range, yet still exhibit local variations.

On Figure 2.18**ab**, continuous white contours denote cross-sections through the sheared ellipsoids obtained by the best fit procedure. These automatically acquired ellipsoids are seen to match well the recorded grain crossings, and to reliably capture nearly all grains. Nevertheless, the algorithms miss a few grain crossings, and sometimes misidentify two successive grain crossings as one single crossing of longer duration. For this and some other runs, a manual procedure was applied to fill in missed grains and correct misidentified events. On Figure 2.18**ab**, dashed white contours are used to plot the corresponding ellipsoid cross-sections.
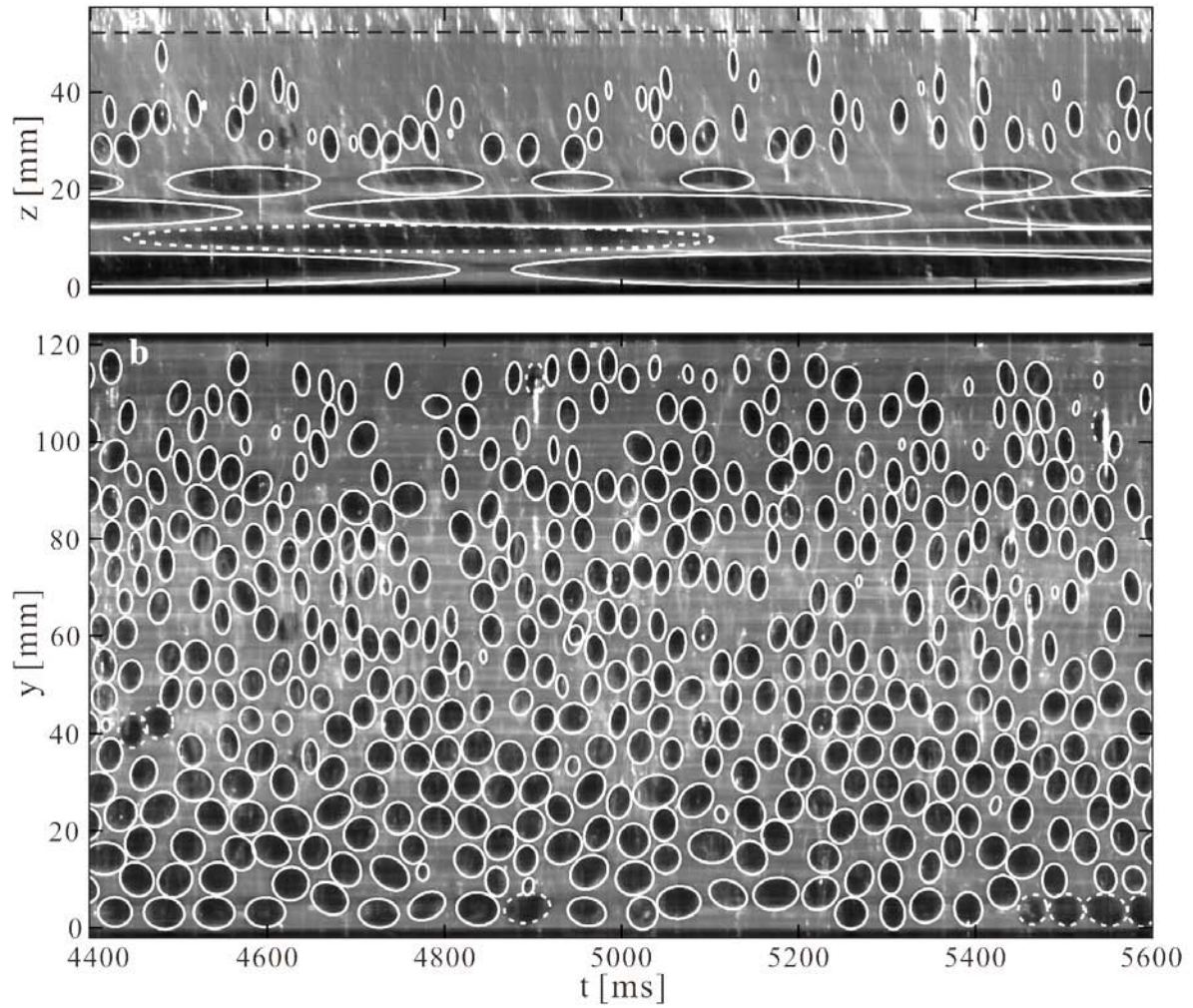
Figure 2.18 Time-space cross sections through the longitudinal scan and captured grain crossing surface (white outlines) from SWSF: **a** vertical cross section at $y = 60mm$; **b** horizontal cross section at $z = 30mm$;Continuous white contours: cross section through the automatically captured and fited sheared ellipsoids of revolution; Dashed contours: manually add or corrected ellipsoid; Black dashes on **a**: flow free surface.
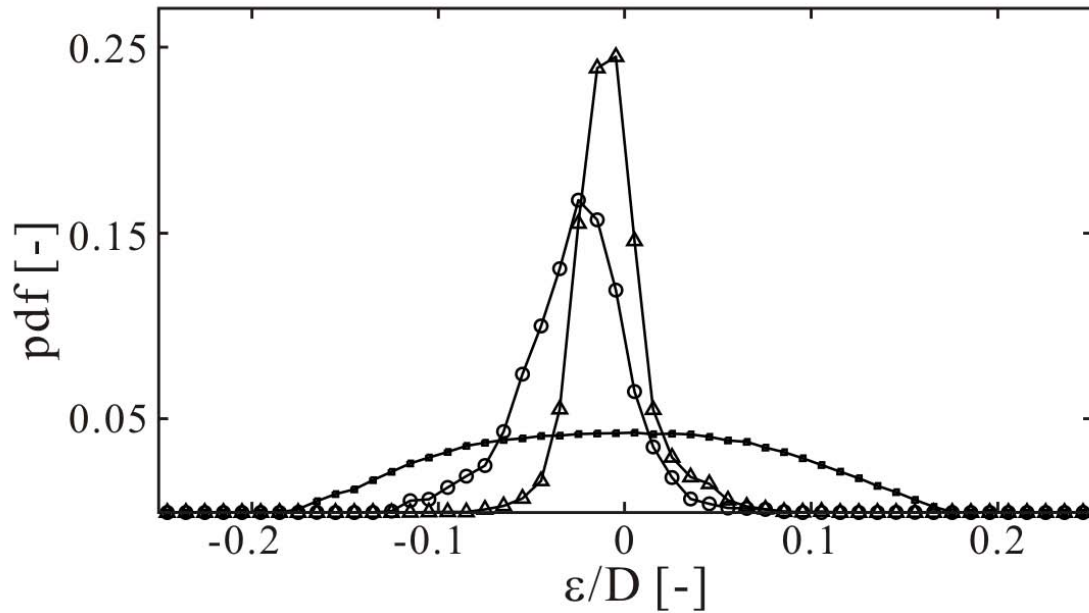
Figure 2.19 The comparison of the position errors for the measurements of the lowermost granular layer from the transverse scan footage using the method introduced in sec. 2.3.1 and the grain crossing velocimetry.

Since the lowermost granular layer remains stationary during the experiments, we can compare for that layer the sphere positions captured by the longitudinal laser scan with those captured earlier using the transverse scans. Separately for the three coordinates X, Y and Z, Figure 2.19 shows the probability density distribution of the resulting discrepancies, obtained by subtracting the two sets of positions. Because halos captured during the transverse scan are only approximately equatorial, the error on coordinate Y (of the order of 0.25 D) is larger than the error on coordinates X and Z (of the order of 0.1 D).

2.5   Conclusion

In the Chapter, we proposed a new approach to measure the internal flow of the refractive-index -matched solid-liquid mixture, based on the combination of transverse and longitudinal laser scanning. We applied the two dimensional particle tracking velocimetry to capture the motion of solid and liquid by transverse scans, acquired two dimensional velocity over a three dimensional volume, different masks were developed and applied to reduce the wrong data captured, as shown in results, over 10^4 data of solid and 10^5 data of liquid were obtained for one run. By identifying grain crossing events on the longitudinal scan, it is possible to deduce the 3 dimensional velocities and spatial/temporal distributions over scanned volume, obtaining the accurate solid fraction distribution, both algorithm is automatic.

Chapter 3

Phase averaging and cross sectional/ longitudinal mapping[1]

From the imaging measurements, we have acquired the datasets containing solid velocities and liquid velocities which are obtained by transverse scans, and solid grain positions and velocity vectors which are obtained by longitudinal scan, in this chapter we calculated the averaged quantities with respect to specific plane in the scanned voxel. First, we introduce the phase-averaging approach described by *Drew* (1983), this volume-averaging based approach help us to calculate averaging velocity and volume fraction distribution from the discrete PTV data. Second, by this approach we took averaged to the data over the longitudinal and cross-sectional plane, which can reveal the flow patterns and grain organizations for each channel boundary types. As the results, we obtained the averaged solid velocity, liquid velocity and solid fraction maps over $[y, z]$ and $[x, z]$ plane with grid size 10 times finer than grain diameter. Finally we calculated the volumetric solid and liquid discharge for all runs, and compared them with the discharges measured at channel outlet to verify the mass balance relation for imaging measurements.

3.1   Phase averaging: cross sectional mapping

The phase-averaging approach described by Drew (1983) is adopted, conceptually, the approach is based on two phase functions $\chi_L(x, y, z, t)$ and $\chi_S(x, y, z, t)$,

$$\chi_L(x, y, z, t) = \begin{cases} 1, (x, y, z) \in \text{liquid phase art time } t, \\ 0, \text{otherwise}, \end{cases} \tag{3.1}$$

and

$$\chi_S(x, y, z, t) = \begin{cases} 1, (x, y, z) \in \text{solid phase art time } t, \\ 0, \text{otherwise}, \end{cases} \tag{3.2}$$

As the flows under consideration are fully saturated, we have that

$$\chi_L + \chi_S = 1 \tag{3.3}$$

---

[1]Most of the materials in this Chapter was earlier presented in the publication: Ni, W.-J., and Capart, H. (2015). Cross-sectional imaging of refractive-index-matched liquid-granular flows. *Experiments in Fluids* 56, 163.

everywhere in the immersed domain comprised between the free surface, the sidewalls, and the channel bottom. One can further define the averaging operator

$$\langle f \rangle (y, z) = \frac{1}{T} \frac{1}{X_2 - X_1} \int_0^T \int_{X_1}^{X_2} f(x, y, z, t) dx dt \qquad (3.4)$$

where averaging is conducted both in time, over the duration T of the experiment, and along longitudinal distance x between the upstream and downstream limits X_1, X_2 of the observation volume. We are most interested in the following averaged quantities: the solid and liquid fractions

$$c_L = \langle \chi_L \rangle \text{ and } c_S = \langle \chi_S \rangle \qquad (3.5)$$

the liquid and solid discharge intensities (or volumetric fluxes per unit area)

$$q_L = \langle \chi_L u \rangle \text{ and } q_S = \langle \chi_S u \rangle \qquad (3.6)$$

and the longitudinal components of the phase-averaged liquid and solid velocities

$$u_L = \frac{\langle \chi_L u \rangle}{\langle \chi_L \rangle} \text{ and } u_S = \frac{\langle \chi_S u \rangle}{\langle \chi_S \rangle} \qquad (3.7)$$

where similar expressions can be written for the other velocity components.

In practice, we do not have complete knowledge of the fields $\chi(x, y, z, t)$ and $u(x, y, z, t)$ throughout the time-space volume of interest. Instead, we only have the discrete PTV measurements $(X_k, Y_k, Z_k, U_k, W_k)$ and $(x_k, y_k, z_k, u_k, w_k)$, collected by the transverse scans, and the discrete grain crossing measurements $(X_k, Y_k, Z_k, U_k, V_k, W_k)$ acquired by the longitudinal laser scan (here for simplicity we use the same symbol k to index the various sets of measurements, without implying that sets correspond or have the same cardinality). For the transverse scans, we pool together the PTV data captured through the left and right sidewalls, restricting each set to the data captured over the two thirds of the channel width closest to the camera. The data acquired from the left and right viewpoints therefore overlap over the middle third of the channel width, where they are combined together.

To estimate averaged fields from the measured data, we first discretize the channel cross section $0 \leq y \leq B$, $0 \leq z \leq H$, where B and H are the channel width and flow depth, into the Cartesian grid

$$y_j = (j - \tfrac{1}{2})\Delta y \qquad (3.8)$$

where we set $\Delta y = \Delta z = 0.5$ mm. We then process the measurement data using the following averaging procedures. To process the liquid tracer PTV data acquired by the transverse scans, we define the gridding function

$$G_{i,j}(y, z) = \begin{cases} 1, (y_j - \tfrac{1}{2}\Delta y \leq y \leq y_j + \tfrac{1}{2}\Delta y) \cap (z_i - \tfrac{1}{2}\Delta z \leq z \leq z_i + \tfrac{1}{2}\Delta z), \\ 0, \text{otherwise}, \end{cases} \qquad (3.9)$$

The phase-averaged liquid velocity is then calculated using the formula

$$u_L(y_j, z_i) = \frac{\sum_k G_{i,j}(y_k, z_k) u_k}{\sum_k G_{i,j}(y_k, z_k)} \qquad (3.10)$$

64

where all liquid tracers are weighed equally because they represent point values assumed to be distributed randomly throughout the liquid phase. The procedure amounts to binning the liquid tracer PTV data into non-overlapping spatial bins, and computing the corresponding averages.

To process the solid grain PTV data acquired by the transverse scans, we introduce the length function

$$L_{i,j}(Y, Z) = \begin{cases} 2\sqrt{R^2 - d_{i,j}^2}, d_{i,j}(Y, Z) \leq R \\ 0, \text{otherwise,} \end{cases} \tag{3.11}$$

$$\text{where } d_{i,j}(Y, Z) = \sqrt{(y_j - Y)^2 + (z_i - Z)^2}. \tag{3.12}$$

We then calculate the longitudinal component of the phase-averaged solid velocity using

$$u_S(y_j, z_i) = \frac{\sum_k L_{i,j}(Y_k, Z_k)U_k}{\sum_k L_{i,j}(Y_k, Z_k)} \tag{3.13}$$

where each granular measurement is weighted by the length over which it affects the line $y = y_j, z = z_i$.

To process the grain crossing measurements acquired by the longitudinal scan, we refer back to the time-evolution of the grain cross section associated with each crossing. Based on the best fit sheared ellipsoid of revolution, the duration of each crossing event is

$$T_k = \frac{D}{U_k - U_\Pi} \tag{3.14}$$

where D is the grain diameter, and $U_k - U_\Pi$ the normal component of the grain velocity relative to the laser plane. During the crossing event, the time-evolving center and radius of the grain cross section intercepted by the laser plane are given by

$$Y_{C,k}(t') = Y_k + V_k t', \tag{3.15}$$

$$Z_{C,k}(t') = Z_k + W_k t', \tag{3.16}$$

$$\text{and } R_{C,k}(t') = R\sqrt{1 - (2t'/T_k)^2}, \tag{3.17}$$

where $t' = t - t_k$ is the time relative to the instant at which the sphere center crosses the laser plane. We can therefore define the phase function

$$\chi_{i,j,k}(t') = \begin{cases} 1, d_{i,j,k}(t') \leq R_{C,k}(t') \\ 0, \text{otherwise,} \end{cases} \tag{3.18}$$

$$\text{where } d_{i,j,k}(t') = \sqrt{(y_j - Y_{C,k}(t'))^2 + (z_i - Z_{C,k}(t')^2)}, \tag{3.19}$$

such that $\chi = 1$ when the grid point (y_j, z_i) is inside a grain cross-section. The average solid fraction at grid point (y_j, z_i) can then be obtained from

$$c_S(y_j, z_i) = \frac{1}{T} \sum_k \int_{-T_k/2}^{T_k/2} \chi_{i,j,k}(t')dt' \tag{3.20}$$

where T is the total duration of the longitudinal scan. Likewise, the longitudinal component of the phase-averaged solid velocity can be calculated from

$$u_S(y_j, z_i) = \frac{\sum_k U_k \int_{-T_k/2}^{T_k/2} \chi_{i,j,k}(t') dt'}{\sum_k \int_{-T_k/2}^{T_k/2} \chi_{i,j,k}(t') dt'} \tag{3.21}$$

where the contribution of each velocity measurement associated with a grain crossing event is weighted by the duration over which this crossing event affects grid location (y_j, z_i) . The corresponding local granular discharge intensity is given by

$$q_S(y_j, z_i) = \frac{1}{T} \sum_k U_k \int_{-T_k/2}^{T_k/2} \chi_{i,j,k}(t') dt' \tag{3.22}$$

Combining results from the transverse and longitudinal scans, we can also obtain for the local liquid discharge intensity the estimate

$$q_L(y_j, z_i) = (1 - c_S(y_j, z_i)) u_L(y_j, z_i) \tag{3.23}$$

3.2   Phase averaging: longitudinal mapping

For the longitudinal mapping of solid and liquid velocities using the measurements of transverse scan, the averaging operator would be defined in similar way as cross sectional mapping by replacing Y with Z

$$\langle f \rangle (x, z) = \frac{1}{T} \frac{1}{Y_2 - Y_1} \int_0^T \int_{Y_1}^{Y_2} f(x, y, z, t) dy dt \tag{3.24}$$

where Y_1, Y_2 represent the transversal limits bounded by channel side walls, the gridding function and the phase-averaged liquid velocity therefore become

$$G_{i,j}(x, z) = \begin{cases} 1, (x_j - \frac{1}{2}\Delta x \leq x \leq x_j + \frac{1}{2}\Delta x) \cap (z_i - \frac{1}{2}\Delta z \leq z \leq z_i + \frac{1}{2}\Delta z), \\ 0, \text{otherwise}, \end{cases} \tag{3.25}$$

$$u_L(x_j, z_i) = \frac{\sum_k G_{i,j}(x_k, z_k) u_k}{\sum_k G_{i,j}(x_k, z_k)} \tag{3.26}$$

The length function for the solid phase is defined as

$$L_{i,j}(X, Z) = \begin{cases} 2\sqrt{R^2 - d_{i,j}^2}, d_{i,j}(X, Z) \leq R \\ 0, \text{otherwise}, \end{cases} \tag{3.27}$$

$$\text{where } d_{i,j}(X, Z) = \sqrt{(x_j - Y)^2 + (z_i - Z)^2}. \tag{3.28}$$

thus the longitudinal component of the phase-averaged solid velocity is calculated by

$$u_S(x_j, z_i) = \frac{\sum_k L_{i,j}(X_k, Z_k) U_k}{\sum_k L_{i,j}(X_k, Z_k)} \tag{3.29}$$

For the longitudinal mapping of solid fraction, the averaging function would be little different, the phase function mapped onto the plane (x_j, z_i) would be a sheared ellipse

66

defined by its velocities (U_k, V_k, W_k), as illustrated in Figure 2.18, by equation (2.27) to (2.31), the explicit expression of the sheared ellipse function is defined as

$$d_{i,j,k}^2(t') = (x_j - X_{C,k}(t'))^2 (\frac{U_k - U_\Pi}{U_\Pi})^2 + (z_i - Z_{C,k}(t'))^2, \tag{3.30}$$

and the major axis $R_{C,k}$ of the ellipse is related to y and t',

$$R_{C,k}^2(y, t') = R^2 - (y - Y_{C,k}(t'))^2, \tag{3.31}$$

where $t' = t - t_k$ is the time relative to the instant at which the sphere center crosses the laser plane. We can therefore define the phase function

$$\chi_{i,j,k}(t', y) = \begin{cases} 1, d_{i,j,k}^2(t', y) \leq R_{C,k}^2(t', y) \\ 0, \text{otherwise}, \end{cases} \tag{3.32}$$

such that $\chi = 1$ when the grid point (x_j, z_i) is inside a sheared ellipse for a given y plane. The average solid fraction at grid point (y_j, z_i) can then be obtained from

$$c_S(x_j, z_i) = \frac{1}{T} \sum_k \int_{y(-T_k/2)}^{y(T_k/2)} \chi_{i,j,k}(t', y) dt' \tag{3.33}$$

3.3 Cross sectional and longitudinal mapping results

We applied the phase-averaging to all the experiments and in (y, z) and (x, z) plane, these maps show similar and different characteristics among the three different channel boundaries. The results are arranged by the following ways, the maps of each experiment are resented by 3x2 figure array, the left column of the array shows the longitudinal mapping results which represents the cross section distribution $\overline{f}(y, z)$, the right column of array are averaged over transverse direction, represent the averaged distribution in flow direction $\overline{f}(x, z)$. The first row of figure array illustrates the solid fraction distribution , the second row shows the averaged solid velocity, and the third row are the averaged liquid velocity, only longitudinal velocity maps were shown here, but the same phase-averaging calculations were applied to w_S, w_L, too.

For the solid fraction distribution for the SWSF case (Figure 3.1 to 3.3), the map of (y, z) plane show that the grains are layered in a highly-organized way, the layering effect is significant even in the dilute part, the slight anisotropic distribution of in y axis direction can be observed, but not significantly different, so does the variation from near-wall zone to the middle zone. From the map of (x, z) plane, layers are also spaced evenly and uniformly. For the solid velocity and liquid velocity, also asymmetry can be observed, the distribution are reasonable uniform over the cross section for the same elevation z, although it seems to be uniform for liquid velocity map in (x, z) plane, there are convective acceleration happened here, we will discuss this in Chapter 5.

For the SWRF case, cylinders of the same diameter were put onto the bottom of channel with inter-space equal to $6D$ (center-to-center distance = 42 mm), the arrangement broke the organized packing pattern of the grains with a period of 6d, causing the solid fraction distributed more randomly and loosely packed, as shown in Figure 3.4 to 3.5, for the map

67

of (y, z) plane, the layering effect can also be observed, the overall solid fraction is smaller than SWSF, and distributed in a higher range, there are slight difference between near wall and middle area. From the map of (y, z) plane, bottom cylinders were presented as the circle area of $c_S = 1$, a periodic disturbance were induced by the cylinders which disconnected the layering effects, the effect of bottom cylinder made the distribution of solid fraction more loose and more random. For the distributions of solid velocity and liquid velocity of (y, z) plane, the boundaries between layers becomes blur and more asymmetry distribution were occur in transverse direction, but we still treat these maps as uniformly distributed over y for specific elevation z.

For the RWRF case, cylinders were put onto the bottom and along two sides of channel with inter-space equal to $6D$ (center- to-center distance = 42 mm), this arrangement enlarge the wall friction effect can made the flow 3 dimensional, as shown in Figure 3.6 to 3.8, for the map of (y, z) plane, we can observed the contributions of cylinders on the bottom and near side walls.There is still the layering effect but it is weaker as z higher, the distribution shows anisotropy in transverse direction, it is more dense in near wall zone than middle area. From the map of (x, z) plane, we averaged over $40mm \leq y \leq 80mm$ to exlcude the large variations around the near wall area, beside the non-moving grains the solid fraction were distributed in a higher range and more randomly. In this case, the solid and liquid velocity varied significantly in y and z, for the solid velocity distribution in (y, z) plane, the grains flows in the middle section of channel and forming a eye-shaped flowing zone, for the place near side walls, the side cylinders blocked the grains thus the near wall velocity of grains is about zero. For the liquid velocity shows the similar pattern, but in a more complex way, velocity gradients are large in z direction as well as in y direction, in the area near free surface and near wall, a low velocity area were also observed. For the map of (x, z) plane, however there are a velocity difference right around the area of vertical cylinders which are caused by the anisotropic refractive index of the PMMA cylinders, the anisotropic refractive index happened when the PMMA is manufactured by the method of extrusion, which would made the cylinder as a lens distorting light rays in the liquid.
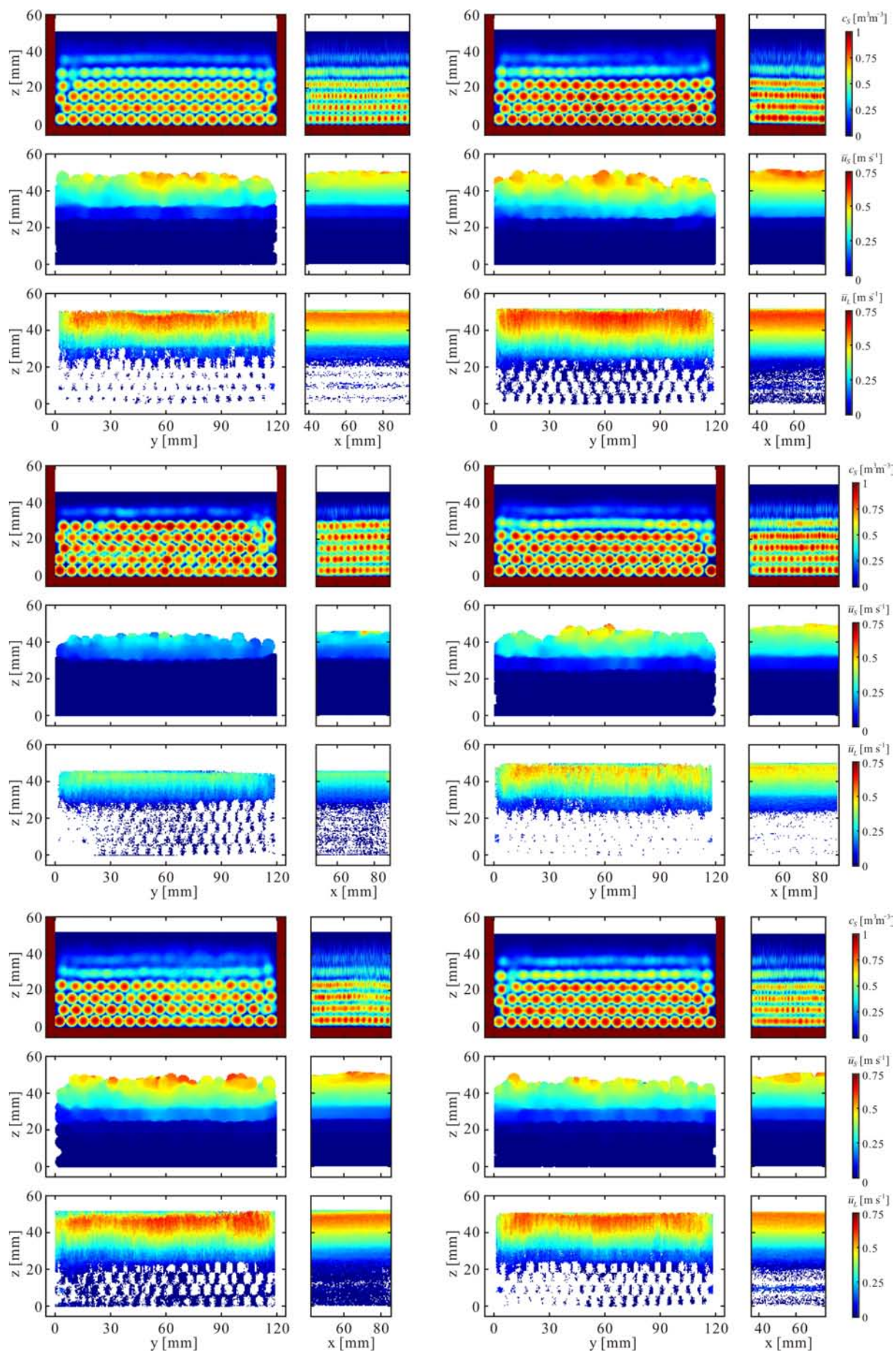
68

Figure 3.1 Phase-averaged maps of solid fraction, solid velocity and liquid velocity for SWSF case: 1:6.
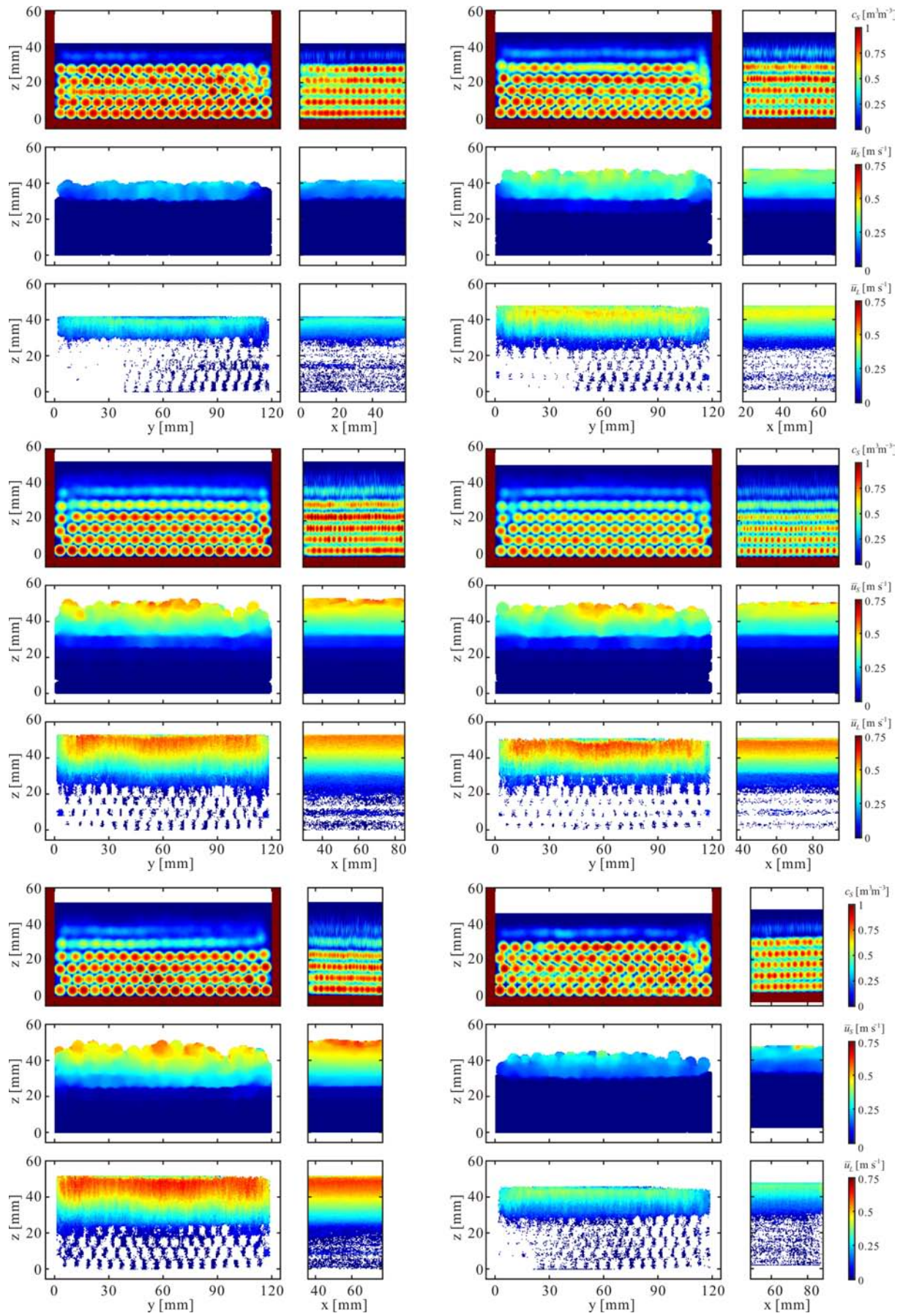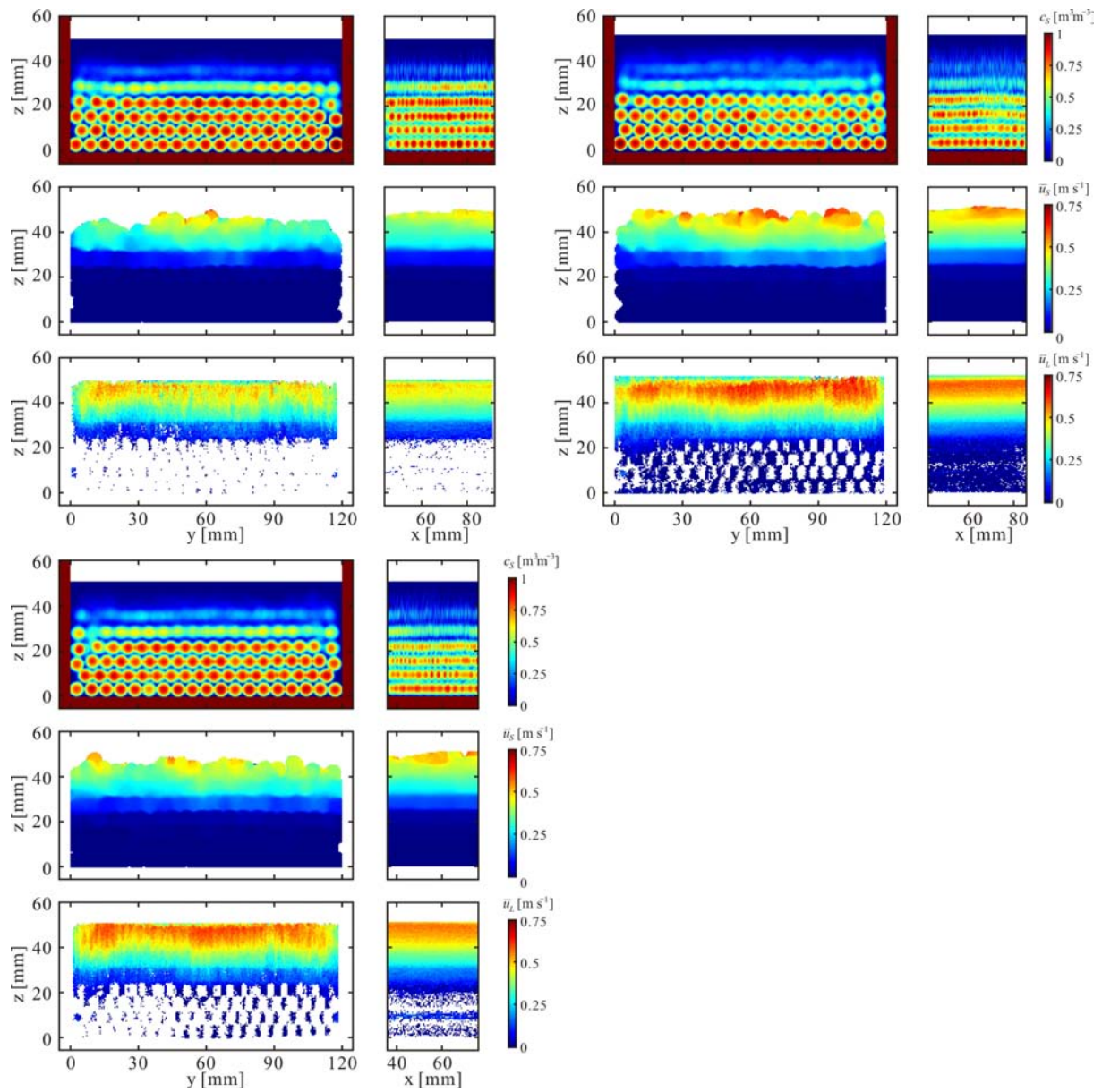
Figure 3.2 SWSF case: 7-12.
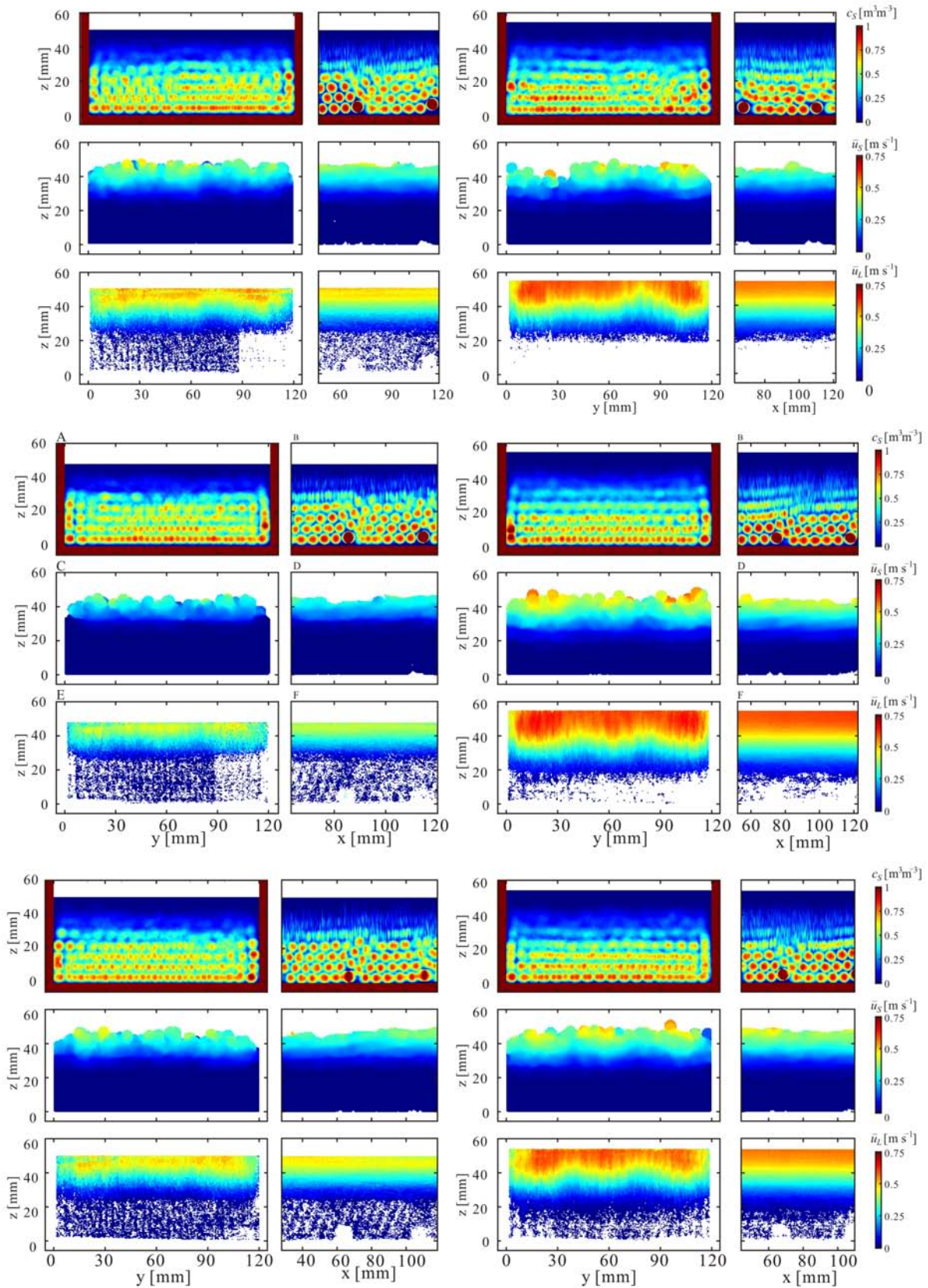
70

Figure 3.3 SWSF case: 13-15.

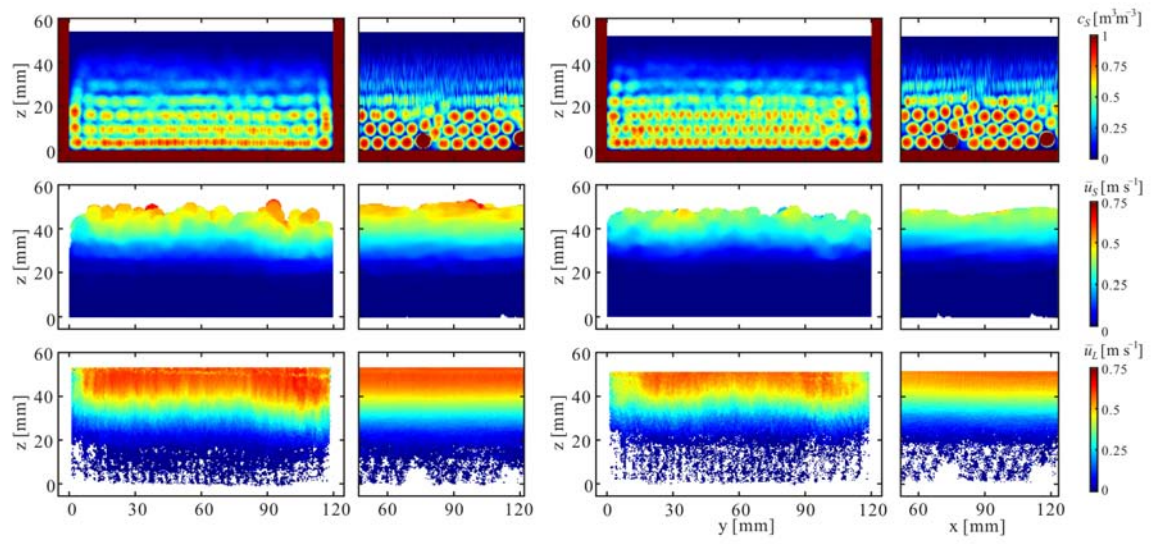Figure 3.4 Phase-averaged maps of solid fraction, solid velocity and liquid velocity for SWRF case: 1-6.
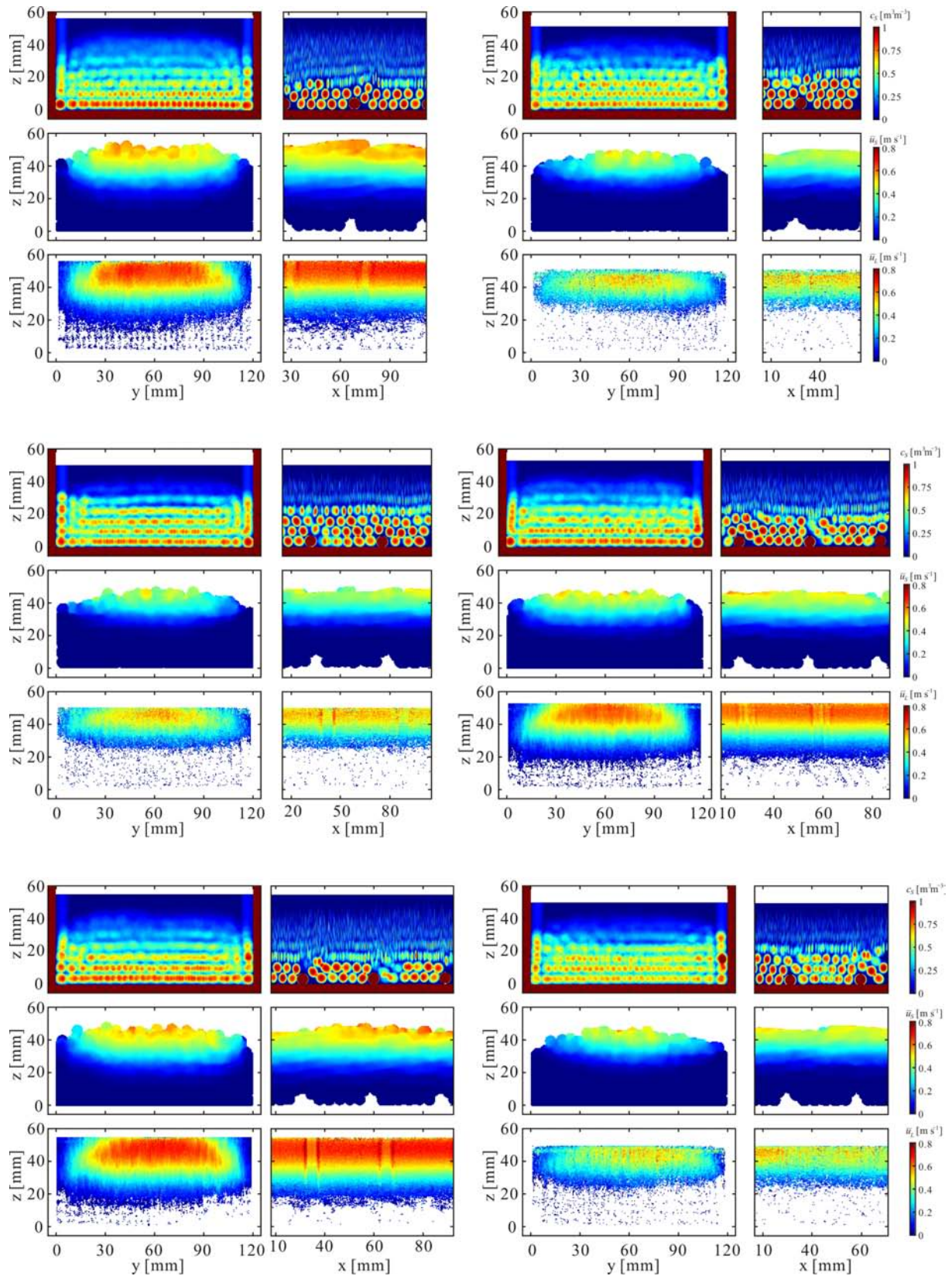
Figure 3.5 SWRF case: 7-8

Figure 3.6 Phase-averaged maps of solid fraction, solid velocity and liquid velocity for RWRF case: 1:6.
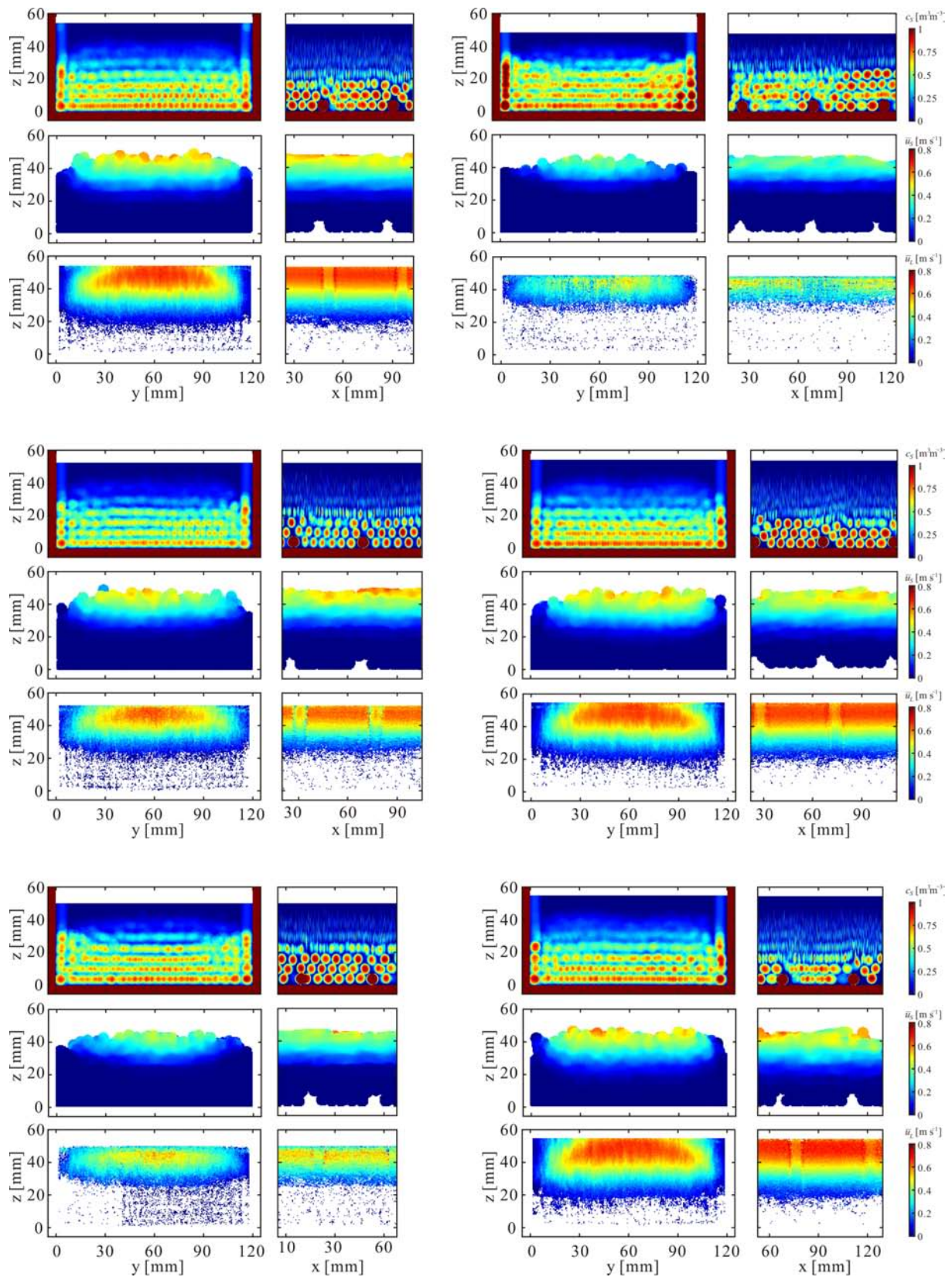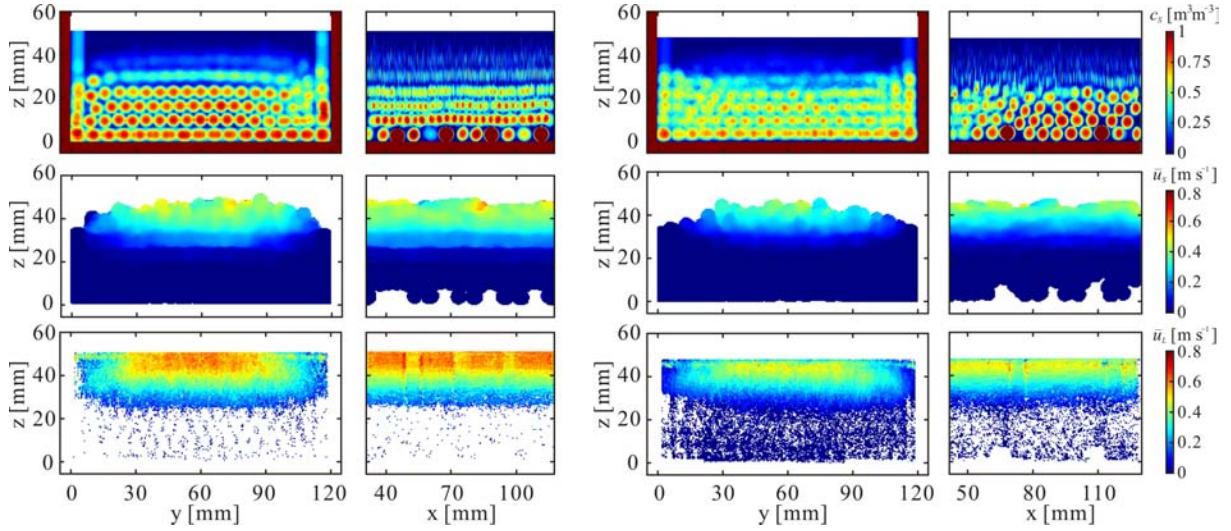
Figure 3.7 RWRF case: 7:12

75

Figure 3.8 RWRF case: 13:15

3.4 Volumetric flux comparisons

Integrated over the cross section, the total liquid discharge can be calculated from the cross sectional mapping result

$$Q_L = \int_0^H \int_0^B q_L(y,z)dydz \approx \sum_i \sum_j q_L(y_j, z_i)\Delta y \Delta z \qquad (3.34)$$

$$Q_S = \int_0^H \int_0^B q_S(y,z)dydz \approx \sum_i \sum_j q_L(y_j, z_i)\Delta y \Delta z \qquad (3.35)$$

It is instructive to work out the expression for solid discharge in more detail. Upon substituting (3.22) into (3.35), then changing the order of summation and integration, we obtain

$$Q_S = \frac{1}{T}\sum_k \int_{-T_k/2}^{T_k/2} \int_0^H \int_0^B \chi_K(y,z,t')dydzdt' = \frac{1}{T}\sum_k \int_{-T_k/2}^{T_k/2} \pi R_{C,k}^2(t')dt', \qquad (3.36)$$

where the area $\pi R_{C,k}^2(t')$ of the grain cross section at relative time t' results from the integration of phase function $\chi_K(y,z,t')$ over the channel cross section. One can then make the change of variable $x' = 2Rt'/T_k = (U_k - U_\Pi)t'$ to obtain

$$Q_S = \frac{1}{T}\sum_k \frac{U_k}{U_k - U_\Pi} \int_{-R}^R \pi(R^2 - x'^2)dx', \qquad (3.37)$$

and finally

$$Q_S = \frac{\frac{4}{3}\pi R^3}{T}\sum_k \frac{U_k}{U_k - U_\Pi} \qquad (3.38)$$

This formula for the total granular discharge yields simple results in two special cases. When all grains are stationary, $U_k = 0$ for all k and the volumetric granular discharge is 0, as it should. Were the laser to be stationary, on the other hand, then $U_\Pi = 0$

76

and the volumetric granular discharge becomes $Q_S = N(\frac{4}{3}\pi R^3)/T$. This amounts to the number N of grains that have crossed the stationary laser plane over the duration of observation T, multiplied by the volume of each grain. The result again is consistent with the physical meaning of the volumetric discharge. For these two special cases, we therefore check theoretically that the local formula (3.35) integrated over the channel cross section produces the expected volumetric granular discharge.
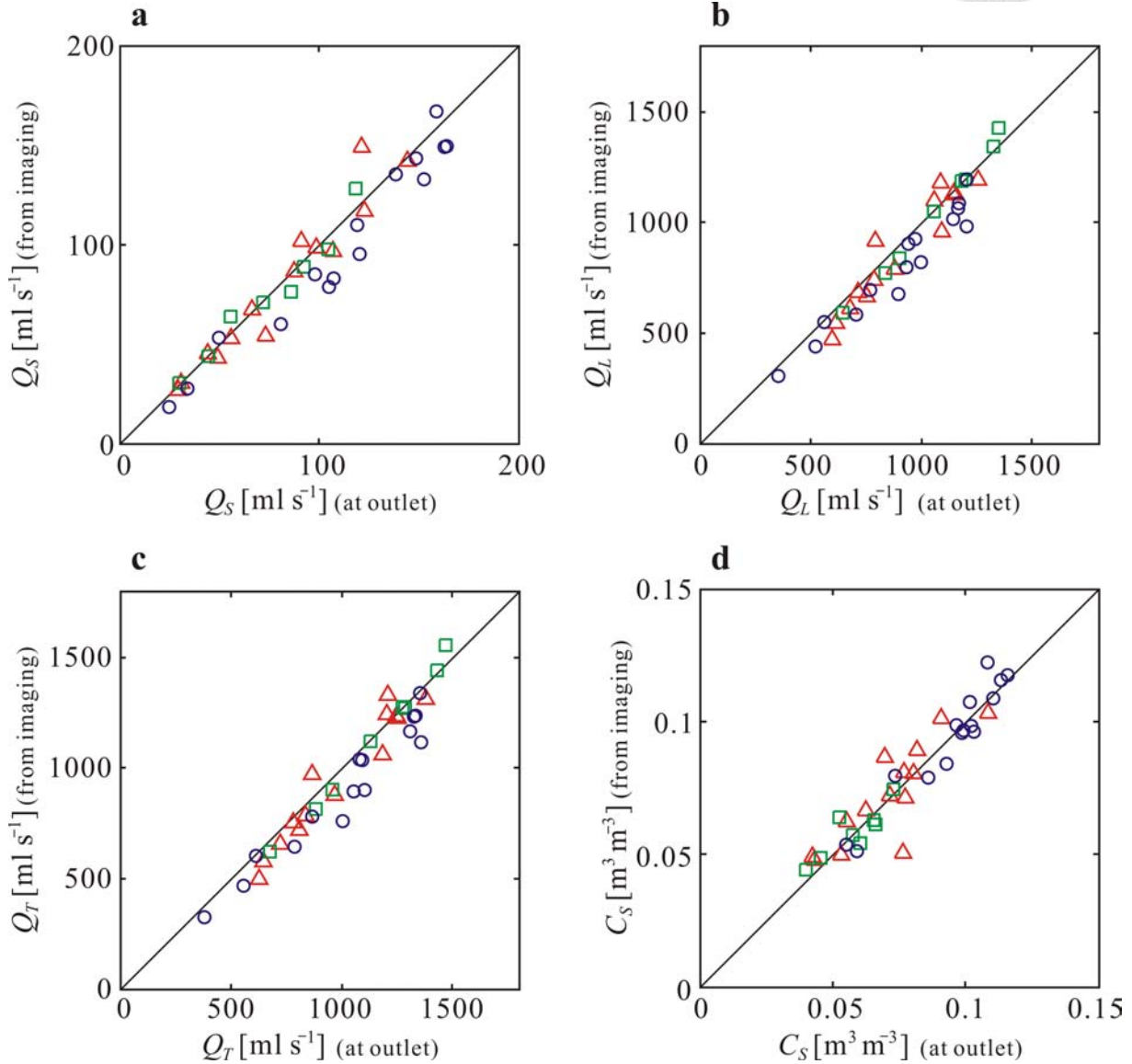
Figure 3.9 Comparison of discharges between outlet measurements and imaging measurements; ○ represents SWSF, □ represents SWRF and △ is for RWRF: **a** liquid discharge; **b** solid discarge; **c** total discharge; **d** delivered solid concentration.

From the solid and liquid discharge, we can further deduce the total discharge $Q_T = Q_L + Q_S$, and the delivered solid concentration $C_S = Q_S/Q_T$. All four quantities Q_L, Q_S, Q_T, and C_S can therefore be calculated by integrating the imaging measurements over the channel cross section. As an aggregate check, we can compare these integral values with the bulk measurements acquired at the channel outlet at the conclusion of each run. The comparisons are shown in Figure 3.9 for three series of experiments conducted at

different flow rates. Figure 3.9**a** plots results for the liquid discharge Q_L, with the bulk outlet measurements in abscissa and the integrals of the imaging measurements in ordinate. Figure 3.9**b** plots the corresponding results for the solid discharge Q_S. Results for the total discharge Q_T are shown in Figure3.9**c**. Finally Figure 3.9**d** shows the results for the delivered granular concentration C_S as estimated independently from the bulk and imaging measurements.
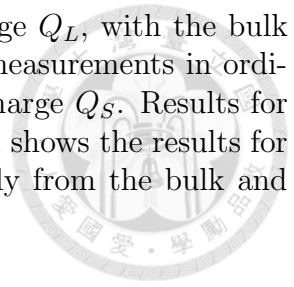
Chapter 4

Influence of channel boundaries on internal flow structure

With the averaged maps of solid fraction, solid velocity and liquid velocity, we hoped to develop a approach to describe and characterize the flow maps. To do so, we need to identify the major factors that dominate the flow changes. In Section 4.1, we developed a approach to divide the cross-sectional flow maps into different domains by the averaged discharge maps. We defined the flow domain, the bed-load transport domain and clear liquid domain by bounded contours. In Section 4.2, we used the domains to calculate a series of bed-load transport factors from the averaged maps, reduced the maps to the factors for solid fraction, transport area, and transport velocity, then tested the dependencies with the solid discharge. Finally, in Section 4.3, we made the factors dimensionless and compared with the kinematic parameter, the Mobility parameter $\hat{\Theta}$, and dynamic parameter, the Shields number, $\hat{\tau}$, to see and clarify how the kinematic and dynamic parameters respond to the variation of flow factors caused by channel boundary change, and we also tested some choice of variables that used to normalize the Mobility parameter and Shields number.

4.1 Cross section sub-division

In this section we divided the flow into different zone or domains through the averaged cross-sectional discharge maps. The solid and liquid discharge maps are defined by Eq. (3.22) and Eq. (3.23), the total disgharge is the summation of the two.

$$q_T(y_j, z_i) = q_S(y_j, z_i) + q_L(y_j, z_i) \tag{4.1}$$

First we defined the domain of bed-load transport (bed-load domain), which is equivalent to the transport depth of sheet flow structure. we assume that the bed-load domain Ω_B is bounded by a equivalent discharge intensity contour $q_S^{X\%}$ and the integration of solid discharge distribution over the domain equals to 98 percent of the total:

$$\int_{\Omega_B} q_S(y, z) dy dz = 0.98 Q_S \tag{4.2}$$

this could be solved by deriving the relation of the discharge of unit area $q_S^{n\%}$ versus the accumulated discharge $Q_S(q_S^{n\%})$, then found the specific contour by the Bi-section

method. We assume that no bed-load transport occured outside the domain, and for the area below this domain, we treated it as stationary zone. For the SWRF and the RWRF cases, the operations were good, but for the SWSF case, holes might occur within the dishcarge contour for the well organized grain layers, dishcarge intensity in these holes would be included to keep the domain intact.

Then we defined the flow domain which is equivalent to the total depth for the sheet flow. To determine the total discharge domain (flow domain), at first we use the same way as finding the transport domain by replacing Q_S by Q_T,

$$\int_{\Omega_T} q_T(y,z)dydz = 0.98Q_T \tag{4.3}$$

since the total discharge is about 10 times larger than the solid discharge, the lower boundary of the contour might be higher than that of the bed-load domain, so we take union of the total flow contour with the bed-load domain, establishing the flow domain Ω_F:

$$\Omega_F = \Omega_T \cup \Omega_B \tag{4.4}$$

and the complement area of flow domain and bed-load domain would be the domain of clear liquid (clear domain) Ω_C.

$$\Omega_C = \Omega_T \cap \Omega_B' \tag{4.5}$$

The total and solid discharge maps in (y,z) plane and the domains are illustrated in the following pages, we selected one map for each cases with similar solid discharge and illustrated in Figure 4.1

Different channel boundary types result in different shape and area of the domain, for SWSF and SWRF case, the shape of the flow domain and the bed-load domain are approximately rectangles, they had similar size of bed-load domain, but the flow domain of SWRF was larger than that of SWSF, although some circular arc-shaped peninsulas were found at the bottom of the bed-load domain, we may assumed that the SWSF and SWRF cases were the sheet flow. For RWRF case, the shape of both domains are like a piece of cloud, suggesting that the vertical cylinders near wall strongly effected the discharge distribution for both phase. Comparing the total discharge Q_T of each cases, SWFR carried the most ($\approx 1600 cm^3 s^{-1}$), RWRF were of the middle ($\approx 1400 cm^3 s^{-1}$), the SWSF case sustained the lowest discharge ($\approx 1000 cm^3 s^{-1}$).

Next we see the difference of the discharge maps, the solid discharge maps shows that the discharge varied strongly by layers in the SWSF case, the top layer carried most of grains and discharge decreasing with the depth, it differs from the SWRF and RWRF case which the solid discharge were uniformly distributed, the high discharge area are near the center of the bed-load domain, and the side wall influences were within the range less than grain diameter. For the total discharge maps layering effects was also observed in SWSF case, while the discharge gradient over z were smooth in SWRF case, for RWRF case the discharge gradient varied with y and z, almost zero discharge in the near-wall zone. The full results of three cases were illustrated from Figure 4.2 to Figure 4.10. The bed-load domain, the flow domain and the clear liquid domain contour for all experiments were plotted in Figure 4.12, Figure 4.12, and Figure 4.12 respectively.
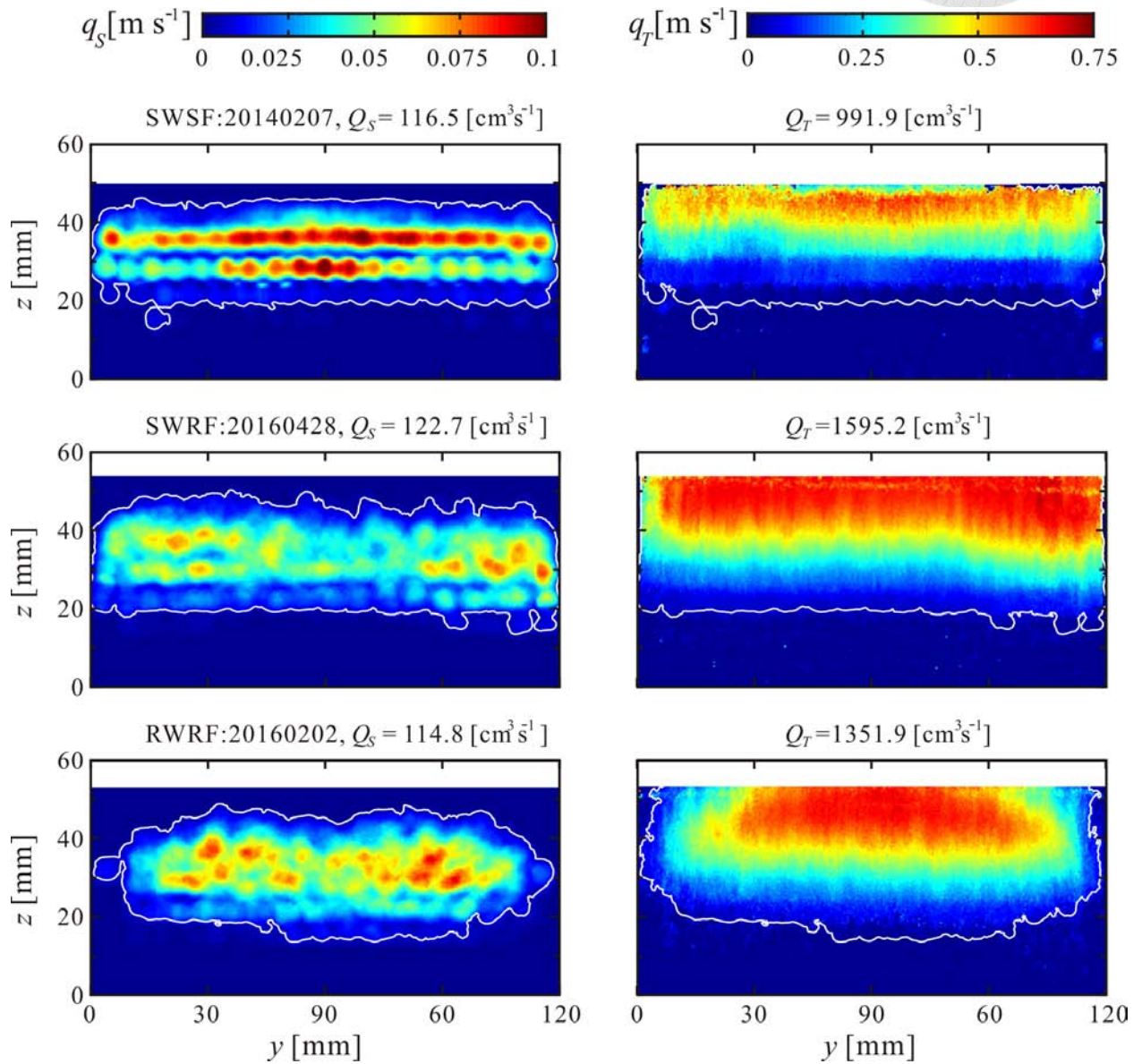
Figure 4.1 Comparison of the discharge maps, the bed-load domain(left), flow domain (right) with three cases of similar solid discharge: SWSF(top); SWRF(middle); RWRF(bottom).
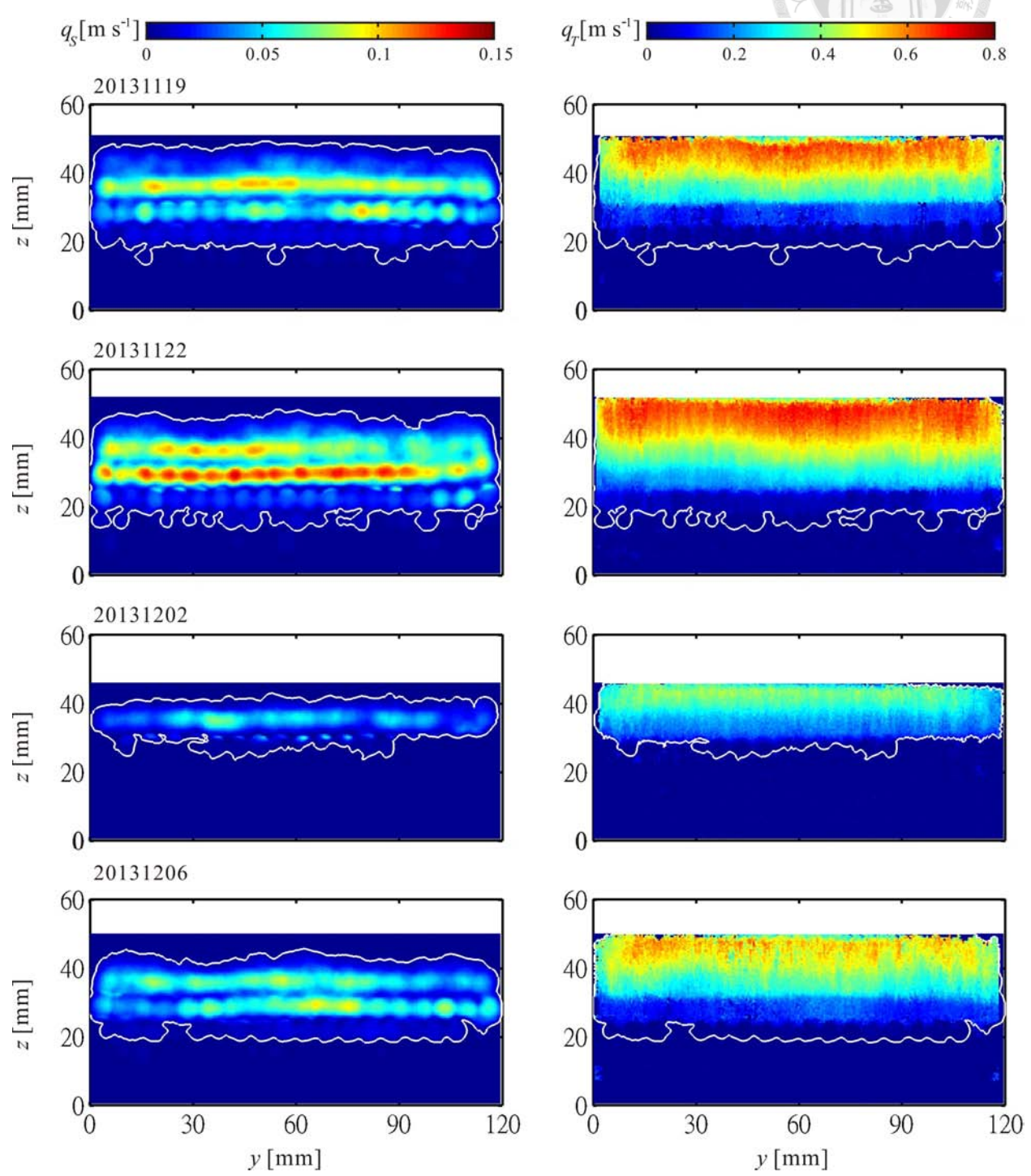
Figure 4.2 Discharge maps and the domains of transport, SWSF case:1-4
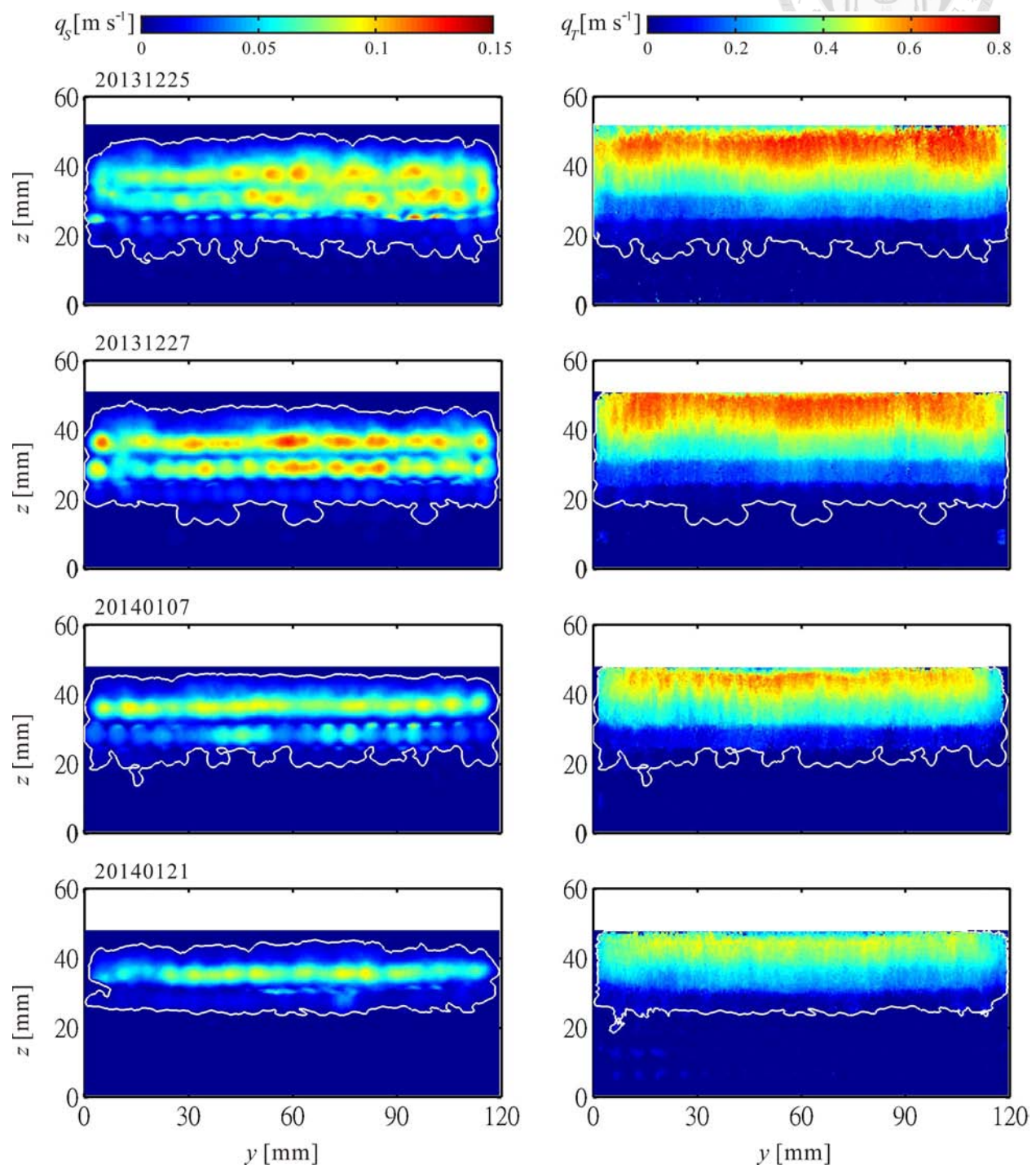
Figure 4.3 SWSF case:5-8
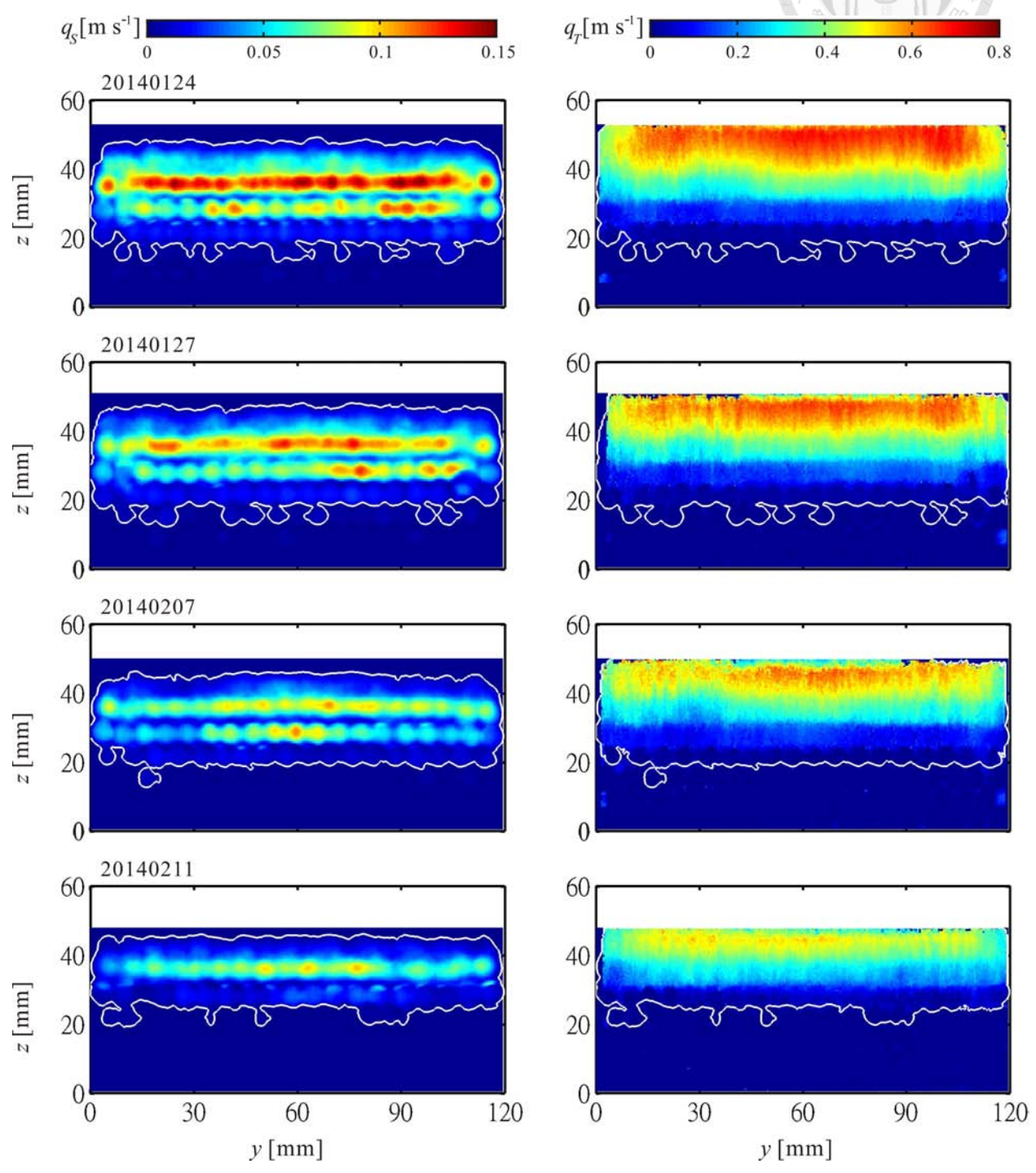
Figure 4.4 SWSF case:9-12

84
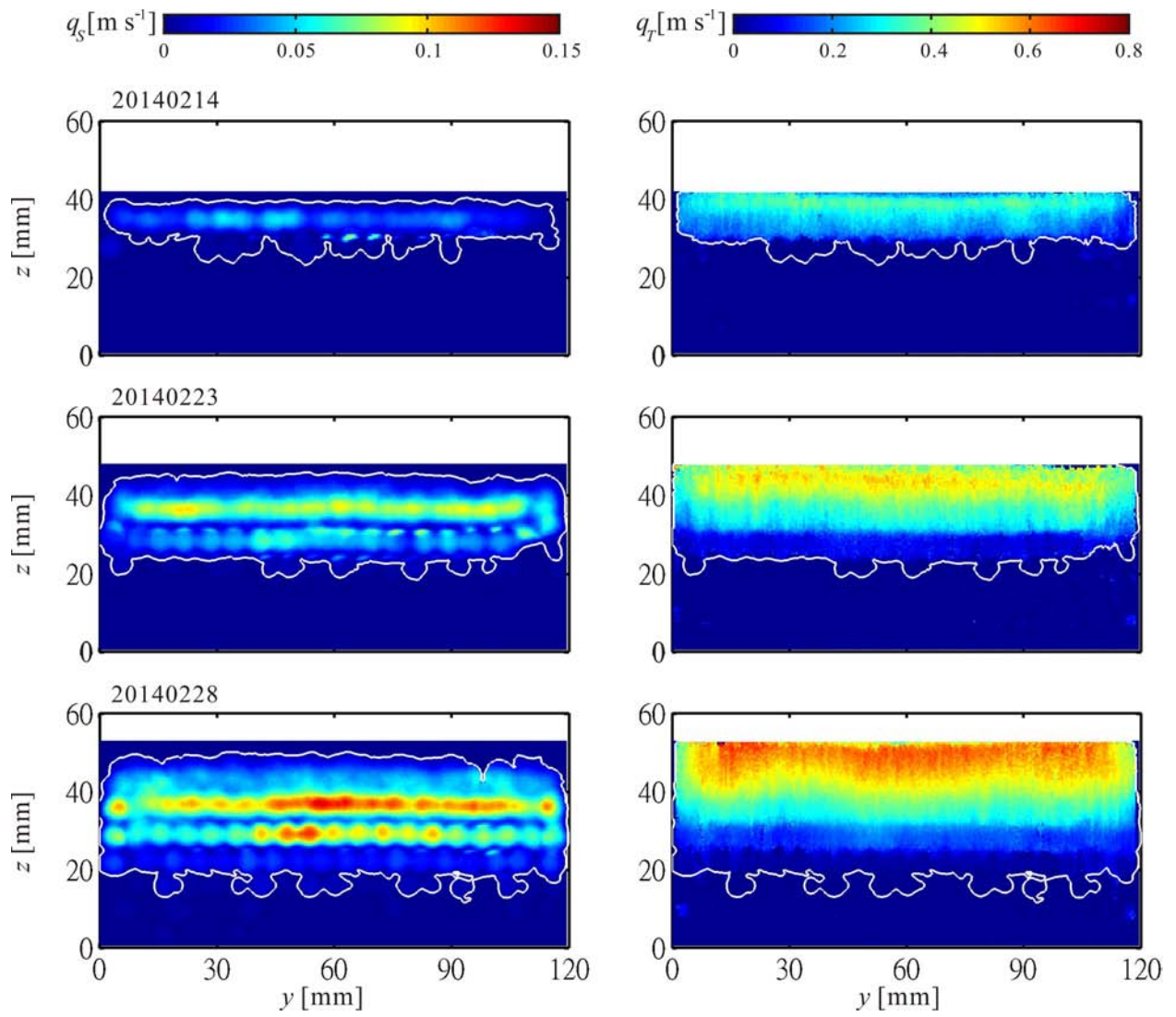
Figure 4.5 SWSF case:13-15
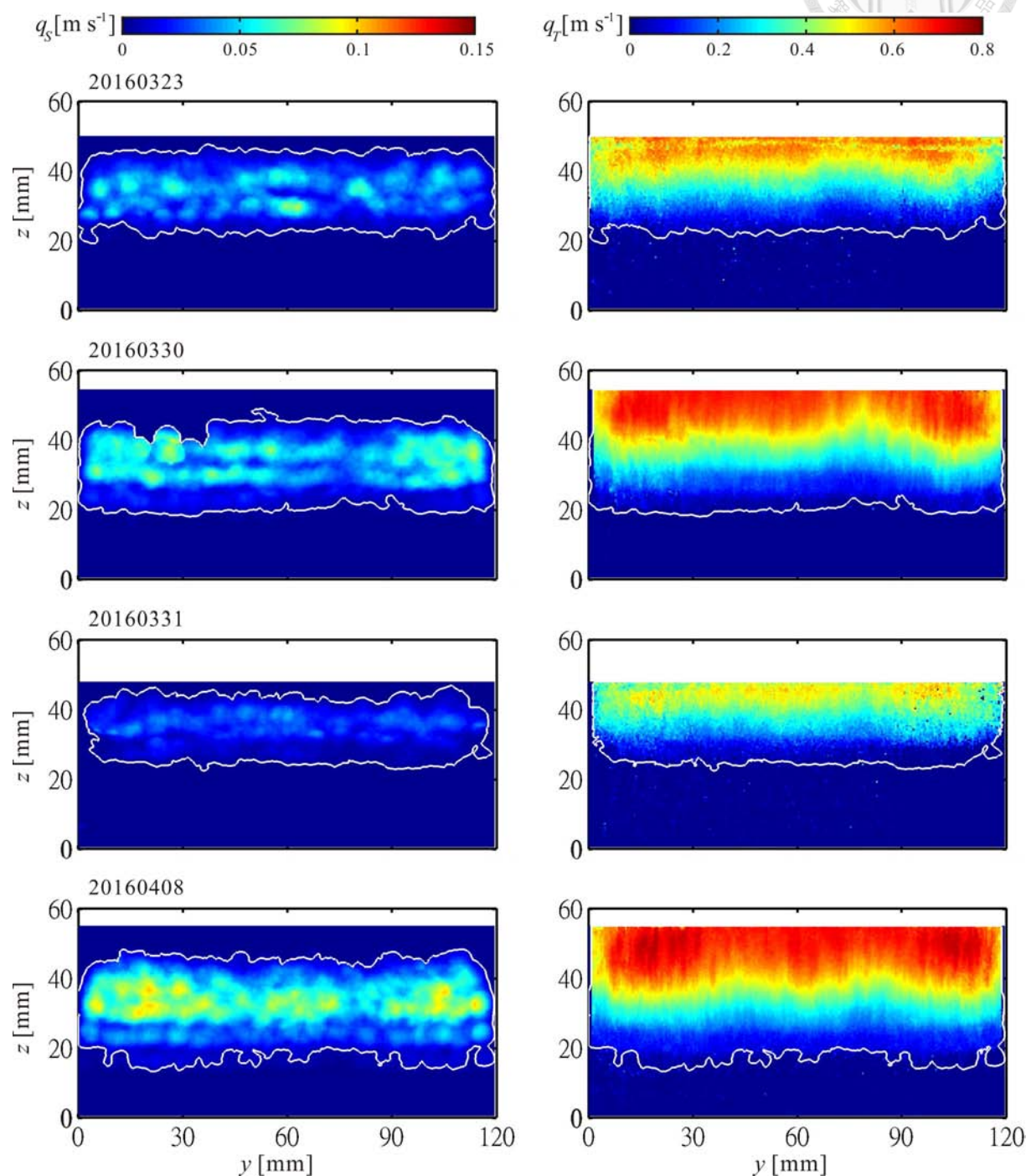
Figure 4.6 Discharge maps and the domains of transport, SWRF case:1-4
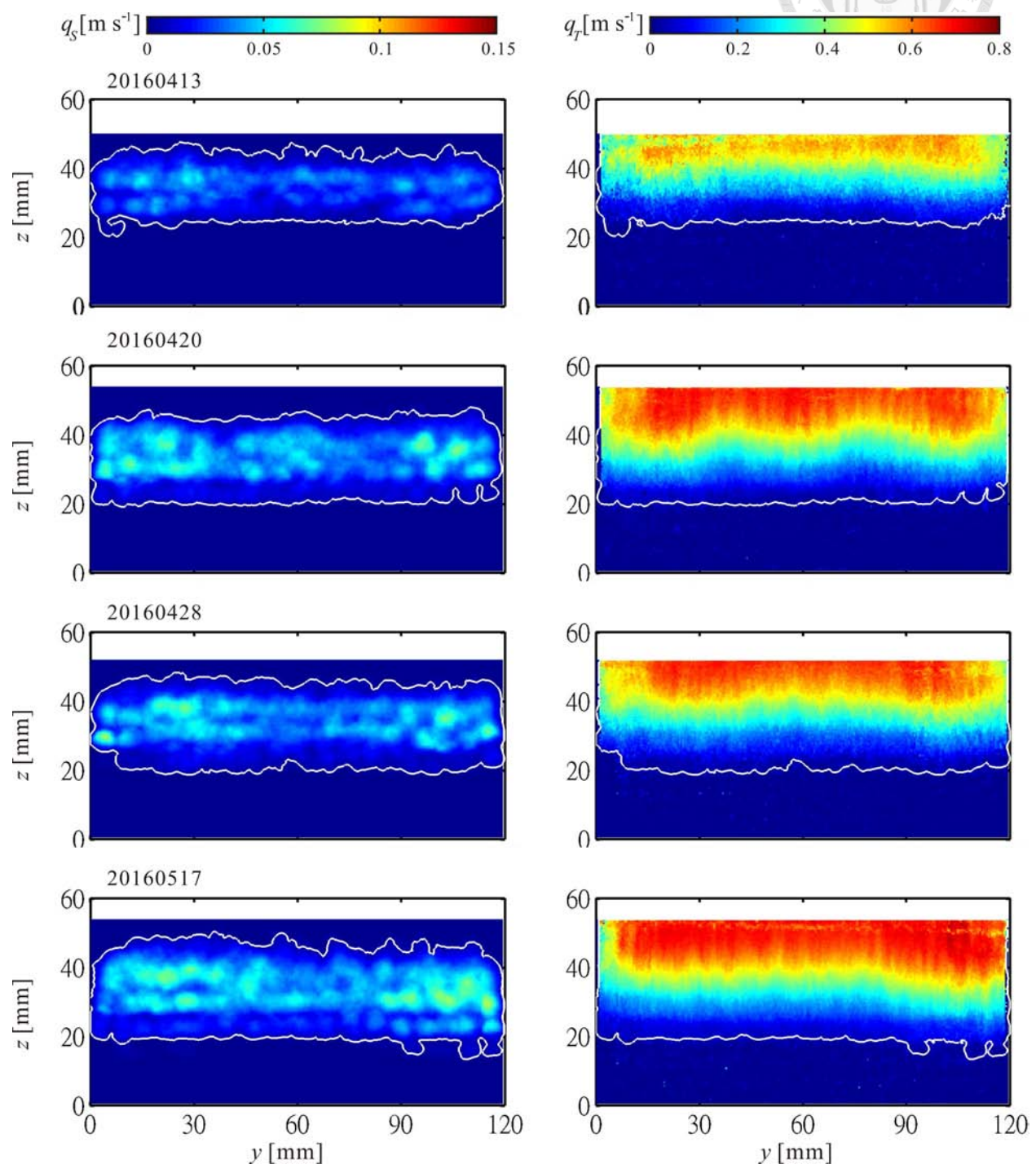
Figure 4.7 SWRF case:5-8
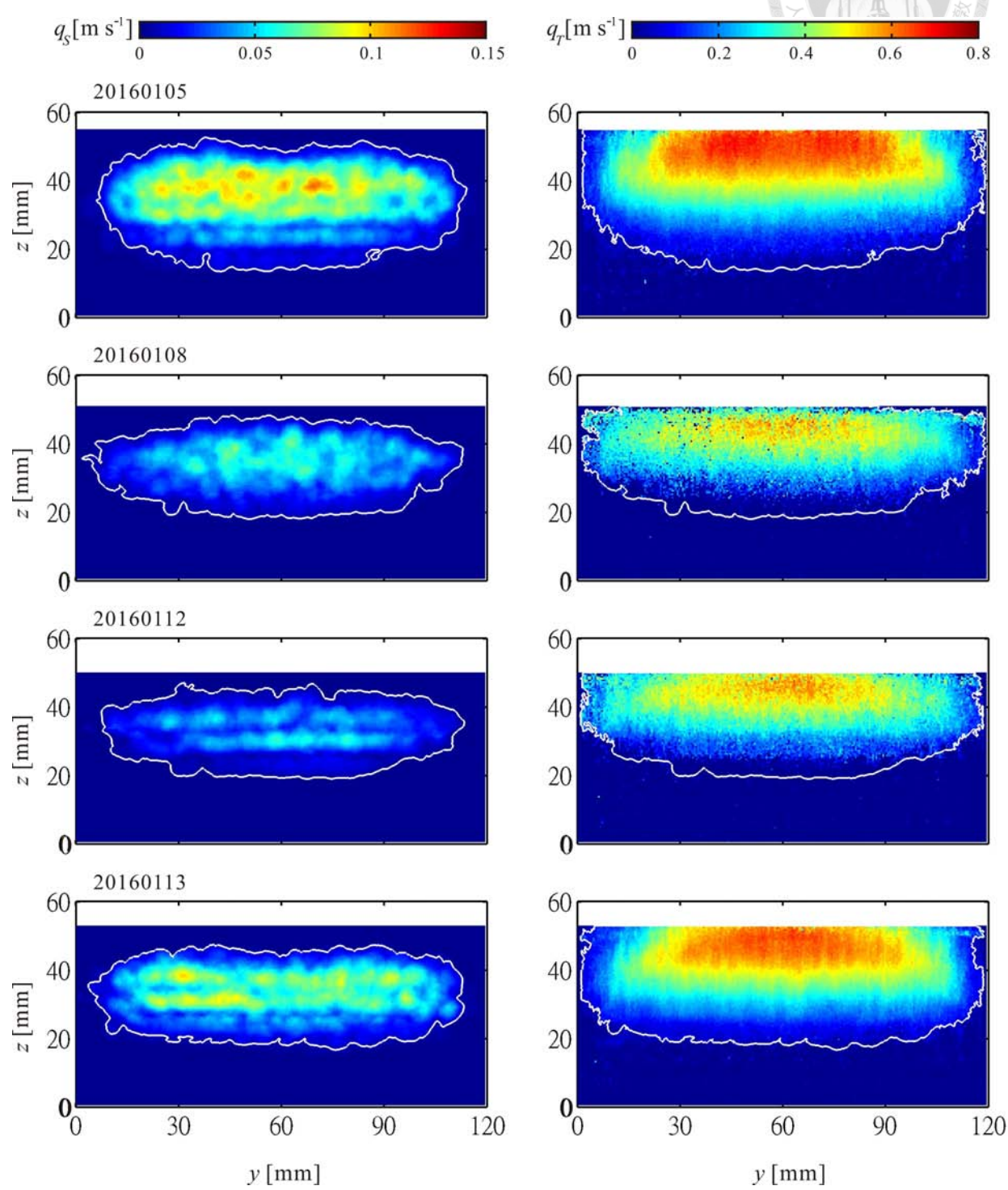
Figure 4.8 Discharge maps and the domains of transport, RWRF case:1-4
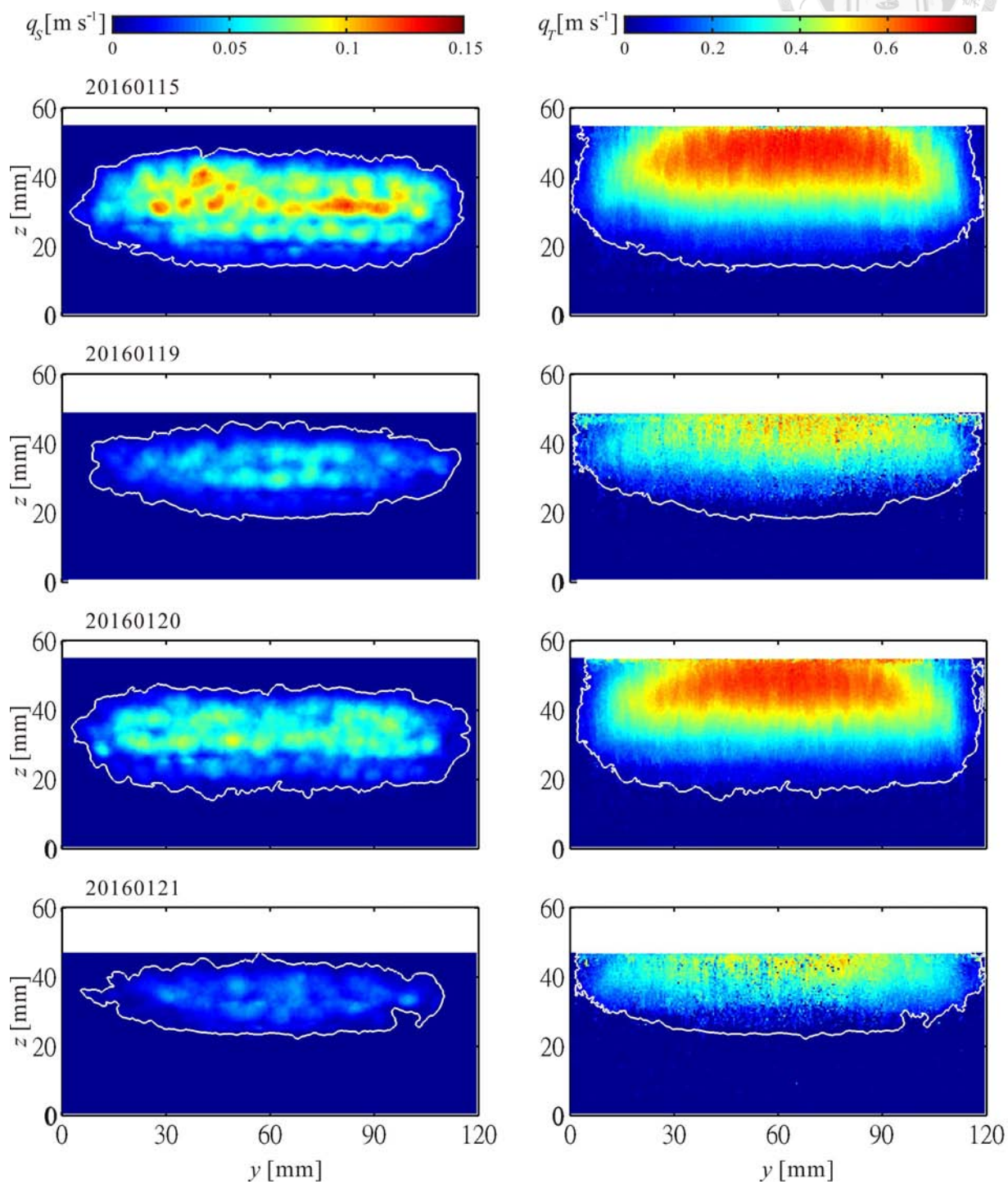
Figure 4.9 RWRF case:5-8
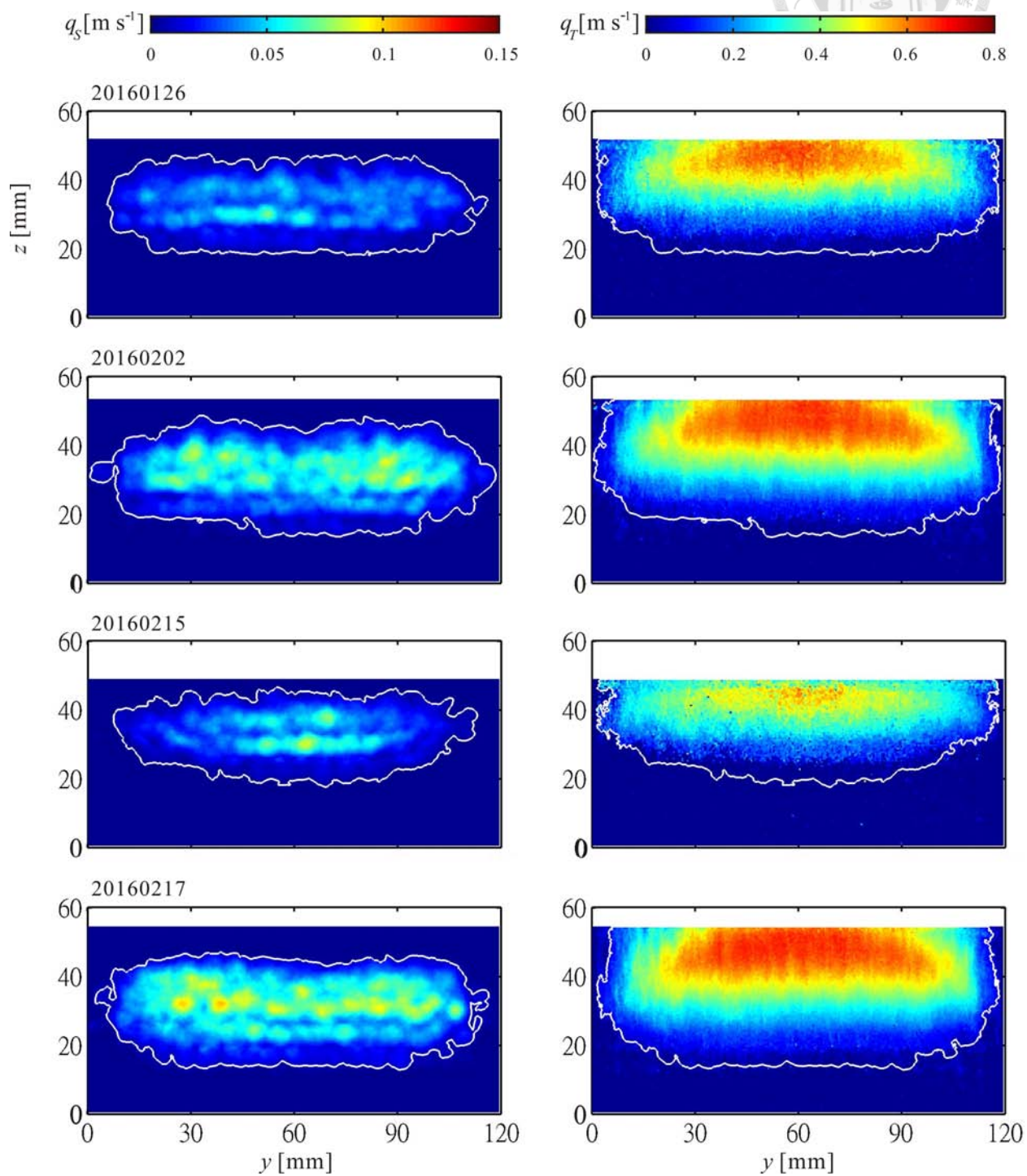
Figure 4.10 RWRF case:9-12
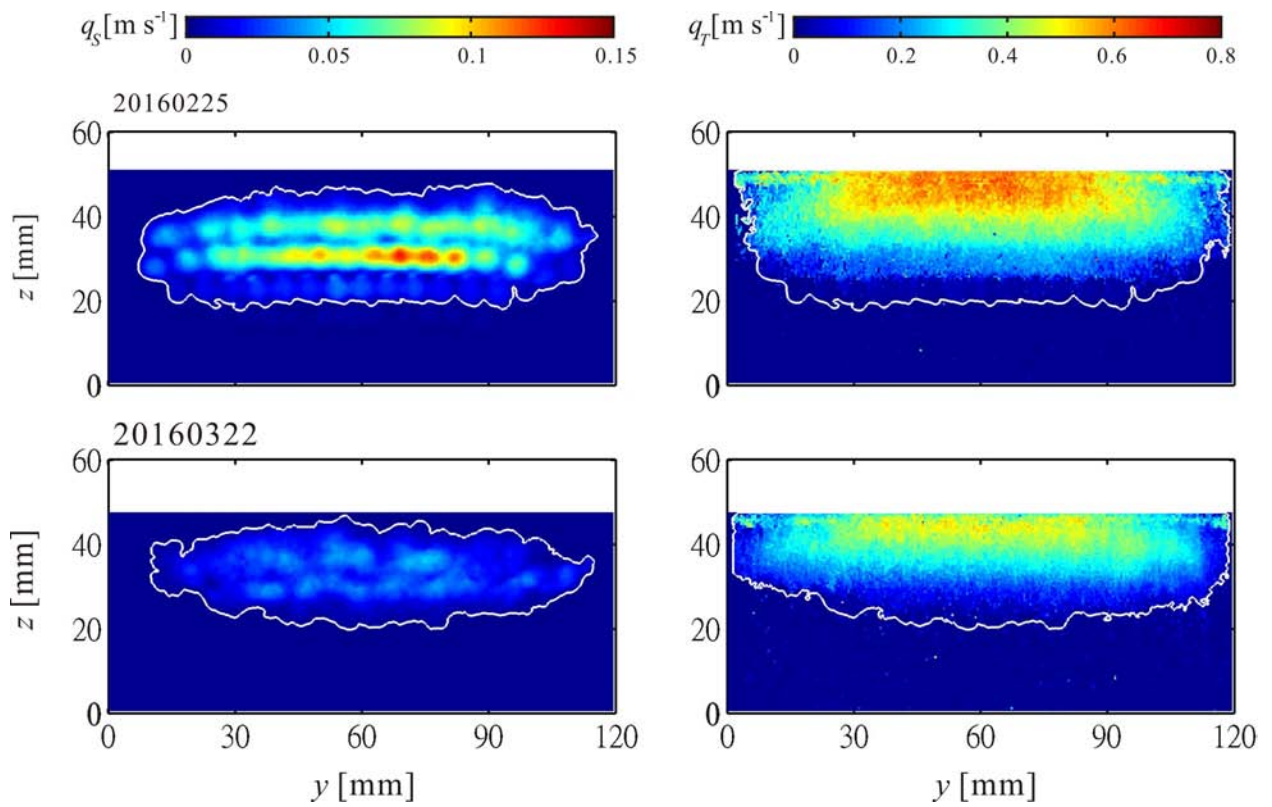
Figure 4.11 RWRF case:13-14
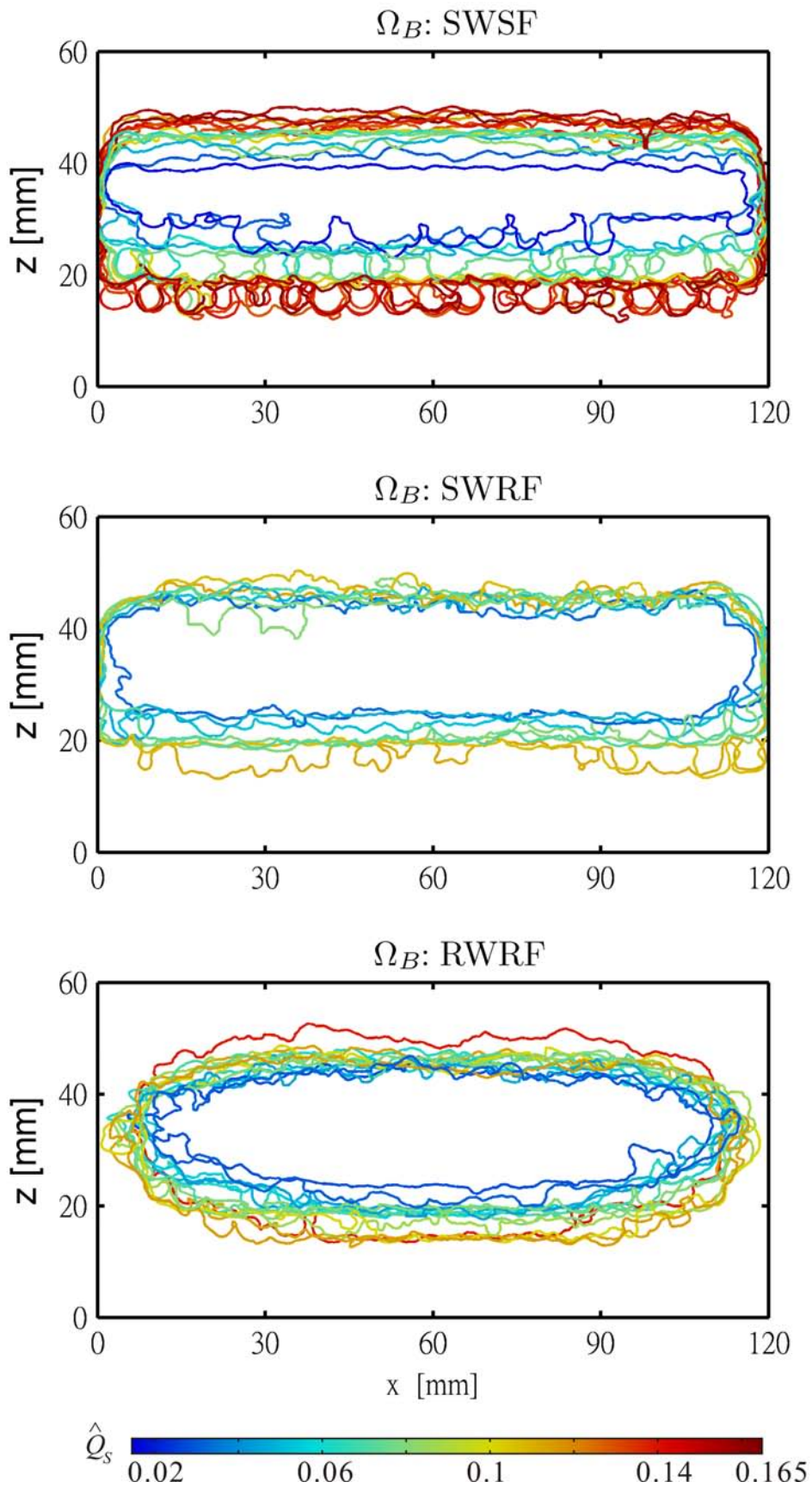
Figure 4.12 The bed-load domain contours of three cases: SWSF (top); SWRF (middle); RWRF (bottom); The color code is defined by the dimensionless solid discharge $\hat{Q}_S$

92
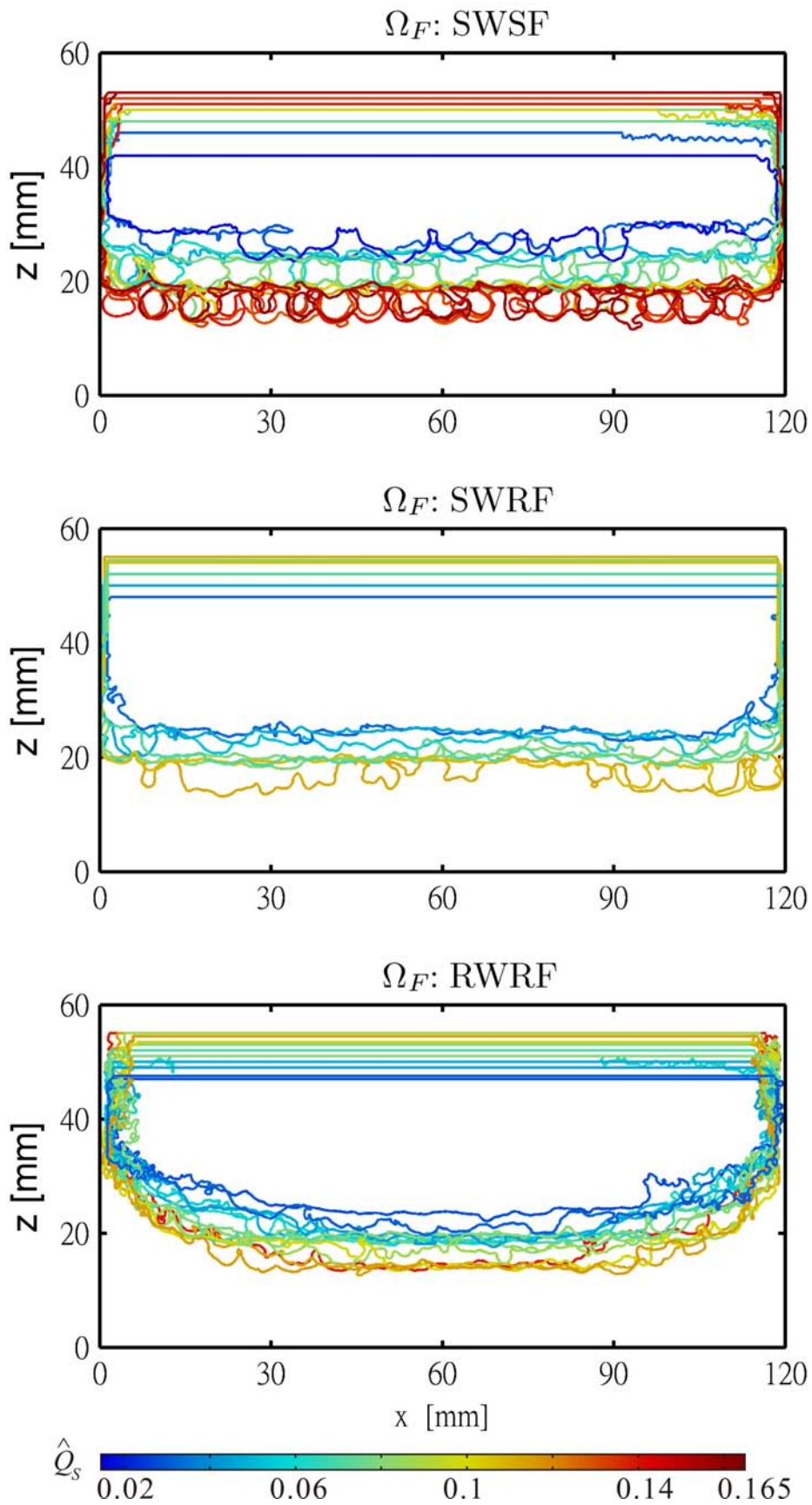
Figure 4.13 The flow domain contours of three cases: SWSF (top); SWRF (middle); RWRF (bottom); The color code is defined by the dimensionless solid discharge $\hat{Q}_S$
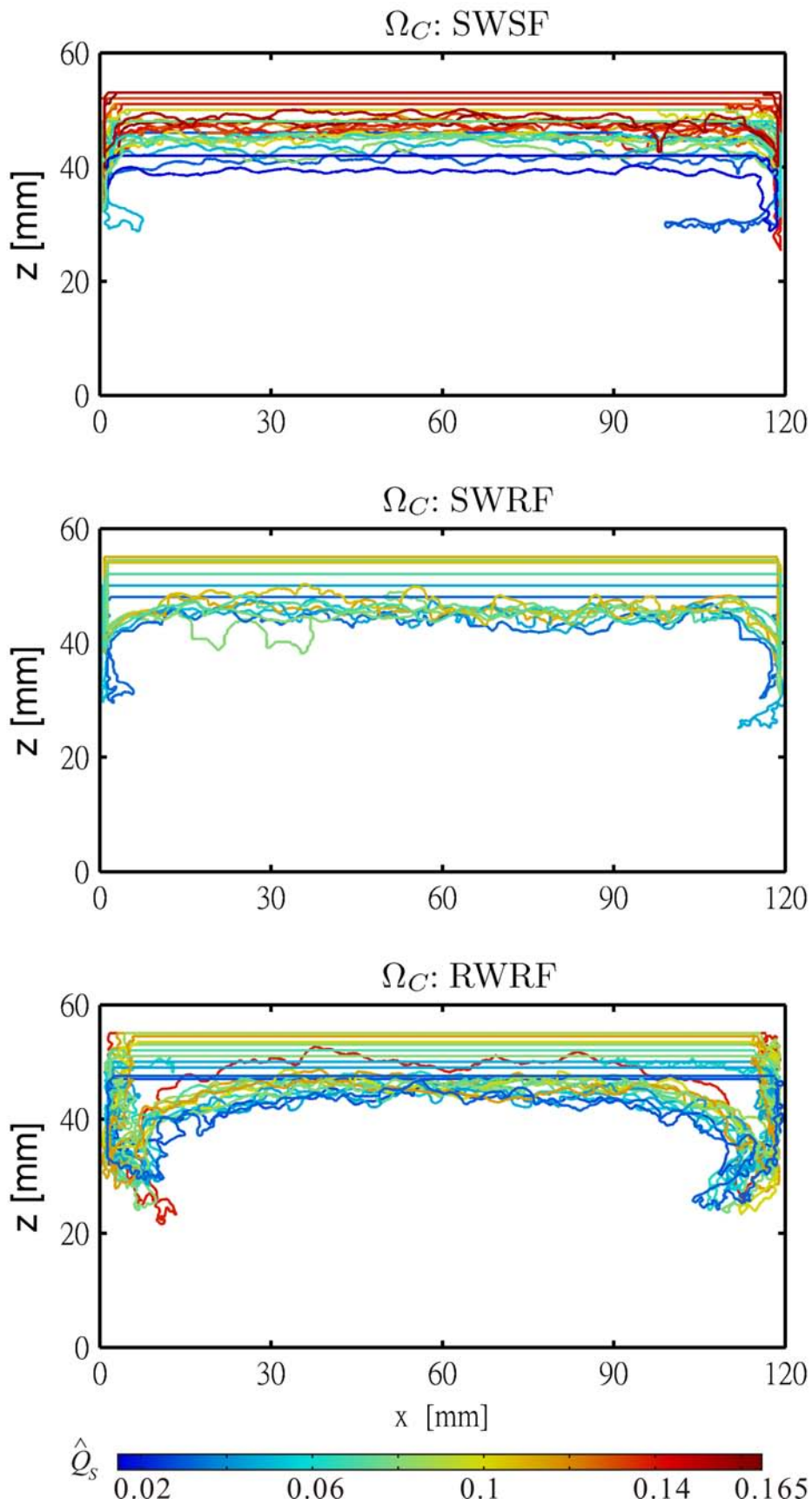
Figure 4.14 The clear liquid domain contours of three cases: SWSF (top); SWRF (middle); RWRF (bottom); The color code is defined by the dimensionless solid discharge $\hat{Q}_S$

94

4.2 Factorizatione of bed-load transport rate

From the definitions above, we could derived the factors that control the bed-load transport Q_S. First we calculated the area of bed-load, area of total flow and area of clear liquid directly by the domain integration.

$$\int_{\Omega_B} dA = A_B \tag{4.6}$$

$$\int_{\Omega_F} dA = A_F \tag{4.7}$$

$$\int_{\Omega_C} dA = A_C \tag{4.8}$$

To quantify the contributions of solid velocity and solid fraction distribution to the solid discharge, we defined the accumulated solid fraction Γ_S:

$$\Gamma_S = \int_{\Omega_F} c_S dA \tag{4.9}$$

Γ_S represents the transported solid inside the flow domain, then the delivered solid fraction C_S can be derived as

$$C_S = \frac{\int_{\Omega_F} c_S dA}{\int_{\Omega_B} dA} = \frac{\Gamma_S}{A_B} \tag{4.10}$$

and the corresponding solid velocity would be expressed as

$$U_S = \frac{\int c_S u_S dA}{\int_{\Omega_B} c_S dA} = \frac{Q_S}{\Gamma_S} \tag{4.11}$$

thus the bed-load transport rate Q_S could be expressed in terms of these factors: C_S, U_S and A_B,

$$Q_S = \frac{\Gamma_S}{A_B} \frac{Q_S}{\Gamma_S} A_B = C_S U_S A_B \tag{4.12}$$

We could also defined the velocity in the clear liquid domain and in the flow domain:

$$U_C = \frac{Q_C}{A_C} \tag{4.13}$$

$$U_T = \frac{Q_T}{A_T} \tag{4.14}$$

With the factors derived above, we plotted them versus Q_S to see if there is any relationship between variables, results are shown in Figure 4.15

95

Figure 4.15 Relations of the transport factors versus the solid discharge Q_S in linear scale, symbol ○ represent SWSF, □ represent SWRF, △ represent RWRF, solid lines represent log-law relation (4.15) with exponent $\beta = 1/3$, for dashed lines, the exponent β were obtained by fitting the data: **a** delivered solid fraction; **b** solid velocity; **c** area of bed-load domain; **d** mixture velocity; **e** velocity of clear liquid; **f** area of clear liquid domain.

For Figure 4.15**a** to **c** show the relations between bed-load transport rate Q_S and its decomposed variables C_S, U_S and A_B. For the delivered solid fraction C_S in **a**, the data of SWSF were higher than the other two cases, while in Figure 4.15**b** the solid velocity U_S of SWSF were in the lower region. For the factor A_B, three cases collapse in the same trend. Comparing to the other cases, the results show that in SWSF case C_S were increased but U_S were decreased for a given Q_S . In Figure 4.15**d** and **e** show that SWRF case could sustain the higher mixture velocity U_T and higher velocity in clear liquid domain U_C than the other cases. In Figure 4.15**f** shows the SWSF case had the lowest clear liquid area for a given Q_S. Then we used the log-law to fit the data and obtain the trends among these relations. we tried first with the equation which has a coefficients α and an exponent β:

$$Q_S = \alpha X^\beta \tag{4.15}$$

where X represents different parameters of Eq.(4.6)- (4.14), the fitting curves were plotted as dashed lines. The second fitting strategy was adopted from the approach proposed by *Capart and Fraccarollo* (2011) with modifications, we assumed that the solid discharge

Q_S would be scaled with C_S, U_S, A_B in the same manner,

$$Q_S = C_S U_S A_B \propto Q_S^{1/3} Q_S^{1/3} Q_S^{1/3} \qquad (4.16)$$

therefore in this version $\beta = 1/3$, only the coefficient α was to be solved, least-squared method was adopted to solve fitting problems and the results were plotted in solid lines. The fitting results were in agreement with data, the deviations between fitting lines were in the range of data scattering, and one can notice that for SWRF case which have lowest data scattering and the dashed lines are very close to the solid lines from Figure 4.15**a** to **e**, which shows that Eq.(4.16) might be good enough to describe the relations between solid discharge and it factors. We adopted this formulation and re-plotted the variables in log-log scale in Figure 4.16, and these variables related to bed-load transport would be compared with the kinematic and dynamic similarities in the following section.
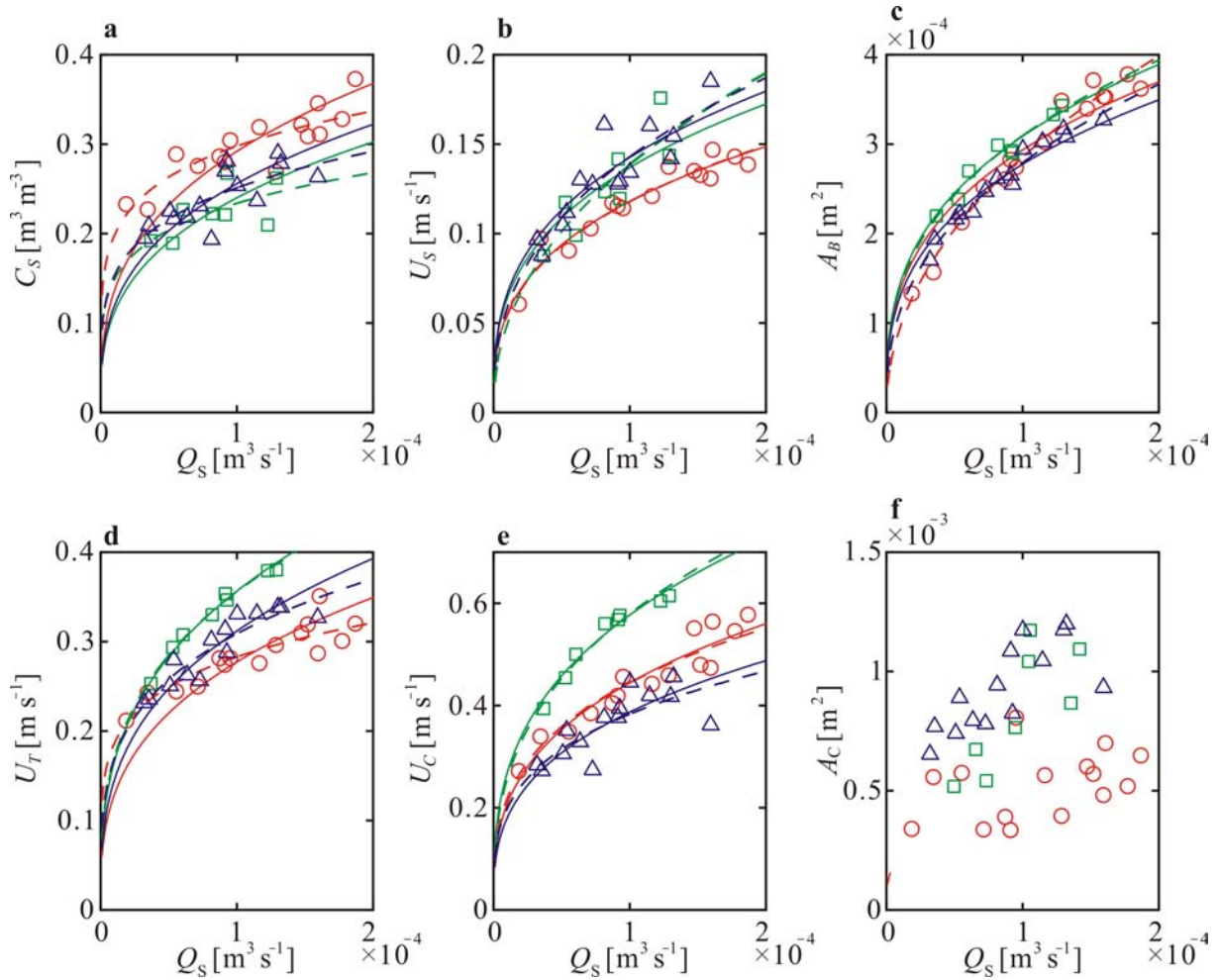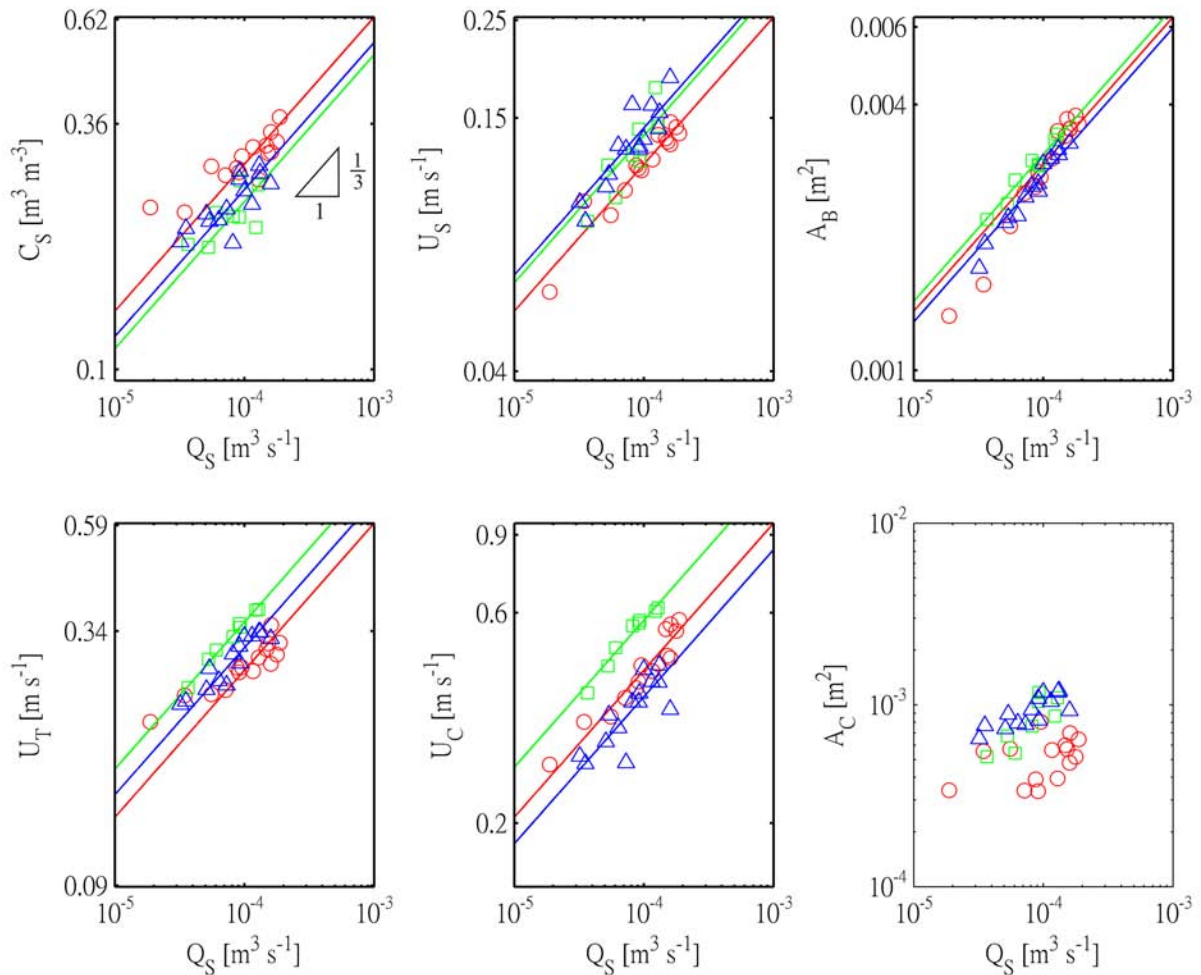

Figure 4.16 Relations of the transport factors versus the solid discharge Q_S in log-log scale, symbol ◯ represents SWSF, □ represents SWRF, and △ represents RWRF: **a** delivered solid fraction; **b** solid velocity; **c** area of bed-load domain; **d** mixture velocity; **e** velocity of clear liquid; **f** area of clear liquid domain.

97

4.3 Dimensional analysis

To further characterize the relations between bed-load transport and physical variables within the flow, we selected the related variables and see how they respond to the dimensionless parameters which represent the kinematic and dynamic conditions for the flow. first we chose the variables obtained in Section 4.2, C_S, A_B and U_S, and the physical variables related to the dimensions:

$$O = F(I, S, \rho_S, \rho_L, g, D, B, P), \text{ where } I = U_C, U_T, \text{ for kinematic similarity.} \quad (4.17)$$

For the RHS of the relation are the input and dimensional variables, S is the channel slope, g is the gravitational acceleration, D is the particle diameter, B is the channel width and P is the perimeter, these variables represent the physical dimensions of the experiments, for variables, ρ_S and ρ_L and g, could be reduced to $g' = \frac{\rho_S - \rho_L}{\rho_L} g$ to include the buoyancy and gravity effects. For LHS of Eq. (4.17), O represents the outcome variables which were composed with

$$O : (Q_S, C_S, A_B, U_S) \quad (4.18)$$

we selected these variables to see the responds of the bed-load transport rate to the input parameter and we tell which components dominate this variation. We make the outcome variables dimensionless by g', D and B

$$\hat{Q}_S = \frac{Q_S}{B\sqrt{g'D^3}} \quad (4.19)$$

$$\hat{U}_S = \frac{U_S}{\sqrt{g'D}} \quad (4.20)$$

$$\hat{A}_B = \frac{A_B}{BD} \quad (4.21)$$

where $\hat{Q}_S$ is the dimensionless parameter called Einstein number, and C_S is dimensionless itself. I in RHS is the input variable, and we chose Mobility parameter Θ as the dimensionless parameter which is defined by

$$\hat{\Theta} = \frac{U^2}{g'D} \quad (4.22)$$

where U is the amplitude of the velocity outside the boundary layer adopted by *Asano* (1995) to compare the relation with sediment transport rate in oscillatory sheet flow, the relation between Mobility parameter and the dimensionless bed-load transport rate was also suggested by *Asano* (1995)

$$\hat{Q}_S \propto \hat{\Theta}^{3/2} \quad (4.23)$$

therefore from Eq. (4.23) we could test the log-law of the solid discharge Eq. (4.16) and plotted with data. For each outcome variables it scales with Mobility parameter in this way:

$$C_S, \hat{U}_S, \hat{A}_B \propto \hat{\Theta}^{1/2} \quad (4.24)$$

In our cases we selected the velocity in the clear liquid domain U_C and the total transport velocity U_T as the velocity scale of the Mobility parameter Eq. (4.25) and Eq. (4.26),

and compared with the normalized outcome variables, the results were plotted in Figure 4.17 and Figure 4.19 on linear scale, in Figure 4.18 and Figure 4.20 on log-log scale.

$$\hat{\Theta}_C = \frac{U_C^2}{g'D} \tag{4.25}$$

$$\hat{\Theta}_T = \frac{U_T^2}{g'D} \tag{4.26}$$

Figure 4.17 Relations with the clear liquid domain Mobility parameters $\hat{\Theta}_C$ of the outcome variables on linear scale: **a** C_S; **b** $\hat{U}_S$; **c** $\hat{A}_B$; **d** $\hat{Q}_S$; symbol definitions: red $\bigcirc$ for SWSF, green $\square$ for SWRF, and blue $\triangle$ for RWRF; lines: from **a** to **c** fitting results for $\beta = 1/2$, **d** fitting result for $\beta = 3/2$.

Figure 4.18 Relations with the clear liquid domain Mobility parameters $\hat{\Theta}_C$ of the outcome variables on log-log scale: **a** C_S; **b** $\hat{U}_S$; **c** $\hat{A}_B$; **d** $\hat{Q}_S$; symbol definitions: red $\bigcirc$ for SWSF, green $\square$ for SWRF, and blue $\triangle$ for RWRF; lines: from **a** to **c** fitting results for $\beta = 1/2$, **d** fitting result for $\beta = 3/2$.

Figure 4.19 Relations with the clear liquid domain Mobility parameters $\hat{\Theta}_T$ of the outcome variables in linear scale: **a** C_S; **b** $\hat{U}_S$; **c** $\hat{A}_B$; **d** $\hat{Q}_S$; Symbol definitions: red $\bigcirc$ for SWSF, green $\square$ for SWRF, and blue $\triangle$ for RWRF; lines: from **a** to **c** fitting results for $\beta = 1/2$, **d** fitting result for $\beta = 3/2$.
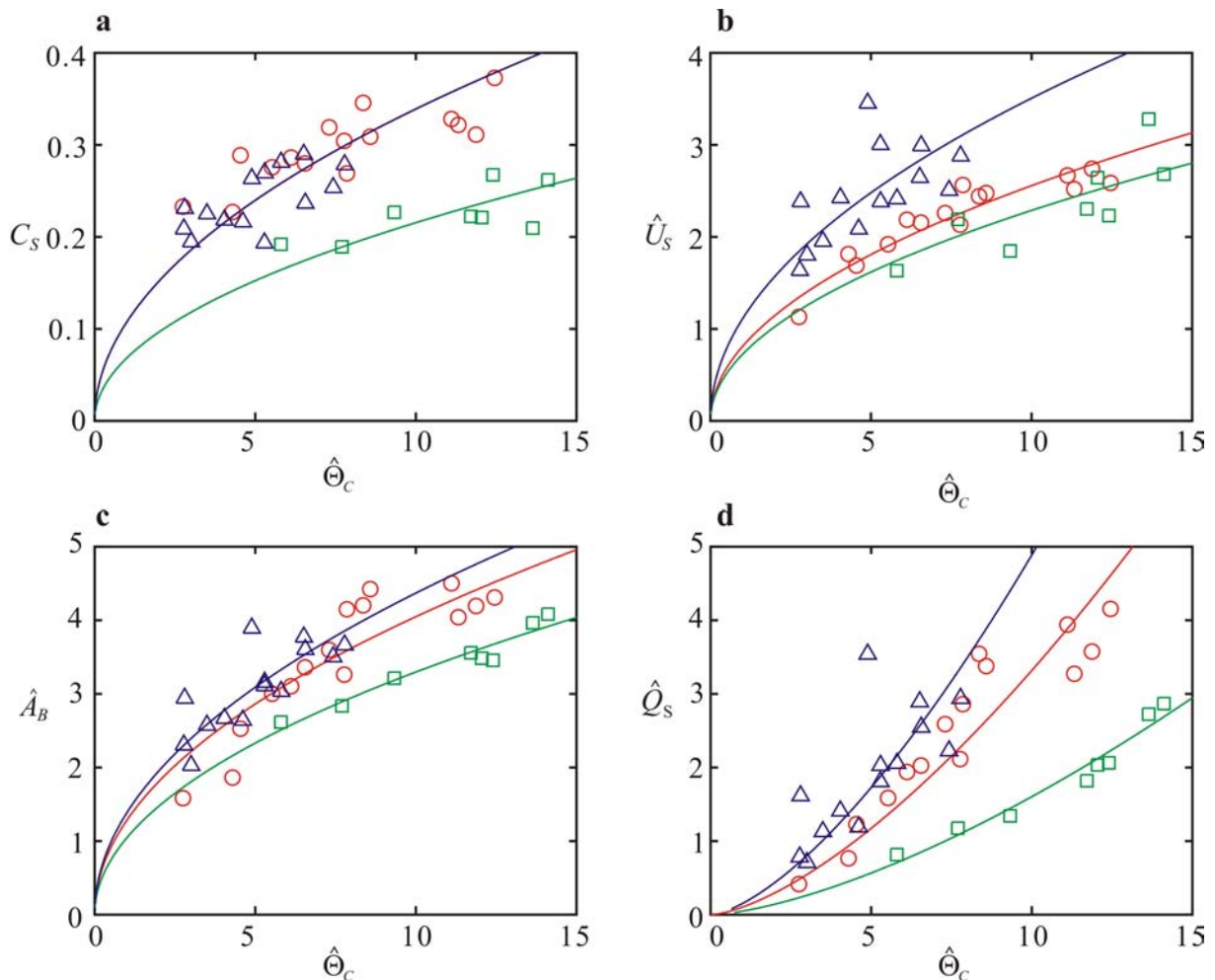
Figure 4.20 Relations with the clear liquid domain Mobility parameters $\hat{\Theta}_T$ of the outcome variables in log-log scale: **a**, C_S; **b**, $\hat{U}_S$; **c**, $\hat{A}_B$; **d**, $\hat{Q}_S$; symbol definitions: red $\bigcirc$ for SWSF, green $\square$ for SWRF, and blue $\triangle$ for RWRF; lines: from **a** to **c** fitting results for $\beta = 1/2$, **d** fitting result for $\beta = 3/2$.

The range of Mobility parameters $\hat{\Theta}_C$ are from 0.25 to 15, for all case, the data collapse for all four outcome variables, and for all four outcome variables, the SWRF data shows the lowest responds to the Mobility parameter, the lines plotted in Figures represent the relations of Eq. (4.23) to (4.24), the exponents we assumed are in agreement with data. For Mobility parameters $\hat{\Theta}_T$,data shows less correlated, in Figure 4.20**cd** the slopes of the data seem steeper than we assumed, while in Figure 4.20**a** the slope of data seems more gentle.

For the dynamic similarity, we chose the classical Shields number to illustrated the bed-load transport variables with shear stress, Shields number can be expressed in the following equation

$$\hat{\tau}_B = \frac{H_F S}{g' D} \tag{4.27}$$

where $H = A_F/B$ represents the flow depth, to represent the 3 dimensional flow doamin for the RWRF case, we also chose the Shield number expressed by the perimeter

$$\hat{\tau}_P = \frac{A_F}{P} \frac{S}{g' D} \tag{4.28}$$

102

where P is the perimeter which can be obtained from the flow domain, the outcome variables $\hat{A}_B$ and $\hat{Q}_S$ need to be modified by replacing B with P.

$$\hat{A}_{BP} = \frac{A_B}{PD} \tag{4.29}$$

$$\hat{Q}_{SP} = \frac{Q_S}{P\sqrt{g'D^3}} \tag{4.30}$$
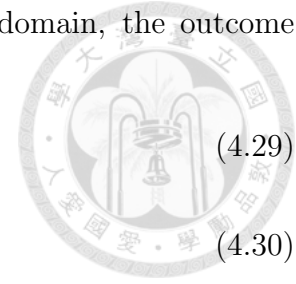
and we assumed the same relationship for dimensionless bed-load transport rate and Shields number:

$$\hat{Q}_S \propto \hat{\tau}^{3/2} \tag{4.31}$$

the relationship is in the same form as the empirical law of *Meyer-Peter and Müller.* (1948), and was compared with the experiments and verified by *Capart and Fraccarollo* (2011). The outcome variables scale with $\hat{\tau}$ as below, the relations with Shields number $\hat{\tau}_B$ and $\hat{\tau}_P$ of the outcome variables were plotted in Figure 4.21 and Figure 4.23 on linear scale, in Figure 4.22 and Figure 4.24 on log-log scale.

$$C_S \propto \hat{\tau}^{1/2} \tag{4.32}$$

$$\hat{U}_S \propto \hat{\tau}^{1/2} \tag{4.33}$$

$$\hat{A}_B \propto \hat{\tau}^{1/2} \tag{4.34}$$

103
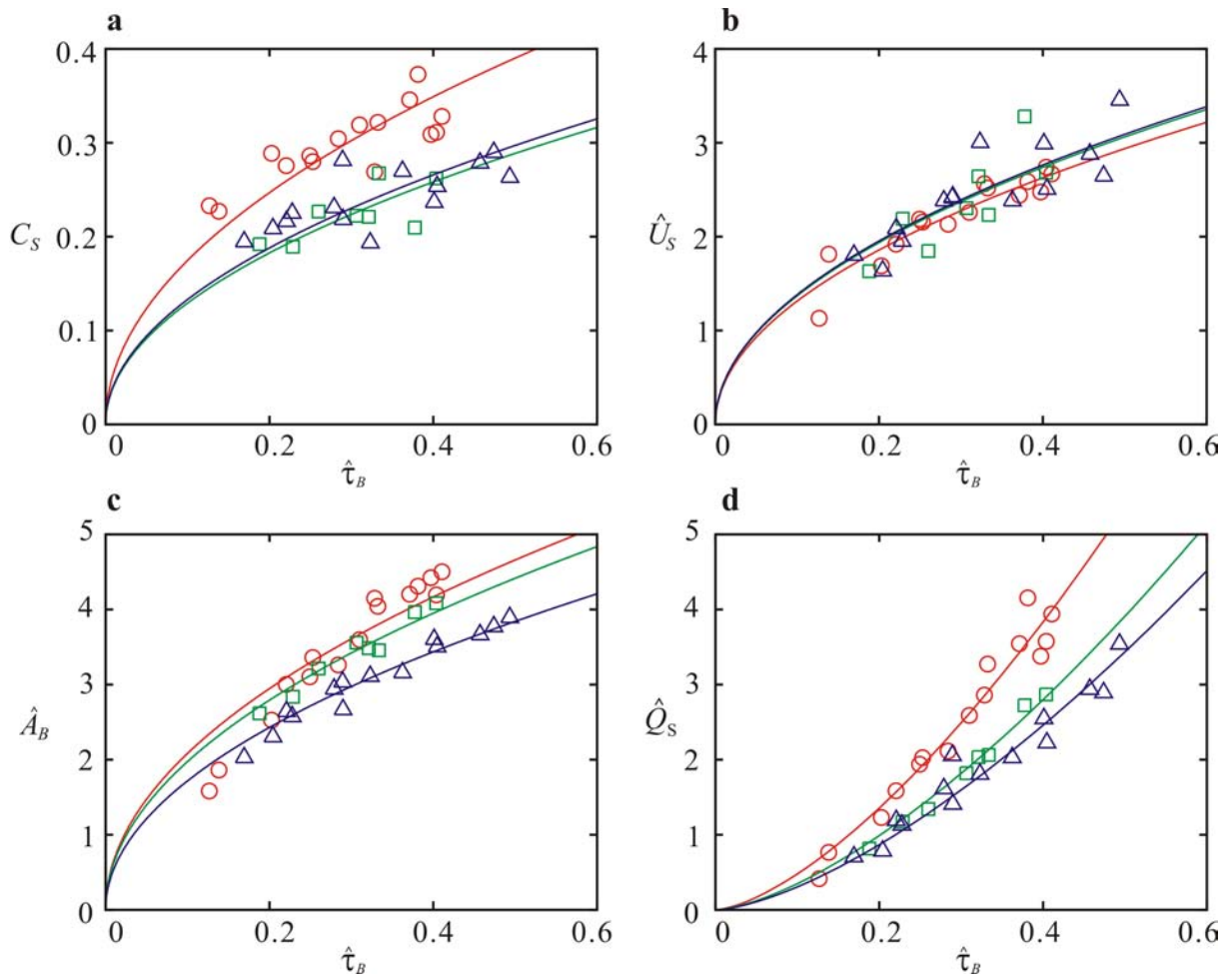
Figure 4.21 Relations with Shields number $\hat{\tau}_B$ of the outcome variables on linear scale: **a**, C_S; **b**, $\hat{U}_S$; **c**, $\hat{A}_B$; **d**, $\hat{Q}_S$; Symbol definitions: red $\bigcirc$ for SWSF, green $\square$ for SWRF, and blue $\triangle$ for RWRF; solid lines: from **a** to **c** fitting results for $\beta = 1/2$, **d** fitting result for $\beta = 3/2$.
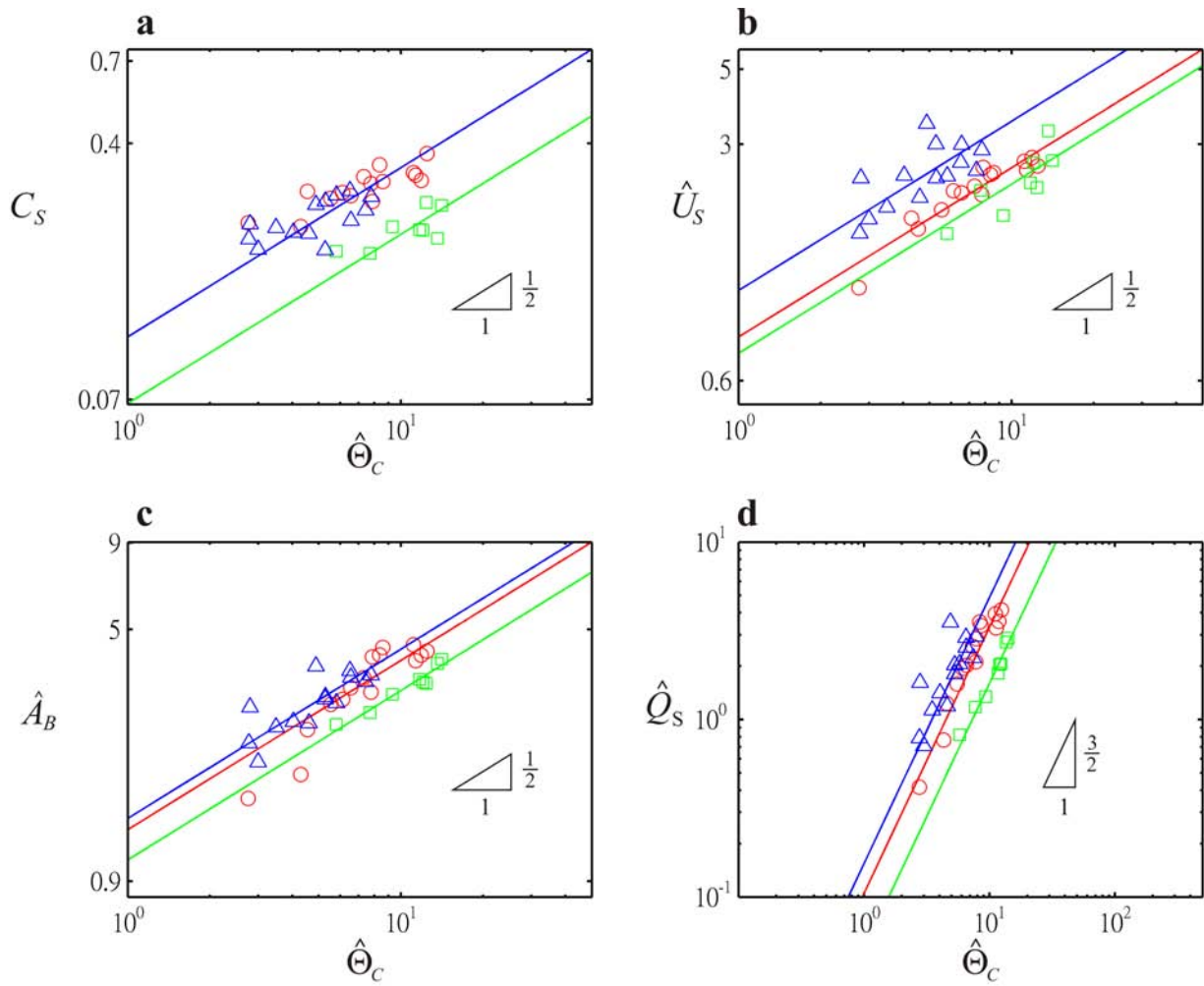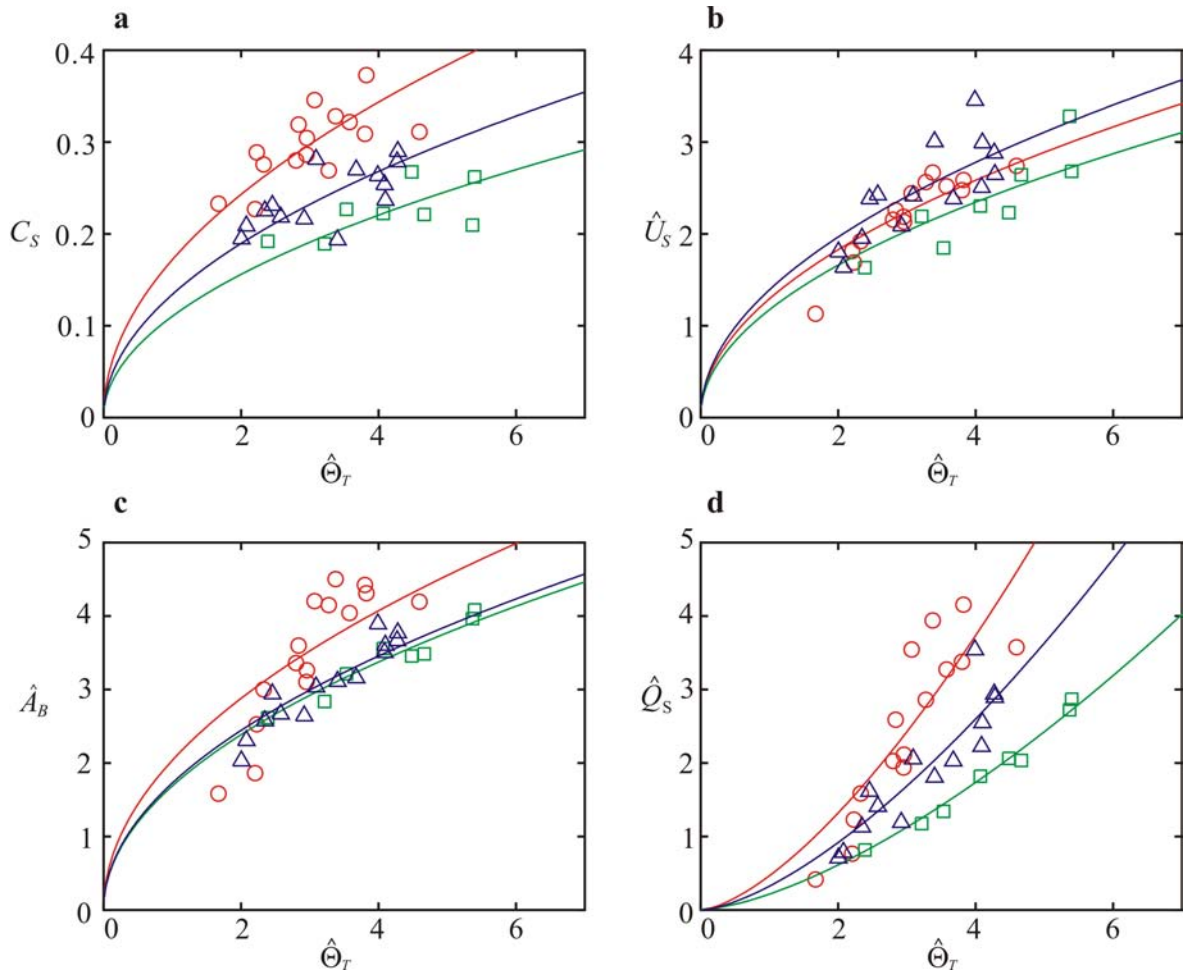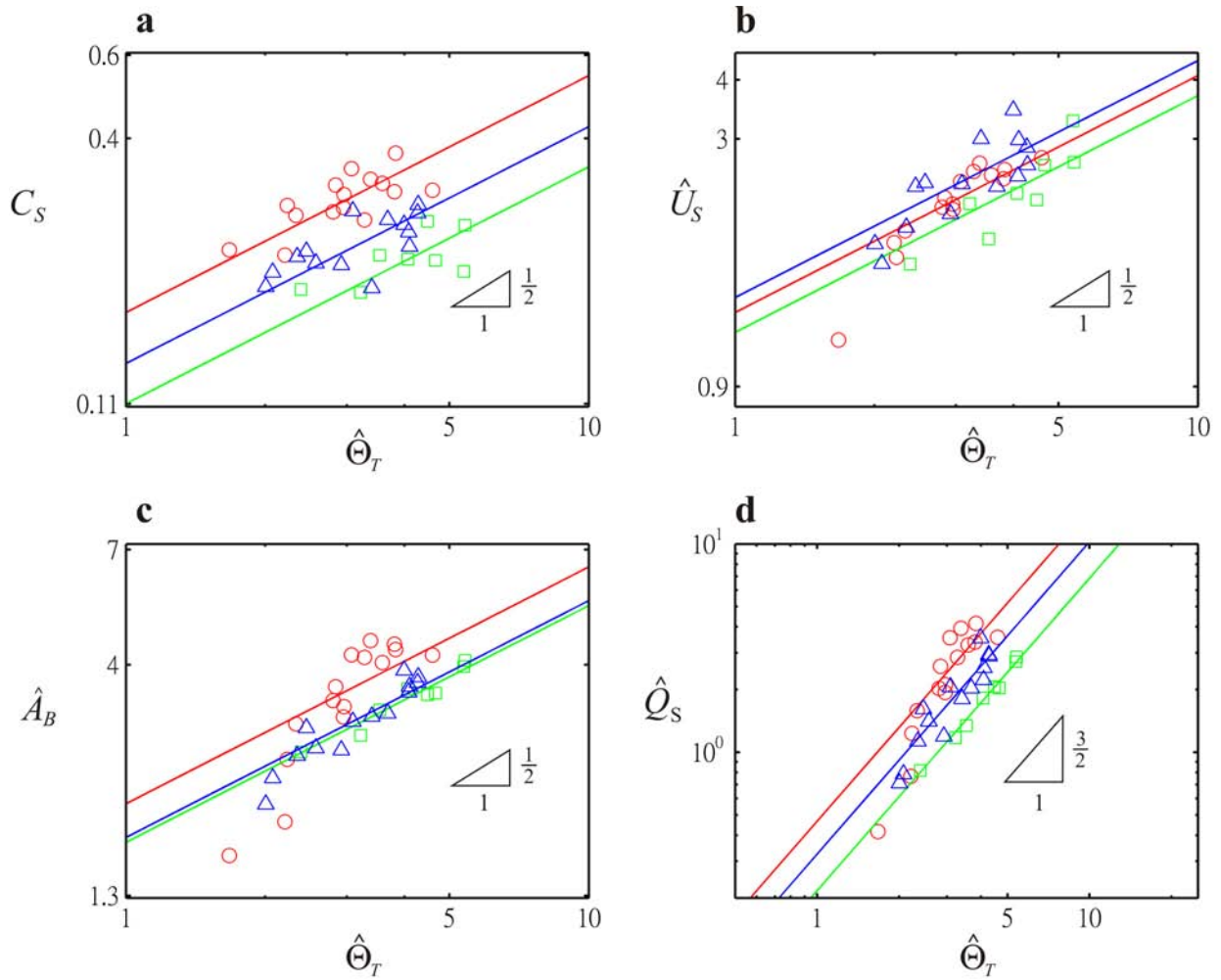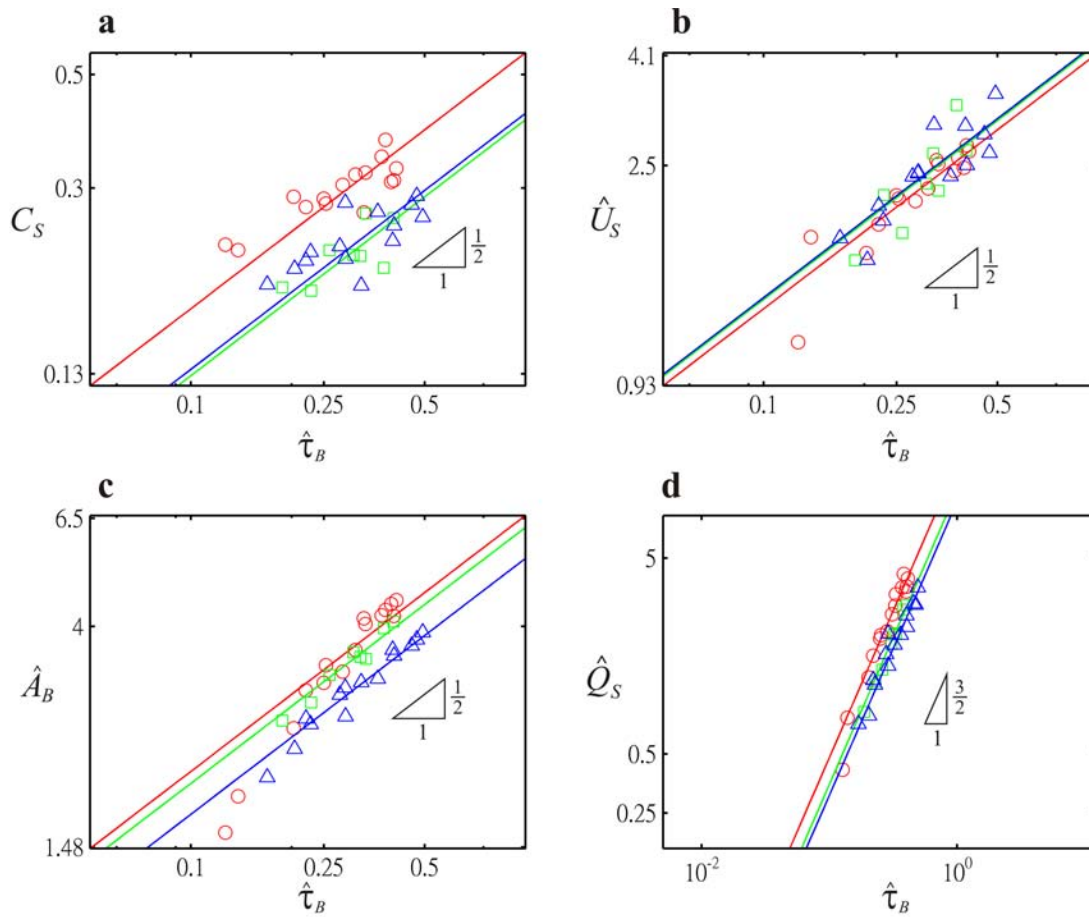
Figure 4.22 Relations with Shields number $\hat{\tau}_B$ of the outcome variables on log-log scale: **a** C_S; **b** $\hat{U}_S$; **c** $\hat{A}_B$; **d** $\hat{Q}_S$; symbol definitions: red ◯ for SWSF, green ▢ for SWRF, and blue △ for RWRF; lines: from **a** to **c** fitting results for $\beta = 1/2$, **d** fitting result for $\beta = 3/2$.
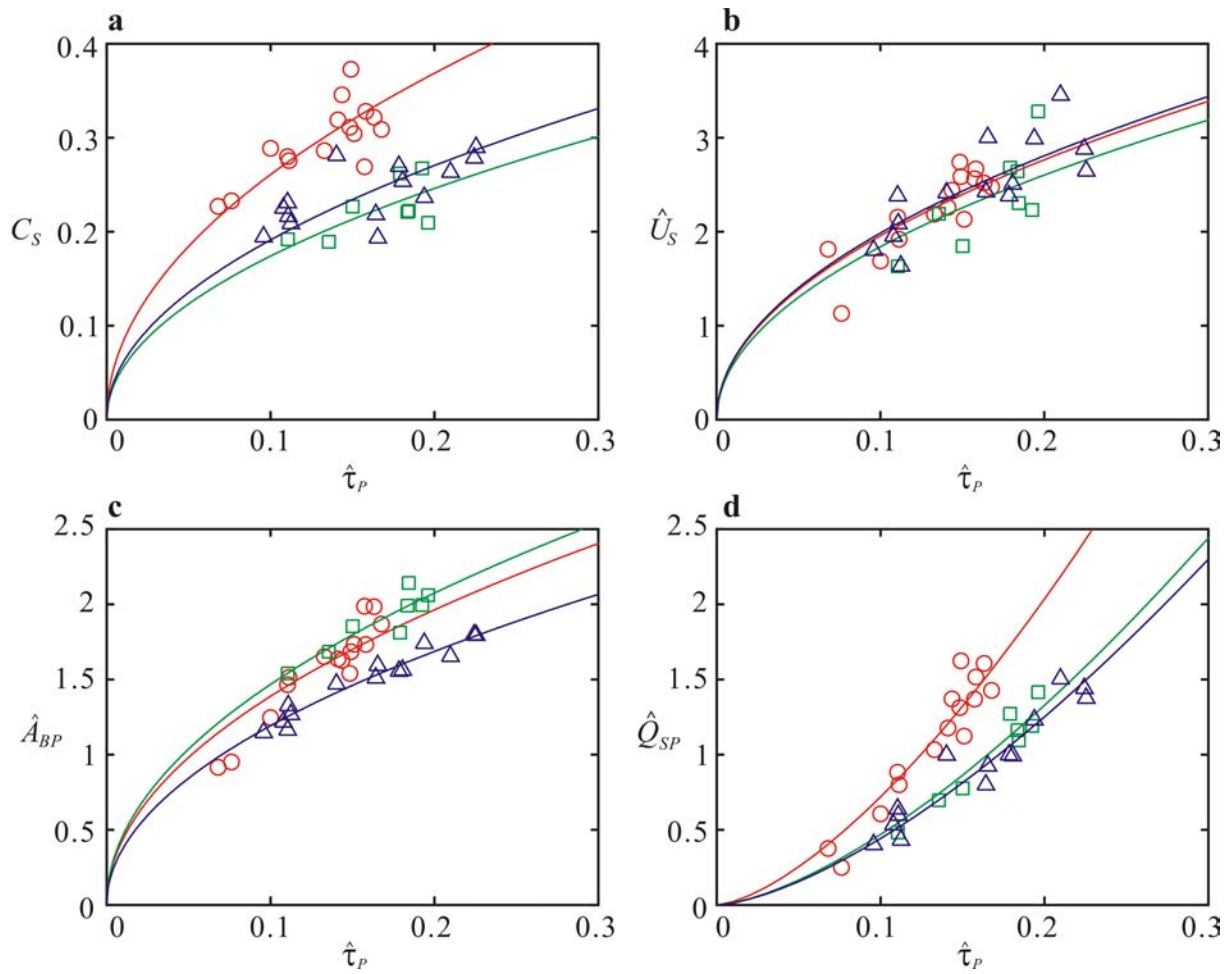
Figure 4.23 Relations with Shields number $\hat{\tau}_P$ of the outcome variables on linear scale: **a** C_S; **b** $\hat{U}_S$; **c** $\hat{A}_B$; **d** $\hat{Q}_S$; symbol definitions: red ◯ for SWSF, green □ for SWRF, and blue △ for RWRF; lines: from **a** to **c** fitting results for $\beta = 1/2$, **d** fitting result for $\beta = 3/2$.
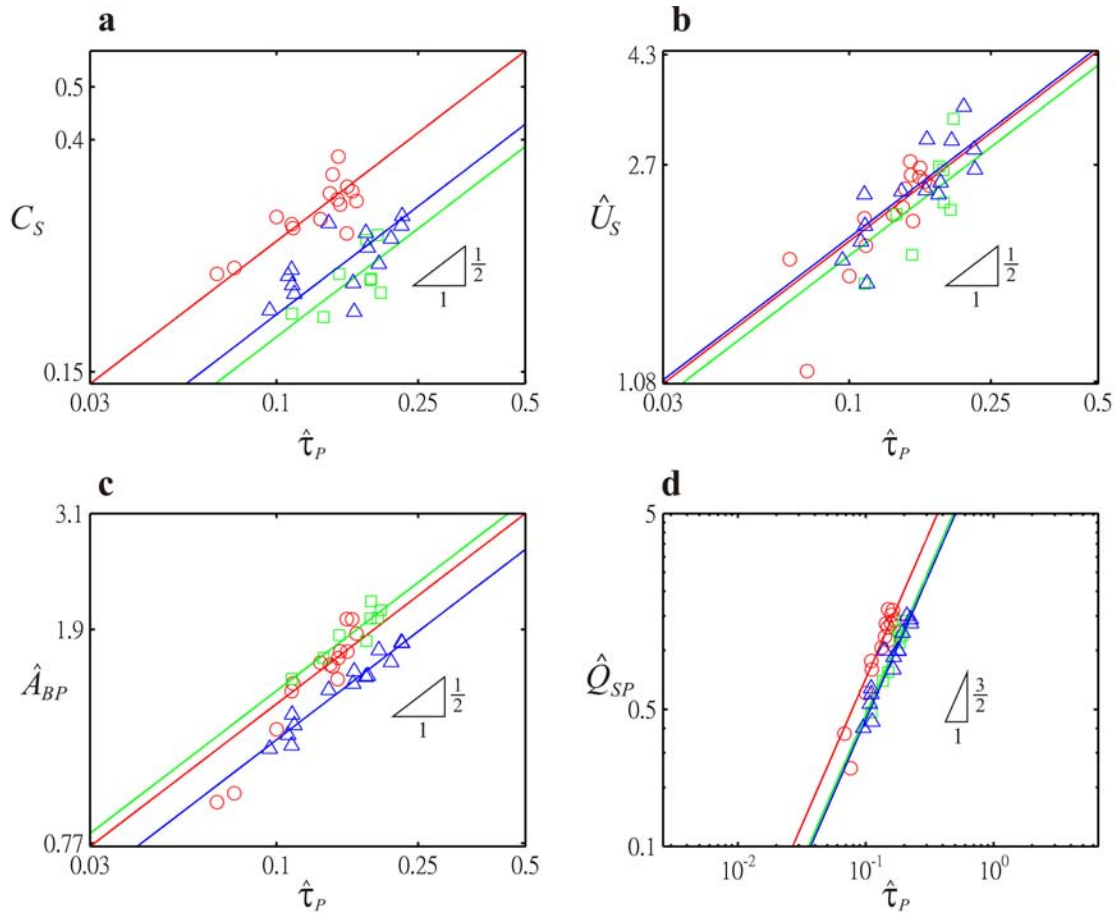
Figure 4.24 Relations with Shields number $\hat{\tau}_P$ of the outcome variables on log-log scale: **a**, C_S; **b**, $\hat{U}_S$; **c**, $\hat{A}_{BP}$; **d**, $\hat{Q}_{SP}$; Symbol definitions: red ◯ for SWSF, green □ for SWRF, and blue △ for RWRF; lines: from **a** to **c** fitting results for $\beta = 1/2$, **d** fitting result for $\beta = 3/2$.

The data show better correlation with the Shields numbers than with Mobility numbers. In Figure 4.21**a** and 4.23**a** it shows that C_S of SWRF case and RWRF case collapse together, and for the SWSF case the value are larger. In Figure 4.21 **b** and 4.23 **b** the value of $\hat{U}_S$ collapse for all three cases, indicating that the three types of channel boundary we adopted would not alter the relation between $\hat{U}_S$ and $\hat{Q}_S$ or $\hat{Q}_{SP}$. For the transport area $\hat{A}_B$ or $\hat{A}_{BP}$, the RWRF data show the lowest value, it represents the influence of boundary roughness. As the combination of the C_S, $\hat{U}_S$ and $\hat{A}_B$ results, SWRF data and RWRF data collapse in the relation of dimensionless bed-load transport rate and Shields number, and for SWSF case the data deviate from the other cases and show higher bed-load transport rate, from **a** to **c**, we can say the primary variable that dominates the deviation is C_S.

4.4   Conclusion

In this Chapter, we investigate the relationship of bed-load transport rate by the flow maps, we used volumetric solid and total discharge to cut different domains of transport, and integrated the different physical quantities over those domains to deduce these map to the factors called outcome variables for three channel boundaries. It shows that the

outcome variables, C_S, U_S and A_B were scaled with bed-load transport rate Q_S in the same manner that followed Eq. (4.16). The dimensional analysis was applied to these outcome variables and compared with two dimensioless parameters: Mobility parameter $\hat{\Theta}$ and Shields number $\hat{\tau}$, for all three channel boundaries, the outcome variables showed their relationship with both Mobility parameter and Shields number having the exponent of 0.5, and for the dimensionless discharge $\hat{Q}_S$, the exponent is about 1.5.
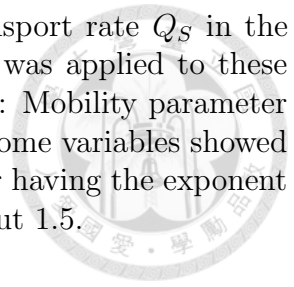
Chapter 5

Internal stresses and drag in turbulent bed-load [1]

In this Chapter, we considered the nearly two-dimensional experiments SWSF and SWRF for further analysis. The objective is to establish the momentum balance equations for solid and liquid phase by the measured data. First we used the phase-averaging maps obtained in Chapter 3 to calculate the vertical profiles for both phases by depth integration, then recovered each terms in the two dimensional momentum equations of steady state, but non-uniform flow, These derivations would be introduced in Section 5.1. In Section 5.2 we tested the stresses relations and drag force relation using the deduces stresses profiles, which are the granular pressure P_S, liquid shear stress τ_L, the solid shear stress τ_S and the drag force f_D. For shear stresses and granular pressure, we normalized these data and compared with the predictions of kinetic theory (*Jenkins and Hanes*, 1998). For drag force, we adopt the empirical relation proposed by *Di Felice* (1994), to verify the empirical law with the materials we used, a series of seepage test were performed, and we modified and verified this empirical law to be applied to the drag force in turbulent bed-load.

5.1 Depth profiles and two-phase momentum balance

With the averaged flow maps of the solid velocity, liquid velocity and solid fraction in high resolution, and after check the mass conservation law, we could step further to investigate the principle contributions of the momentum balance of each phase. In particular, with the experiments SWSF and SWRF, the experiment profiles are obtained for the stresses and interphase drag force, they are used to test the constitutive relationships derived from kinetic theory, turbulent theory, fludization cell and the seepage experiments.

We now focus on variations over depth by averaging the data over both the length and width of the scanned volume. Figure 5.1 and 5.2 shows profiles of granular concentration c_S (magenta), mean longitudinal solid velocity $\overline{u}_S$ (red) and mean longitudinal liquid velocity $\overline{u}_L$ (blue) for two runs representing low and high discharges, respectively. From top to bottom, three distinct zones can be distinguished. Below the flow free surface, there is a clear liquid layer where granular concentration is nearly zero, save for occasional flights by

---

[1]Most of the materials presented in this Chapter was earlier presented in the publication: Ni, W.-J. and Capart, H. (2018) Stresses and drag in turbulent bed-load from refractive-index-matched experiments. *Geophysical Research Letters*, in press, GRL57678.

ballistic grains. The middle zone is the turbulent bed-load layer, where both the velocities and granular concentration exhibit steep gradients. The loose bed layer beneath the bed-load layer, finally, features nearly immobile grains close to the loose packing concentration $c_S \approx 0.6$. The coherent peaks and troughs of the concentration profiles are produced not by measurement error, but by preferential layering of the particles at interdistances of the order of their diameter D, as observed earlier on the maps from Figure 3.1 to 3.3 for SWSF case, and from Figure 3.4 to 3.5 for SWRF case. This particle layering is strongest in the static bed, but also apparent inside the bed-load layer, where it induces step-like variations of the granular velocity profile $\overline{u}_S$. In the transport layer, the liquid velocities are measurably faster than the granular velocities, the more so towards the top of the layer where the granular concentration drops.

Although boundaries between the three zones are not sharply defined, we can determine upper and lower limits of the bed-load layer as the loci $\tilde{z}$ and $\underline{z}$ accounting respectively for 1 % and 99 % of the granular transport rate per unit width when integrating the product $c_S\overline{u}_S$ from the free surface down. These limits are shown as dashed lines on Figure 5.2. Defining the transport layer thickness as $\delta = \tilde{z} - \underline{z}$ and the flow depth as $H = Z - \underline{z}$, we can determine various dimensionless quantities of interest. Flow and particle Reynolds numbers, respectively, can be calculated from $Re = U_L H/\nu$ and $Re_p = U_L D/\nu$, where $U_L = Q_L/(BH)$ is the depth-averaged liquid velocity. The resulting values are in the range $Re = 5000 - 12000$, and $Re_p = 1400 - 2000$, sufficiently high to guarantee turbulent, hydraulically rough flows. Likewise, we can determine the dimensionless bed-load layer thickness δ/D, dimensionless Shields stress $\hat{\tau} = \underline{\tau}/((\rho_S - \rho_L)gD)$ and ratio of fall speed to friction velocity $\omega/u_\star$, where $\underline{\tau} = \rho_L gHS$ and $u_\star = \sqrt{\underline{\tau}/\rho_L}$. The resulting values are in the range $\delta/D = 3 - 4.4$, $\hat{\tau} = 0.20 - 0.43$, and $\omega/u_\star = 2.5 - 3.6$, indicating bed-load transport far above incipient motion, with no turbulent suspension *Sumer et al.* (1996). The experimental conditions, different for each run, are provided in table format.

In addition to the mean velocities, quantities dependent on the velocity fluctuations can also be determined. Using the measured liquid velocities, we can determine the Reynolds stress

$$\tau_L = -\rho_L c_L \overline{u'_L w'_L}. \tag{5.1}$$

As shown in Figure 5.1**be** and Figure 5.2**be**, the resulting $\overline{u'_L w'_L}$ profiles (in green) approach zero at the free surface and at the base of the bed-load layer, and attain their extrema at mid-depth. Next, we estimate the kinetic energies (per unit mass) of the solid and liquid velocity fluctuations from the lateral scans using

$$k_\alpha = \frac{1}{2}\left(\overline{u'^2_\alpha} + 2\overline{w'^2_\alpha}\right), \tag{5.2}$$

where for instance $u'_\alpha = u_\alpha - \overline{u}_\alpha(y, z)$. Since the lateral scans do not measure the spanwise component $\overline{v'^2_\alpha}$, we have approximated $\overline{v'^2_\alpha} \approx \overline{w'^2_\alpha}$, as these two components have roughly the same magnitude in both granular and turbulent flows . In Figure 5.1**be** and Figure 5.2**be**, we plot the resulting profiles for k_S (red) and k_L (blue). For both runs, the liquid fluctuations (in blue) are more energetic than the granular fluctuations (in red). Although the granular fluctuations drop to zero at the base of the bed-load layer, liquid fluctuations there remain finite.

For both the mean and fluctuating velocities, signals for the liquid and granular phases thus exhibit clear differences as well as similarities. The motions of the two phases are

therefore shown to be tightly, but not perfectly coupled together.
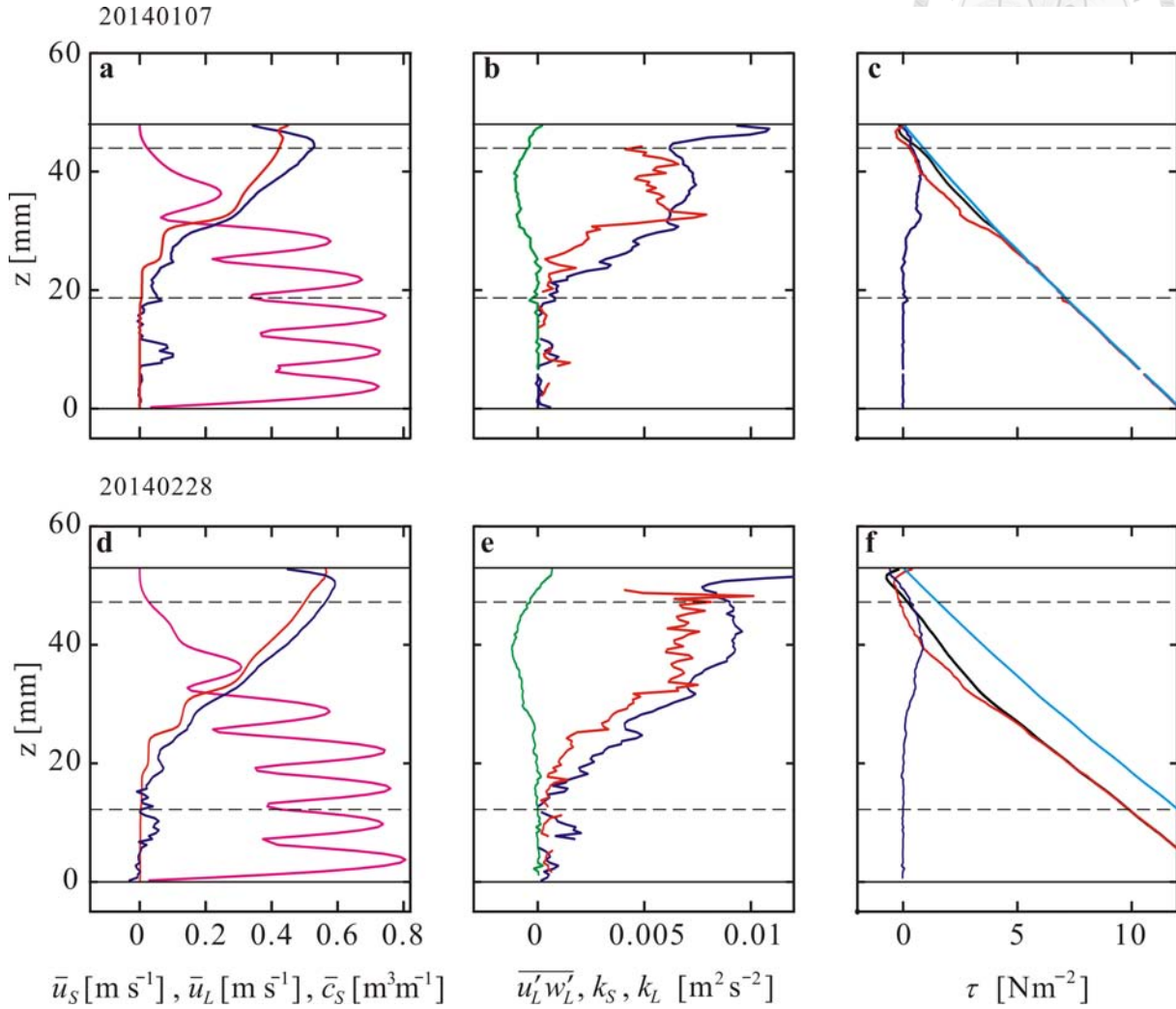
Figure 5.1 Depth profiles for two representative runs of low (**a-c**) and high (**d-f**) total discharge of SWSF case: (**a,d**) granular concentration c_S (magenta), mean solid velocity $\overline{u}_S$ (red), and mean liquid velocity $\overline{u}_L$ (blue); (**b,e**) Reynolds stress distribution $\overline{u'_L w'_L}$ (green), kinetic energy of the solid velocity fluctuations k_S (red), and kinetic energy of the liquid velocity fluctuations k_L (blue); (**c,f**) uncorrected total stress τ_T (cyan), corrected total stress τ_T (black), liquid stress τ_L (blue) and granular stress τ_S (red). Solid lines indicate the channel bottom and free surface, and dashed lines indicate the upper and lower boundaries of the bed-load layer.

The profile measurements can now be interpreted using two-phase equations expressing the momentum budget of each phase (*Anderson and Jackson*, 1967; *Drew*, 1983; *Jenkins and Hanes*, 1998; *Hsu et al.*, 2004; *Revil-Baudard and Chauchat*, 2013; *Cheng et al.*, 2018; *Gonzalez-Ondina et al.*, 2018). For this purpose, we consider steady, shallow flows and neglect variations across the channel width. Assuming that the submerged weight of the solid grains is entirely supported by granular contacts, we obtain for the liquid and granular pressure (or effective normal stress) the profiles

$$p_L(z) = \rho_L g \cos\theta (Z - z), \tag{5.3}$$

111

doi:10.6342/NTU201804057
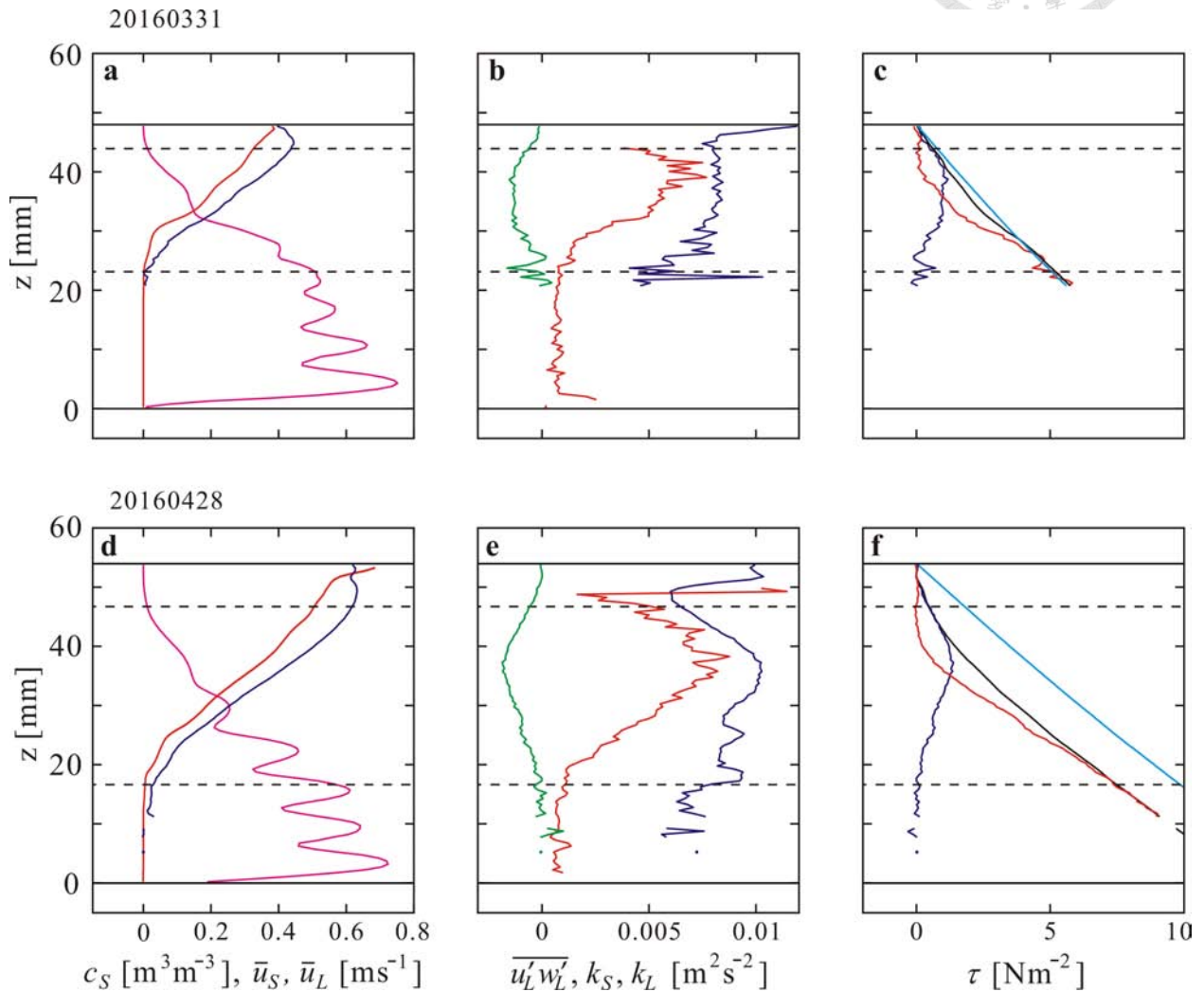
Figure 5.2 Depth profiles for two representative runs of low (**a-c**) and high (**d-f**) total discharge of SWRF case: (**a,d**) granular concentration c_S (magenta), mean solid velocity $\overline{u}_S$ (red), and mean liquid velocity $\overline{u}_L$ (blue); (**b,e**) Reynolds stress distribution $\overline{u'_L w'_L}$ (green), kinetic energy of the solid velocity fluctuations k_S (red), and kinetic energy of the liquid velocity fluctuations k_L (blue); (**c,f**) uncorrected total stress τ_T(cyan), corrected total stress τ_T (black), liquid stress τ_L (blue) and granular stress τ_S (red). Solid lines indicate the channel bottom and free surface, and dashed lines indicate the upper and lower boundaries of the bed-load layer. .

$$p_S(z) = (\rho_S - \rho_L)g\cos\theta \int_z^Z c_s(\zeta)d\zeta \,, \qquad (5.4)$$

where θ is the inclination angle of the channel, Z is the elevation of the free surface and ζ a variable of integration. For the longitudinal momentum balance, equations for the liquid and granular phases can be written (*Anderson and Jackson*, 1967; *Jackson*, 2000)

$$\rho_L c_L \left(\overline{u}_L \frac{\partial \overline{u}_L}{\partial x} + \overline{w}_L \frac{\partial \overline{u}_L}{\partial z} \right) = \rho_L c_L g \sin\theta - c_L \frac{\partial p_L}{\partial x} + \frac{\partial \tau_L}{\partial z} - f_D \,, \qquad (5.5)$$

$$\rho_S c_S \left(\overline{u}_S \frac{\partial \overline{u}_S}{\partial x} + \overline{w}_S \frac{\partial \overline{u}_S}{\partial z} \right) = \rho_S c_S g \sin\theta - \frac{\partial p_S}{\partial x} - c_S \frac{\partial p_L}{\partial x} + \frac{\partial \tau_S}{\partial z} + f_D \,, \qquad (5.6)$$

where τ_L and τ_S are respectively the liquid and granular shear stresses, and f_D the longitudinal drag force per unit volume exerted by the liquid on the grains. Because of the high Reynolds number, we neglect the viscous contribution to the liquid shear stress, which reduces to the turbulent Reynolds stress (5.1). Since the slope in the present experiments is adjusted to make the free surface parallel to the channel floor, $\partial p_L/\partial x \approx 0$. Likewise, we neglect longitudinal gradients of the granular concentration ($\partial c_S/\partial x \approx 0$), hence $\partial p_S/\partial x \approx 0$. As in *Jackson* (2000) and *Hsu et al.* (2004), we consider separately the contributions of buoyancy and drag to the force between the liquid and granular phases, and neglect other contributions. In numerical simulations, lift forces at high particle Reynolds numbers were found negligible for grains more than one particle radius away from the bed (*Lee and Balachandar*, 2017). Likewise, the added mass force associated with mean relative acceleration between the grains and liquid (see e.g. (*Geurst*, 1985)) can be neglected because the latter is one order of magnitude smaller than the convective acceleration of the mean flow. Because the flows are nearly uniform, we expected that we could likewise neglect the convective accelerations on the left-hand-sides of (5.5) and (5.6). Upon calculating these terms from the measured velocities, however, we found that they have the same order of magnitude as the right-hand-side terms, and therefore cannot be neglected.

Having measured profiles of granular concentration c_S, mean velocities $\overline{u}_\alpha$, convective accelerations $\overline{u}_\alpha \partial \overline{u}_\alpha/\partial x + \overline{w}_\alpha \partial \overline{u}_\alpha/\partial z$ and Reynolds stress τ_L, we see that all terms in Eq. (5.5) and (5.6) are known except two: the granular shear stress τ_S and the interphase drag force f_D. Adding (5.5) and (5.6), we can eliminate f_D and calculate the total shear stress $\tau_T = \tau_S + \tau_L$ by integrating the other terms from z to Z (using the stress-free boundary conditions $\tau_S = \tau_L = 0$ at the free surface). The granular shear stress can then be obtained by subtraction as $\tau_S = \tau_T - \tau_L$. Finally, we can calculate the drag force profile f_D from either (5.5) or (5.6). All principal terms of the two-phase momentum balance can therefore be determined from the present experiments.

Figure 5.1**cf** and Figure 5.2**cf** show the resulting shear stress profiles. The liquid shear stress τ_L (in blue) is the turbulent Reynolds stress (5.1) estimated from $\overline{u'_L w'_L}$. Two estimates of the total shear stress $\tau_T = \tau_L + \tau_S$ are also shown: the first profile (in cyan) is the estimate

$$\tau_T(z) = \left(\rho_L + (\rho_S - \rho_L) \int_z^Z c_S(\zeta)d\zeta \right) g\sin\theta \,, \qquad (5.7)$$

obtained upon neglecting the convective acceleration terms, and the second (in black) our corrected estimate taking convective accelerations into account. In the upper liquid layer

113

of the flow, there are very few solid particles hence we expect $\tau_S \approx 0$ and $\tau_T \approx \tau_L$. This is verified for the estimate (in black) that takes convective accelerations into account, but not for the uncorrected estimate (in cyan). Convective accelerations may also be responsible for similar discrepancies observed in previous experiments (*Revil-Baudard et al.*, 2015). By subtracting the liquid shear stress τ_L from the corrected total shear stress τ_T, finally, we can deduce the granular shear stress τ_S, plotted (in red) on Figure 5.1**cf** and Figure 5.2**cf**. It varies across the bed-load layer from zero at the top to the full value of the total shear stress at the base. Conversely, the liquid shear stress bears the total shear stress at the top, then decreases to zero at the base of the bed-load layer. Via drag, the downslope component of the liquid weight is gradually transferred to the granular phase. This has long been hypothesized to be a key feature of bed-load transport (*Bagnold*, 1956; *Hsu et al.*, 2004; *Maurin et al.*, 2016), but had not previously been verified in experiments. All results are illustrated from Figure 5.3 to 5.6 for SWSF case, Figure 5.7 and 5.8 for SWRF case.

Figure 5.3 Depth profiles of all runs for SWSF case: 1-4.

Figure 5.4 SWSF case: 5-8.

116

20140124

20140127

20140207

20140211

$\bar{u}_S [\mathrm{m\ s^{-1}}]$, $\bar{u}_L [\mathrm{m\ s^{-1}}]$, $\bar{c}_S [\mathrm{m^3 m^{-1}}]$

$\overline{u_L' w_L'}$, k_S, k_L $[\mathrm{m^2 s^{-2}}]$

τ $[\mathrm{Nm^{-2}}]$
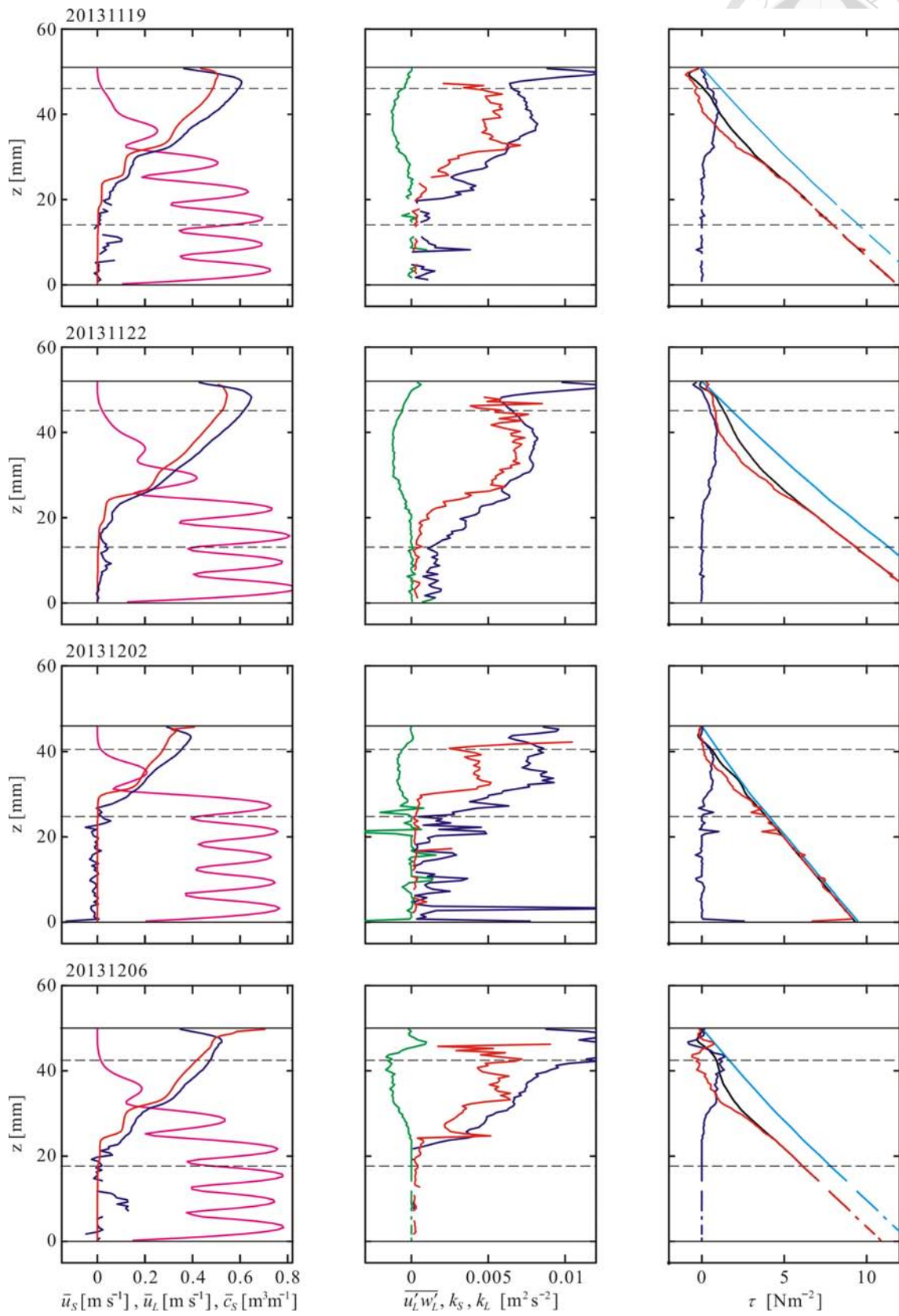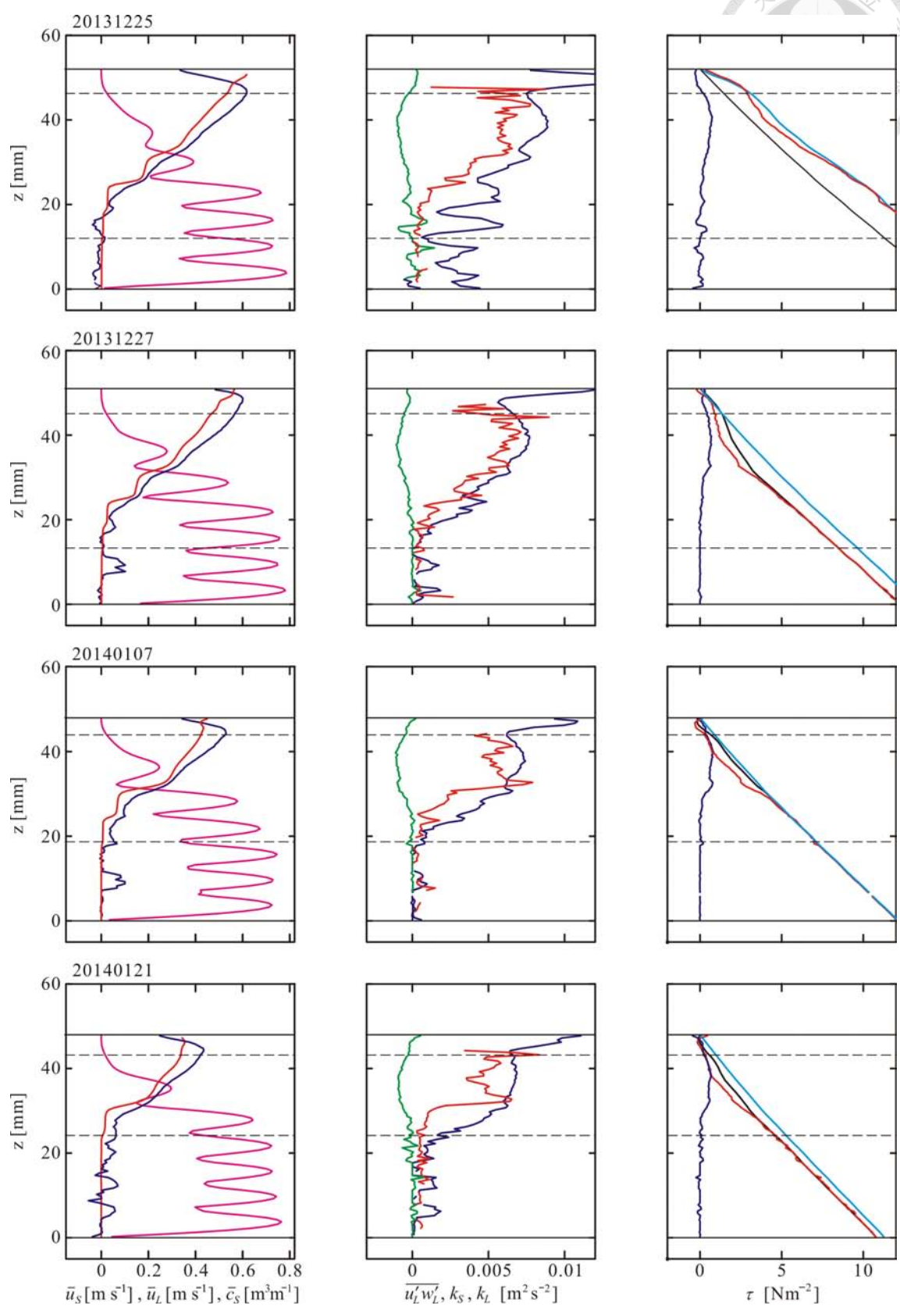
Figure 5.5 SWSF case: 9-12.
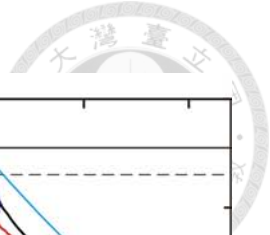
117

Figure 5.6 SWSF case: 13-15.

Figure 5.7 Depth profiles of all runs for SWRF case: 1-4.

119

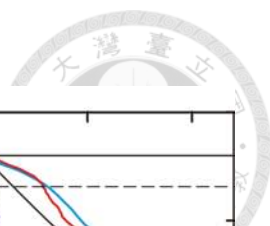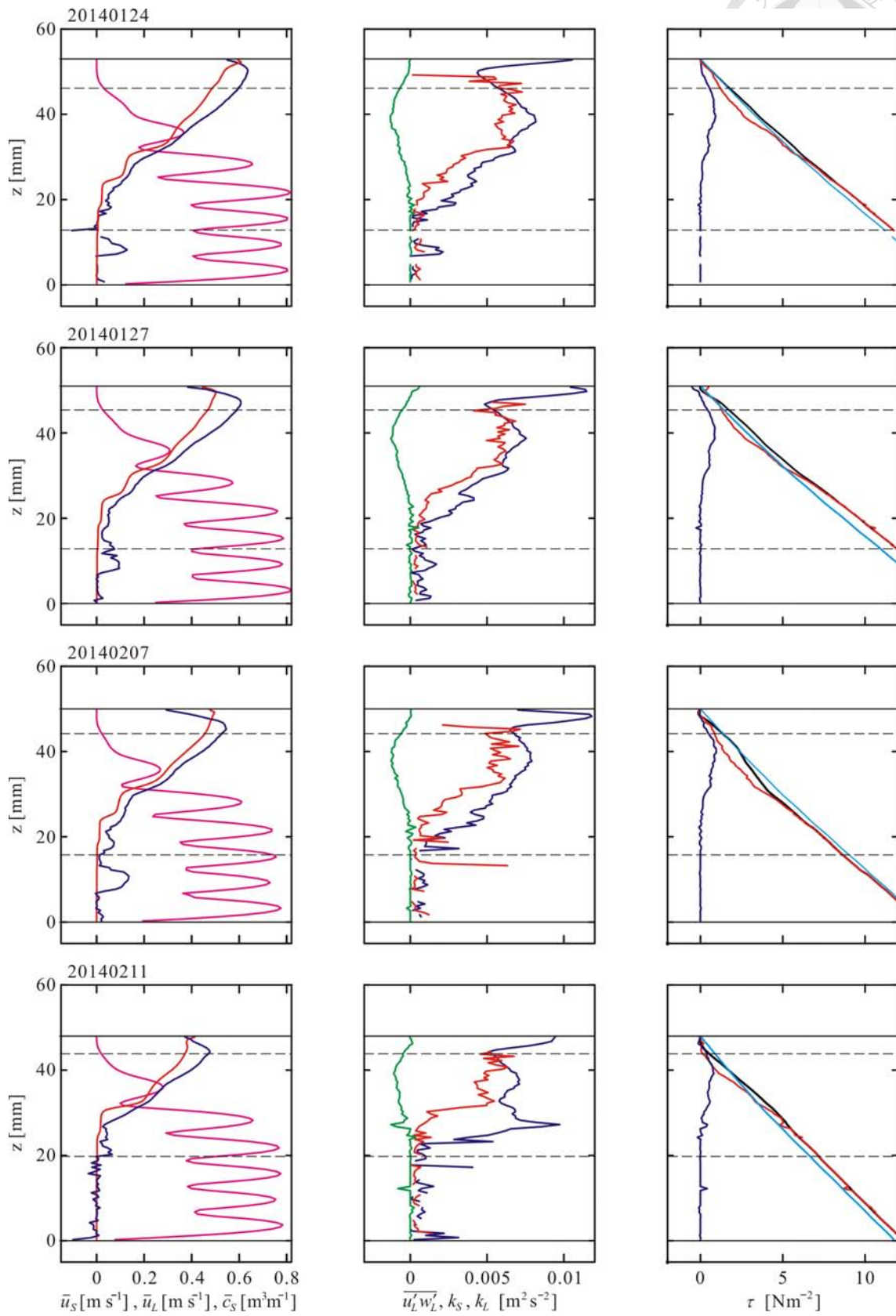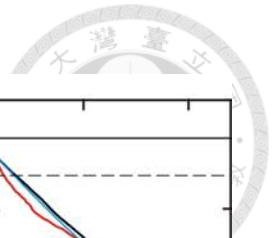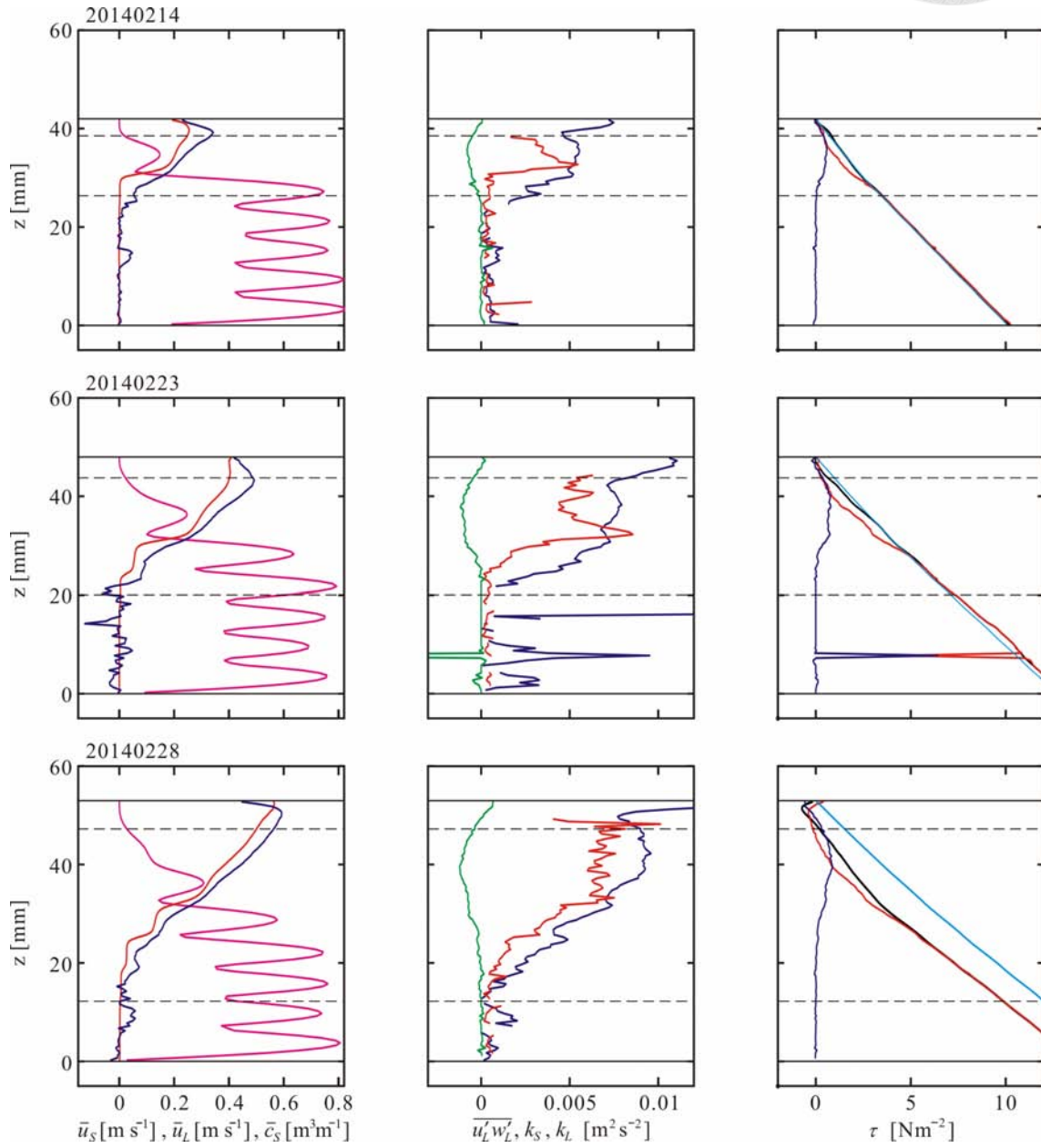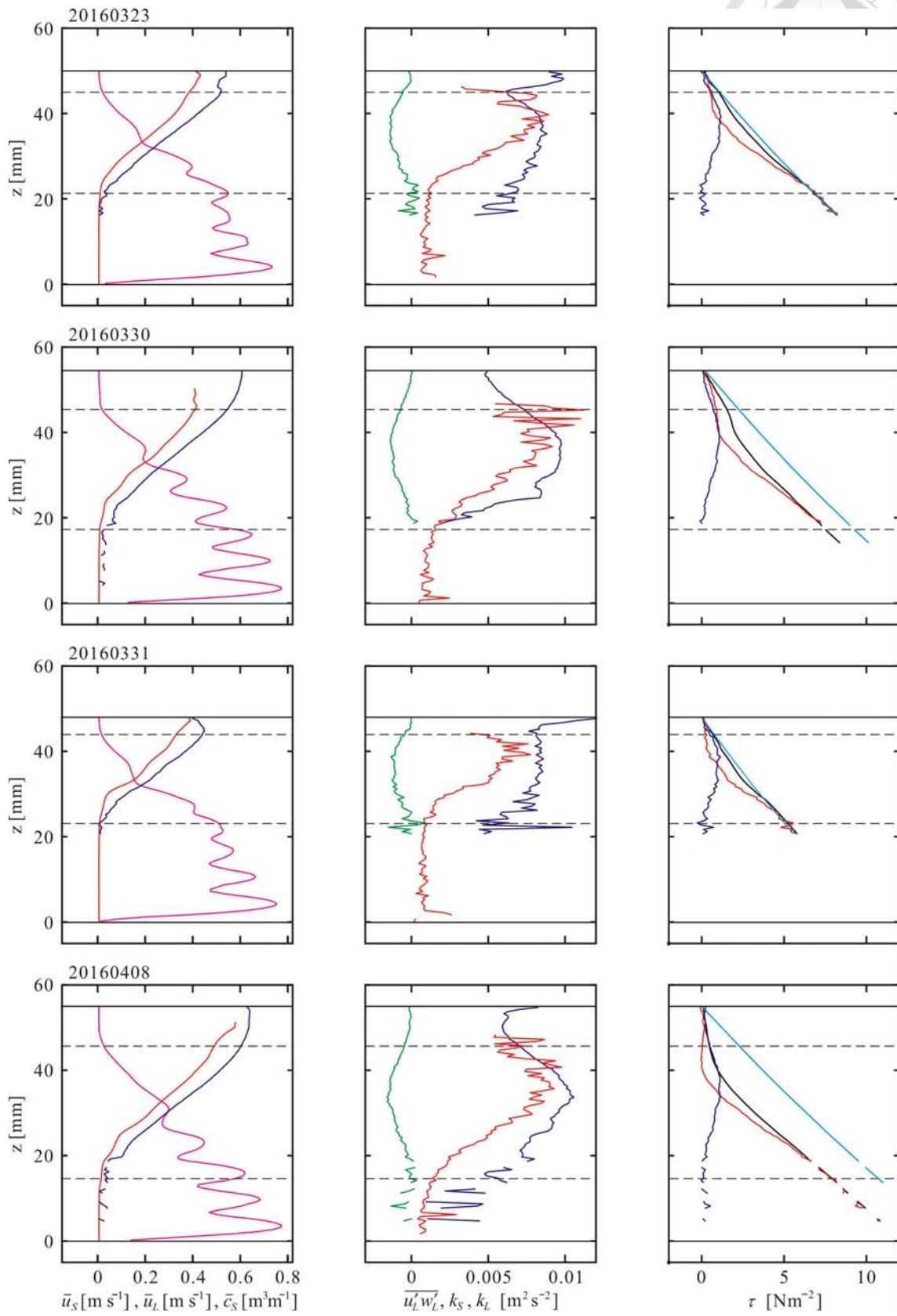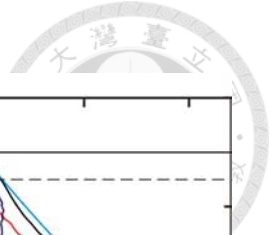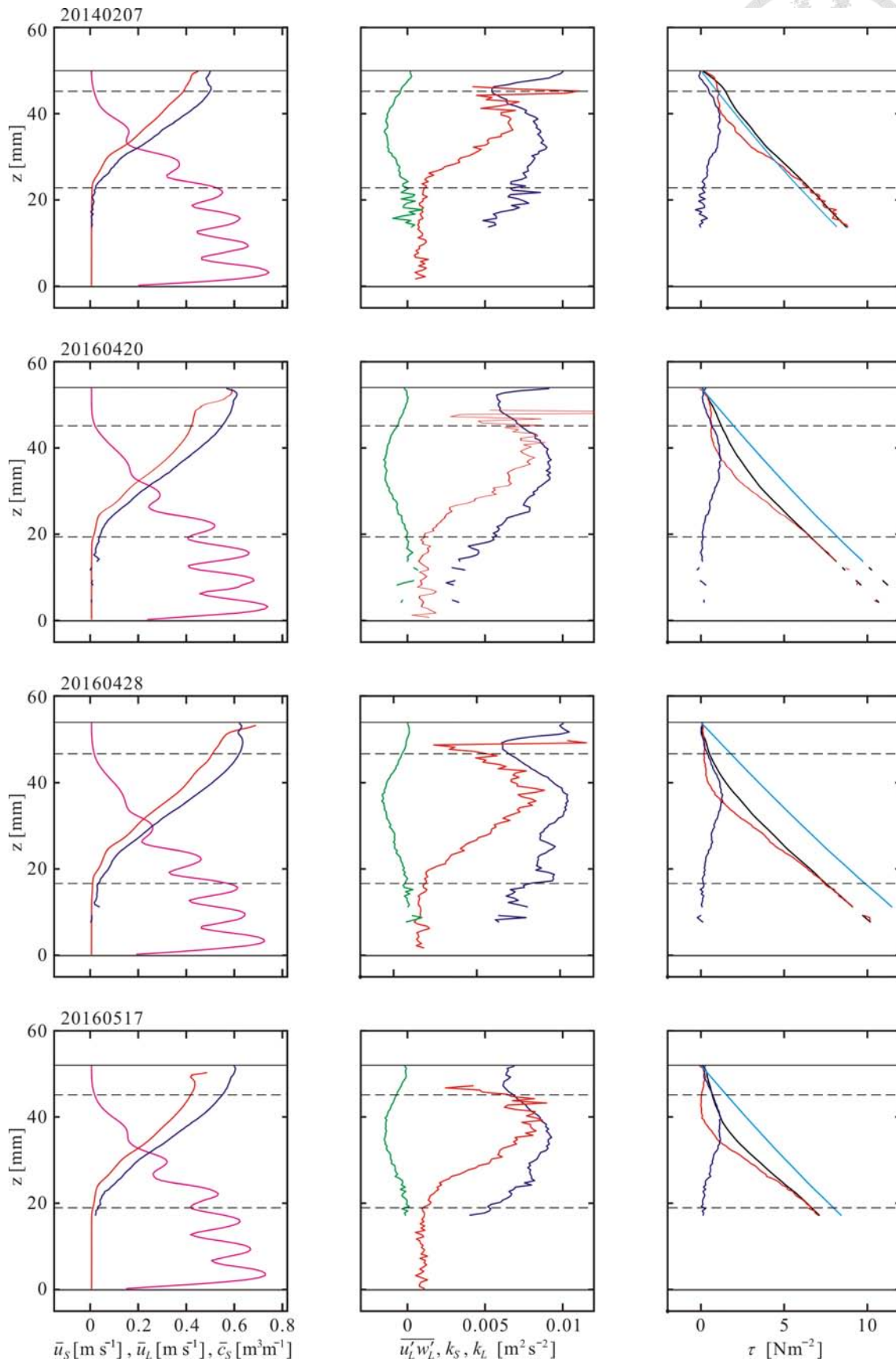Figure 5.8 SWRF case: 5-8

5.2 Stress relations

From the refractive index matched experiments, it is possible to determine profiles for the stresses and drag force. Also measured are profiles of the principal quantities they are expected to depend on, such as the granular concentration c_S, shear rates $\dot{\gamma}_\alpha = \partial \overline{u}_\alpha / \partial z$, granular temperature $T = 2/3k_S$, turbulent kinetic energy k_L, and relative velocity between the liquid and granular phases $\overline{u}_R = \overline{u}_L - \overline{u}_S$. We can therefore compare the experimentally observed relationships for the stresses and drag with constitutive laws proposed earlier for turbulent liquid-granular flows.

We compare observed relationships for the granular pressure and shear stress with relations deduced from the kinetic theory of collisional granular flows (*Jenkins and Hanes*, 1998; *Garzó and Dufty*, 1999; *Berzi and Fraccarollo*, 2015), modified as in *Armanini et al.* (2005) to take into account added mass effects. The resulting equation of state for the granular pressure, or effective normal stress, can be written

$$\hat{p}_S = \frac{p_S}{\rho_S T} = \left(c_S + 4c_S^2 g_0(c_S) \frac{1 + e_f}{2} \right) \left(1 + \frac{\rho_L}{\rho_S} a(c_s) \right) , \qquad (5.8)$$

where the dependence on granular concentration is expressed as the product of two factors. The first factor is the relation for dry granular flows derived from kinetic theory. In this factor, $g_0(c_S)$ is the radial distribution function at contact given by *Torquato* (1995), and e_f the effective coefficient of restitution for which the value $e_f = 0.6$ is recommended by *Berzi and Fraccarollo* (2015). The second factor, dependent on the liquid density, represents the influence of added mass. When granular collisions occur in a liquid, impulses produced by impacts must alter not on ly the grain velocities, but also the conjugate liquid velocities induced by granular motions (*Zenit et al.*, 1997). This effect is heightened when liquid motions are constrained by nearby grains (*Zuber*, 1964), hence the concentration-dependent added mass coefficient $a(c_S) = (1 + 2c_S)/(2(1 - c_S))$. The corresponding relation for the granular shear stress can be written

$$\hat{\tau}_S = \frac{\tau_S}{\rho_S D T^{1/2} \dot{\gamma}_S} = \frac{8J c_S^2 g_0(c_S)}{5\pi^{1/2}} \left(1 + \frac{\rho_L}{\rho_S} a(c_S) \right) , \qquad (5.9)$$

where the second factor again represents added mass effects. In the first factor, from the kinetic theory of dry granular flows, the coefficient J is given by (*Garzó and Dufty*, 1999)

$$J = \frac{1 + e_f}{2} + \frac{\pi}{32} \frac{(5 + 2(3e_f - 1)(1 + e_f)c_S g_0) (5 + 4(1 + e_f)c_S g_0)}{(24 - (1 - e_f)(11 - e_f)) c_S^2 g_0^2} . \qquad (5.10)$$

5.3 Drag force relation

We compare the drag force per unit volume f_D deduced from the experiments with those acting in porous media and fluidization cells. In contrast with these two cases, for which granular velocity fluctuations are zero or weak, in turbulent bed-load the granular fluctuations are strong and should be taken into account (*Jenkins and Hanes*, 1998; *Maurin et al.*, 2015). In a two-phase medium of granular concentration c_S, the x-component of the drag force exerted by the liquid on a single spherical grain can be estimated from (*Di Felice*, 1994)

$$F_{Dx} = \frac{1}{2} \rho_L C_D A_S (1 - c_S)^{2-\beta} v_R (u_L - u_S) , \qquad (5.11)$$

121

where $v_R = ((u_L - u_S)^2 + (v_L - v_S)^2 + (w_L - w_S)^2)^{1/2}$, $C_D = (0.63 + 4.8/Re^{1/2})^2$ is the drag coefficient for an isolated grain, $A_S = \pi D^2/4$ is the frontal area of one grain, and $\beta = 3.7 - 0.65 \exp(-(1.5 - \log Re)^2/2))$ is the exponent governing concentration dependence. To check the applicability of this empirical relation to our experimental materials, we conducted a series of seepage tests figure out.
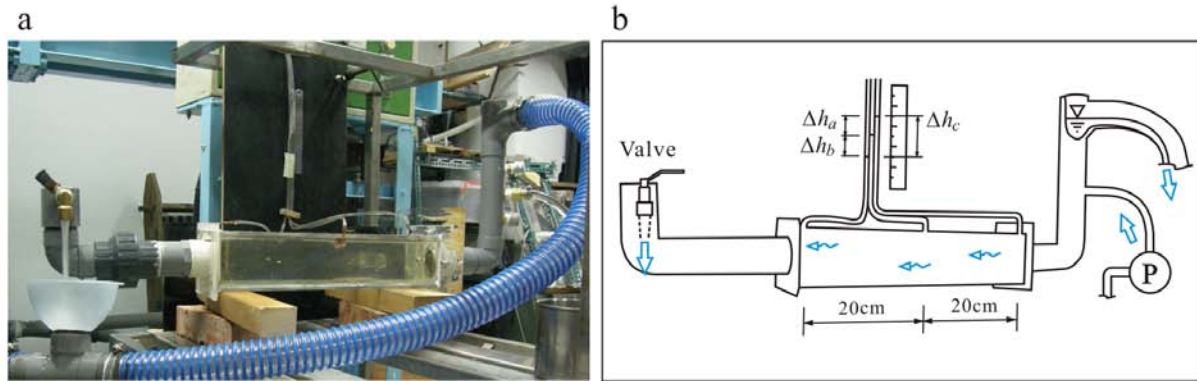
Figure 5.9 The experimental set-up for the seepage tests: **a** The set-up of the seepage test, the transparent tank ws packed with particles, and liquid flow from right side to left side;**b** three' thin tubes connected to the tank were used to monitor the total head of each locations.

This test is to verify the drag force relation developed by Di felice for the case of porous median flow. To test this relation we need to measure the flow rate and the corresponding hydraulic gradient. The experimental set-up is shown in Figure 5.9. The rectangular tank whose dimension is about 8cm x 8cm x 43cm and placed horizontally, it was filled with PMMA particles in which the resultant solid volume fraction is about 59.7%. One right side (upstream direction) of the tank a vertical gray tube connected with a pump and overflow bypass(the blue tube) provided a constant piezometric head, while on the left side we used a valve to control the flow rate in the porous median, and the valve also helped us to measure the flow rate directly.

To measure the hydraulic gradient, i, three thin tubes (3mm in diameter) were connected to the tank in upstream, midstream and downstream site with 20cm inter-distance, the tubes were fixed vertically thus we could directly read the relative piezometric head of each location. Figure 5.10 shows the variations of the piezometric heads corresponding to different flow rates.

The measurements of the tests are listed in Table 5.1, the hydraulic gradient and specific discharge are plotted in Figure 5.11, by the test data itself a clear trend could be observed, as the discharge increased, the hydraulic gradient and specific discharge relation deviated from the linear Darcy's law is also observed in the test measurements. These measurements now is ready for us to test the drag force formula we adopted. In the theory the relation of the drag force in fixed bed have been derived,

$$i = \Delta h/L = \frac{F_D}{\rho_L g V} \frac{c_S}{(1 - c_S)},\tag{5.12}$$

the pressure gradient is replace by hydraulic gradient for our needs, where F_D is the drag force exerted on a particle, V is one particle volume. the Reynolds number for porous
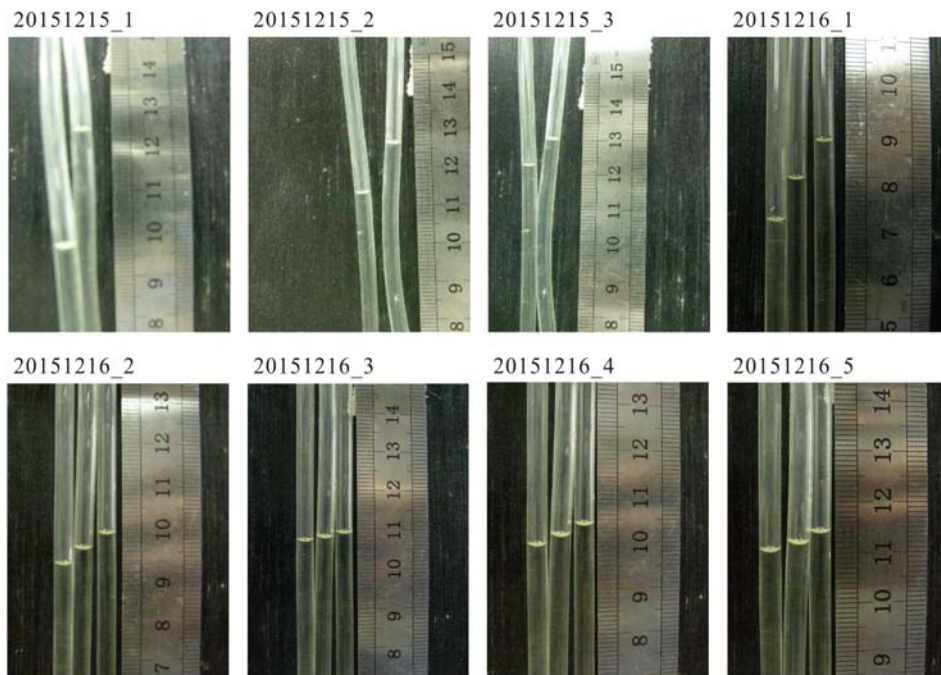
Figure 5.10 The variations of the piezometric heads of the tests.

Table 5.1 Measurements of seepage tests

test id	Q [cm³ s⁻¹]	q [cm s⁻¹]	Δh_c [cm]	Δh_a [cm]	Δh_b [cm]	$\Delta h_x/L_x$
1215_1	78.05	1.21	2.70	-	-	0.0700
1215_2	50.98	0.79	1.30	-	-	0.0325
1215_3	35.45	0.55	0.80	-	-	0.0200
1216_1	66.78	1.03	1.65	0.80	0.85	0.0413
1216_2	37.91	0.59	0.70	0.35	0.35	0.0175
1216_3	15.55	0.24	0.20	0.10	0.10	0.0050
1216_4	26.61	0.41	0.40	0.20	0.20	0.0100
1216_5	22.99	0.36	0.35	0.15	0.20	0.0087

media is defined as:

$$Re = \frac{qD}{\nu},$$

(5.13)

where

$$q = \frac{Q_L}{A_C} = (1 - c_S)u_L.$$

(5.14)

q is the specific discharge and ν is the kinematic viscosity of liquid. Using the Eq. (5.11) and (5.12) and set $u_S = 0$, the theoretical relation between hydraulic gradient and the specific discharge q could be derived explicitly, the results are plotted in Figure 5.11. The prediction (light blue line) was in good agreement with data, we confirmed this empirical law can be applied to the fixed bed experiments.
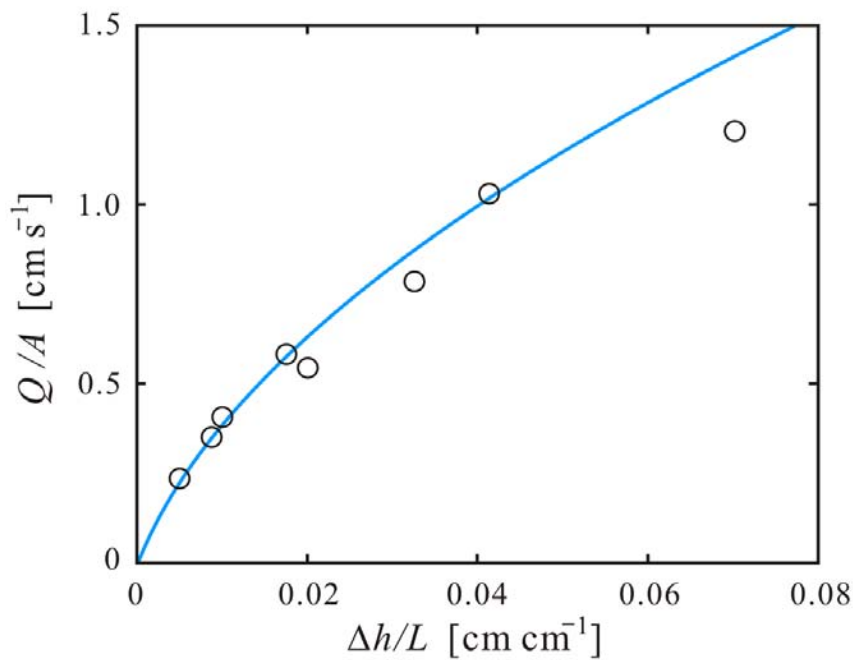
Figure 5.11 The relation of the hydraulic gradient and the specific discharge, circles are from the test measurements, and the line represents the result from the drag force theory *Di Felice* (1994).

5.4 Comparison with the bed-load experiments

Comparisons of the two granular stress relations with the two smooth-wall experimental data are shown in Figure 5.12 and 5.13. For the granular pressure p_S in **a** and granular shear stress τ_S in **b**, the data agree reasonably well with the relations Eq.(5.8) and (5.9). Some of the scatter is likely due to particle layering, observed earlier to be more pronounced at high concentrations, the scatters are shown in different degree between SWSf and SWRF. The kinetic theory relations, however, overestimate the data at low concentrations (for the shear stress) and conversely underestimate the data at high concentrations (for both the pressure and shear stress). This suggests that streaming and binary collisions, the two mechanisms assumed by kinetic theory, do not fully describe immersed granular behavior in the dilute upper zone, where particles saltate, or in the dense basal zone where contact chains may connect multiple grains. For both relationships, agreement is slightly improved by taking added mass effects into consideration (solid lines), as compared with curves calculated without added mass effects (dashed lines).
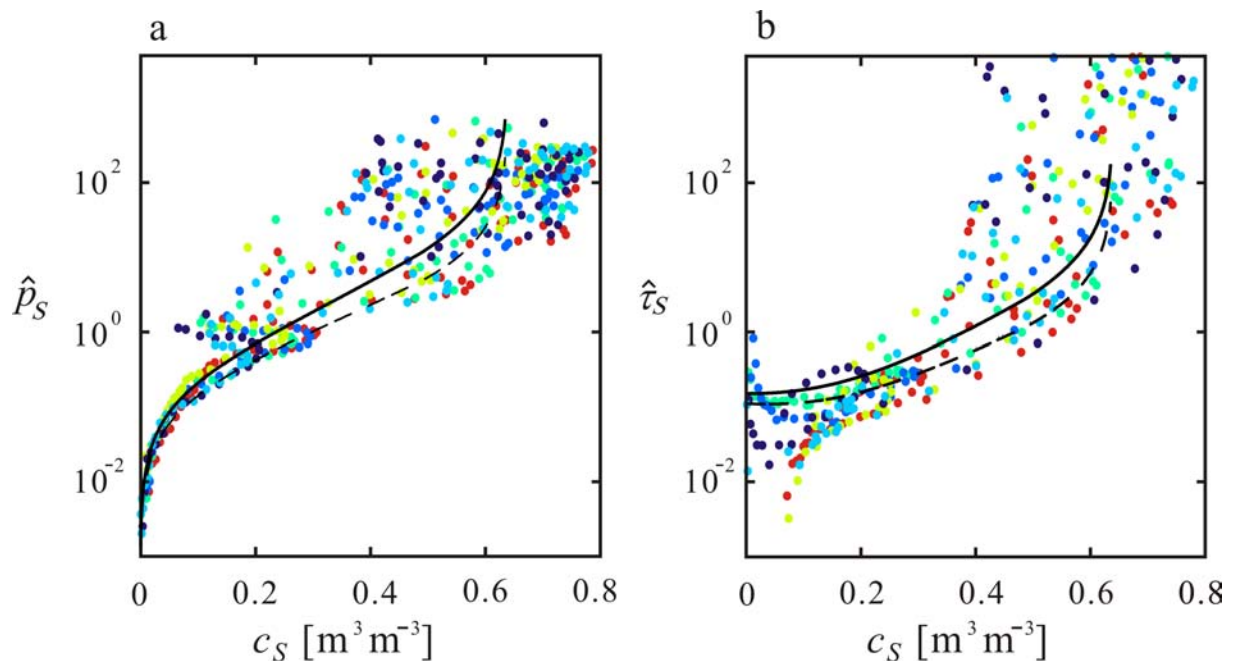
Figure 5.12 Granular stresses data for selected runs in SWSF (distinguished by color) compared with the constitutive relations: **a** dimensionless granular pressure $\hat{p}_S$ compared with kinetic theory relation Eq. (5.8) with (solid line) and without (dashed line) added mass effect; **b** dimensionless granular shear stress $\hat{\tau}_S$ likewise compared with kinetic theory relation.

Figure 5.13 Granular stresses data for all runs in SWRF (distinguished by color) compared with the constitutive relations: **a** dimensionless granular pressure $\hat{p}_S$ compared with kinetic theory relation Eq. (5.8) with (solid line) and without (dashed line) added mass effect; **b** dimensionless granular shear stress $\hat{\tau}_S$ likewise compared with kinetic theory relation.
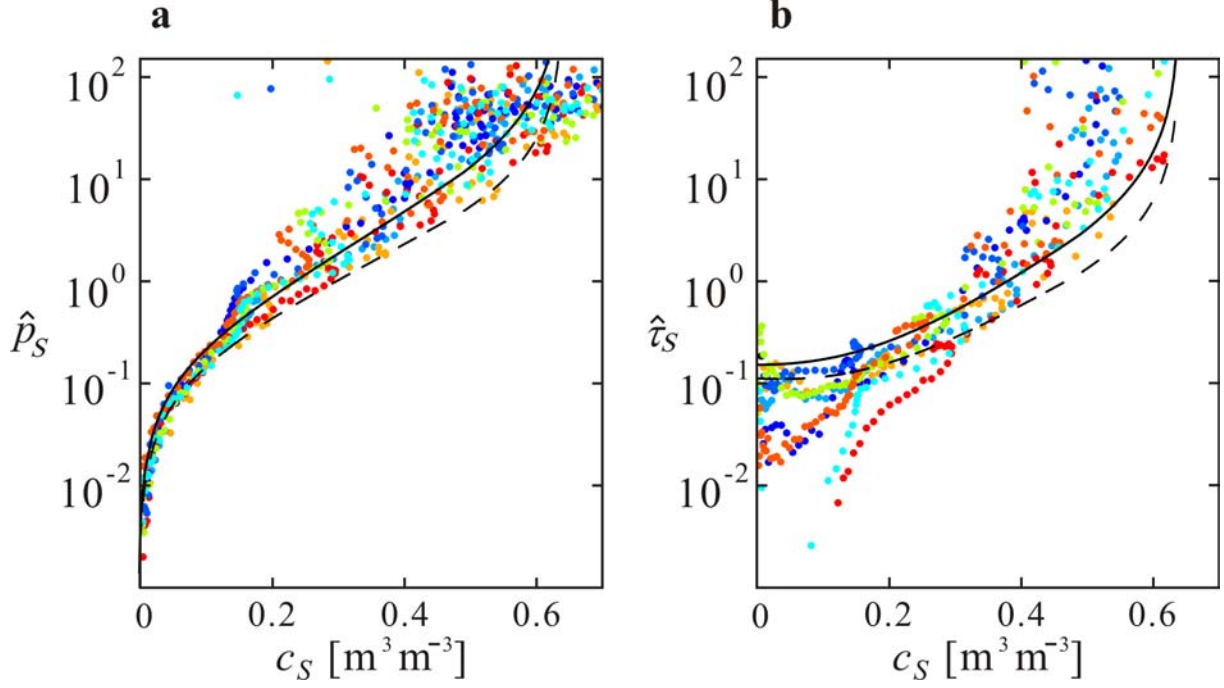
Next, we compare measurements of the Reynolds stress τ_L with the mixing length relation *Berzi and Fraccarollo* (2015). In Figure 5.14**a** and 5.15**a**, we examine a possible concentration-dependence by plotting the dimensionless ratio $\hat{\ell}_m = \ell_m/D$ against the concentration c_S. In contrast with the relation proposed by *Berzi and Fraccarollo* (2015) (dashed line), the present data are found to vary little with concentration, and to be well approximated by the constant ratio $\ell_m/D \approx 0.2$ (continuous line). This falls within the range suggested by *Wiberg and Smith* (1991), indicating that wake effects dominate the vertical momentum balance within the transport layer.

With confidence on the empirical drag law after validation test, for simplicity, we approximate the Reynolds number Re in these drag formulas by the terminal Reynolds number $Re_t = \omega D/\nu$. The mean longitudinal drag force per unit volume experienced in turbulent bed-load can therefore be written

$$f_D = \frac{c_S}{V_S}\overline{F}_{Dx} = \hat{f}_D(c_S)\rho_L D^{-1}\overline{v_R(u_L - u_S)}, \qquad (5.15)$$

where $V_S = \pi D^3/6$ is the volume of one grain, $\hat{f}_D(c_S) = 3/4 C_D c_S (1 - c_S)^{2-\beta}$ is a dimensionless function retaining the concentration dependence, and $\overline{v_R(u_L - u_S)}$ represents the influence of the relative velocity between the liquid and solid phases. To calculate this influence, we assume that granular velocity fluctuations are isotropic and uncorrelated, and neglect liquid velocity fluctuations. Taylor expansion to second order with respect to the mean (without fluctuations) then yields the approximation

$$\overline{v_R(u_L - u_S)} \approx \left(|\overline{u}_L - \overline{u}_S| + \frac{2T}{|\overline{u}_L - \overline{u}_S|}\right)(\overline{u}_L - \overline{u}_S), \qquad (5.16)$$

126

hence the granular temperature T increases the mean drag force. The resulting relationship is compared with the experimental data on Figure 5.14 and 5.15**b**. Although some scatter is apparent, the data deduced from all experiments agree well with the expected relationship (solid line). Without accounting for the granular temperature in (5.16), the drag force would be significantly underestimated. For comparison, we also plot in Figure 5.14 and 5.15**b** the drag forces (triangles) determined by *Teng* (2003) from fluidization cell experiments carried out with the same solid and liquid materials, with T set to zero in this case. Provided that granular temperature is taken into account, we find that drag in turbulent bed-load satisfies the same empirical function as fluidization cell flows.

Figure 5.14 Liquid stress and drag force data for selected runs in SWSF (distinguished by color) compared with the constitutive relations: **a** dimensionless turbulent mixing length $\hat{\ell}_m$ compared with the constant approximation $\hat{\ell}_m \approx 0.2$ (solid line), and the relation proposed by *Berzi and Fraccarollo* (2015) (dashed line);**b** dimensionless drag force $\hat{f}_D$ compared with relation (5.15) (solid line) and fluidization cell data (triangles).
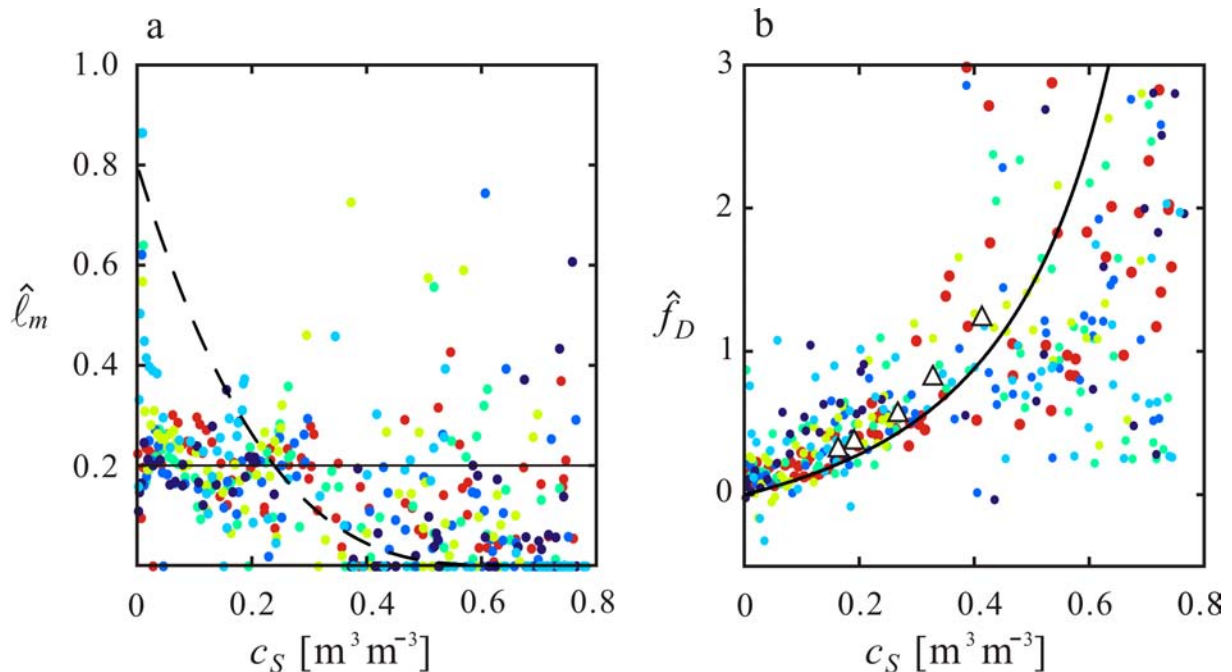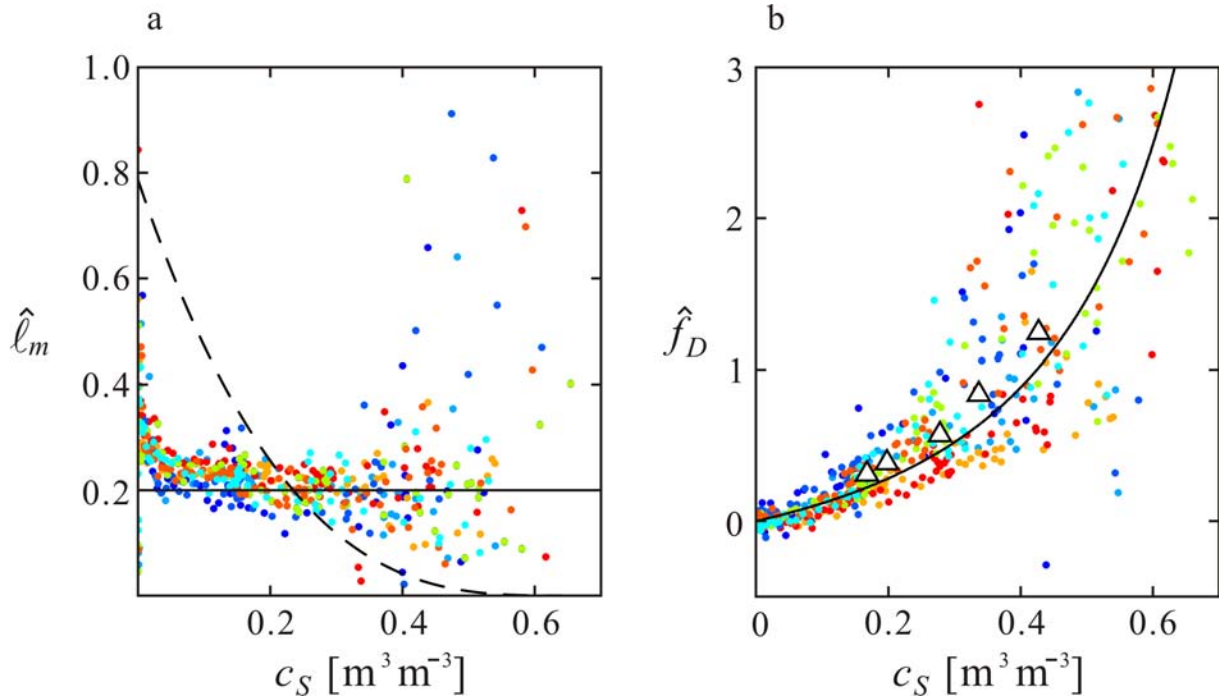
Figure 5.15 Liquid stress and drag force data for all runs in SWRF (distinguished by color) compared with the constitutive relations: **a** dimensionless turbulent mixing length $\hat{\ell}_m$ compared with the constant approximation $\hat{\ell}_m \approx 0.2$ (solid line), and the relation proposed by *Berzi and Fraccarollo* (2015) (dashed line);**b** dimensionless drag force $\hat{f}_D$ compared with relation (5.15) (solid line) and fluidization cell data (triangles).

5.5   Conclusion

In this Chapter, we used the maps of smooth wall experiments to obtained the depth profiles, we found that the convective acceleration appeared in experiments and can't be neglect. Take the convective acceleration term into account, we determined each terms in the two dimensional, steady state momentum equations of two phases, deduced the depth profiles of granular pressure, solid shear stress and liquid shear stress. By comparing the granular stresses with the kinetic theory, it shows in good agreement which is confirmed that the granular pressure which is created by grain collisions could support the submerged weight of the solid grains in turbulent flow without the effect of turbulence or lift force exerted by liquid. For the solid shear stress it could be also described by kinetic theory.

For the liquid stress, the Reynold stress were dominant and it could be scaled by grain diameter, suggesting that the wake effect dominate in the transport layer. For drag force, we adpoted the empirical law derived by *Di Felice* (1994) and used the refractive-index-matched materials to verify the law, from the fludization cell experiments and the seepage tests we confirmed the applicability of this relation, and we found out that to apply this relation to the turbulent bed-load flow, the effect of granular temperature must be taken into consideration, the velocity agitations in solid phase increase the drag between liquid and solid.

As the comparisons presented in this Chapter, we confirmed that for steady state tur-

bulent bed-load transport, and with Reynolds number range 5000-12000, the stresses of the turbulent bed-load flow could be described by the constitutive relations of the kinetic theory. We also found that the drag force relation derived from fixed pack and fluidization cell could be applied to turbulent bed-load if the contribution from solid velocity fluctuation was considered.
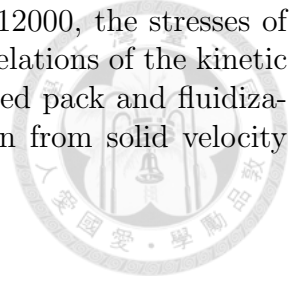
Appendix: Derivation the relation of drag force with granular temperature

The drag force of a particle in steady, unidirectional, two-phase flow can be simplified as the multiplication of a function of the relative velocities and a function of the other parameters.

$$F_D = f(\rho_L, d, c_S, \omega_T, Re_p)g(\mathbf{u_R}, u_S) = \frac{1}{2}\rho_L A_S C_D |\mathbf{u_R}| (\bar{u}_L - u_S) \tag{5.17}$$

where A_S is the cross-sectional area of a particle, C_D is the drag coefficient determined by the solid fraction, the liquid viscosity, the terminal velocity and the shape of the particle, $|\mathbf{u_R}|$ is the relative speed which is defined as $|\mathbf{u_R}| = \sqrt{(\bar{u}_L - u_S)^2 + (\bar{v}_L - v_S)^2 + (\bar{w}_L - w_S)^2}$, we use the Lagrangian solid velocities here to include the effect of solid velocity fluctuation, and $\bar{u}_L - u_S$ is the relative velocity in stream-wise direction.

Supposing u_S, v_S, w_S be the normal random variables which are mutually independent, then the solid velocities are expressed as $u_S = N[\bar{u}_S, \sigma_u]$, $v_S = N[\bar{v}_S, \sigma_v]$, $w_S = N[\bar{w}_S, \sigma_w]$, where the $\bar{u}_S$, $\bar{v}_S$, $\bar{w}_S$ are the means and σ_u, σ_v, σ_w are the standard deviations. $\bar{v}_L$, $\bar{w}_L$ and $\bar{v}_S$, $\bar{w}_S$ equal to zero because of the unidirectional flow, let the function $g(u_S, v_S, w_S) = |\mathbf{u_R}| (\bar{u}_L - u_S)$, we can estimate the expectation of $g(u_S, v_S, w_S)$ by the means and the variances of the solid velocities and average liquid velocities.

$$E[g(u_S, v_S, w_S)] \approx (\bar{u}_L - \bar{u}_S)^2 + \frac{1}{2}[2\sigma_u^2 + \sigma_v^2 + \sigma_w^2] \tag{5.18}$$

we assume the variances are approximately the same, $\sigma_u^2 = \sigma_v^2 = \sigma_w^2 = \sigma_S^2$, and by the definition of granular temperature.

$$T = \frac{1}{3}(\langle u_s'^2 \rangle + \langle v_s'^2 \rangle + \langle w_s'^2 \rangle) = \frac{1}{3}(\sigma_u^2 + \sigma_v^2 + \sigma_w^2) = \sigma_S^2 \tag{5.19}$$

then the expectation of $g(u_S, v_S, w_S)$ can be expressed as the function of mean liquid velocities, mean solid velocities and granular temperature.

$$E[g(u_S, v_S, w_S)] \approx (\bar{u}_L - \bar{u}_S)^2 + 2T \tag{5.20}$$

Chapter 6

Conclusion

To increasing our understanding for turbulent bed-load transport, we used the experimental method to study the phenomena under idealized condition: steady state and nearly uniform turbulent flow with the identical solid spheres transported inside. To make it more idealized, we use the refractive index-matched solid and liquid combination to investigate the internal flow structure. Three different channel boundaries were applied to the experiments to see how the flow responds to these changes. Although it is more complex to deal with the para-cymene and PMMA grains than water-opaque grain combination, there is no problem for RIM materials to do the successful steady state turbulent bed-load experiments. The uniform flow condition was failed to achieve for the reason of the limited length of our channel. The measurements during experiment yields reasonable results, for measurements of slope and outlet discharge, original methods were modified to obtain the better results. The characteristic tests also gives us the basic properties of solid and liquid which can be use for numerical and theoretical modelling.

We also introduce the experimental set-up and procedures for refractive-index -matched experiments, the steps and cautions were explained and mentioned. Although it is more complex to deal with the para-cymene and PMMA grains than water-opaque grain combination, now it seems plausible for RIM materials to do something more complex. The uniform flow condition was failed to achieve for the reason of the limited length of our channel. The steady re-circulation of solid grains was achieved by jet entrainment mechanism. it was verified again that the temperature of the mixture is crucial to the index matching condition, in our case is about 17°C. The uniform flow condition was achieved by changing channel slope, since the variation of the slope is little (1°–2°), checking the uniform condition by ruler may not as accurate as we expected. We measured the channel slope, flow depth and the outlet discharge for solid and liquid during the experiments, these data were used to verify or check the data obtained from imaging analysis. A series of tests were also performed to obtained the basic properties of both grains and liquid, the data were not only used for the turbulent bed-load experiment itself, but also be used for the numerical modelling or theory verification.

In the aspect of imaging analysis, we proposed a new approach to measure the internal flow of the refractive-index-matched solid-liquid mixture, based on the combination of transverse and longitudinal laser scanning. We applied the two dimensional particle tracking velocimetry to capture the motion of solid and liquid by transverse scans, acquired two dimensional velocity over a three dimensional volume, different masks were

developed and applied to reduce the wrong data captured. By identifying grain crossing events on the longitudinal scan, it is possible to deduce the 3 dimensional velocities and spatial/temporal distributions over scanned volume, obtaining the accurate solid fraction distribution, both algorithm is automatic. As shown in results, over 10^4 data of solid and 10^5 data of liquid were obtained for one run. with large number of data, we used phase-averaging method to calculate the averaged maps of velocities and solid fraction with sub-grain resolution, The volumetric discharge integrated from the maps were compared with measurement at outlet and in good agreement. However the under-estimated velocity were found around the vertical cylinders in RWRF, this remind us that the refractive index could be different for the objects made of the same material, but be manufactored by different process.

From these flow maps, we investigate the relationship of bed-load transport rate with variables, the solid and total discharge maps were used to define different domains of transport. integration the different physical quantities over those domains to deduce these map to the factors called outcome variables for three channel boundaries. We show that the outcome variables, C_S, U_S and A_B were scaled with bed-load transport rate Q_S in the same manner that followed Eq. (4.16). The dimensional analysis was applied to these outcome variables and compared with two dimensioless parameters: Mobility parameter $\hat{\Theta}$ and Shields number $\hat{\tau}$, for all three channel boundaries, the outcome variables showed its relationship with both Mobility parameter and Shields number having the power of 0.5, and for the dimensionless discharge $\hat{Q}_S$, the power was about 1.5.

To clarify the principle contributions to the momentum balance of each phase, nearly two dimensional flow experiments were selected to obtained the depth profiles. We found that the convective acceleration appeared in experiments and can't be neglect. Take the convective acceleration term into account, we determined each terms in the two dimensional, steady state momentum equations of two phases, deduced the depth profiles of granular pressure, solid shear stress and liquid shear stress. By comparing the granular stresses with the kinetic theory, it shows in good agreement which is confirmed that the granular pressure which is created by grain collisions could support the submerged weight of the solid grains in turbulent flow without the effect of turbulence or lift force exerted by liquid. For the solid shear stress it could be also described by kinetic theory.

For the liquid stress, the Reynold stress were dominant and it could be scaled by grain diameter, suggesting that the wake effect dominate in the transport layer. For drag force, we adopted the empirical law derived by *Di Felice* (1994) and used the refractive-index-matched materials to verify the law, from the fludization cell experiments and the seepage tests we confirmed the applicability of this relation, and we found out that to apply this relation to the turbulent bed-load flow, the contribution from the granular velocity fluctuations must be taken into consideration, this effect increased the drag force between liquid and solid. As the comparisons resented in last Chapter, we confirmed that the stresses of the turbulent bed-load flow could be described by the constitutive relations of the kinetic theory, and we could decompose the contributions of each phase using continuum two phase flow theory.

Bibliography

Allen, B., and Kudrolli, A. (2017). Depth resolved granular transport driven by shearing fluid flow. *Phys. Rev. Fluids* 2, 024304.

Ancey, C., Davison, A. C., Böhm, T., Jodeau, M., and Frey, P. (2008). Entrainment and motion of coarse particles in a shallow water stream down a steep slope. *J. Fluid Mech.* 595, 83–114.

Anderson, T. B., and Jackson, R. (1967). Fluid mechanical description of fluidized beds. Equations of motion. *Ind. Engng Chem. Fundam.* 6, 527–539.

Armanini, A., Capart, H., Fraccarollo, L., and Larcher, M. (2005). Rheological stratification in experimental free-surface flows of granular-liquid mixtures. *J. Fluid Mech.* 532, 269–319.

Asano, T. (1995). Sediment Transport under Sheet-Flow Conditions. *J. Waterway, Port, Coastal, Ocean Eng.* 121, 239–246.

Aussillous, P., Chauchat, J., Pailha, M., Médale, M., and Guazelli, É. (2013). Investigation of the mobile granular layer in bedload transport by laminar shearing flows. *J. Fluid Mech.* 736, 594–615.

Bagnold, R. A. (1956). The flow of cohesionless grains in fluids. *Philos. Trans. R. Soc. A* 249, 235–297.

Bareš, V., Zrostlík, S., Picek, T., Krupička, J., and Matoušek, V. (2016). On local velocity measurement in gravity-driven flows with intense bedload of coarse lightweight particles. *Flow Meas. Inst.* 51, 68–78.

Berzi, D., and Fraccarollo, L. (2015). Turbulence locality and granularlike fluid shear viscosity in collisional suspensions. *Phys. Rev. Lett.* 115, 194501.

Björk, Å. (1996). Numerical methods for least square problems. *SIAM*, Philadelphia.

Böhm, T., Frey, P., Ducottet, C., Ancey, C., Jodeau, M., and Reboud, J. L. (2006). Two-dimensional motion of a set of particles in a free surface flow with image processing. *Exp. Fluids* 41, 1–11

Brodu, N., Dijksman, J. A., and Behringer, R. P. (2015). Spanning the scales of granular materials through microscopic force imaging. *Nat. Commun.* 6, 6361

Burger, W., and Burge, M. J. (2008). *Digital Image Processing.* Berlin, Springer.

Campbell, C. S. (1989). The stress tensor for simple shear flows of a granular material. *J. Fluid Mech.* 203, 449–473.

Capart, H., and Fraccarollo, L. (2011). Transport layer structure in intense bed-load. *Geophys. Res. Lett.* 38, L20402.

Capart, H., Hung, C.-Y., and Stark, C. P. (2015). Depth-integrated equations for entraining granular flows in narrow channels. *J. Fluid Mech.* 765–R4

Capart, H., Young, D.-L., and Zech, Y. (2002). Voronoï imaging methods for the measurement of granular flows. *Exp. Fluids* 32, 121–135

Cheng, Z., Hsu, T.-J., and Chauchat, J. (2018). An Eulerian two-phase model for steady sheet flow using large-eddy simulation methodology. *Adv. Water Resour.* 111, 205–223.

Chi, T.-A. (2007). Laser halo measurements of solid-liquid two-phase flows. MSc thesis, National Taiwan University, Taiwan

Chou, H.-T., and Lee, C.-F. (2011). Falling process of a rectangular granular step. *Granul. Matter* 13, 39–223.

Cui, M. M., and Adrian, R. J. (1997). Refractive index matching and marking methods for highly concentrated solid-liquid flows. *Exp. Fluids* 22, 261–264

Di Felice, R. (1994). The voidage function for fluid-particle interaction systems. *Int. J. Multiphase Flow* 20, 153–159.

Dijksman, J. A., Rietz, F., Lörincz, K. A., van Hecke, M., and Losert, W. (2012). Refractive index matched scanning of dense granular materials. *Rev. Sci. Inst.* 83, 011301.

Dijksman, J. A., Brodu, N., and Behringer, R. P. (2017). Refractive index matched scanning and detection of soft particles. *Rev. Sci. Inst.* 88, 051807.

Drew, D. A. (1983). Mathematical modeling of two-phase flow. *Ann. Rev. Fluid Mech.* 15, 261–291.

Douxchamps, D. (2004). Multidimensional Photogrammetry of Short-Lived Events. PhD Thesis, Université Catholique de Louvain, Louvain-la-Neuve, Belgium.

Foerster, S. F., Louge, M. Y., Chang, H., and Allia, K. (1994). Measurements of the collision properties of small spheres. *Phys. Fluids* 6, 1108.

Fraccarollo, L., Larcher, M., and Armanini, A. (2007). Depth-averaged relations for granular-liquid uniform flows over mobile bed in a wide range of slope values. *Granul. Matter* 9, 145–157.

Fredsøe, J., and Deigaard, R. (1992). *Mechanics of Coastal Sediment Transport.* Singapore, World Scientific.

Frey, P., and Church, M. (2009). How river beds move. *Science* 325, 1509–1510.

Frey, P. (2014). Particle velocity and concentration profiles in bedload experiments on a steep slope. *Earth Surf. Process. Landf.* 39, 646–655.

Garzó, V., and Dufty, J. W. (1999). Dense fluid transport for inelastic hard spheres. *Phys. Rev.E* 59, 5895–5911.

Geurst, J. A. (1985). Virtual mass in two-phase bubbly flow. *Physica A* 129, 233–261.

Gladden, L. F., Akpa, B. S., Anadon, L. D., Heras, J. J., Holland, D. J., Mantle, M. D., Matthews, S., Mueller, C., Sains, M. C., and Sederman, A. J. (2006). Dynamic MR imaging of single- and two-phase flows. *Chem. Eng. Res. Des.* 84, 272–281.

Gonzalez-Ondina, J. M., Fraccarollo, L., and Liu, P. L.-F. (2018). Two-level, two-phase model for intense, turbulent sediment transport. *J. Fluid Mech.* 839, 198–238.

Haam, S. J., Brodkey, R. S., Fort, I., Klaboch, L., Placnik, M., and Vanecek, V. (2000). Laser Doppler anemometry measurements in an index of refraction matched column in the presence of dispersed beads? Part I. *Int J Multiphase Flow* 26, 1401–1418.

Houssais, M., Ortiz, C. P., Durian, D. J., and Jerolmack, D. J. (2015). Onset of sediment transport is a continuous transition driven by fluid shear and granular creep. *Nature Comm.* 6, 6527.

Hsu, T.-J., Jenkins, J. T., and Liu, P. L.-F. (2004). On two-phase sediment transport: sheet flow of massive particles. *Proc. R. Soc. Lond. A* 460, 2223–2250.

Hsu, H.-C., and Capart, H. (2007). Enhanced upswing in immersed collisions of tethered spheres. *Phys. Fluids* 19, 101701.

Huang, A. Y. L., Huang, M. Y. F., Capart, H., and Chen, R.-H. (2008). Optical measurements of pore geometry and fluid velocity in a bed of irregularly packed spheres. *Exp. Fluids* 45, 309–321.

Ikeda, T., and Durbin, P. A. (2007). Direct simulations of a rough-wall channel flow. *J. Fluid Mech.* 571, 235–263.

Jackson, R. (2000). *The Dynamics of Fluidized Particles.* Cambridge, Cambridge University Press.

Jähne, B. (1995). *Digital image processing.* Springer, Berlin.

Jenkins, J. T., and Hanes, D. M. (1998). Collisional sheet-flow of sediment driven by a turbulent fluid. *J. Fluid Mech.* 370, 29–52.

Konagai, K., Tamura, C., Rangelow, P., and Matsushima, T. (1992). Laser-aided tomography: a tool for visualization of changes in the fabric of granular assemblage. *Struct. Dyn./Earthq. Eng.* 9, 193–201, Japan Soc. of Civil Eng..

Lanckriet, T., Puleo, J. A., Masselink, G., Turner, I. L., Conley, D., Blenkinsopp, C., and Russell, P. (2014). Comprehensive field study of swash-zone processes. II: Sheet flow sediment concentrations during quasi-steady backwash. *J. Waterway, Port, Coastal, Ocean Eng.* 140, 29–42

Larcher, M., and Jenkins, J. T. (2013). Segregation and mixture profiles in dense, inclined flows of two types of spheres. *Phys. Fluids.* 25, 113301.

Lee, H., and Balanchandar, S. (2017). Effects of wall roughness on drag and lift forces of a particle at finite Reynolds number. *Int. J. Multiphase Flow* 88, 116–132.

Lee,C.-H, and Huang, C.-J. (2012). Kinetic-theory-based model of dense granular flows down inclined planes. *Phys. Fluids* 24, 073303.

Matousek, V., Krupicka, J., Picek, T. (2013). Validation of transport and friction formulae for upper plane bed by experiments in rectangular pipe. *J. Hydrol. Hydromech.* 61, 120–125.

Maurin, R., Chauchat, J., Chareyre, B., and Frey, P. (2015). A minimal coupled fluid-discrete element model for bedload transport. *Phys. Fluids* 27, 113302.

Maurin, R., Chauchat, J., and Frey, P. (2016). Dense granular flow rheology in turbulent bedload transport. *J. Fluid Mech.* 804, 490–512.

Meyer-Peter, E. and Müller, R. (1948). Formulas for bed-load transport. paper presented at 2nd Meeting, Int. Assoc. for. Hydraul. Environ. Engin. Res., Madrid.

Mouilleron, H., Charru, F., and Eiff, O. (2009). Inside the moving layer of a sheared granular bed. *J. Fluid Mech.* 628, 229–239.

Ni, W.-J., and Capart, H. (2006). Groundwater drainage and recharge by networks of irregular channels. *J. Geophys. Res.* 111, F02014

Ni, W.-J., and Capart, H. (2015). Cross-sectional imaging of refractive-index-matched liquid-granular flows. *Exp. Fluids* 56, 163.

Ovarlez, G., Bertrand, F., and Rodts, S. (2006). Local determination of the constitutive law of a dense suspension of non-colloidal particles through magnetic resonance imaging. *J. Rheol.* 50, 259–292.

Patil, V. A., and Liburdy, J. A. (2012). Optical measurement uncertainties due to refractive index mismatch for flow in porous media. *Exp. Fluids* 53, 1453–1468.

Papoulis, A., and Pillai, S. U. (1991). *Probability, random variables, and stochastic processes.* Boston: McGraw-Hill.

Pope, S. B. (2000). *Turbulent flows.* Cambridge, Cambridge University Press.

Revil-Baudard, T., and Chauchat, J. (2013). A two-phase model for sheet flow regime based on dense granular flow rheology. *J. Geophys. Res.* 118, 619–634.

Revil-Baudard, T., Chauchat, J., Hurther, D., and Barraud, P.-A. (2015). Investigation of sheet-flow processes based on novel acoustic high-resolution velocity and concentration measurements. *J. Fluid Mech.* 767, 1–30.

Sanvitale, N., and Bowman, E. T. (2012). Internal imaging of saturated granular free-surface flows. *Int. J. Phys. Model. Geo.* 12, 129–142.

Shapiro, L. G., and Stockman, G. C. (2001). *Computer vision.* Prentice-Hall, New Jersey.

Spinewine, B., Capart, H., Larcher, M., and Zech, Y. (2003). Three-dimensional Voronoï imaging methods for the measurement of near-wall particulate flows. *Exp. Fluids* 34, 227–241.

Spinewine, B., Capart, H., Fraccarollo, L., and Larcher, M. (2011). Laser stripe measurements of near-wall solid fraction in channel flows of liquid-granular mixtures. *Exp. Fluids* 50, 1507–1525.

Spinewine, B., and Capart, H. (2013). Intense bed-load due to a sudden dam-break. *J. Fluid Mech.* 731, 579–614

Sumer, B. M., Kozakiewicz, J., Fredsøe, J., and Deigaard, R. (1996). Velocity and concentration profiles in sheet flow layer of movable bed. *J. Hydraul. Eng.* 122, 549–558.

Teng, C.-L. (2003). Interactions of rigid particles and liquid in a concentrated dispersion: Lagrangian computations and stereo imaging of RIM fluidisation experiments. M.Sc. Thesis, Dept Civil Engineering, National Taiwan University, Taipei, Taiwan.

Torquato, S. (1995). Nearest-neighbor statistics for packings of hard spheres and disks. *Phys. Rev. E* 51,3170–3182.

Wiberg, P. L., and Smith, J. D. (1991). Velocity distribution and bed roughness in high-gradient streams. *Water Resour. Res.* 27, 825–838.

Wiberg, P. L., and Smith, J. D. (1991). Velocity distribution and bed roughness in high-gradient streams. *Water Resour. Res.* 27, 825–838.

Winoto, S. H., Li, H., and Shah, D. A. (2000). Efficiency of jet pumps. *J. Hydraul. Engng.* 126, 150–156.

Wu, F.-C., and Shih, W.-R. (2012). Entrainment of sediment particles by retrograde vortices: Test of hypothesis using near-particle observations. *J. Geophys. Res.* 117, F03018.

Yang, F.-L., and Hunt, M. L. (2006). Dynamics of particle-particle collisions in a viscous liquid. *Phys. Fluids* 18, 121506.

Zenit, R., Hunt, M. L., and Brennen, C. E. (1997). Collisional particle pressure measurements in solid-liquid flows. *J. Fluid. Mech.* 353, 261–283.

Zuber, N. (1964). On the dispersed two-phase flow in the laminar flow regime. *Chem. Engng Sci.* 19, 897.